The University of Southern Mississippi
The Aquila Digital Community

Dissertations

Fall 12-2020

A Library of Low Molecular Weight Fluorescent Probes for the Detection of Cu(II) and Fe(III) Ions

Ashley Johnson

Follow this and additional works at: https://aquila.usm.edu/dissertations

 Part of the Inorganic Chemistry Commons

Recommended Citation

Johnson, Ashley, "A Library of Low Molecular Weight Fluorescent Probes for the Detection of Cu(II) and Fe(III) Ions" (2020). *Dissertations*. 1832.
https://aquila.usm.edu/dissertations/1832

This Dissertation is brought to you for free and open access by The Aquila Digital Community. It has been accepted for inclusion in Dissertations by an authorized administrator of The Aquila Digital Community. For more information, please contact Joshua.Cromwell@usm.edu.

A LIBRARY OF LOW MOLECULAR WEIGHT FLUORESCENT PROBES FOR THE DETECTION OF COPPER(II) AND IRON(III) IONS

by

Ashley D G Johnson

A Dissertation
Submitted to the Graduate School,
the College of Arts and Sciences
and the School of Mathematics and Natural Sciences
at The University of Southern Mississippi
in Partial Fulfillment of the Requirements
for the Degree of Doctor of Philosophy

Approved by:

Dr. Karl J. Wallace, Committee Chair
Dr. Julie Pigza Member
Dr. Vijay Rangachari Member
Dr. Jason Azoulay Member
Dr. Wujian Miao Member

December 2020

COPYRIGHT BY

Ashley D G Johnson

2020

Published by the Graduate School

ABSTRACT

This dissertation reports the synthesis and photophysical properties of a family of rhodamine dyes (compounds **3.9**-**3.13** and **4.6**). The rhodamine dyes are prepared in two steps, and fully characterized by ESI-MS (Low and High resolution), X-Ray crystallography, NMR spectroscopy, and FT-IR spectroscopy. The coordination environment of the low molecular weight fluorescent probes (LMFPs) was systematically changed to investigate the thermodynamic behavior between the LMFPs and an array of metal ions (Cu^{2+}, Fe^{2+}, and Hg^{2+} ions) in protic and aprotic solvent systems. Upon coordinating to metal ions, the π-conjugation of the LMFPs changed, resulting in a transition from the colorless, spirolactam form of the rhodamine dyes to the colored, ring open forms. Ultimately, the goal was to prepare LMFPs that are soluble and functional in aqueous systems.

An extensive photophysical study was carried out in pure organic solvents (MeOH, DMSO, CH_3CN, and THF). Molecular probe **3.11a**, which contains a tridentate binding motif was found to coordinate both Fe^{3+} and Cu^{2+} in each of the solvents with calculated binding constants as high as $K = 7.1 \times 10^8\ M^{-2}$ for Fe^{3+} ions and $K = 2.1 \times 10^7\ M^{-1}$ for Cu^{2+} ions. In contrast, the binding affinity for compound **3.10** could not be determined. The binding constants are significantly influenced by the counterions of the metal ions. The triflate ion was found to dissociate more readily than the other counterions that were analyzed and is less likely to form bridging species in solution. This is consistent with the calculated binding constants obtained. Moreover, oxygen containing solvents inhibited the formation of coordination compounds between the LMFPs and metal ions.

Once we obtained an understanding of the coordination environments in organic solvents, attempts were made to investigate the optical properties in water. This proved to be challenging as Fe^{3+} hydrolysis inhibited the ability of the LMFPs to coordinate to the metal ion. The analysis of Cu^{2+} ions in aqueous environments was however possible. The calculated binding constant between compound **4.6** and Cu^{2+} in a 1:1 water-organic solvent system was found to be 1.6×10^{8} M^{-2}, showing that this LMFP could be used in aqueous environments. Due to the low solubility of $Fe(OH)_3$ (s) in water ($\log K_{sp} = 3.50 \pm 0.20$), these ions must be solubilized prior to coordination. In nature, Fe^{3+} ions are often bound to a class of organic molecules known as siderophores. Therefore, we incorporated the rhodamine dye into a siderophore motif. The artificial rhodamine siderophore, compound **5.13,** was designed and its synthesis is reported.

ACKNOWLEDGMENTS

I would like to first thank my graduate advisor, Dr. Karl J. Wallace, for his support, guidance, and encouragement during my time at the University of Southern Mississippi. He has taught me invaluable research skills and I look forward to continuing to learn from him as I transition into this new chapter in life. Additionally, I would like to acknowledge all members of the Wallace group, past and present. It has been a pleasure getting to know each of you.

I would also like to thank all of my committee members: Dr. Julie Pigza, Dr. Vijay Rangachari, Dr. Jason Azoulay, and Dr. Wujian Miao, for their advice and support throughout this endeavor.

I would like to recognize Mrs. Tina Masterson, Mrs. Sharon King and Dr. Hugh Broome. I am eternally grateful for your continued support and willingness to assist me even when it inconvenienced you. I want to also acknowledge to the University of Southern Mississippi Department of Chemistry and Biochemistry for the continued support of the faculty and staff.

Finally, I show gratitude to my family, friends, and Alvin. Thank you for your words of wisdom and encouragement. Your support is what brought me through.

DEDICATION

This study is wholeheartedly dedicated to my mother and father, Yvonne and Matthew Johnson. They have been my source of inspiration and continually provide me with their spiritual, emotional, and financial support.

TABLE OF CONTENTS

LIST OF TABLES

LIST OF ILLUSTRATIONS

LIST OF SCHEMES

LIST OF ABBREVIATIONS

ESI	Electrospray Ionization
LMFP	Low Molecular Weight Fluorescent Probe
MS	Mass Spectrometry
CID	Collision Induced Dissociation
NMR	Nuclear Magnetic Resonance
FT-IR	Fourier Transform Infrared Spectroscopy
CH_3CN	Acetonitrile
MeOH	Methanol
THF	Tetrahydrofuran
DMSO	Dimethyl sulfoxide
MES	2-(N-morpholino)ethanesulfonic acid
DMF	Dimethyl formamide
LoD	Limit of Detection
UV-Vis	Ultraviolet Visible
PPM	Parts Per Million
PPB	Parts Per Billion
PET	Photoinduced Electron Transfer
FRET	Fluorescence Resonance Energy Transfer
HOMO	Highest Occupied Molecular Orbital
LUMO	Lowest Unoccupied Molecular Orbital

CHAPTER I – General Introduction

1.1 Sensor Technology

Sensors are used in almost every aspect of modern life; from the "check-engine" light in a car, to the smoke detectors in homes, people encounter some form of a chemical sensor daily without even thinking about it. In industry, fiber-optic sensors monitor process variables like temperature and pressure, whereas medical applications rely on the use of sensors for detecting and monitoring different medical conditions such as spikes in the blood glucose levels of a patient with Type 1 diabetes. Over the last several decades, the field of sensor technology has continued to expand rapidly and as a result, scientists have divided sensor technology into two broad types- (1) chemical sensors and (2) biosensors.[1] Both types of sensors have the same purpose; to measure an analyte quantitatively or qualitatively, however, the mechanism by which this sensing occurs may differ.[2]

Due to the ambiguous nature of the word "sensor", there is no universal definition of the term chemical sensor; the term is highly debated in the scientific community. One definition states that "*chemical sensors are miniaturized devices which can deliver real-time and online information in the presence of a specific compound or ions in complex samples*".[3] This information can then be used to measure, monitor, or identify different chemical compounds or species. Much like chemical sensors, the term "biosensor" is also broad, however, the International Union of Pure and Applied Chemistry (IUPAC) defines a biosensor as "*a device that uses specific biochemical reactions mediated by isolated enzymes, immune systems, tissues, organelles or whole cells to detect chemical compounds, usually by electrical, thermal or optical signals*".[4]

From the definition above, chemical sensors can be described as devices that convert a response into a measurable signal, such as an optical signal or a binary "on" or "off" signal. The focus of this dissertation is to prepare low molecular weight fluorescent probes (LMFP) as chemical sensors for Cu^{2+} and Fe^{3+} metal ions. Low molecular weight fluorescent probes are small organic or inorganic molecules with molecular weights less than 1,000 Daltons.[5] Throughout this work, the use of these chemical sensors for monitoring transition metal ions will be emphasized, as LMFPs can provide useful information about the concentrations of metal ions in solution as well as how the metal ions interact with ligand groups on a chemical sensor. Specifically, our aim is to be able to quantitatively analyze the concentrations of transition metal ions in 100% aqueous solutions.

1.2 Analytical Techniques for Metal Ions

All life forms have a need for regulated amounts of metal ions, which aid in physiological processes such as osmotic regulation, catalysis, metabolism, and signal transduction.[6] These metal ions are typically group I and group II metal ions such as Na^{+}, Ca^{2+}, Mg^{2+}, and K^{+} ions.[6] All of the other metals involved in biological processes are present in trace amounts. The term trace element is used to define any element having an average concentration of less than 100 ppm atoms or less than 100 $\mu g \cdot g^{-1}$; these elements constitute less than one percent of the elemental content in the human body.[7-8] These trace metal ions, specifically, Fe^{2+}, Fe^{3+}, Zn^{2+}, Cu^{2+}, Mn^{2+}, Co^{2+}, Ni^{2+}, Mo^{4+}, W^{6+}, and Cr^{3+}ions, are generally recognized as playing critical roles in the biology of different living organisms.[9]

Transition metal abundance and biological usage varies vastly across different superkingdoms.[6] One initial step in defining the usage of these metals by organisms is to quantify the metal content and speciation in the cells and tissues of different organisms. Metal ions can exist in different forms, these include hydrated species, "tightly" bound forms found within larger biological molecules such as proteins and nucleic acids, and "loosely" bound or labile species.[6] The total metal content (measured in ppm) is the summation of each of these diverse forms. Therefore, it is important to develop analytical techniques capable of detecting and measuring the chemical forms or speciation of metal ions in a complex matrix. Currently, there are a number of analytical techniques that permit the analysis of various metal species within the same specimen, some of these techniques will be highlighted in this chapter; however, the use of fluorescent sensors serves as an indispensable tool for the analysis of different metal species in biological and environmental samples.

Historically, a variety of analytical techniques for monitoring and measuring metal ions in different matrixes are used for example, atomic absorption spectroscopy (AAS),[10] atomic emission spectroscopy (AES),[11] inductively coupled plasma mass spectrometry (ICP-MS),[12] electrochemical techniques,[13] surface plasmon resonance, and X-ray spectroscopic methods (e.g., X-ray fluorescence (XRF), X-ray photoelectron spectroscopy (XPS), and X-ray absorption spectroscopy (XAS)).[14] Each of these techniques offer unique advantages for detecting and/or measuring different metal ion concentrations, however, they all suffer from similar problems, including low signal-to-noise ratio, low sensitivity, selectivity, and specificity, reusability, cost of the specialized technique, the preparation of the samples, and fouling/clogging of instruments.

To ensure that data obtained from the techniques described above is reliable, a professionally trained technician is often employed to prepare samples, operate and maintain instrumentation, and interpret results. Another drawback is that many of the instruments are only suitable for lab analysis only. This means that conducting on-site analysis is often unrealistic. A summary of the disadvantages and advantages are highlighted in table 1. Despite some drawbacks, these techniques are all valuable and will continue to play important roles in the analysis of metal ions.

Table 1.1 *Comparison of various metal sensing applications*

Analytical Technique	Advantages	Disadvantages
AAS [15]	High nanomolar LoD's; Can measure concentration of >68 elements in a sample	Liquid or dissolved samples only; Requires large sample volumes; Destroys samples; Takes 10-15 seconds to analyze each element Non-portable
ICP-MS [16]	Picomolar LOD's; Can analyze a sample and distinguish between ~82 elements in a sample in less than one minute	Laborious sample preparation; Sample requires acid digestion; Non-portable; High operational costs
Anodic Stripping Voltammetry [17]	Quantitatively determines specific ion species; Nanomolar-picomolar LOD's	Amalgam forming metals only (cannot monitor Fe^{2+}); Skilled analysts required
X-ray Fluorescence [18]	Non-destructive; Samples can be solid or liquid.	Non-portable; Requires large samples>1 gram; Micromolar LOD's

1.3 Chemosensors

The need to develop analytical methods that are simple, fast, reliable and portable has led to a greater reliance on the field of optical spectroscopy for the inexpensive and ultrasensitive detection of chemical analytes. Optical spectroscopy consists of a group of spectroscopic analytical techniques that measure the intensity and wavelength of radiation absorbed and emitted by a sample. Optical spectroscopy, for example, UV-Vis and fluorescence spectroscopy are of interest to the sensor community. Both techniques provide useful information regarding the interactions between LMFPs and different chemical species and. The advantage of fluorescence spectroscopy is the number of mechanisms that can be utilized in monitoring the analyte of interest These mechanisms include- photoinduced electron transfer (PET),[19] intramolecular change transfer (ICT),[20] metal-to-ligand charge transfer (MLCT),[21] Förster (coulombic) resonance energy transfer (FRET),[22] eximer/exciplex formation, twisted intramolecular charge transfer (TICT), aggregation induced emission (AIE),[23] excited-state intramolecular proton transfer (ESIPT),[24] and chelation enhancement fluorescence (CHEF).[25]

Metal ions have long been detected and analyzed by colorimetric methods due to their light absorbing properties which yield characteristic optical transitions.[9] However, in a complex environment where multiple metal ions and other light absorbing species are present, such as that of a cell, unique approaches are required to analyze the target analyte. One strategy is to use derivatized chromogenic dyes or chromophores. A chromophore is the part of a molecule that is responsible for its color and is usually made up of a series of conjugated π-bonds. The electrons are able to absorb photons as the electrons in the system resonate throughout the π-system .[26] Typically, the more

conjugated or longer the π-system, the longer the wavelength of the photon that can absorbed, i.e. red shift. This means that it is possible to design chromophores that will absorb light within a desired wavelength range. This can be achieved by derivatizing chromophores to produce a unique signal which changes upon interacting with specific analytes. Metal analysis via the use of LMFPs, which will be referred to as chemosensors and fluorophores, relies on the theory that the chemosensor-analyte complex will exhibit an optical response easily distinguishable from that of the unbound chemosensor.[27]

There are several general types of sensing mechanisms that can be exploited for studying the formation of host-guest complexes in solution (Figure 1.1). The chemosensors used in these mechanisms contain three components: a binding site, a spacer, and a signaling group (chromophore). The binding site is the part of the sensor that binds to the guest. These are specific ligand groups that are known to be selective for target analytes. A spacer is included to separate the chromophore and the receptor. They can be flexible in nature and range from simple alkyl chains to more complicated motifs that assists in electron transfer between the receptor and the signaling group. Lastly, signaling groups vary and may be composed of a variety of functional groups. They aid in observing a spectral change that indicates target binding.[28]

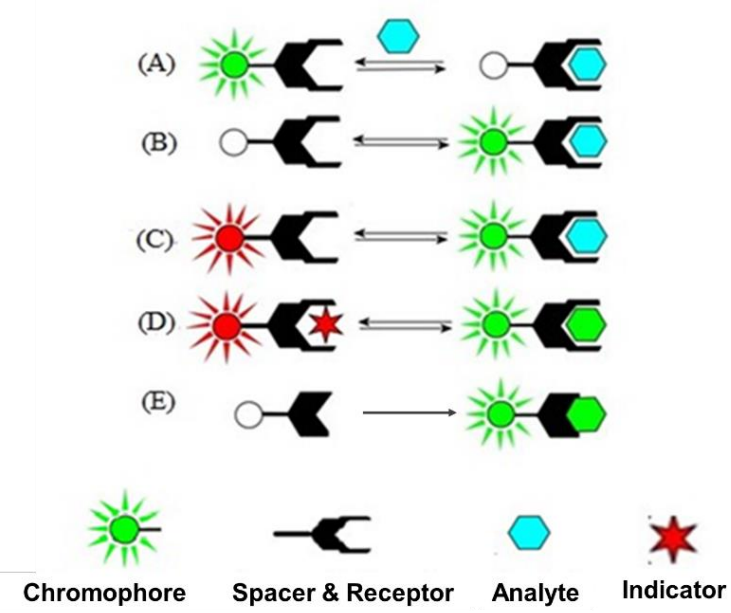

Figure 1.1 *General types of molecular sensors whereby the optical properties of the sensor changes upon binding to the target analyte (A) on-OFF (B) off-ON (C) Ratiometric (D) Displacement, and (E) Chemoreactand*

In the on-OFF sensing mechanism (figure 1.1a), the addition of a target analyte results in a decrease in the fluorescence intensity of the chromophore i.e., quenching. These types of sensing systems are very common; however, they can sometimes be less reliable than some of the other mechanisms highlighted, as there are numerous factors that can lead to a hypochromic shift (fluorescence quenching). Factors that induce fluorescence quenching will be addressed in chapter 3. Conversely, in the off-ON mechanism (figure 1.1B), the addition of a specific analyte to the system results in the amplification of the chromophore's fluorescence signal. The ratiometric sensor, shown in figure 1.1C, operates on the principle that the unbound sensor displays a unique spectral signal easily distinguishable from that of the bound sensor. The addition of a target analyte results in a gradual decrease in the fluorescence or absorbance signal of the unbound sensor, while a new signal, corresponding to the cooordinated species, emerges

at a different wavelength. Similar to the ratiometric sensor, the displacement assay (figure 1.1D) demonstrates a simultaneous hypochromic and hyperchromic shift in its spectra. These spectral changes are however due to the replacement of an indicator species, which was initially coordinated to the sensor binding site, for a target analyte. This type of system relies on the idea that the spectral signal of the receptor changes in accordance with the species that is bound to its binding site. Lastly, the chemoreactand system (figure 1.1E), can be used for sensing neutral species, whereby non-reversible bonds are formed between the receptor and analyte The ligands in the binding site of the receptor form covalent bonds with the analyte, resulting in a change in the fluorescence signal of the chromophore. This change can be in the form of a bathochromic or hypsochromic shift or a turn on/off the chromophore's fluorescence.

Fluorescence spectroscopy is ubiquitous in biological research and has been used for many years, for example, SYBR green- an asymmetrical cyanine dye, has been used as a commercially available fluorescent stain to bind to and visualize DNA bands in agarose gel electrophoresis since the early 1990's.[29] The vast and continuously expanding selection of commercially available fluorophores, some of which are highlighted in figure 1.2, provides scientists with the flexibility needed to design molecular probes that can be applied to a broad range of sensing applications. Fluorophores, which are similar to chromophores in terms of π-bond delocalization, are fluorescent compounds that can re-emit light upon light excitation. Despite the similarities between fluorophores and chromophores, it is important however to note that not all chromophores can fluoresce because the spontaneous emission process is dominated by rapid non-radiative decay.

Examples of non-fluorescent chromophores include hemoglobin and cytochromes.[30] Fluorescent molecules can be divided into two classes:

1. *Intrinsic fluorophores*: These are fluorophores that occur naturally. They include aromatic amino acids, reduced nicotinamide adenine dinucleotide (NADH), flavins, derivatives of pyridoxyl, and chlorophyll. These molecules are typically very large (measured in kiloDaltons).[31]
2. *Extrinsic fluorophores or fluorescent particles*: These are added to a sample to produce fluorescence signals, or to change the spectral properties of the sample.[31] These can be in the form of:

- *Organic and inorganic small molecules*: Organic and inorganic small molecules: Non-protein, synthetic molecules composed of various functional groups which affect the molecules properties. They are typically much smaller than intrinsic fluorophores (measured in Daltons).
- *Quantum dots*: Fluorescent semiconductor nanoparticles whose optical properties are controlled by their sizes, which range from 1-10 nm.[32]

The molecules in each of these groups offer unique features which should be taken into consideration when determining which fluorophore to use for a specific application. A variety of fluorophores belonging to the organic small molecule class are shown in figure 1.2. The derivatization of these molecules contributes to their overall photostability and improved solubility, selectivity, and sensitivity for use in biological and environmental systems. The size of organic small molecules can be a benefit over naturally occurring biological fluorophores for bioconjugation strategies, and they also tend to be less cost prohibitive than quantum dots, which have been found to pose notable

risks to human health and the environment under certain conditions.[33] Organic small molecules can be crosslinked to macromolecules, such as cell penetrating peptides without interfering with proper biological function, and they can also be designed to mimic biologically relevant metal-chelating motifs, thus making them viable candidates for bioimaging applications and other forms of molecular sensing.[32]

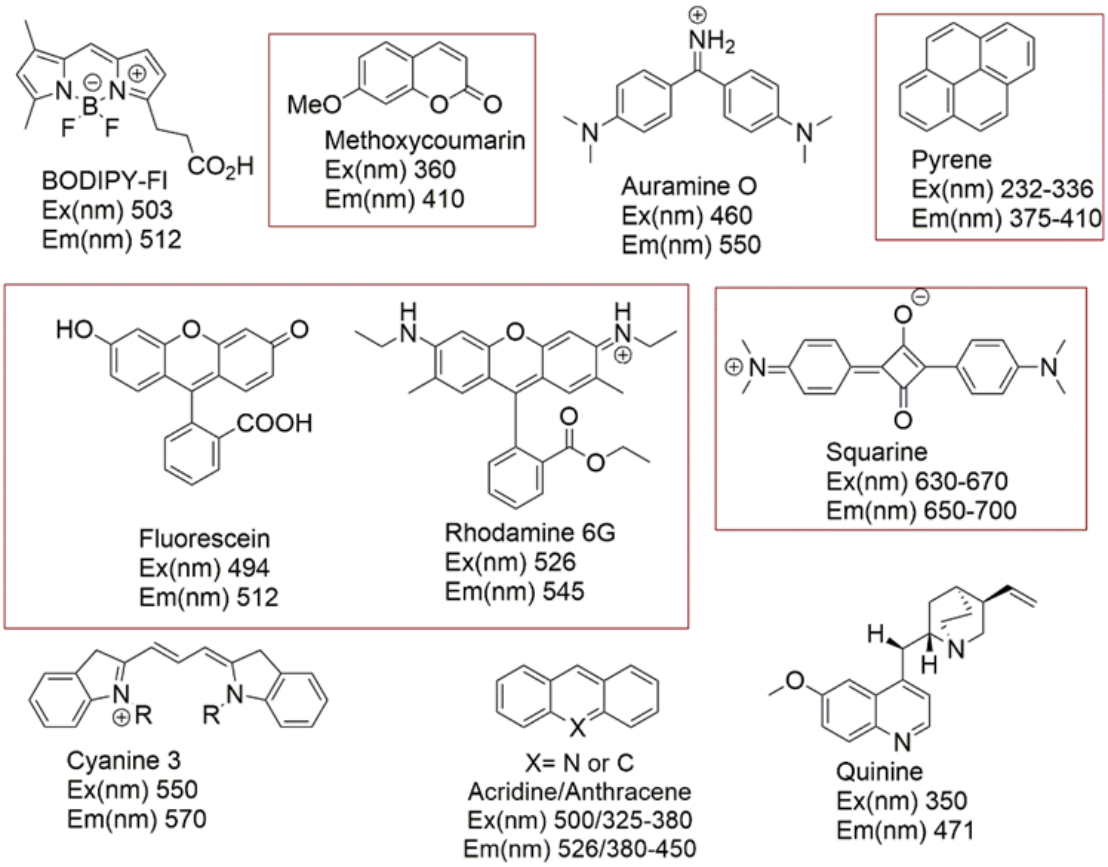

Figure 1.2 *Small molecule organic fluorophores commonly used in molecular probe design. Fluorophores highlighted are those used in the Wallace research group for molecular probe design. Note: The typical values listed are maximal excitation and emission wavelengths as fluorophores typically emit over a fairly wide range of wavelengths. These values may vary slightly depending on the solvent system.*

Donor ligands, attached to fluorophores act as Lewis bases and form coordination complexes with metal cations through coordinate covalent bonds (dative bonds).[34] The

formation, and stability of a coordinate covalent bond depends on the environment in which the complex forms, i.e., organic or aqueous solvent, as well as the complementarity of the acid-base pairs. Hard Lewis bases on the chromophore typically form more stable complexes with hard Lewis acids (metals) and soft Lewis bases form stable complexes with Lewis acids. This concept was established by the Pearson acid-base concept (HSAB), proposed by Pearson in the 1960's.[35] There is both a qualitative and a quantitative aspect to this concept. Firstly, to use empirical rules established by HSAB to predict the stability of distinct metal complexes, and secondly, to use Klopman's frontier molecular orbital (FMO) analysis by studying the interactions between the HOMO's and LUMO's of different species. According to FMO analysis, the interaction between an acid and a base are regulated by the relative energies of the participating HOMO of the base and LUMO of the acid. Large energy gaps between the HOMO and LUMO of a species increase its hardness. Quantitatively, the absolute hardness of a species can be determined using equation 1.1 or 1.2

$$\text{Hardness} = n = \frac{\text{Ionization energy(I)-Electron affinity(EA)}}{2} \tag{1.1}$$

$$\text{Hardness} = n = \frac{E_{LUMO}-E_{HOMO}}{2} \tag{1.2}$$

Qualitatively, the terms "hard" and "soft" serve to describe the relative polarizability, ionic radii, charge and molecular orbitals of the Lewis acid and base pairs that are associated through dative bonds. Generally, polarizability increases as the volume occupied by electrons increases. Larger atoms tend to have more 'loosely' held electrons in contrast to smaller atoms with 'tightly' held electrons, [36] Polarizability

therefore decreases from left to right, and increases as we move down the columns of the periodic table. 'Hard' species are generally harder to polarize, whereas 'soft' species tend to be easily polarizable. [35] In short, hard acids and bases have small ionic radii, are weakly polarizable, and have high positive and negative charges, whereas soft acids and bases have large ionic radii, are more polarizable and have lower positive and negative charges. An extensive list of species that are classified as hard, soft, and borderline acids and bases can be found in appendix A.1.

The large electronegativity differences between hard acids and bases result in complexes with ionic characteristics, whereas the small electronegativity differences between soft species give rise to covalent-like interactions. Interactions between hard and soft species are polar-covalent in nature and tend to be less stable. These polar-covalent compounds readily react with complementary species to form more ionic and covalent compounds. An example of the stable covalent interactions that exist between two soft species, S atoms and Ag^+ ions, is shown in figure 1.3. The interactions between the sulfur atoms in the macrocycle and the Ag^+ ion, give rise to a stable octahedral complex, with optimal bond angles. The complex is even further stabilized by the macrocycle effect. On the other hand, the polar-covalent interactions between Ag^+ ions and the oxygen atoms of 18-crown-6 in figure 1.3, give rise to a less stable complex with strained bond angles. Use of the HSAB theory is important for sensor design and will be further emphasized in chapters 2 through 5 of this work.

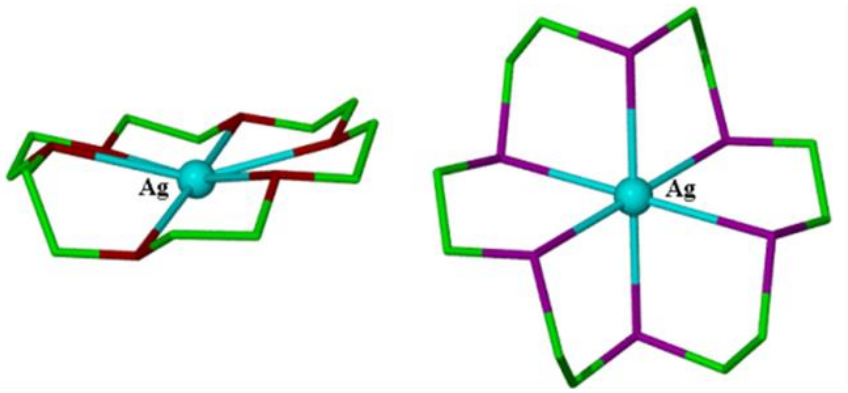

Figure 1.3 *Silver complexes formed via polar covalent bonds and covalent bonds to oxygen and sulfur, respectively.*

1.3.1 Fluorescence Mechanisms

When a fluorophore absorbs a photon of light, an energetically excited state is formed. This process is extremely fast and lasts for about 10^{-15} seconds. The electron in the excited state is paired to a second electron in the ground state (Figure 1.4A). The electron remains in this excited state for a very short time, and return to the ground state is spin allowed and occurs rapidly by the emission of a photon (Figure 1.4B).[37] During the electrons return to the ground state, energy is emitted. Emitted light is always at a longer wavelength than the absorbed light due to limited energy loss by the molecule prior to emission.[38] The fate of this species is dependent on a number of factors, for example, the nature of the fluorophore and its solvent system, but the end result is deactivation (loss of energy) and return to the ground state.

An excited electron can also undergo other forms of relaxation and emission aside from fluorescence. Each electronic state has several vibrational states. If the electron is excited to one of these states it will undergo a vibrational relaxation (non-radiative deactivation) before it can return to the ground state (S_0). The electron can also

experience intersystem crossing, where the electron spin flips to a triplet excited state. An electron that is in the (T_1) triplet excited state is no longer spin paired with the electron in its original ground state orbital. The electron that is in the excited triplet state will relax to the singlet ground state and emit a photon as phosphorescence.[39]

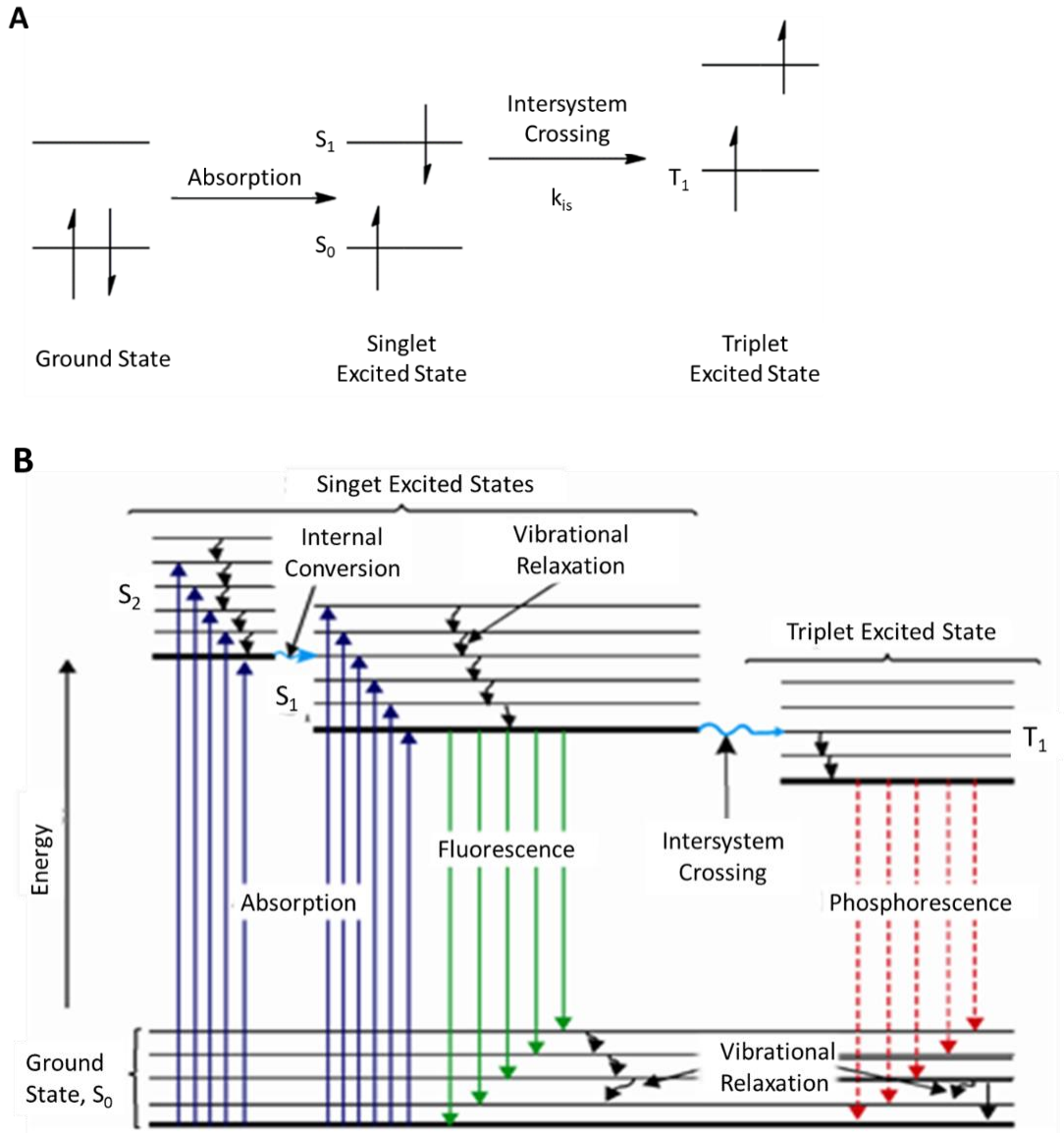

Figure 1.4 *(A) Illustration of the spin-pairing of electrons in the singlet and triplet excited states. (B) Jablonski diagram showing the excitation and deactivation pathways of photon.*

Fluorescence Resonance Energy Transfer

There are various energy transfer mechanisms that induce fluorescence in molecules. One such mechanisms is the Fluorescence Resonance Energy Transfer (FRET) mechanism. The FRET mechanism can be explained using classical physics as an electrodynamic phenomenon. Whereby, the FRET process occurs when the fluorescence spectrum of a molecule in an excited state, known as the donor, overlaps with the absorbance spectrum of a molecule in the ground state, known as the acceptor (see figure 1.5). There is no photon produced in this energy transfer from the donor to the acceptor.[40] This energy transfer is the result of long range dipole-dipole interactions between the donor and the acceptor. The FRET mechanism is 50% efficient at a range of about 20 to 60 Å, this is known as the Förster distance and is denoted as "J" in Figure 5.[40] The transfer efficiency is a quantitative value and is the fraction of photons that are absorbed by the donor that is transferred to the acceptor. The transfer efficiency of FRET can be calculated by considering the relative fluorescence intensity of the donor when it is in the presence of the acceptor and in the absence of the acceptor.

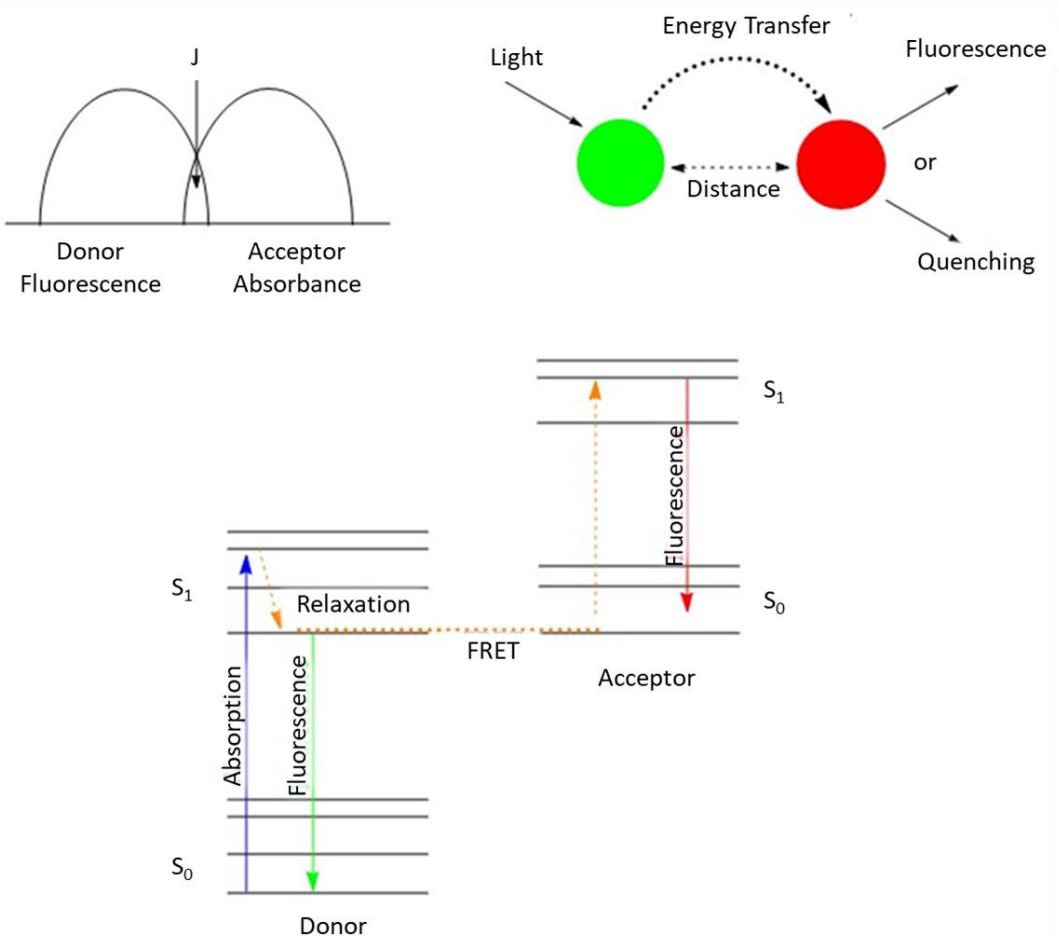

Figure 1.5 *FRET mechanism between a donor and acceptor molecule within an acceptable Förster distance to promote the energy transfer.*

Excited-State Intramolecular Proton Transfer

Another unique fluorescence mechanism that is utilized by the sensor community is the excited-state intramolecular proton transfer (ESIPT) mechanism. This mechanism is the result of a proton transfer between tautomers, such as imine-enol and keto-enamine tautomers.[24] The ESIPT mechanism is stabilized by a strong intramolecular hydrogen bond and resonance assisted hydrogen bonding.[41] Though this process occurs rapidly, energy is lost during the proton transfer which often results in a very large Stoke's shift. A large Stoke's shift is an extremely attractive property in the design on molecular probes

as it minimizes the likelihood of inaccuracies in measurements as a result of the inner-filter effect.

Photoinduced Charge Transfer

When a fluorophore contains both an electron withdrawing group and an electron donating group, an intramolecular charge transfer can take place between the donor and acceptor upon excitation of the sample with the appropriate wavelength of light. Excitation of the fluorophore results in a change in the dipole moment within the sample; the effects are then observed as either a bathochromic or hypsochromic shift in the absorption and emission spectra. This same logic can be applied to the coordination of a donor or acceptor moiety with an anion or cation. The coordination of an electron donating group to a cation decreases the electron donating character. This in turn, reduces the conjugation of the system and ultimately results in a hypsochromic shift, along with a decrease in the molar extinction coefficient of the fluorophore. In contrast, the coordination between and electron withdrawing group and a cation enhances the electron withdrawing character which results in a bathochromic shift as well as an increase in the molar extinction coefficient. [42] In addition to these wavelength shifts, changes in the fluorescence lifetimes and quantum yields may also be observed. Fluorescence lifetimes and quantum yields will be discussed in detail in chapter 2.

Other fluorescence mechanisms such as and “On or Off” excimer emission and photoinduced electron transfer (PET), which results in fluorescence quenching, will be discussed in chapters 2 and 3 of this work, respectfully.

1.4 Target Analytes

The World Health Organization (WHO) and the Environmental Protection Agency (EPA) have outlined daily intake limits for most trace metals (see appendix A.1). as the accumulation of these metals in humans can pose serious health risks. A variety of the metals in this class have demonstrated important roles in biological processes and a number of them also serve as alloys for use in mechanical engineering and in the manufacturing of artefacts, machinery, buildings, automobiles, and jewelry.[6] Furthermore, the optical properties of these metals, which are a consequence of their unique electronic transitions, contribute to their continued use as pigments in paints and inks.[43]

The main source of trace metals for plants is via their root system, whereas animals are exposed to these metals by mechanisms such as inhalation, the consumption of foods and beverages, and manual handling. The toxicity and symptomatology of each metal depends on several factors, including the speciation of the metal in question, as metals can exhibit multiple oxidations states with varying levels of toxicity affiliated with each of the different states[44]. Another important factor is the total dose absorbed, and whether the exposure was acute or chronic (see appendix A.1), the age of the person and the route of exposure.

Due to their non-biodegradability, trace metal contaminations of land resources continue to be the focus of numerous environmental studies and attract a great deal of attention worldwide.[45] The intensive use of sewage sludge, municipal compost, pesticides, fertilizers, and the development of industries without effective effluent controls has resulted in accumulation of these metals in soil.[46] Trace metals can remain in

the soil for decades after initial introduction because most metal ions do not readily undergo chemical degradation.[47] They are therefore a potential cause of phytotoxicity which ultimately leads to poisoning along the food chain.[46]

1.4.1 Copper Ions

Copper is a trace metal nutrient essential for most forms of life; it is also the third most abundant transition metal found in humans.[48] Copper occurs in two oxidation states within biological systems, either the reduced, cuprous form (Cu^{+}) or the oxidized cupric form (Cu^{2+}). The Cu^{+} ion is thought to be the dominant oxidation state of labile copper in cells due to the function of membrane reductases which reduce extracellular Cu^{2+} prior to import.[6] The 2+ oxidation state of copper plays several key roles in enzymes along with functions in redox reactions, and it is also incorporated into a number of metalloenzymes involved in hemoglobin formation, carbohydrate metabolism, catecholamine biosynthesis, and cross-linking of collagen, elastin, and hair keratin.[44] Though the redox capabilities of copper ions are critical in several physiological processes, unregulated concentrations of copper in persons can induce oxidative damage and toxicity in cells.

Cupric ion poisoning typically results from the ingestion of gram quantities of Cu^{2+} ions in foodstuffs and beverages.[49] Cupric ions can undergo Fenton chemistry resulting in the formation of reactive oxygen species (ROS). Examples of ROS include peroxides, superoxide, hydroxyl radical (scheme 1.1) and singlet oxygen species. These radicals lead to oxidative damage in cells which ultimately causes irreversible damage to vital organs and systems. The rate of oxygen consumption is particularly high in soft tissue like the brain, therefore if there is an excess in the production of ROS in vital cells,

they become vulnerable to oxidative damage. Prolonged exposure to these radicals can result in hemolysis and jaundice, convulsions, hypotension, cirrhosis of the liver, Wilson's disease, and Alzheimer's disease.[50].

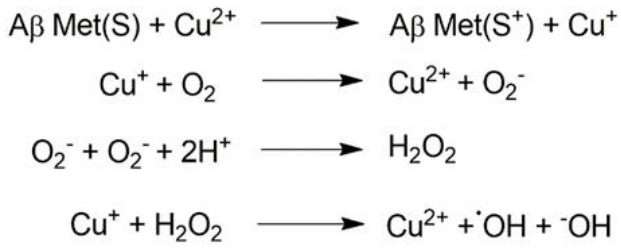

Scheme 1.1 *Cu^{+} ion mediated Fenton reaction. Aβ Met(S) = Cu^{2+} ion binding protein*

1.4.2 Ferrous and Ferric Ions

Iron is the most abundant transition metal in the human body, totaling between 3-5g in the average adult human with a cellular concentration of 50-100μM.[51] Trace amounts of Fe^{2+} and Fe^{3+} ions are important for biochemical processes in all living organisms.[52-54] Both Fe^{2+} and Fe^{3+} ions are involved oxygen transport,[55] electron transfer for DNA and RNA synthesis,[56] electron transfer in sulfur-iron clusters for mitochondrial respiration,[57] myelin synthesis,[58] neurotransmitter synthesis[58-60] and metabolism.[61, 62] The overall health of an organism depends to a certain extent on the homeostasis of chelatable and redox-active iron ions, also known as the cellular labile iron pool. This iron pool serves as a crossroad of cellular iron metabolism. However, despite the many positive biological functions of iron in the body, the U.S. Environmental Protection Agency (EPA) advises that the allowable amount of iron in drinking water be limited to 0.3 $mg \cdot L^{-1}$ as the overabundance of iron can result in irreversible damage to the human body.

In humans, if the homeostasis of this iron pool is disturbed, resulting in the accumulation of Fe^{2+} and Fe^{3+} ions in the body, persons may experience kidney and liver damage, hematological effects, and damage to their cardiovascular and central nervous systems. [61, 63] For example, Alzheimer's,[56, 64-66] Huntington's,[64] and Parkinson[65, 66] disease can all be linked to the overabundance of iron ions in the human body. Under cytosolic conditions (pH 7.4), labile iron is in a reducing environment with reactive oxygen species (ROS), such as peroxides, which allows for the conversion of any free Fe^{3+} ions to Fe^{2+} ions through Fenton chemistry (Scheme 1.2). The reaction of these ions with hydrogen peroxide, increases the amount of ROS in the body leading to irreversible cellular and organ damage.[67]

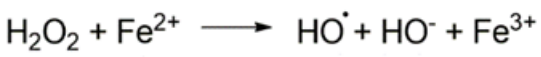

Scheme 1.2 *Fe^{2+} ion mediated Fenton Reaction*

Another unignorable reaction that ferrous ions undergo is the hydrolysis reaction. At neutral pH, the readily soluble iron 2+ is oxidized to iron 3+ which forms insoluble ferric hydroxides upon hydrolysis of the free ion. The formation of these insoluble hydroxides reduces the concentration of labile iron available for biochemical processes.[68]

1.5 Metal Hydrolysis Reactions

The term hydrolysis refers to the elimination, and fragmentation reactions in which water is the nucleophile, for example ester hydrolysis.[69]Amides also undergo hydrolysis reactions similar to those observed in esters, and polysaccharides can be hydrolyzed by glycoside hydrolases to yield more soluble and digestible sugars.[70]

Hydrolysis reactions are also related to energy metabolism and storage whereby the hydrolysis of pyrophosphate linkages in adenosine triphosphate (ATP) to produce inorganic orthophosphates, adenosine diphosphate (ADP), and adenosine monophosphate (AMP) releases energy that is used for biosynthetic processes necessary to maintain life.[71] Aside from organic mechanisms and biological reactions, hydrolysis reactions also play a major role in inorganic chemistry, more specifically metal ions in aqueous solution.

The ubiquity of water and metal ions that are present in the universal solvent means that hydrolysis reactions are ongoing and essential in nature. Therefore, one cannot ignore the presence of metal aquo complexes and the hydrolysis reactions that they undergo when designing molecular recognition systems for metal ions, this is particularly true for highly charged species, such as ferric ions. The conditions (i.e. pH) under which metal ions hydrolyze are largely dependent on the physical properties of the metal ion in question, namely, the ionic charge (z), and the ionic radius (r). Typically, the larger the charge on the metal, the smaller the radius and the lower the pH at which the metal ion will hydrolyze.[72] An example of this is the ferric ion which will be discussed in this work. Ferric ions form a variety of species across the pH scale. At pH values greater than 4, the species formed are typically insoluble in water. The formation of these precipitates and other iron species that will be highlighted in section 1.5.3, often complicate efforts to monitor the concentration of metal species in solution by classical potentiometric and spectrometric analysis.

Due to its amphoteric nature, water can serve as a Lewis base and hydrate ions present in aqueous solutions. Metal ions act as Lewis acids in aqueous solution and form

metal hydrated ions with the general formula $[M(H_2O)_n]^{z+}$, where "n" corresponds to the solvation number (the number of water molecules in the metal ion's inner coordination sphere) and "z+" is the charge on the species. The water that is bound to the metal can also ionize (hydrolyze).[72] The positive charge on the metal ion draws electron density from the O-H bond in water. This increases the bond's polarity and ultimately causes it to break, producing a proton and a metal hydroxide complex which lowers the overall pH of the solution. The reaction may be written as:

$$[M(H_2O)_n]^{z+} + H_2O \rightleftarrows [M(H_2O)_{n-1}(OH)]^{z-1} + H_3O^+$$

Scheme 1.3 *General ionization of a hydrated metal ion species yielding a metal hydroxide and hydronium ion*

The first-row transition metal ions typically have four or six water molecules coordinated to the metal ion (inner coordination sphere). Additional water molecules then form hydrogen bonding interactions to those hydrated metal water molecules, forming an outer coordination sphere, which has a more ordered structure when compared to the bulk solvent, figure 1.6. Ligands can displace water molecules from the inner coordination sphere of metals via ligand exchange reactions, forming inner sphere complexes. These ligand exchange reactions often result in the formation of extremely stable products due to an increase in the entropy of the system upon product formation. This is especially true for multidentate ligands that can bind to metals through multiple donor sites. As is shown in scheme 1.4, ligand exchange reactions involving multidentate ligands increase the disorder of the of the system as we move from the reactant side to the product side. As a result, the products formed between multidentate ligands and metal ions display much

smaller ΔG than those observed for reactions between monodentate ligands and metal ions. Reversing this process would require moving from a highly disordered state to a much more ordered one. For this reason, the products formed in these types of reactions are very stable; this is known as the chelate effect.

$$[Cu(H_2O)_6]^{2+} + 2NH_3 \rightleftharpoons [Cu(NH_3)_2(H_2O)_4]^{2+} + 2H_2O \quad \textbf{log K = 7.86}$$

$$[Cu(H_2O)_6]^{2+} + EDTA^{4-} \rightleftharpoons [Cu(EDTA)]^{2-} + 6H_2O \quad \textbf{log K = 18.7}$$

Scheme 1.4 *Example showing reserved entropy in a ligand exchange reaction using NH_3, a monodentate ligand, vs increased entropy with $EDTA^{4-}$, a hexadentate ligand.*

Outer sphere complexes on the other hand are the result of no direct bond formation between the ligand and metal ion. The ligand is rather held to the metal ion by a combination of hydrogen bonding and electrostatic attractions. It is however important to acknowledge the importance of outer sphere complexes as they are the initial step in all complex formation processes and therefore affect the kinetics of inner sphere complex-formation.[73]

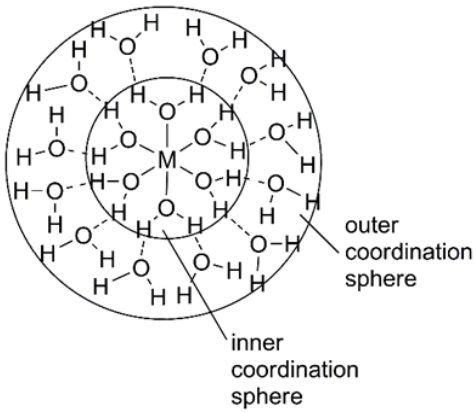

Figure 1.6 *Metal aquo ion in water showing the inner and outer coordination spheres.*

The chemistry of water is vastly different depending on the pH of the solution. As demonstrated in scheme 1.4, the reaction of water with metal ions results in the formation of hydrated metal hydroxides as well as hydronium ions, which often lowers the pH of the solution. An example of this is demonstrated in the addition of various hydrated aluminum sulphate species ($Al_2(SO_4)_3 \cdot 16H_2O$ and $Al_2(SO_4)_3 \cdot 16H_2O$) to garden soil to reduce its pH. The aluminum sulphate reacts with the water molecules in the soil and hydrolyzes, forming aluminum hydroxide and dilute sulfuric acid. The resultant aluminum hydroxide is amphoteric and can then serve as a Bronsted-Lowry acid or base depending on the pH of the surrounding water, allowing for further adjustment of the pH of the water. As a consequence of this varying pH, the speciation of the metal ion also changes.[72] By taking advantage of the acid-base behavior of aqueous systems, metal ions can be remediated from water as metal hydroxides.

It is however important to note that the change in speciation of metal ions over various pH ranges directly affects the specificity of molecular sensors. Take for example a sensor that is stated to be selective for Fe^{2+} ions in aqueous environments. To accurately determine the selectivity of the sensor for Fe^{2+} ions over Fe^{3+} ions, extensive studies in oxygen deprived environments would be necessary, as Fe^{2+} ions are readily oxidized to Fe^{3+} ions under acidic or neutral, oxygen rich conditions.[74] Upon conducting extensive literature searches, we have found that such precautions are often omitted from published work. Not only must the oxidation state of the metal species be taken into consideration but also the different organic and inorganic forms of the metal that are present in solution. Oh et al., developed a fluorescent sensor capable of distinguishing between methyl

mercury and inorganic Hg^{2+} ions in aqueous solutions as well as cells. Oftentimes, research papers reference the selectivity a LMFP for a particular metal ion, but do not highlight speciation selectivity. This work will demonstrate the level to which different conditions such as the effect of solvent and counterions affect the binding ratios between LMFP's and metal ions.

As the work presented in this dissertation mainly highlights LMFP's for analyzing cupric, ferrous, and ferric ions, it is important to specifically discuss the hydrolysis reactions of these specific metals over a range of pH values in aqueous environment.

1.5.1 Hydrolysis of Copper

The thermodynamic stabilities of Cu^{+} and Cu^{2+} species in aqueous solution depend on the nature of anions and other ligands present in solution. The thermodynamic stability of a species is a measure of the extent to which the species will form or be transformed into other species under certain conditions. For example, in weakly acidic freshwater systems (pH ≈ 6), void of organic ligands, Cu^{2+} speciation is dominated by the $Cu^{2+}_{(aq)}$ species, with $CuSO_{4(aq)}$ as a minor species.[75, 76] This means that $CuSO_{4(aq)}$ has a relatively low stability constant in weakly acidic fresh water. This is contrary to seawater (pH 7.9- 9)where $CuCO_{3(aq)}$ is the dominating species and $Cu^{2+}_{(aq)}$ and other cupric species are minor species.[75] In aqueous environments containing inorganic ligands, the Cu^{2+} species is the predominant oxidation state due to the disproportionate reaction shown in scheme 1.5. Electrochemical studies conducted by Fenwick, report an equilibrium constant of log K ≈ 6 for the equilibrium between cupric ions, cuprous ions, and metallic copper in the presence of inorganic ligands like $[ClO_4]^{-}$ and $[SO_4]^{-}$, which

are considered as hard Lewis bases.[77] However, in the presence of strong field ligands, like carbon monoxide (CO), which are capable of π-backbonding, Cu^{+} may become the dominant oxidation state, as both Cu^{+} and CO are soft species whereas Cu^{2+} is a borderline species.[75]

$$2Cu^{+}_{(aq)} \rightleftharpoons Cu^{2+}_{(aq)} + Cu_{(s)}$$

Scheme 1.5 *Scheme showing the disproportionate reaction as Cu^{+} is converted to Cu^{2+} and metallic copper in aqueous environments containing hard Lewis bases.*

The redox capability of Cu^{+} and Cu^{2+} ions is what makes copper useful in various steps of energy generation but it is also what allows them to aid in the generation of reactive oxygen species in organisms via Fenton Chemistry (see chapter 1.4.1).[78] The hydrolysis of copper ions in aqueous environments reduces their toxicity, as the concentration of labile Cu^{+} and Cu^{2+} ions decreases due to the formation hydrated copper species or insoluble copper hydroxides. The Cu^{+} ion forms a limited number of hydrolysis products, these include $CuOH_{(aq)}$ and $Cu(OH)_{2(s)}$. The Cu^{+} ion also forms the antifouling agent, $Cu_2O_{(s)}$, in the presence of oxygen.[79] Unlike Cu^{+} ions, the hydrolytic reactions that occur for Cu^{2+} ions result in the formation of both monomeric and polymeric species. The products of these hydrolysis reactions include $CuOH^{+}$, $Cu(OH)_2$, $Cu(OH)_4^{2-}$, $Cu_2(OH)_2^{2+}$, $Cu_2(OH)^{3+}$, and $Cu_3(OH)_4^{2+}$.[75,79] Above pH >7 for moderately dilute solutions (micromolar concentrations), and pH ~5 for concentrated solutions, amphoteric cupric hydroxide precipitates form in aqueous environments (figure1.7). These precipitates can be dissolved in strongly alkaline solutions, resulting in the formation of species such as $Cu(OH)_3^{-}$ and $Cu(OH)_4^{2-}$.[75,76] To avoid the formation of insoluble copper precipitates during chemical analysis, a low concentration of the metal

ion should be maintained (< 10^{-7} M). At such low concentrations, the $Cu(OH)_{2(aq)}$ species is the dominant form between pH 8.5-10.5.[79]

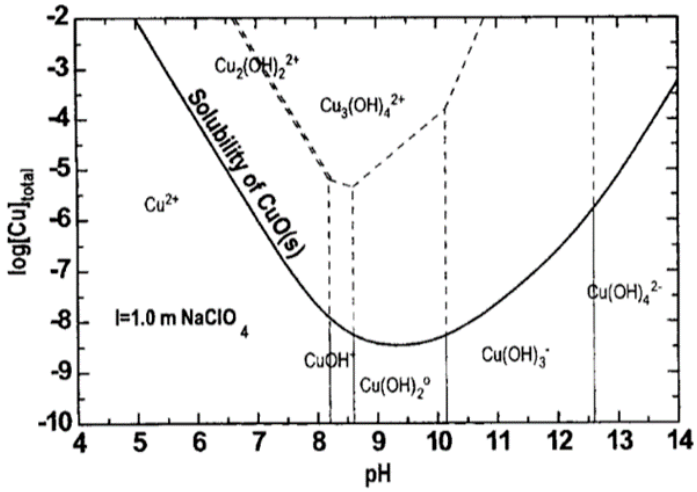

Figure 1.7 *Predominance diagram of Cu^{2+} hydroxo-complexes in 1.0M $NaClO_4$ at 25C. Cu^{2+} concentration is 1×10^{-5}M. Reprinted with permission from (Plyasunova, N. V.; Wang, M.; Zhang, Y.; Muhammed, M., Critical evaluation of thermodynamics of complex formation of metal ions in aqueous solutions II. Hydrolysis and hydroxo-complexes of Cu2+ at 298.15 K. Hydrometallurgy 1997, 45, 376-51). Copyright (1997) Elsevier."*

The speciation of Cu^{2+} ions in solution requires careful consideration when interrupting data, otherwise the results might be misleading and imprecise. One cannot ignore the existence of different Cu^{2+}species in solution when calculating binding constants between organic ligands and copper ions, as the formation of a Cu^{2+}-coordination compound often requires initial displacement of the hydroxide ions before coordination between the metal and ligand can occur. The strength of the interaction between reagents that come together to form a coordination complex, in this case Cu^{2+} and OH^- ions, is measured in terms of a stability constant (β). The stability constant is a cumulative value of all the stepwise *K* binding constants. The larger the value of β, the more stable the complex and the less likely it will be for a ligand to be able to displace

the existing Lewis bases to form a complex with the copper ions. From the stability constant, the K_{eq} for each step during complex formation can be calculated.

$\text{Log}\beta = K$

$M + L \rightleftharpoons ML$	$K_1 = \frac{[ML]}{[M][L]}$ $[ML] = K_1[M][L]$	$\beta_1 = K_1$
$ML + L \rightleftharpoons ML_2$	$K_2 = \frac{[ML_2]}{[ML][L]}$ $[ML_2] = K_2[ML][L]$	$\beta_{I2} = K_1 \times K_2$
$ML_2 + L \rightleftharpoons ML_3$	$K_3 = \frac{[ML_3]}{[ML_2][L]}$ $[ML_3] = K_3[ML_2][L]$	$\beta_{I3} = K_1 \times K_2 \times K_3$

Scheme 1.6 *Relationship between stability constant, β, and equilibrium constant, K, during complex formation.*

The β values and solubility constants (K_{sp}) for some copper hydrolysis products are shown in table 1.2. It should be noted that the monomeric hydrolytic species of both valency states have similar stability despite trends of metal species lower oxidation states to hydrolyze at much higher pH than the higher oxidation state.

Table 1.2 *Summary of the standard equilibrium and stability constants for Cu^{2+}-OH^- systems at 298.15 K, 1 bar. Refer to references* [79,80]

Reaction	**Constant**
$Cu^+ + H_2O \rightleftharpoons CuOH + H^+$	$\log\beta_1 = -7.85 \pm 0.41$
$Cu^+ + 2H_2O \rightleftharpoons Cu(OH)_2^- + H^+$	$\log\beta_2 = -18.64 \pm 0.60$
$Cu^{2+} + H_2O \rightleftharpoons Cu(OH)^+ + H^+$	$\log K_1 = -7.95 \pm 0.16$
$Cu^{2+} + 2H_2O \rightleftharpoons Cu(OH)_{2(aq)} + 2H^+$	$\log\beta_2 = -16.2 \pm 0.2$
$Cu^{2+} + 3H_2O \rightleftharpoons Cu(OH)_3^- + 3H^+$	$\log\beta_3 = -26.60 \pm 0.09$
$Cu^{2+} + 4H_2O \rightleftharpoons Cu(OH)_4^{2-} + 4H^+$	$\log\beta_4 = -39.74 \pm 0.18$
$2Cu^{2+} + H_2O \rightleftharpoons Cu_2(OH)^{3+} + H^+$	$\log\beta_{2,1} = -6.40 \pm 0.12$
$2Cu^{2+} + 2H_2O \rightleftharpoons Cu_2(OH)_2^{2+} + 2H^+$	$\log\beta_{2,2} = -10.43 \pm 0.07$
$3Cu^{2+} + 4H_2O \rightleftharpoons Cu_3(OH)_4^{2+} + 4H^+$	$\log\beta_{3,4} = -21.1 \pm 0.2$
$CuO(s) + 2H^+ \rightleftharpoons Cu^{2+} + H_2O$	$\log K_{sp} = 7.64 \pm 0.06$
$Cu(OH)_2(s) + 2H^+ \rightleftharpoons Cu^{2+} + 2H_2O$	$\log K_{sp} = 8.67 \pm 0.05$
$CuO(s) + H_2O \rightleftharpoons Cu^{2+} + 2OH^-$	$\log K_{sp} = -20.36 \pm 0.06$
$Cu(OH)_2(s) \rightleftharpoons Cu^{2+} + 2OH^-$	$\log K_{sp} = -19.33 \pm 0.05$

1.5.2 Hydrolysis of Iron

Similar to copper hydrolysis, the importance of iron chemistry in environmental, metallurgical, industrial and biological contexts makes understanding iron chemistry in water of fundamental significance.[81] In its metallic form, iron is a white, lustrous metal and exhibits high reactivity. In moist air, the metal is rapidly oxidized, producing hydrated Fe_2O_3, and when the metal is dissolved in dilute mineral acids, in the absence of air and with nonoxidizing acids, Fe^{2+} is formed.[82] The +2 and +3 oxidation states are the most common oxidation states for iron species, however oxidation states ranging from -2 to +7 have been reported.[82, 83]

In aqueous environments, such as seawater, labile iron concentrations are very low due to solubility restraints of the thermodynamically stable +3 oxidation state,

coordination by organic ligands, and photo- and bio-reduction of ferric chelates followed by dissociation and re-oxidation of Fe^{2+}, which increases the concentration of reactive inorganic Fe^{2+} and Fe^{3+} species.[84] Another major factor affecting the concentrations of ferric and ferrous ions in seawater is the precipitation of iron hydroxides followed by dehydration and crystallization to form insoluble oxyhydroxides.[84] The aqueous chemistry of iron is very complicated, and the low solubility of some iron species has made obtaining an unambiguous understanding of iron chemistry a challenege.[85] However, despite how complex the analysis of iron hydrolytic reactions may be, the precipitation of iron oxyhydroxide phases is extremely useful as these species are used as a means of remediating toxic arsenic from drinking water via surface adsorption.[86]

The hydrolytic reactions of Fe^{3+} ions are more frequently reported in the literature than those of the +2 oxidation state due to difficulties maintaining reducing conditions that inhibit the formation of even small amounts of Fe^{3+} ions in solution. Equally problematic is the tendency of Fe^{2+} hydroxo phases to precipitate after less than 1% of the total aqueous Fe^{2+} content has been hydrolyzed within the concentration ranges that allow for potentiometric and spectrometric measurements to be made.[74] The predominance diagrams in figures 1.8a-b highlight the concentration and pH ranges over which aqueous ferrous and ferric species can be efficiently analyzed at 25 ˚C. Despite the existence of a substantial amount of research on iron hydrolysis reactions, a significant amount of conjecture remains with respect to the stability of iron hydrolytic species.[87] The predominance diagrams suggest that at very low iron concentrations it is possible to inhibit the formation of iron hydroxide precipitates in solution. One drawback of this however is that extremely sensitive analytical techniques would be required to accurately

measure the concentration iron complexes in solution, and techniques to prohibit redox reactions between the two oxidation states would still be required.

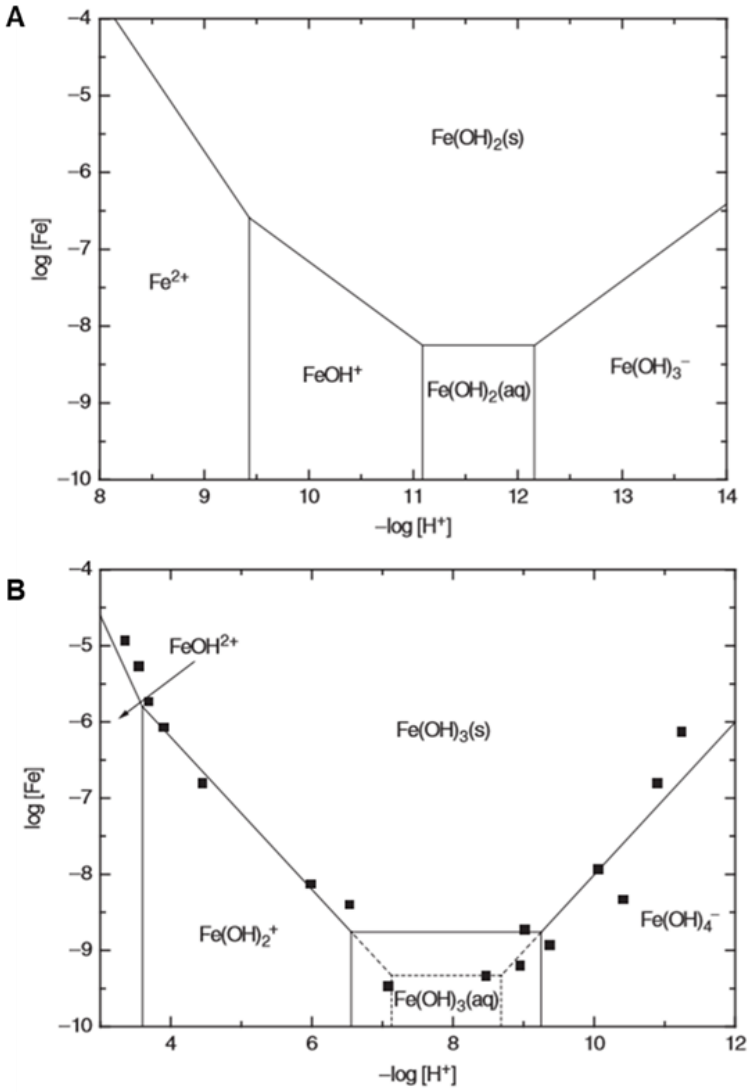

Figure 1.8 *(A) Predominance diagram for the speciation of the Fe^{2+} ion based on cumulative date collected at 25˚C in 2.0M $NaClO_4$ ionic medium. (B) Predominance diagram for the speciation of the Fe^{3+} ion based on cumulative UV-vis spectrophotometric measurements, potentiometric titrations, and solubility measurements at 25˚C in 0.01M $NaClO_4$. Solid squares represent the measured solubility found under these conditions.[81] UV-vis and potentiometric studies were performed with 10µM [Fe^{3+}]. "Reprinted with permission from (Brown, P. L.; Ekberg, C., First Transition Series Metals. In Hydrolysis of Metal Ions Vol. 2.). Copyright (2016) John Wiley and Sons."*

As previously stated, a significant amount of conjecture remains with respect to the stability of iron hydrolytic species. However, a study by Brown and Ekberg highlights the likely stability constants of the major iron hydrolysis products based on reproducibility of the results, reliability of the techniques used, and correlation of the results to similar works. The stability constants for the major hydrolytic reactions are shown in table 1.3.

Table 1.3 *Summary of equilibrium and stability constants for major iron hydrolysis products as reported by Brown and Eckberg. Refer to references* [74, 79, 81, 88]

Reaction	**Constant**
$Fe^{2+} + H_2O \rightleftharpoons Fe(OH)^+ + H^+$	$\log\beta_1 = -9.43 \pm 0.10$
$Fe^{2+} + 2H_2O \rightleftharpoons Fe(OH)_{2(aq)} + 2H^+$	$\log\beta_2 = -20.52 \pm 0.08$
$Fe^{2+} + 3H_2O \rightleftharpoons Fe(OH)_3^-{}_{(aq)} + 3H^+$	$\log\beta_2 = -32.68 \pm 0.15$
$Fe(OH)_2(s) + 2H^+ \rightleftharpoons Fe^{2+} + 2H_2O$	$\log K_{sp} = 12.27 \pm 0.88$
$Fe(OH)_3(s) + 3H^+ \rightleftharpoons Fe^{2+} + 3H_2O$	$\log K_{sp} = 3.50 \pm 0.20$
$Fe^{3+} + H_2O \rightleftharpoons Fe(OH)^{2+}{}_{(aq)} + H^+$	$\log\beta_1 = -2.20 \pm 0.02$
$Fe^{3+} + 2H_2O \rightleftharpoons Fe(OH)_2^+{}_{(aq)} + 2H^+$	$\log\beta_2 = -5.71 \pm 0.10$
$Fe^{3+} + 3H_2O \rightleftharpoons Fe(OH)_{3(aq)} + 3H^+$	$\log\beta_3 = -12.26 \pm 0.26$
$Fe^{3+} + 4H_2O \rightleftharpoons Fe(OH)_4^-{}_{(aq)} + 4H^+$	$\log\beta_4 = -21.60 \pm 0.23$
$2Fe^{3+} + 2H_2O \rightleftharpoons Fe_2(OH)_2^{4+}{}_{(aq)} + 2H^+$	$\log\beta_{22} = -2.75 \pm 0.08$

1.6 Summary

In summary, the importance of Cu^{2+} and Fe^{3+} ion detection has been highlighted in terms of their biological and environmental roles. Several analytical methods capable of detecting these analytes under varying conditions were discussed, such as atomic absorption and emission spectroscopy, ICP-MS, and anodic stripping voltammetry (section 1.2). Each of these methods however suffer from certain limitations, for example, the expensive cost of instrumentation, destruction of the sample, tedious sample

preparation, and the need for gram quantity amounts of the analyte. Optical spectroscopy was discussed as a suitable alternative to the previously mentioned techniques for the detection of Cu^{2+} and Fe^{3+} ions in environmental and biological samples. The use of fluorescent chemosensors serves as a sensitive, selective, inexpensive, and rapid detection method for specific analytes, without destroying the sample during analysis.

In this work, rhodamine and pyrene sensing motifs will be derivatized to contain appropriate binding sites for selective binding to target analytes. The photophysical properties of these two chromophores and the various sensing mechanisms that they undergo will be discussed in detail in this work. The pyrene sensing motif will be used to highlight metal ion detection in organic solvents. As pyrene is hydrophobic, it is difficult to functionalize this chromophore to prepare water soluble pyrene LMFPs. As a result, we changed the sensing motif to the rhodamine group as this family of chromophores is well known to be easily derivatized to improve water solubility. This introduction describes a general background however, specific introductory material that is relevant to each part of this work is highlighted at the beginning of each chapter.

CHAPTER II – A Pyrene Based Molecular Probe for Fe^{3+} Ion Detection

2.1 Background

The LMFP that will be discussed in this chapter belongs to the pyrene family and was designed for the detection of metal ions in aqueous solution. The addition of a sugar functional group to the pyrene backbone served two purposes: - to improve the water solubility of the probe, and as a source of Lewis basic sites to coordinate selectively to Fe^{3+} ions.

Pyrene and its derivatives are among the most commonly used fluorophores in the design of LMFPs. Their continued use as signaling motifs is owed to their intense fluorescence signals (Φ = 0.32 in cyclohexane), long excited state lifetimes (> 100 ns),[89] and ability to form excimer species.[90] Pyrene and its derivatives display strong emission bands between 375 and 420 nm in their monomeric forms, whereas the aggregated (dimeric) species display broad, red-shifted excimer bands between 410 and 490 nm, depending on the distance between the pyrene moieties.[91] The monomer- excimer equilibrium is used frequently throughout the literature as a means of studying the conformational changes in pyrene-based LMFPs that are used in host guest recognition.[92-95]

The term excimer is used to describe an excited dimer and is defined as a short-lived (ns) dimeric species which becomes associated in an electronic excited state and then dissociates once the molecule returns to its ground state.[96] When the interactions occur between the same molecules, the result is an excimer. However, if the interactions are between two different species, also known as a heterodimer, then an exciplex is observed (see figure 2.1). The absorption and emission bands associated with the

excimer/exciplex are typically observed at a longer wavelength than the monomeric species and the fluorescence bands are typically broad and featureless.[97]

Formation of the excimer is attributed to the overlap of the HOMO of one pyrene unit with the LUMO of another pyrene unit, this is known as a dynamic excimer.[91] In contrast, a static dimer, is the result of the excitation of the ground state dimer formed via π-π stacking or hydrophobic effects. The molecular components of dynamic excimers are able to fully overlap in comparison to static excimers which are held together by forces such as van der Waals forces that do not maximize the overlap of the two molecules. Static excimers therefore have lower stabilization energy than dynamic excimers and occur at higher energies.[96] As a result, dynamic excimers are typically observed at longer wavelengths than static excimers.

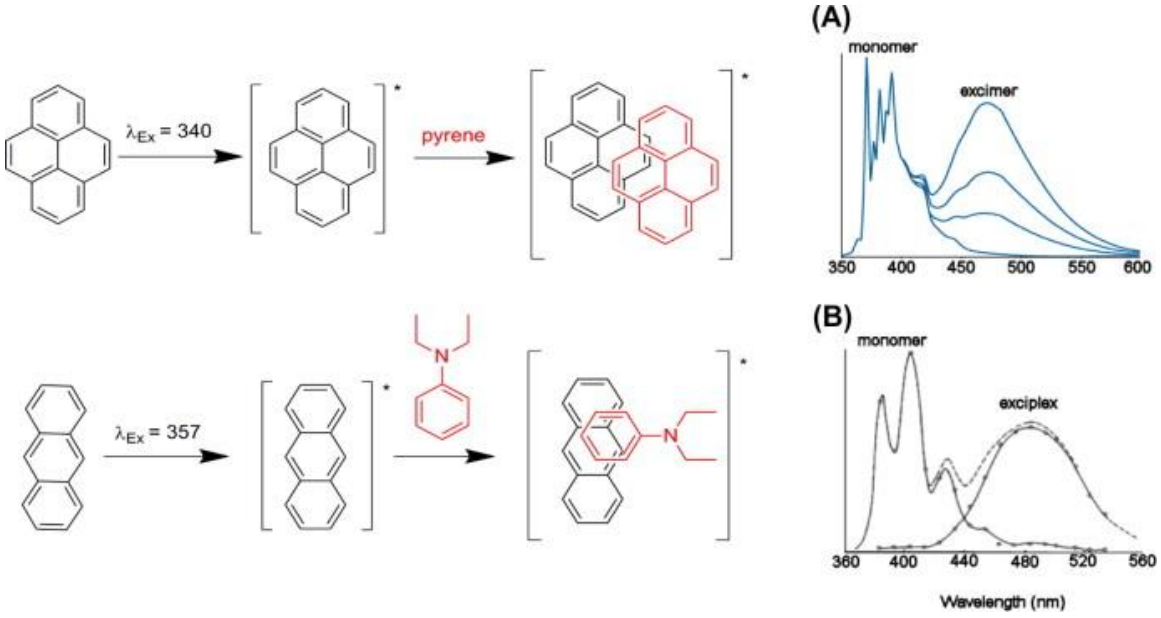

Figure 2.1 *(A) Emission spectra of pyrene and its excimer. As the concentration decreases (6 mM to 0.09 mM), the excimer band at 470 nm loses intensity. (B) The emission spectrum of anthracene containing diethylaniline. Reprinted from Inorganica Chimica Acta, Vol 381, Wallace, K.J.; Manandhar, E.; Host-guest chemistry of pyrene-based molecular receptors., 15-43., Copyright (2012), with permission from Elsevier*

One factor that is important to consider when working with pyrenyl derivatives is the concentration of the probe in solution. The work presented in this chapter serves to highlight the ability of pyrene- based LMFPs to coordinate to metal ions which ultimately brings two pyrene molecules together, resulting in the emergence of an excimer band. However, as was previously explained, an excimer band can also emerge in the absence of a metal analyte between two adjacent pyrene molecules. False positives can be minimized by ensuring that working probe concentrations are below 10^{-3} mol·dm^{-3}. If excimer formation is still observed at low concentrations, such as sub-micromolar, then it can be inferred that the LMFP could serve as a sensitive method of detection for metal analytes.

The pyrene group and many of its derivatives are hydrophobic in nature. Many literature reports on these types of probes are often reported in organic solvents containing little to no water.[98, 99] This is especially true in the case of Fe^{3+} ion probes as a result of the hydrolysis reactions that these ions undergo, which complicates analysis in aqueous solutions (see chapter 1). It is however possible to drastically improve the water solubility of pyrene compounds by adding hydrophilic groups, such as such as sulphates, carboxylic acid, and sugar groups, to the pyrene scaffold. The addition of anionic sulfonate groups to pyrene LMFPs has been shown to drastically improve the water solubility of these chromophores.[100] However, care must be taken when considering this kind of derivatization as the negatively charged sulfonate groups could also coordinate to non-targeted metal analytes and decrease the selectivity of the probe.[101]

2.2 Literature Examples of Pyrene-based LMFPs

There are many elegant examples of pyrene based LMFPs for metal ion detection in the literature. However, despite their wide-spread use, the vast majority of these probes suffer from poor water solubility which ultimately limits their real-world applications in aqueous systems. This section serves to highlight some of the more recent (within the last 10 years) examples of pyrene derivatives that have been designed to detect metal ions in a range of solvent systems.

A pyrenyl free-thiol containing Schiff base, compound **2.1**, was synthesized by Shellaiah et al., for the detection of Hg^{2+} ions in a self-assembly process in aqueous systems and live cell applications (scheme 2.1).[102] Compound **2.1** proved to be efficient for detecting Hg^{2+} ions in solutions of DMSO-water (7:3 v/v, pH 7.0) via UV-Vis and fluorescence analysis. In this solvent system, compound **2.1** displays two absorbance bands at 275 and 347 nm. The addition of Ag^{+}, Na^{+}, Cd^{2+}, Co^{2+}, Cu^{2+}, Fe^{2+}, Hg^{2+}, Mg^{2+}, Ni^{2+}, Pb^{2+}, Zn^{2+}, Al^{3+}, Cr^{3+}, and Fe^{3+} ions to **2.1** did not result in any spectral changes to the absorbance spectra. However, once Hg^{2+} ions were added to the solution, a bathochromic shift from 347 to 365 nm was observed. Due to the change observed when Hg^{2+} ions were added to the solution of the sensor, Job's plot analysis was performed, from which the stoichiometry was determined to be 2:1 probe: metal (scheme 2.1). Proton NMR studies as well as ESI-MS analysis were also used to confirm the stoichiometry of the coordination compound as well as the coordination environment. When 0.5 equivalents of Hg^{2+} in DMSO was added to one equivalent of **2.1**, the S-H signal completely disappeared and there was also an upfield shift of the CHN peak by 0.21 ppm. This observation confirms that coordination to the metal involves the S and N

atoms on two molecules of **2.1**. Furthermore, the ESI-MS analysis displayed a signal at m/z = 875.4, corresponding to $[Hg(\mathbf{2.1})_2 + H]^+$.

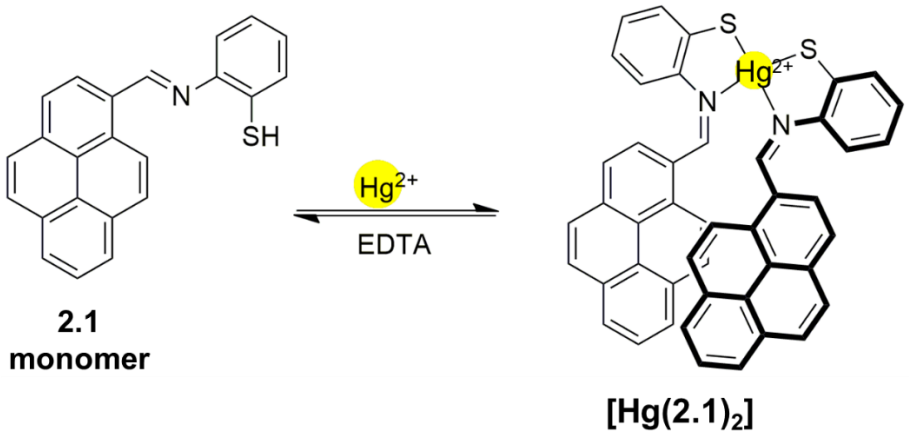

Scheme 2.1 *Proposed binding between **2.1** and Hg^{2+} ions resulting excimer formation.*

A fluorescence metal screen was also performed using the abovementioned metals. This metal screen further highlighted the selectivity of **2.1** for Hg^{2+} ions in the solution of DMSO and water, whereby a notable excimer band was observed at 445 nm once Hg^{2+} ions were added to the solution to the sensor. Fluorescence lifetime studies were also performed from which the lifetime of the free probe and coordination compound were determined to be 2.63, and 3.14 ns, respectively. The data from the fluorescence titration of Hg^{2+} ions into **2.1** was used in a linear regression analysis to determine a LoD of 2.82×10^{-6} M. The Benesi Hildebrand method was used to determine a K_a of 7.36×10^{-4} M^{-1} for the 2:1 complex. This mathematical approach is often applied to reaction equilibria that form 1:1 complexes for the determination of association constants, as a result, this method is limited to linear regression analysis. The use of computer software such as Hypspec and Bindfit,[103] which are capable of non-linear regression analysis, are preferred methods of analysis as they offer more precise results

and account for different coordination compounds present in solution.[103] In fact, these methods are preferred over Job's plot analysis as well which also does not account for different species in solution and can vary depending on the concentration of the probe.

Lastly, counterion studies were performed to determine how the compound **2.1** would interact with different Hg^{2+} salts. This type of study is often ignored in optical studies even though it is very important, as different anions can affect the binding ratios and the stability of the complexes formed in solution. In the presence of CH_3COO^-, Cl^-, ClO_4^-, I^-, NO_3^-, and SO_4^{2-} anions, fluorescence enhancements between 27 to 30-fold were consistently observed for the excimer band. Hence, it was concluded that varying the counterion did not affect the binding between compound **2.1** and Hg^{2+} ions. It would be interesting to determine if the stoichiometry and stability constants of the coordination compounds changed as the counterion was varied, however, this information was not reported.

A reversible pyrene-based LMFP (**2.2**) was synthesized by Mukherjee and Talukder for the selective detection of Fe^{3+} ions in a solution of DMSO-water (2:1 v/v, pH = 7.0) (scheme 2.2).[104] The addition of K^+, Na^+, Ca^{2+}, Cd^{2+}, Co^{2+}, Cu^{2+}, Fe^{2+}, Hg^{2+}, Mg^{2+}, Mn^{2+}, Ni^{2+}, Pb^{2+}, Sn^{2+}, and Zn^{2+} ions to the solution of **2.2** did not result in any drastic changes in the fluorescence spectrum of **2.2**. Upon the addition of Fe^{3+} ions to the solution of **2.1**, an intense excimer band was observed at 430 nm. This indicates that the pyrene moieties were *syn* to each other. Low intensity excimer bands were also observed for Al^{3+} and Cr^{3+} ions, however the intensity of these bands were more than six times lower than the fluorescence increases observed for Fe^{3+} ions. Due to the inductive effect, whereby coordination of **2.1** to the Fe^{3+} ion results in a loss of electron density from the

pyrene moieties, the wavelength of the excimer band (430 nm) is a bit lower than average (470 nm). More energy is required to excite the electron from the ground state to the excited state of the second pyrene unit, therefore a shift in the blue direction is observed.

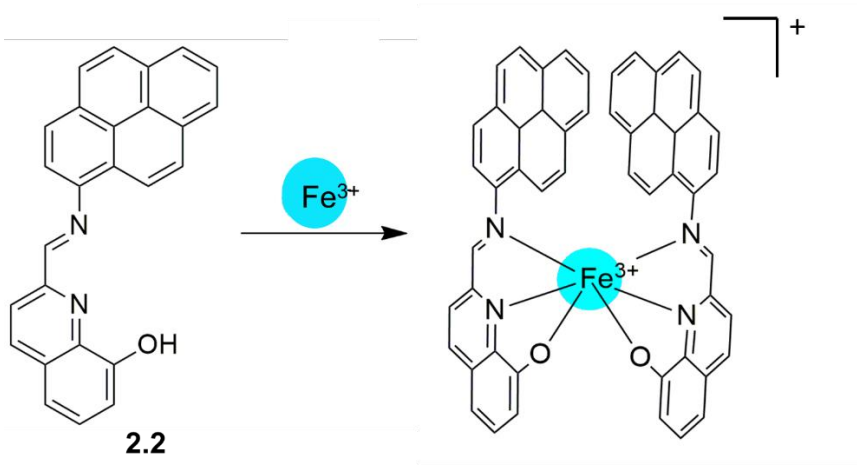

2.2

Scheme 2.2 *Proposed binding between **2.2** and Fe^{3+} ions.*

Jobs plot analysis was used to confirm 2:1 binding between the **2.2** and Fe^{3+} ions and the LoD was found to be 2.82×10^{-8} M using linear regression analysis. As previously stated, the data obtained using Jobs plot analysis should be interpreted loosely as it does not always account for all species present in solution. Confirmation that the excimer band was a result of dimer formation upon coordination to the Fe^{3+} ion was proven by the addition of EDTA which removed the Fe^{3+} ions from the coordination environment. Once more Fe^{3+} ions were added to the solution, the excimer band was recovered. The addition of EDTA and Fe^{3+} ions was repeated over several cycles, allowing for Boolean logic to be used. A weak fluorescence emission was assigned a '0' and a '1' was given to the system when the I/I_0 intensity was greater the 50% intensity upon the addition of Fe^{3+} ions. When both EDTA and Fe^{3+} ions are present, very weak

fluorescence is observed, therefore the input is '0'. From the intensity, a truth table can be generated, displaying INHIBIT logic. This approach is used by many luminescent sensors.

Previous work in the Wallace group shows that excimer formation can be achieved upon an ion induced self- assembly process between compound **2.3** and $ZnCl_2$ in CH_3CN.[92] This was the first time that an excimer emission was seen upon the simultaneous binding of a cation and an anion. The stoichiometry for the probe: $ZnCl_2$ was 2:1 and was calculated using a non-linear fitting method and the K_a was determined to be 1.8×10^6 M^{-1}. These values were obtained using fluorescence titration data whereby the addition of various Zn^{2+} salts (F^-, Cl^-, Br^-, I^-, NO_3^-) to the solution of **2.1** resulted in the emergence of an excimer band centered at 420 nm. Other counterions were also analyzed, specifically, BF_4^-, $CH_3CO_2^-$, SO_4^{2-}, $H_2PO_4^-$, ClO_4^-, and CN^-, however no excimer band was observed in these samples. An increase in the fluorescence intensity of the monomer at 382 and 402 nm was however seen for $CH_3CO_2^-$, SO_4^{2-}, $H_2PO_4^-$, and CN^- salts. Because the distance between the two pyrene moieties is responsible for the formation of the excimer band, it is possible that coordination to some of the larger counterions did not allow for optimal syn alignment of the pyrene groups. Furthermore, it is well known that some species PET quench the fluorescence of chromophores, which may explain why some of the Zn^{2+} salts do not display excimer formation. The fluorescence quenching process decreases the intensity of the emission of an otherwise fluorescent molecule or complex. This process will be discussed in greater depth in chapter 3.

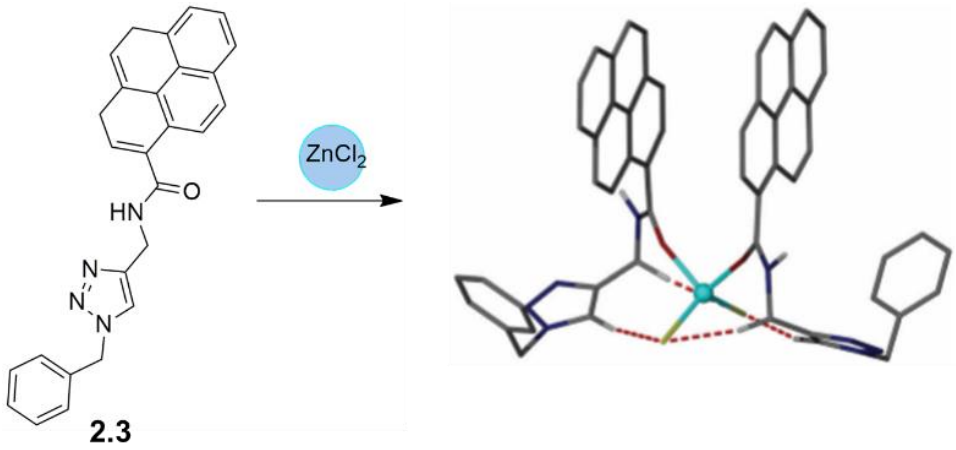

Scheme 2.3 *Proposed binding between compound **2.3** and $ZnCl_2$ in CH_3CN.*

The binding of Zn^{2+} halides to **2.3** was confirmed via ^{1}H-NMR titrations. Changes to the amide proton were observed even though, according to DFT calculations, this proton was not involved in metal coordination (scheme 2.3). Instead, the shift in the NH peak of the amide is due to the inductive effect, whereby, the coordination of the amide oxygen to the Zn^{2+} ion increases the negative character of the oxygen. In turn the carbonyl carbon becomes more positive and the nitrogen atom becomes more negative in character, which shifts the amide proton further downfield. Unfortunately, this self-assembled system did not work in aqueous systems. In fact, only 5% water (v/v) was required to disrupt the self-assembly process. Furthermore, compound **2.3** is insoluble in aqueous systems which limits its applications.

To determine if a simultaneous ion induced excimer could form in aqueous solution, the Wallace group decided to introduce a water-soluble sugar group and compound **2.4** was synthesized. The sugar functionalized pyrene- based triazole receptor (**2.4)** was designed as a fluorescence sensor for the detection of Fe^{3+} ions in aqueous

solutions.[105] However, due to the onset of iron hydrolysis (see chapter 1.5.2), as well as inhibition of the self-assembly process in aqueous solutions, compound **2.4** was only studied in CH_3CN. We have found that CH_3CN inhibits metal coordination to a lesser extent than oxygen containing solvents, such as MeOH and THF. This inhibition process will be discussed in depth in chapter 3.5.5.

Fluorescence metal screens and ECL (electrogenerated chemiluminescence) analysis both proved that **2.4** was selective for Fe^{3+} ions over other metal ions. Of all the metal cations analyzed (Ag^{+}, K^{+}, N^{a+}, Ca^{2+}, Cd^{2+}, Co^{2+}, Cu^{2+}, Fe^{2+}, Hg^{2+}, Mg^{2+}, Zn^{2+}, Al^{3+}, Cr^{3+}) via steady state fluorescence, only Fe^{3+} ions resulted in the emergence of a notable excimer band at 465 nm. It is important to note the difference in the wavelength of the excimer bands for compounds **2.3** and **2.4** as well as the difference in metal ion selectivity. It appears that by replacing the benzene group on **2.3** with a sugar moiety, the selectivity of the probe changed from Zn^{2+} ions to Fe^{3+} ions Though the coordination environment of these two compounds are the same, the excimer band for [Zn(**2.3**)$_2$Cl$_2$] was centered at 420 nm, whereas the excimer band for [Fe(**2.4**)$_2$]$^{3+}$ was centered at 465 nm. The longer wavelength of the latter species is likely due to the formation of a dynamic excimer which has higher stabilizing energy than a static excimer and therefore occurs at lower energies (longer wavelengths).

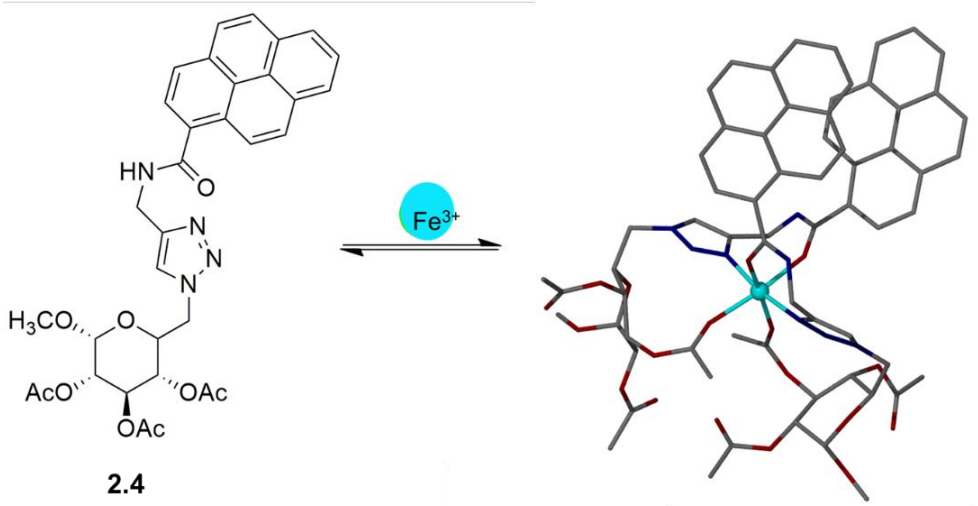

Scheme 2.4 *Proposed binding between compound **2.4** and Fe^{3+} ions in CH_3CN.*

Fitting of the fluorescence titration data for $[Fe(\mathbf{2.4})_2]^{3+}$ via non-linear regression analysis showed that compound **2.4** binds exclusively in a 2:1 ratio with Fe^{3+} ions and forms an extremely stable complex with $K_a = 1 \times 10^{10}\ M^{-2}$. Counterion studies with Br^-, Cl^-, NO_3^-, and ClO_4^-, salts showed that the most intense excimer bands resulted when $Fe(ClO_4)_3$ was used. An excimer band was also observed for the Cl^- anion, however it was only about $\frac{1}{3}$ the size of the band observed for the ClO_4^- salt. No excimer bands were observed for the NO_3^- and Br^- salts. The reasoning for this is likely that the Br^- and NO_3^- salts do not dissociate as readily as the Cl^- and ClO_4^- salts. As a result, the formation of the dimer is inhibited in these systems, and no excimer band is observed. Analysis of compound **2.1** via ECL measurements with Na^+, Ca^{2+}, Cd^{2+}, Cu^{2+}, Fe^{2+}, Al^{3+}, and Fe^{3+} perchlorate salts showed a large increase in the intensity of the chemiluminescence signal in the presence of Fe^{3+} ions. No other metal ions showed a notable increase in the ECL

signal, in fact, Cu^{2+} ions effectively quenched the ECL response of the monomer, which is unsurprising as the Cu^{2+} ion is known to quench fluorescence signals.

This chapter serves to further highlight the unique optical properties of compound **2.4** with emphasis on the molar extinction coefficient (ε) and quantum yield (Φ) of the probe in the presence and absence of Fe^{3+} ions, the fragmentation pattern of the coordination compound and lastly, the fluorescence lifetime (τ) of the coordination compound. This chapter also serves as a brief introduction into LMFPs and demonstrates why the other chapters in this work will focus on utilizing chromophores that display metal binding in aqueous solution and can ultimately be used in more practical applications.

2.3 Results and Discussion

2.3.1 Gas Phase Studies (ESI-MS)

Electrospray ionization mass spectrometry (ESI-MS) allows for the analysis of organic and inorganic species without the concern of of solvent interferences, as the analysis occurs in the gas phase. The masses observed in this technique account for counterions and additional hydrogen atoms that may be coordinated to the analyte as well as configurational rearrangements that may occur within a molecule or species. ESI-MS is especially useful for metal-ligand complex analysis, as it is often difficult to isolate X-ray quality crystals of some coordination compounds. Due to the part per billion (ppb) detection limit of the mass spectrometer and the ability to study complex fragmentation patterns, chemists are able to suggest, with greater confidence, the formation and

existence of metal-ligand complexes in solution. The mass spectra for **2.4** and [Fe(**2.4**)$_2$]$^{3+}$ are highlighted in this section. The full mass spectrum and fragmentation patterns of these compounds were studied using collision induced dissociation (CID), which is a useful technique for gaining insight on the coordination environment of the receptor.

The full mass spectrum of compound **2.4** in CH_3CN is shown in figure 2.2. The signal observed at m/z = 1278.9 corresponds to the [dimer + Na]$^+$ which is typically observed in pyrene species (see section 2.1). The CID pattern of compound **2.4** was also analyzed. The proposed fragmentation pathways for compound **2.4** are shown in figures 2.2C-D. These figures highlight the species that we believe correspond to some of the major signals shown in the CID spectrum of **2.4**. The proposed fragmentation patterns, highlighting cleavage of the acetoxy (OAc) groups from the cyclohexane ring, prove to be similar to the fragmentation patterns observed for glucose and fructose as reported by Taylor et al.[106] There were however, several signals observed in the CID spectra that we were unable to identify. These species are labeled with an asterisk in figure 2.2B.

The mass spectrum of the 2:1 solution of **2.4** with $Fe(CF_3SO_3)_3$ in CH_3CN is shown in figure 2.2E. The solution was allowed to equilibrate for 24 hours prior to analysis. The m/z signals in the full mass spectrum account for a number of species in solution, some of which correspond to the free ligand and others which are representative of the metal: ligand complex. The most intense signal at m/z = 629.2 corresponds to [**2.4** + H]$^+$ which was unexpected. This is either the result of inhibition of the self-assembly process due to the presence of water molecules in the solution or the breakdown of the complex prior to reaching the detector. The former is more likely as the stability of the [Fe(**2.4**)$_2$]$^{3+}$ complex is relatively high ($\log\beta = 10$). A weak signal is observed at m/z =

656.2 for the [Fe(**2.4**)$_2$]$^{2+}$ species. It appears that the Fe^{3+} ion is reduced to the +2 state under the conditions within the spectrometer. The +2 state is also expected to be the predominant state responsible for the signal observed at m/z = 1460, corresponding to the [Fe(**2.4**)$_2$(CF_3SO_3)]$^+$ species. A range of other species are observed in the mass spectrum, corresponding to the dimeric species [(**2.4**)$_2$ + H]$^+$ at m/z = 1256.7, as well as other Fe^{3+} species whereby the counterion and solvent are coordinated to the metal ion. The use of high resolution would be useful in studying the fragmentation patterns of each of these species as there remains some ambiguity in the results of this study.

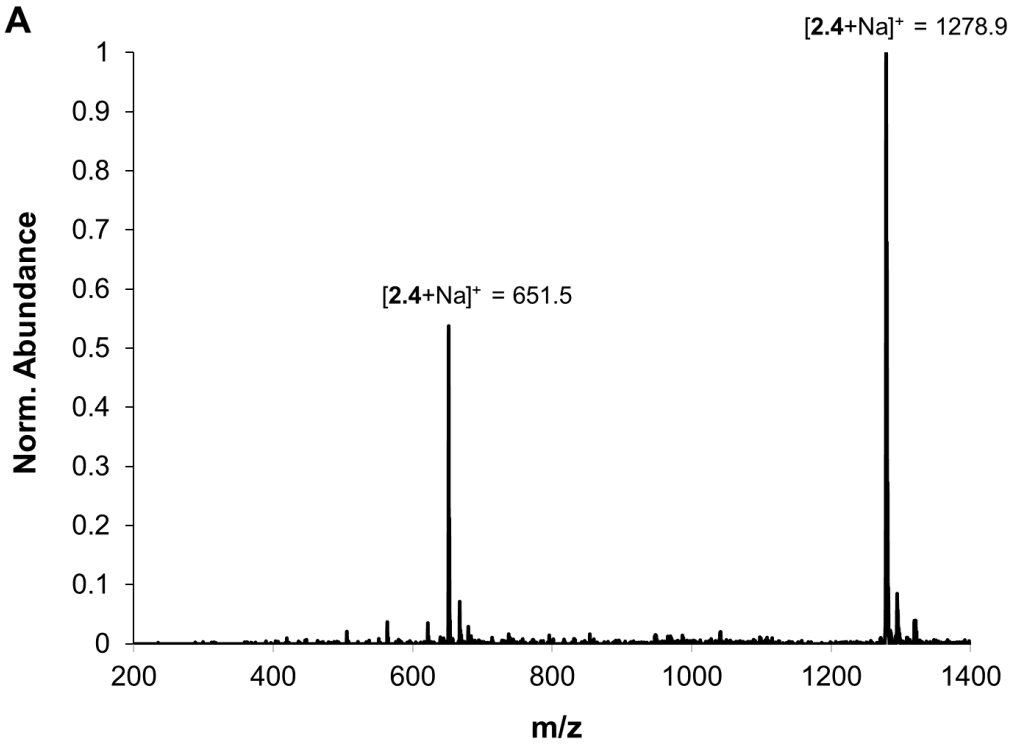

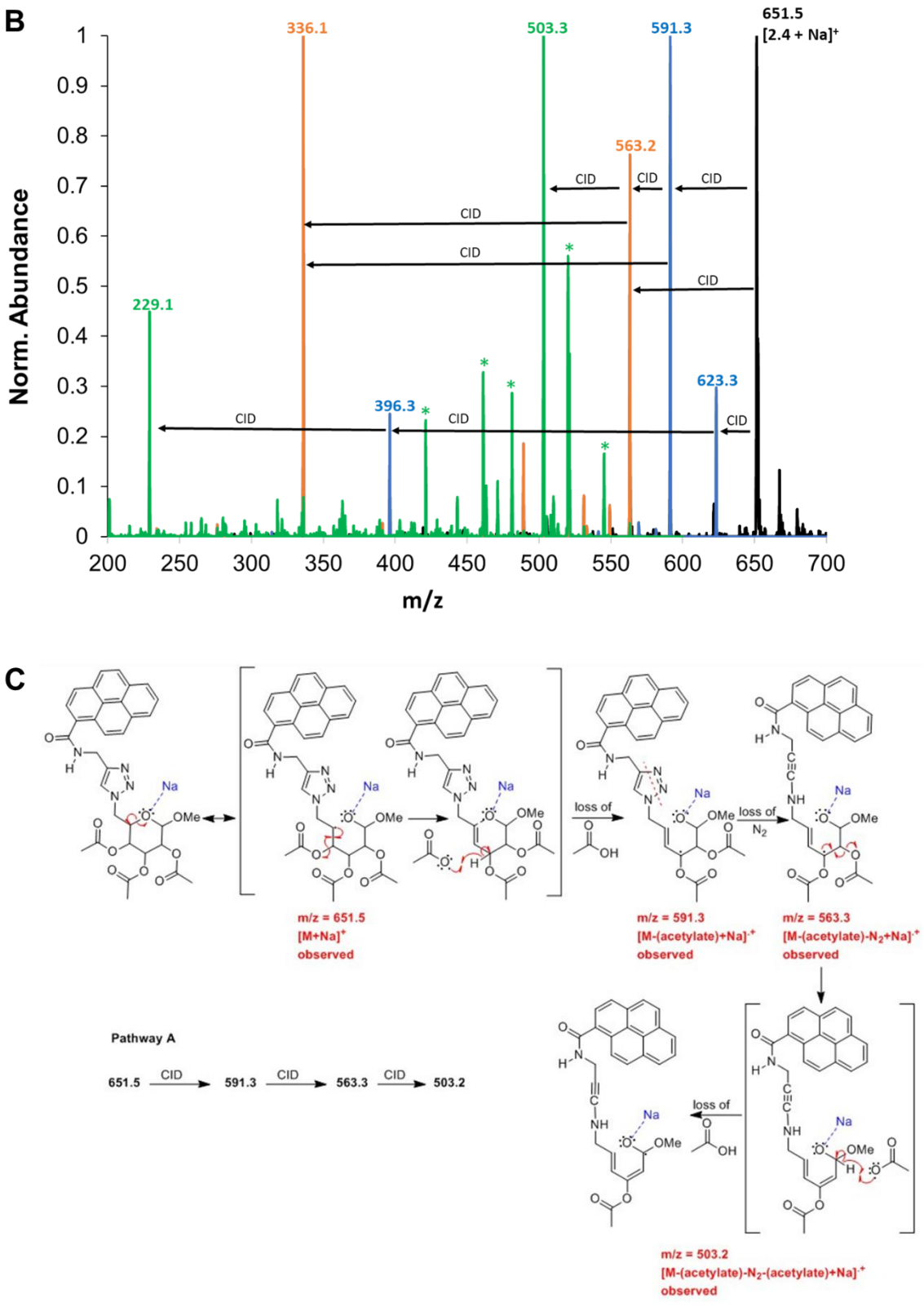
B
Norm. Abundance
m/z
651.5
[2.4 + Na]+
336.1
503.3
591.3
563.2
229.1
396.3
623.3
CID
C
Na
OMe
loss of
loss of
N2
m/z = 651.5
[M+Na]+
observed
m/z = 591.3
[M-(acetylate)+Na]·+
observed
m/z = 563.3
[M-(acetylate)-N2+Na]·+
observed
m/z = 503.2
[M-(acetylate)-N2-(acetylate)+Na]·+
observed
Pathway A
651.5 CID 591.3 CID 563.3 CID 503.2

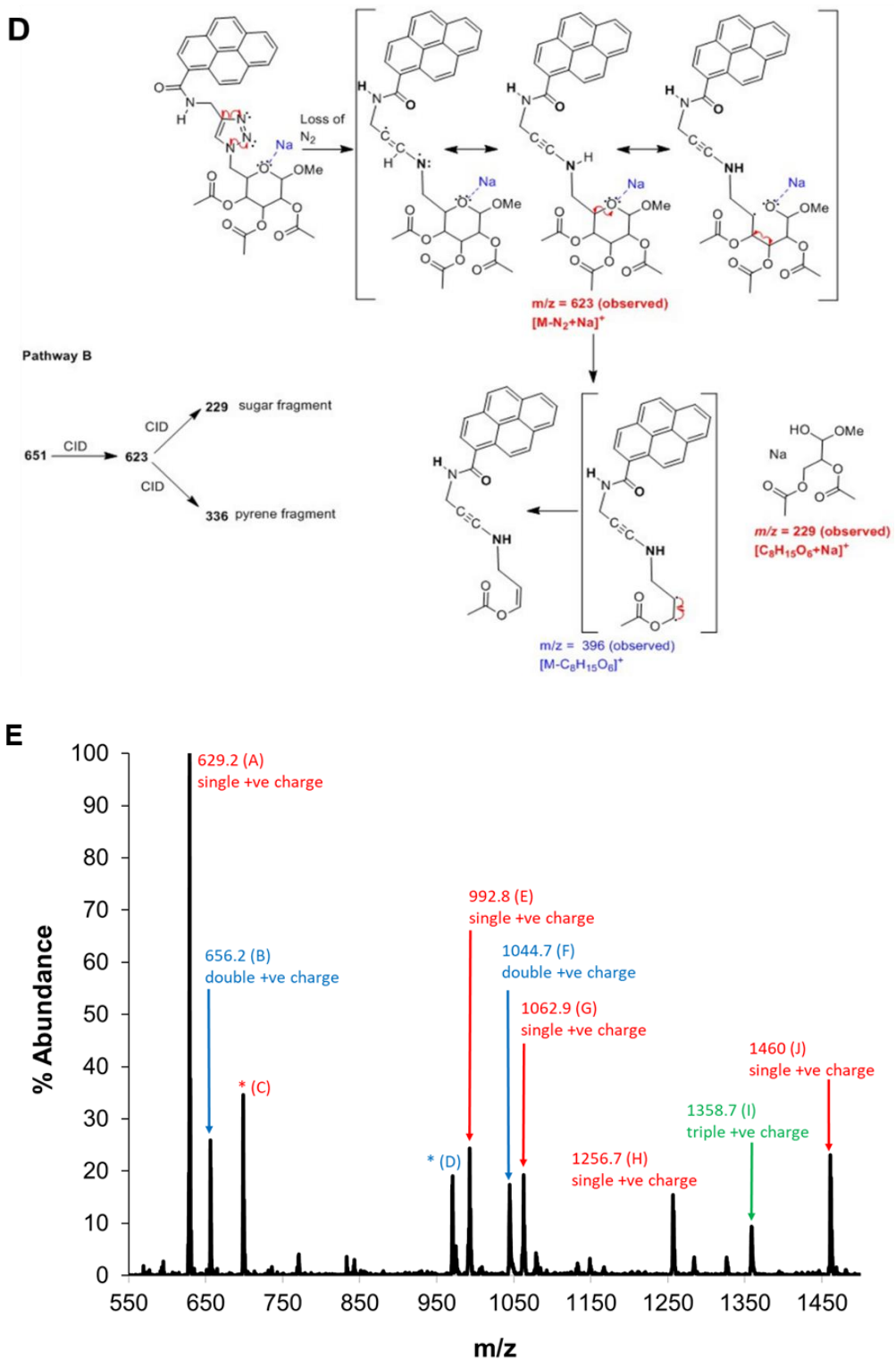

Figure 2.2 *(A) Normalized ESI-MS of compound* ***2.4****. in CH_3CN(B) Normalized fragmentation pattern of* ***2.4*** *(C-D) Proposed fragmentation pathways for* ***2.4*** *(E) ESI-MS of a 2:1 solution of* ***2.4****:$Fe(CF_3SO_3)_3$ in CH_3CN.*

2.3.2 Optical Spectroscopy

Molar Extinction Coefficient and Quantum Yield

One very important characteristic of organic dyes is their ability to strongly absorb light at a given wavelength. Species that are capable of absorbing light are ideal candidates for use as molecular probes as changes in their electronic transitions can be observed even when the dye concentration is very low (< μM). The lower the concentration over which these electronic transitions can be observed allows for the design of very sensitive optical probes that can detect ultralow concentrations (nM) of analytes in solution. According to the Handbook of Fluorescence Spectra of Aromatic Molecules, the molar extinction coefficient (ε) of pyrene in cyclohexane is 54,000 $M^{-1} \cdot cm^{-1}$ at 335 nm.[107] It is important to note that each of the absorbance bands in pyrene has a unique value for (ε) and the wavelengths of these bands will change slightly depending on the solvent used, a process known as the solvatochromic effect.

A dilution study was carried out with compound **2.4** in CH_3CN to determine the value of ε at 342 nm. The absorbance intensity at 342 nm was then plotted against the concentration of **2.4** for each trial which yielded a linear plot- the slope of which was used to determine the value of ε as 21,570 $M^{-1} \cdot cm^{-1}$ (see appendix A5 for ε values for other absorbance bands in **2.4).** This value is much lower than the ε value observed for the unmodified pyrene chromophore in cyclohexane. The decrease in the molar absorptivity as we move from an unmodified pyrene to different pyrenyl derivatives has been reported consistently in the literature.[105,108,109].

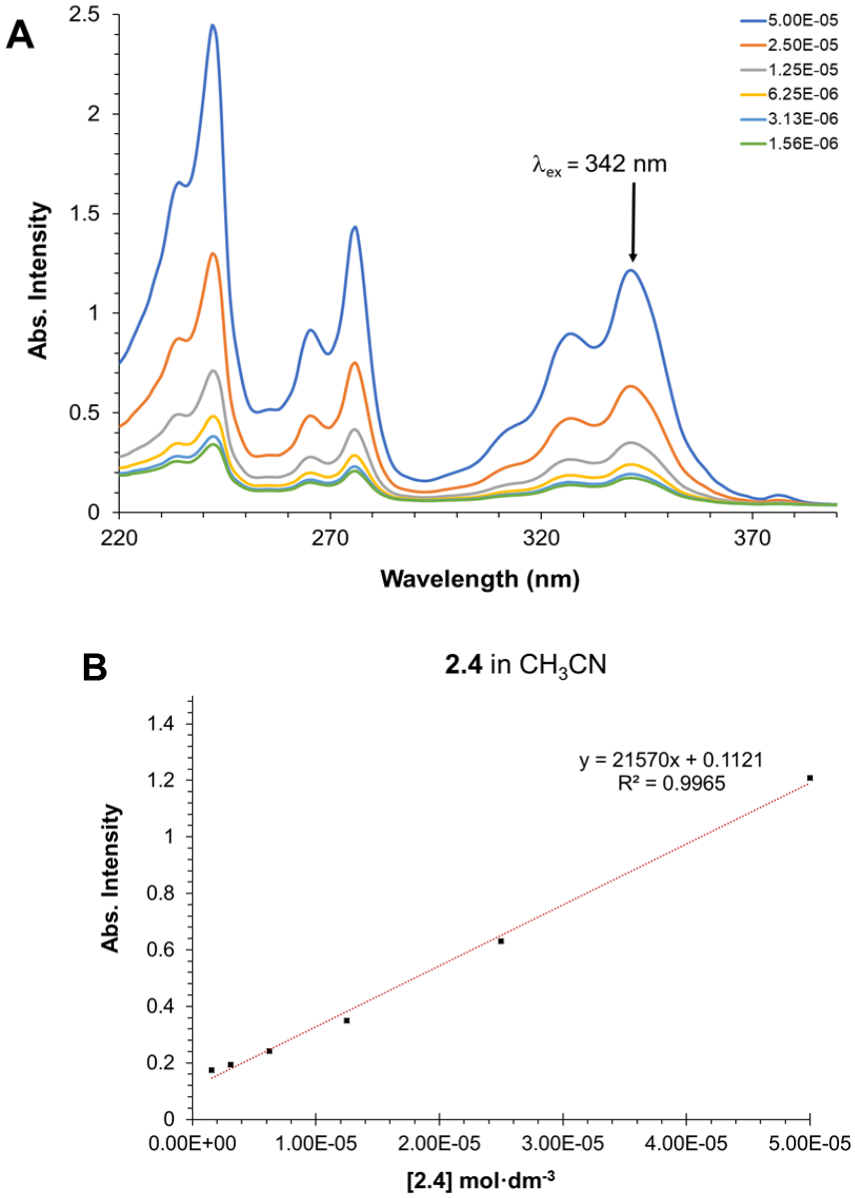

Figure 2.3 *Spectral data used for to determine the molar extinction coefficient (ε) of compound **2.4** (A) Absorbance spectrum of **2.4** in CH_3CN. (B) Linear plot of the absorbance intensity at 342 nm vs the concentration of **2.4** in CH_3CN*

Two of the most important properties of fluorescent compounds are their fluorescence lifetimes (τ)and quantum yields (Φ). Both will be discussed here. When a fluorophore absorbs a photon of light, the fate of the excited state species varies

depending on the nature of the fluorophore and its environment, however, the end result is deactivation and return of the photon to the ground state. The main deactivation processes which occur are internal conversion and vibrational relaxation (non- radiative loss of energy as heat), fluorescence (loss of energy by emission of a photon), and intersystem crossing to the triplet state and subsequent non-radiative deactivation. The fluorescence quantum yield is used to describe the number of emitted photons relative to the number of absorbed photons.[40] The larger the quantum yield of a substance, the more intense or brighter its emission. Species with large quantum yield values are ideal for designing sensitive LMFPs as changes to the fluorescence spectrum of the compound can be observed in the presence of very low concentrations of analyte (nM). The formula for calculating the quantum yield of a fluorophore is shown in Equation 2.1. The Γ symbol represents radiative decay, and non-radiative decay is represented by k_{nr}.

$$Q = \frac{\Gamma}{\Gamma + k_{nr}} \tag{2.1}$$

The quantum yield (Φ) of compound **2.4** was determined using the comparative method which involves the use of well characterized standard samples with known Φ values. In theory, solutions of a test sample and standard that have identical absorbances at the same excitation wavelength should absorb the same number of photons. A ratio of the integrated fluorescence intensities of the two samples produces the ratio of the Φ values. These measurements are slightly more complicated as the use of different solvents, the validity of using the standard sample and its Φ value, and concentration effects of the fluorophores must be taken into consideration. In the literature, authors often report cross calibrating their samples with one standard, however, this is incorrect

as it does not account for errors within the method. It is always best to cross-calibrate two standard samples to ensure that both are behaving as expected and yield Φ values within a 10% margin of error from the accepted values. Furthermore, the standards as well as the LMFP should have similar excitation wavelengths. This is done because species with similar λ_{abs} are expected to absorb similar numbers of photons. If the excitation wavelengths of the standards are too far apart, cross-calibration of the samples would not produce reliable results.

For this experiment, anthracene and 9,10-diphenylanthracene were cross-calibrated to ensure that the observed Φ values for each were within 10% of the expected values. First, the UV-Vis spectrum was recorded for each of the standards. It was imperative to choose a concentration that would not exceed 0.1 absorbance units over the course of five successive trials as the concentration of the fluorophore was increased. Keeping the concentration low minimizes the likelihood of primary inner-filter effects which attenuate the excitation beam and decrease the amount of the light reaching molecules in solution.[110] The fluorescence spectrum of the standards were also recorded for each trial and the area under the fluorescence curve (integrated fluorescence intensity) was calculated. A plot of the integrated fluorescence intensity vs the absorbance intensity at λ_{Ex} yielded a straight line, the gradient of which was used in equation 2.2 to determine the experimental Φ values. The spectral data for the two standards can be found in appendix A5.

$$\Phi_x = \Phi_{st} \cdot \left(\frac{Grad_x}{Grad_{st}}\right)\left(\frac{n_x^2}{n_{st}^2}\right) \qquad (2.2)$$

Once it was determined that the standards had been correctly cross calibrated, the samples of **2.4** and $[Fe(\mathbf{2.4})_2]^{3+}$ were then cross calibrated against both standards to determine what their quantum yields were. More importantly, we wanted to determine how the quantum yield of the free probe would differ from the coordination compound. The quantum yield for unmodified pyrene in cyclohexane is reported as 0.32 in the literature.[107] Similar to the decrease in the molar extinction coefficient that was observed as we moved from the unmodified pyrene to pyrenyl derivatives, a decrease in the fluorescence quantum yield was also observed for compound **2.4**. The observed Φ value for **2.4** was found to be 0.18 ± 0.018. In contrast, the Φ value for $[Fe(\mathbf{2.4})_2]^{3+}$ was found to be 0.32 ± 0.032 (figure 2.4). The increase in the quantum yield as we move from the free probe to the coordination compound is due to an increase in the number of radiative decay processes (Γ) upon excimer formation and can be seen in figure 2.4B. Similar observations were reported for compound **2.1,** whereby, the free probe displays a quantum yield of 0.121 but the quantum yield of the coordination compound, $[Hg(\mathbf{2.1})_2]$, was found to be 0.289.[102] Yet another example of this behavior was reported by Martínez et al., for a symmetrical bichromophoric azine pyrenyl derivative.[111] The free azine species was found to have a quantum yield of 0.016, however, the formation of a coordination compound with Hg^{2+} ions led to a 10-fold increase in the fluorescence quantum yield of the compound.

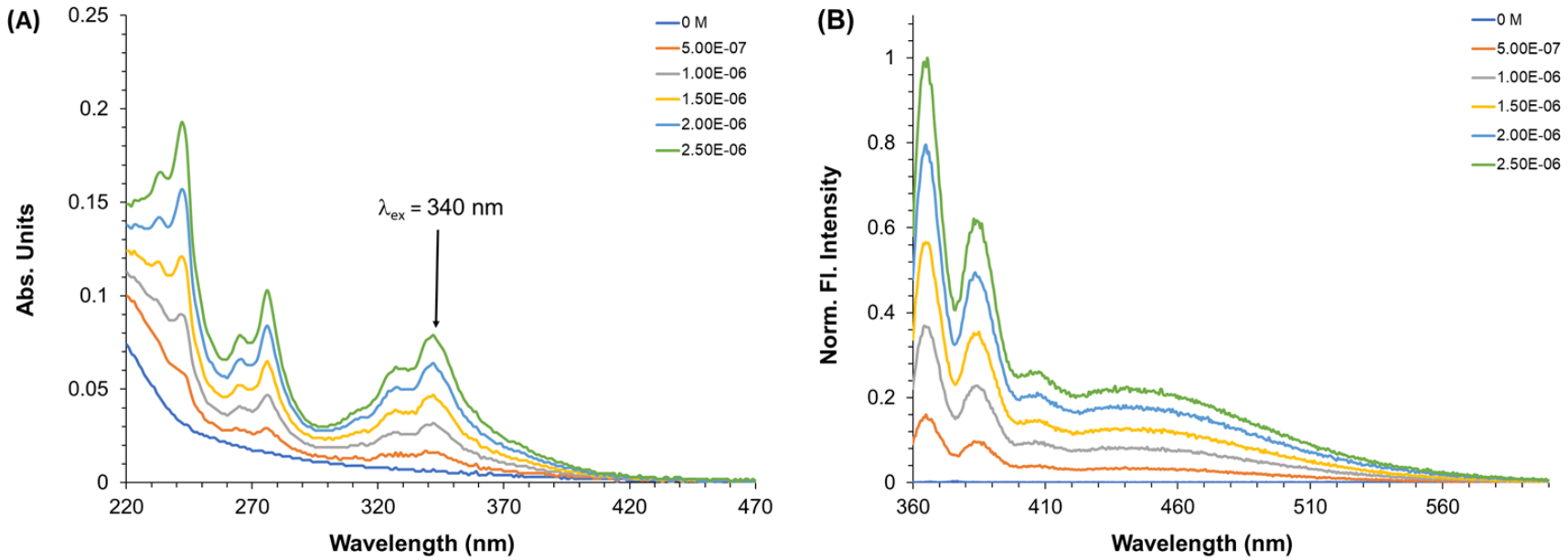
(A)
Abs. Units
0.25
0.2
0.15
0.1
0.05
0
220
270
320
370
420
470
Wavelength (nm)
λex = 340 nm
0 M
5.00E-07
1.00E-06
1.50E-06
2.00E-06
2.50E-06
(B)
Norm. Fl. Intensity
1
0.8
0.6
0.4
0.2
0
360
410
460
510
560
Wavelength (nm)
0 M
5.00E-07
1.00E-06
1.50E-06
2.00E-06
2.50E-06

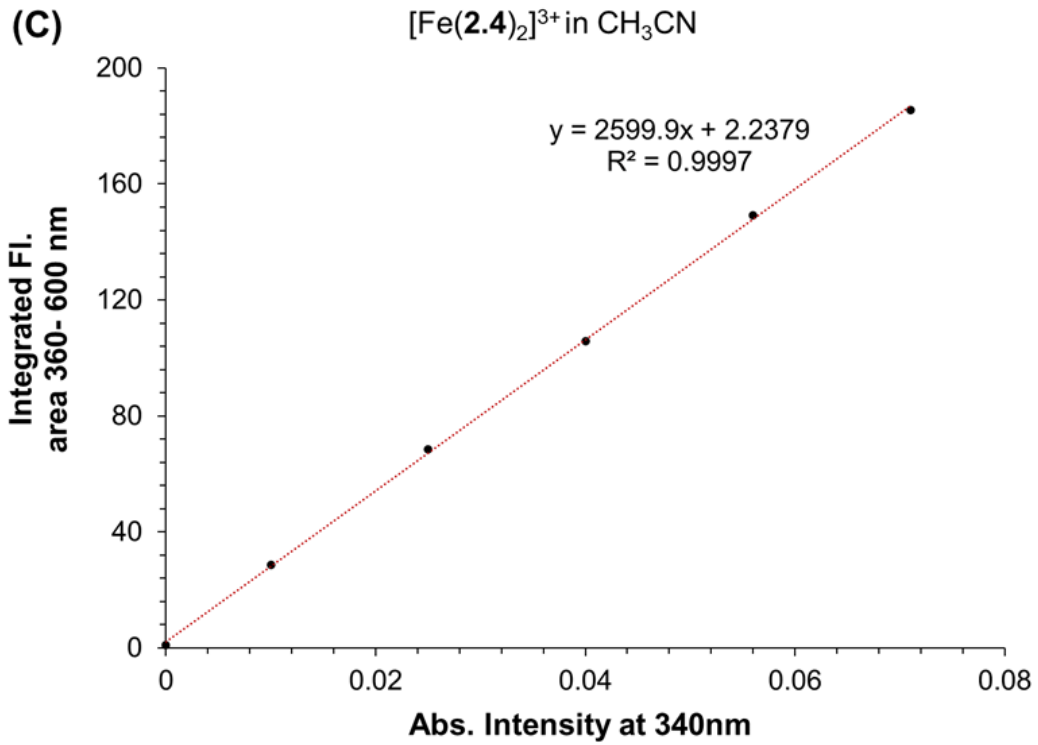

Figure 2.4 *Spectral data used for [Fe(**2.4**)$_2$]$^{3+}$ quantum yield (Φ) calculations. (A) Absorbance spectrum of [Fe(**2.4**)$_2$]$^{3+}$ in CH$_3$CN. (B) Fluorescence spectrum of [Fe(**2.4**)$_2$]$^{3+}$ in CH$_3$CN (λex = 340 nm). (C) Linear plot used in [Fe(**2.4**)$_2$]$^{3+}$ quantum yield calculation.*

Fluorescence Lifetime Measurements

Fluorescence decay measurements are appealing to the sensor community because they tend to be more robust than fluorescent intensity measurements and allow for sample analysis over a broad range of concentrations (mM- μM). This type of measurement also does not require the use of wavelength-ratiometric probes which are based on the ratio between two fluorescence intensities.[112] Intensity-based sensing has proven difficult for use in real-world specimens, such as biological objects, which often time present similar fluorescence spectra (lacking distinctive structure) but display very complex and widely differing fluorescence lifetime decays.[113] The fluorescent decay profiles can be treated as optical signatures of different chemical compositions and can therefore be used to distinguish between compounds that give similar fluorescence spectra, or to help identify molecules by comparing them to the known standards.[40]

As pyrene molecules are known for their characteristically long fluorescence lifetimes (τ), up to 100 ns,[107] we wanted to determine how the τ of **2.4** would compare to unmodified pyrene as well as how the coordination to Fe^{3+} ions would affect the lifetime of **2.4**. The lifetime of the excited state is defined by the average time the molecule spends in the excited state prior to return to the ground state. Due to an increase in the number of radiative decay processes (Γ) upon excimer formation, we expect that the lifetime of the coordination compound will be lower than that of the free probe. This can be explained using equation 2.3.

$$\tau = \frac{1}{\Gamma + k_{nr}} \qquad (2.3)$$

The fluorescence lifetime **2.4** was compared to that of the coordination compound, $[Fe(\mathbf{2.4})_2]^{3+}$, in CH_3CN.The concentration of the receptor was maintained at 25 μM for each sample and the ratio of **2.4** with $Fe(CF_3SO_3)_3$ was 1:2. The fluorescence decay profiles and random distribution of weighed residuals of **2.4** and $[Fe(\mathbf{2.4})_2]^{3+}$ are shown in figure 2.5. The fluorescence decay plots are fitted to a single exponential with excellent χ^2 values very close to 1. All samples were degassed prior to analysis to remove dissolved oxygen which could lead to quenching of the excited state species, and all trials were repeated three times to ensure reproducibility of the results. Compound **2.4** displayed a fluorescence lifetime of 14.33 ± 0.065 ns, while the $[Fe(\mathbf{3.11a})_2]^{3+}$ complex remained in the excited state for 3.80 ± 0.031 ns. As we expected, the increase in the number of radiative decay processes led to a decrease in the fluorescence lifetime. Similar behavior is observed in the LMFPs discussed in chapter 3 and 4 of this work and is also addressed in work by Lakowicz et al., whereby, the fluorescence enhancement observed in DNA oligomers upon binding to silver particles was accompanied by a subsequent decrease in the lifetime of the fluorescent species.[114]

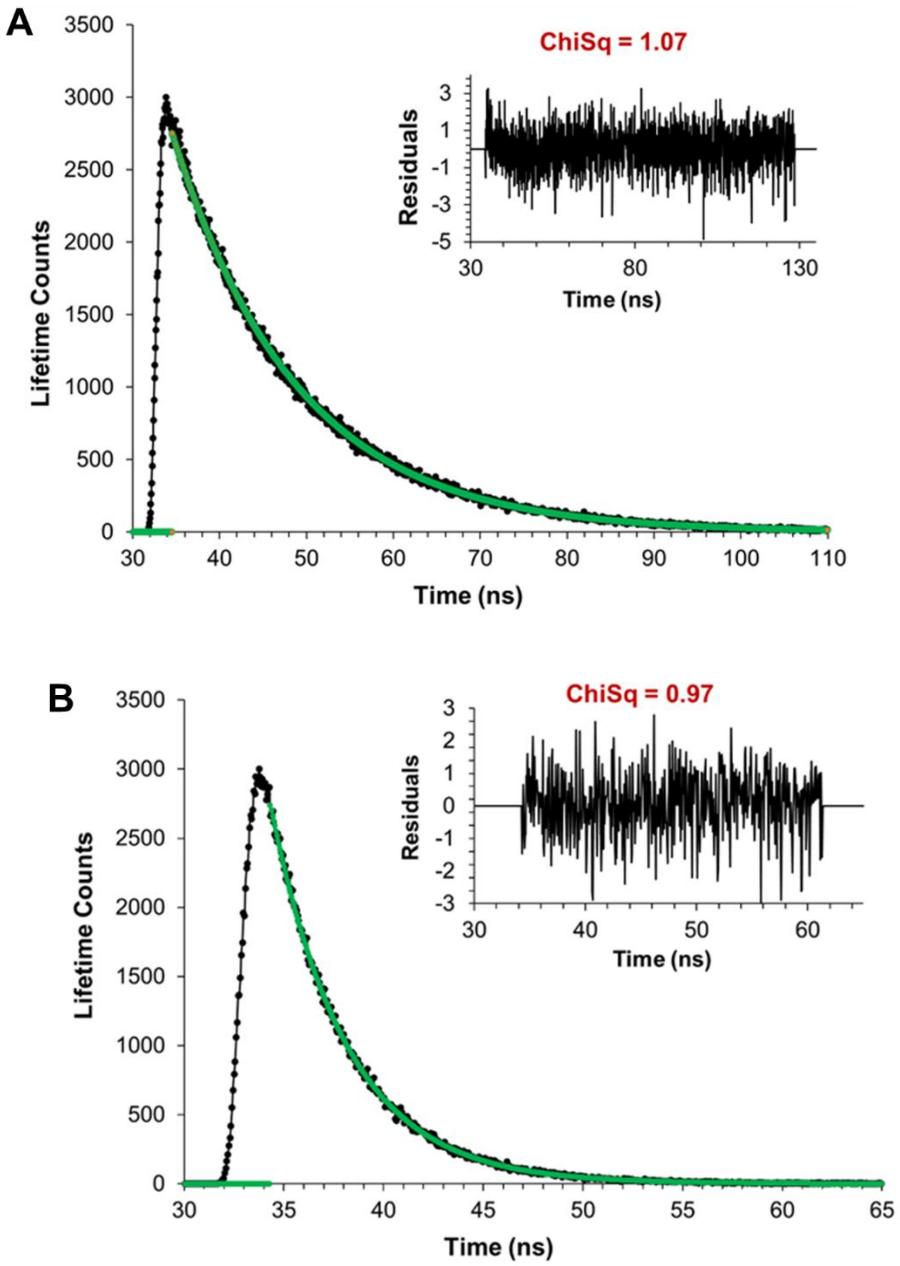

Figure 2.5 *(A) Fluorescence decay of free probe **2.4** in CH_3CN with residuals shown in inset. (B) Fluorescence decay of $[Fe(\mathbf{2.4})_2]^{3+}$ in CH_3CN with residuals shown in inset.*

2.3.3 Summary

We have shown that pyrenyl derivatives have lower molar extinction coefficients and fluorescence quantum yields, as well as shorter fluorescence lifetimes than

unmodified pyrene units. The addition of the triazole-sugar moiety to the pyrene backbone resulted in a notable decrease in the molar extinction coefficient from 54,000 $M^{-1} \cdot cm^{-1}$ to 21, 570 $M^{-1} \cdot cm^{-1}$. Additionally, the derivatization of pyrene units appears to drastically decrease the quantum yield of the fluorophore. Unmodified pyrene has a Φ value of 0.32 while Φ of compound **2.4** was found to be 0.18 ± 0.018. The addition of Fe^{3+} ions to the solution of **2.4** in CH_3CN led to an increase in the Φ. This indicates that the addition of Fe^{3+} ions and subsequent formation of the excimer band leads to an increase in the number of radiative decay processes within the system. This increase in the number of radiative decay processes was proven by comparing the fluorescence decay profile of the free probe, **2.4**, to the coordination compound $[Fe(\mathbf{2.4})_2]^{3+}$. According to equation 2.3, an increase in the number of radiative decay processes within a fluorescent species leads to decrease in the fluorescence lifetime. The lifetime of free probe **2.4** was found to be 14.33 ± 0.065 ns which is much longer than the observed lifetime of 3.80 ± 0.031 ns for the coordination compound, $[Fe(\mathbf{2.4})_2]^{3+}$.

2.4 Experimental Methods

2.4.1 General Experimental Conditions

All spectra reported in this text were collected at ambient temperature, unless otherwise stated. All reagents and chemicals, unless otherwise stated, were utilized as purchased from Sigma-Aldrich or Alfa Aesar. Mass spectrometry studies were conducted using a Thermo Fisher LXQ quadruple mass spectrometer. The fluorescence emission spectra were collected on a Horiba PTI QuantaMaster 400 with slit widths set to 0.50 mm, unless otherwise stated, and the UV-vis spectra were recorded on a Thermo

Scientific Evolution 220 spectrometer. Fluorescence lifetime studies were carried out using a Horiba Deltaflex time correlated single photon counting (TCSPC) system fitted with picosecond detection modules.

2.4.2 Mass Spectrometry Methods

Samples were prepared in HPLC grade acetonitrile at 1.0 $mg \cdot mL^{-1}$. The coordination compounds were prepared in 1:1 and 1:2 ratios of $Fe(CF_3SO_3)_3$ to **2.4** and allowed to equilibrate for two hours prior sample to analysis. The samples were also analyzed again after 24 hours and 48 hours to determine if longer equilibration times would alter the concentrations of different species present in solution. Data was acquired in both the positive and negative ion mode.

2.4.3 Optical Spectroscopy Methods

The molar extinction data was collected by first preparing a 25 µM solution of **2.4** in CH_3CN in a 2 mL quartz cuvette and recording the UV-Vis spectrum of the sample. A 1 mL aliquot was then removed from the cuvette and replaced with 1 mL of fresh solvent, followed by mixing of the solution on a vortex for one minute. The absorbance spectrum of the diluted sample was then recorded. This process was then repeated four additional times after which the data was plotted and analyzed.

The quantum yield data was obtained by titrating the amounts of anthracene, 9,10-diphenylanthracene, **2.4** and $[Fe(\mathbf{2.4})_2]^{3+}$ shown in table 2.1 into the appropriate solvent and analyzing the absorbance and fluorescence spectra of each compound. This process was repeated five times. The area under the fluorescence curve was then plotted versus

the absorbance intensity at λ_{max}, which yielded a straight line. The standards were then cross calibrated ensure that the observed Φ values for each were within 10% of the expected values (see equation 2.2). This was followed by cross calibration of the probe and coordination compound with each of the standards.

Table 2.1 *Concentrations of each compound used for quantum yield calculations.*

Compound	Solvent (2mL)	Aliquots of compound added to cuvette
Anthracene	EtOH	0.5 µL of 0.0025 M solution
9,10-diphenylanthracene	Cyclohexane	0.2 µL of 0.0025 M solution
2.4	CH_3CN	0.5 µL of 0.0025 M solution
$[Fe(\mathbf{2.4})_2]^{3+}$	CH_3CN	0.2 µL of 0.005 M solution

CHAPTER III – Fundamental Study of a Library of Rhodamine 6G Dyes

3.1 Background

A plethora of chromophores are used in sensor recognition mechanisms (Figure 1.1). The previous chapter utilized an excimer response to Fe^{3+} ion detection, however, the pyrene group is very hydrophobic. Therefore, to prepare LMFPs more suited to metal ion detection in aqueous systems, we opted to switch to the rhodamine chromophore. Rhodamine dyes belong to the family of xanthenes, along with fluorescein dyes, and they are known for their characteristically strong emissions in both organic and aqueous solvent systems.[115] These dyes are ideal compounds for developing "off-ON" type fluorescent sensors for recognizing various analytes (see chapter 1.3), owing to their high molar extinction coefficients, fluorescence emission in the visible region, and high fluorescence quantum yields (table 3.1. The general structures of the xanthene group and examples of derivatized xanthene moieties i.e., rhodamine dyes, are represented in Figure 3.1. Fluorescent dyes in this class have been identified as effective analytical tools that can help to monitor concentrations of analytes in various systems due to the simplicity of their design and their excellent spatiotemporal resolution.[116,117] The derivatization of these dyes also allows for tunability of their chemical properties such as their chemical stability in a given solvent, pH dependence, and toxicity.[116]

Since their initial discovery,[118] a large majority of the optical studies conducted with rhodamine dyes have been performed in purely organic solvents, or organic-aqueous solutions, due to characteristics such low water solubility and pH sensitivity. Therefore, there are limited the practical applications to which these sensors can be applied, for example, analyte analysis in water for physiological or environmental systems.

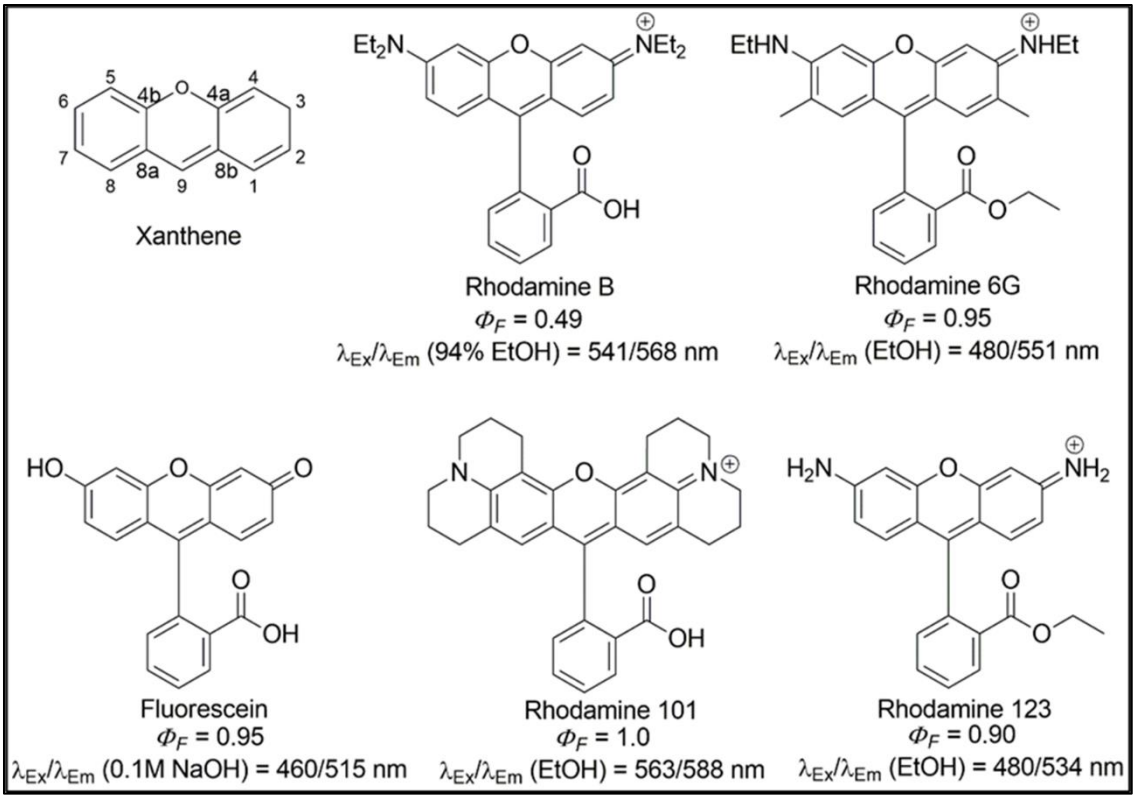

Figure 3.1 *Structures of Rhodamine dyes showing xanthene moiety as well as their quantum yields (Φ_F) in ethanol or water.* [119, 120, 121, 122, 123]

3.1.1 Inducing Ring Opening in Rhodamine Dyes

Spirocyclic-type rhodamine derivatives are non-fluorescent and colorless in solution, as the carbon atom in position nine (see xanthene number scheme 3.1) adopts an sp^3 geometry (closed). In organic solvents, the colorless, lactone form of these dyes is the dominant species. The absorption of the lactone form of rhodamines occurs in the ultraviolet spectral range (280 nm-400 nm) and the molecules display very little to no fluorescence.[115] Upon the change of the hybridization to sp^2, assisted by resonance, a ring open structure is formed. In contrast to the closed structures, the ring open structures yield colored solutions that are strongly fluorescent.[115]

The strong fluorescence of these molecules is owed to their extended π-conjugation and can be explained partly by analyzing their observed quantum yields. Rhodamine 101 is cited as having a quantum yield equal to one (figure 3.1), meaning that all excited state photons return to the ground state through the radiative fluorescence mechanism. Because a large amount of the energy initially absorbed is not dissipated through non-radiative transitions, such as intersystem crossing and internal conversion, these molecules produce very strong fluorescent signals, even at very low concentrations ($<1\times10^{-7}$ M). Scheme 3.1 highlights the spirocyclic (non-fluorescent) and ring open (fluorescent) forms of rhodamine B which result from adjusting solvent pH.

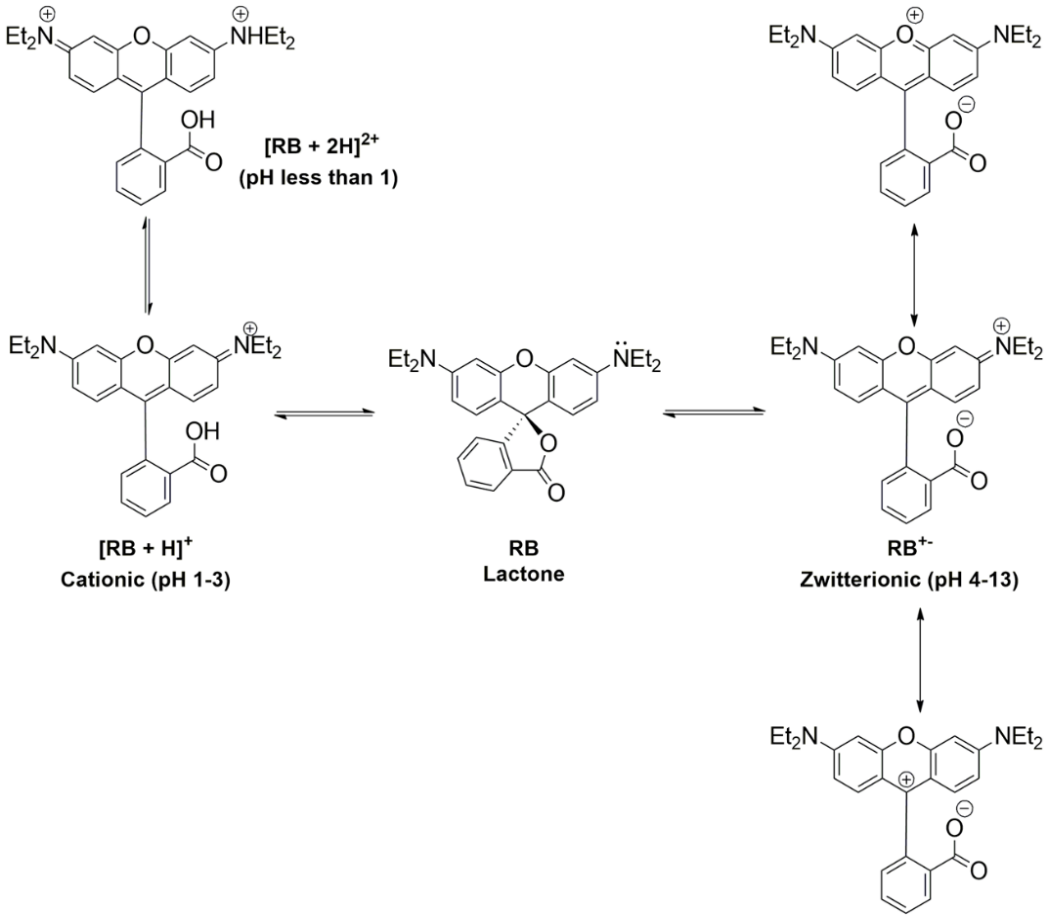

Scheme 3.1 *L-R Cationic, Lactone, and Zwitterionic forms of Rhodamine B (RB) under different pH conditions.*[115, 124]

A number of rhodamine derivatives have been synthesized to bind metal ions.[115] Similar to the pH induced ring opening shown in scheme 3.1, the formation of metal-rhodamine complexes also induces ring-opening and may result in a change in the molecule's fluorescence from the "off" state to the "on" state (hypochromic to hyperchromic shift). This ring opening is typically accompanied by a color change that is observable via naked eye detection.[125] The formation of stable complexes between metal ions and rhodamine dyes typically results in color changes that are easily identifiable, while less stable or weaker complex formation often yields less pronounced color changes. When metal ions interact with ligand groups on the receptor, the degree of conjugation of the π-electron system of the unbound receptor changes. This change in conjugation often alters the fluorescence emission signal, the fluorescent quantum yield, and the fluorescence lifetime.[39] An example of the interaction between a metal ion and a rhodamine receptor is shown in Scheme 3.2. The ability to monitor this change in π-conjugation makes fluorescent molecules like rhodamine dyes ideal for use as molecular sensors for target analytes.

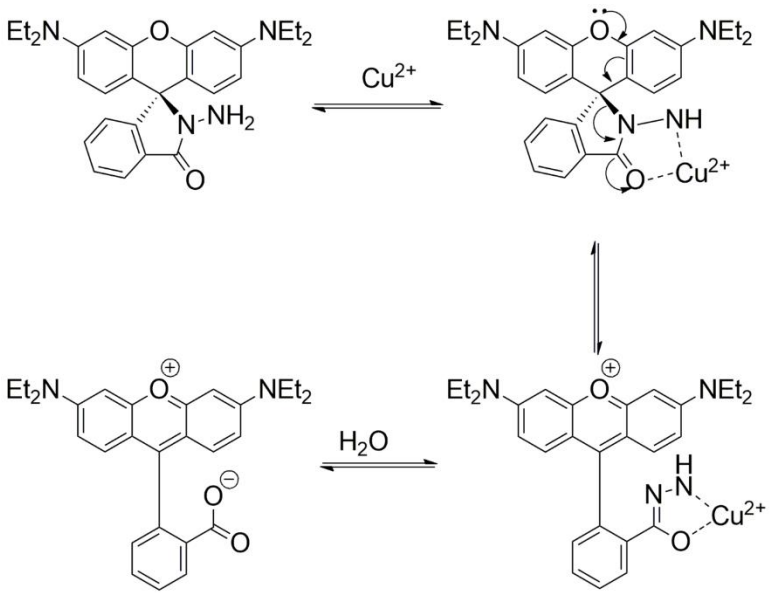

Scheme 3.2 *Proposed mechanism of Cu^{2+} induced ring opening in rhodamine B hydrazide (**3.1**). This mechanism was first proposed by Czarnik et al.*[126]

Despite their characteristically large fluorescence quantum yields, many studies involving rhodamine dyes highlight the tendencies of these dyes to undergo fluorescence quenching in the presence of paramagnetic metal ions i.e., Cu^{2+} and Fe^{3+}. Lone pair electrons on amine and oxygen atoms within the molecule can also induce a PET mechanism which leads to fluorescence quenching (scheme 3.3). Fluorescence quenching is a process which decreases the intensity of the emission of a fluorescent molecule or complex and occurs via two main mechanisms- dynamic (collisional) and static (contact) quenching.[127] Collisional quenching occurs when the excited state fluorophore is deactivated upon interaction with some other molecule (oxygen, halogens, amines and electron deficient molecules) in the solution. Upon contact, the fluorophore returns to its ground state without the emission of light.

Work done by Bakkialakshmi et al., highlights the mechanism of collisional quenching, whereby the fluorescence of rhodamine B base is quenched by the addition of triethylamine and n-butylamine to a solution of the dye in dimethylformamide.[128] As the amines were added to the solution of the dye, a hypochromic shift in the fluorescence spectra was observed as the molecule changed from an "on"-state to an "off" state. Dissolved molecular oxygen behaves in a similar manner and reduces the fluorescence intensity of fluorophores in solution via photochemical oxidation of the fluorescent species. The paramagnetic nature of molecular oxygen promotes intersystem crossing and conversion of excited molecules to the triplet state, ultimately resulting in quenching of the fluorescence. [40] Molecular oxygen affects steady state fluorescence measurements as well as lifetime measurements. Hypochromic fluorescence shifts observed in the presence of molecular oxygen indicate an increase in the number of non-radiative decay processes (k_{nr}). As was highlighted in equation 2.3, an increase k_{nr} quenches the fluorescence lifetimes of fluorophores.

In contrast to dynamic quenching, static quenching occurs when fluorophores form non-fluorescent complexes with other fluorophores or non-fluorescent molecules often referred to as quenchers. When the newly formed complex absorbs energy, the excited state immediately returns to the ground state without emitting a photon, therefore the molecules do not emit fluorescent light. A distinctive feature of static quenching is a change in the absorption spectra of the two molecules upon complex formation. An example of a fluorescence quenching mechanism and subsequent quenching attenuation is shown in scheme 3.3. The fluorescence quenching is attenuated by inhibiting the

ability of the nitrogen atom to undergo a photoinduced electron transfer (PET) mechanism.

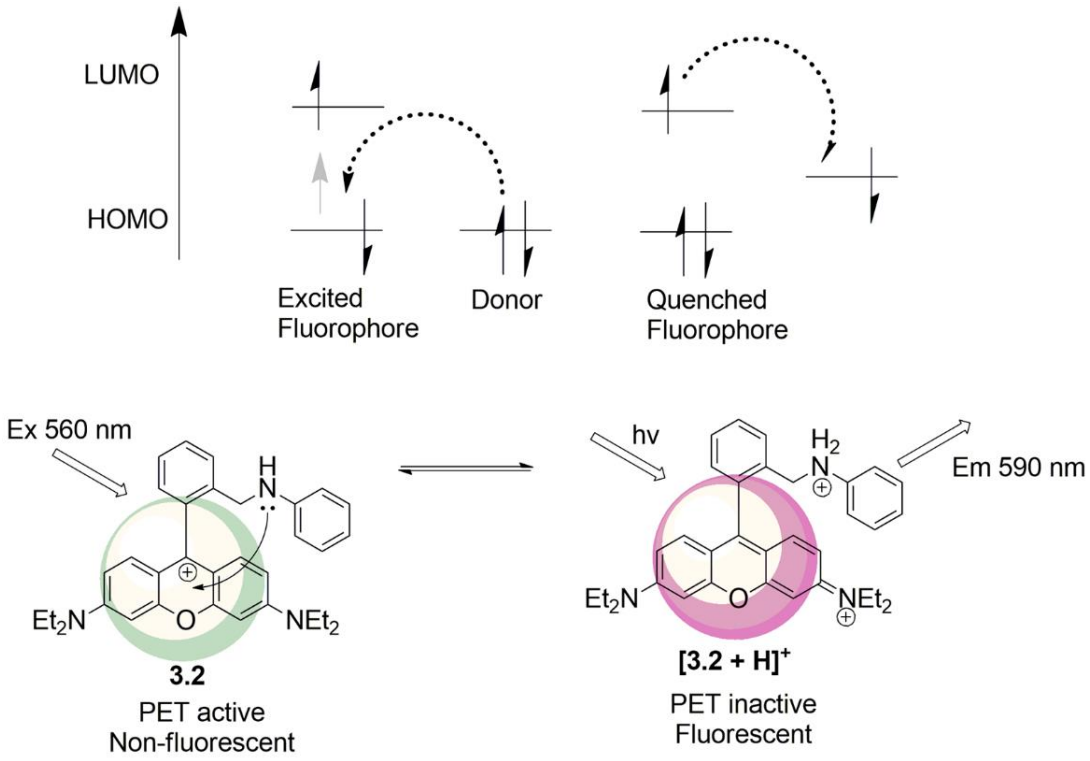

Scheme 3.3 *PET mechanism in rhodamine B cation upon excitation of the fluorophore.*[129]

3.2 Current Rhodamine-based LMFPs for Cupric and Ferric Ions

Due to the environmental and biological significance of Fe^{3+} and Cu^{2+} ions, there is a significant interest designing new sensors to be able to detect and quantify ultralow concentrations (ppb) of these ions in different environments. For some researchers, single ion selectivity is important, while others prefer to take advantage of the multifunctional characteristics of some sensors to be able to detect multiple metal ions in solution.[48, 130] From the first report of the synthesis of a rhodamine dye in 1888, to present day, thousands of papers have been published on the use of rhodamine dyes for different

applications.[118,125,131] This section serves to highlight some of the more recent reports, within the last ten years, on rhodamine-based sensors for the detection of Cu^{2+} and Fe^{3+} ions in organic and aqueous systems.

Geng et al. synthesized a 100% water-soluble polyacrylamide rhodamine sensor **(3.3**), shown in scheme 3.4, for the detection of Hg^{2+} and Cu^{2+} ions.[132] The sensor is stable, and displays virtually no significant fluorescence signals between pH 5.41-11.18. No UV-vis spectral data was reported for this sensor, instead, Geng et al relied on the use of visible light and UV-light at 365nm to determine which metals formed complexes with sensor **3.3** in water. The only two metals that resulted in a noticeable color change in both visible light and UV-light were Cu^{2+} and Hg^{2+} ions. Under visible light, the solution of **3.3** with Cu^{2+} and Hg^{2+} changed from colorless to clear, while under UV-light the sample changed from dark to a greenish-yellow color. The authors reason that the selectivity of the sensor is due to the cooperating influences of a suitable coordination geometry and the proper radius and charge density of the Cu^{2+} and Hg^{2+} ions. The selectivity is also likely due to ability of oxygen containing solvents to inhibit coordination between metals and ligands as well as propensity of some metals to hydrolyze in solution. The limits of detection reported for Cu^{2+} and Hg^{2+} were 8.81×10^{-7} M and 5.05×10^{-8} M, respectively. A unique characteristic of **3.3** is its ability to distinguish between Cu^{2+} and Hg^{2+} ions. The addition of these Cu^{2+} ions to a solution of **3.3** in water resulted in a 4-fold increase in the fluorescence signal observed at 544 nm. In contrast, the addition of Hg^{2+} ion resulted in a 4.5-fold fluorescence enhancement as well as a red shift from 544-550 nm. Furthermore, the addition of competing metal ions, Ag^{+}, K^{+}, Ba^{2+}, Cd^{2+}, Co^{2+}, Fe^{2+}, Mg^{2+}, Ni^{2+}, Pb^{2+},

Zn^{2+}, Cr^{3+} and Fe^{3+}, to solutions of **3.3** with Cu^{2+} and Hg^{2+} ions, appeared to have no notable impact on the observed fluorescence signals.

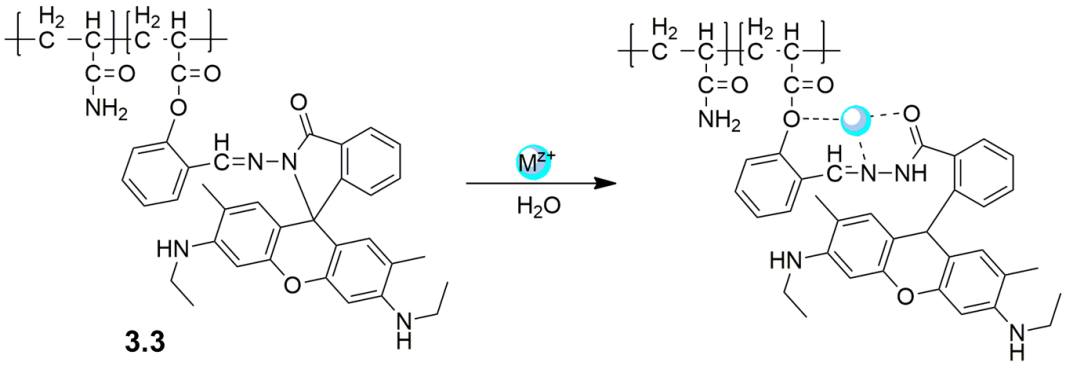

Scheme 3.4 *The proposed binding between sensor **3.3** and Cu^{2+} and Hg^{2+} cations in 100% water*

An off-ON colorimetric and fluorescent chemodosimeter (**3.4)** was synthesized by Wang et al., for the detection of Cu^{2+} ions in aqueous and organic solutions.[133] The N-(2,4-dinitrophenyl) rhodamine B derivative was found to react in an irreversible manner with Cu^{2+} ions in aqueous solvents. Solutions of **3.4** in ethanol-water mixtures (3:1, v/v, Na_2HPO_4-citric acid buffer, pH = 7.0) appear clear, however, the addition of different Cu^{2+} salts, results in a color change to magenta. This color change corresponds to the emergence of a hyperchromic shift at 556 nm in the absorbance spectrum of **3.4**. The addition of Fe^{3+} and Fe^{2+} also resulted in a very small absorbance band at 556 nm, however no visible color change was observed via naked eye detection. It is likely that iron coordination was inhibited due to the hydrolysis reactions discussed in chapter 1.5. The addition of other metal ions, Ag^{+}, K^{+}, Na^{+}, Ca^{2+}, Cd^{2+}, Hg^{2+}, Mg^{2+}, Ni^{2+}, Pb^{2+}, Zn^{2+}, Al^{3+}, Cr^{3+}, did not result in any spectral changes to **3.4**. Fluorescence analysis of **3.4** with Cu^{2+} in ethanol did result in an increase in any fluorescence bands, as the Cu^{2+} ion is a

notorious quencher. However, in the ethanol-water mix, an imine hydrolysis reaction occurs, resulting in the fluorescent rhodamine B species highlighted in scheme 3.5. This reaction was verified through ESI-MS. In the presence of Cu^{2+}, a characteristic m/z signal was observed at 623.6 for the [**3.4** + H]$^{+}$ species, additionally, a signal was also observed at m/z = 443.38. This second peak accounts for the fluorescent compound in scheme 3.5, proving that the Cu^{2+} ion as well as water induced the hydrolysis mechanism.

Optimal pH conditions for detecting the [Cu(**3.4**)]$^{2+}$ complex were found to be between pH 4-8. This is likely due to the possibility of false positives arising below pH 4 and insoluble $Cu(OH)_2$ precipitating from solution above pH 8 (see figure 1.7), as $Cu(OH)_2$ is insoluble in water as well as ethanol. A Benesi-Hilderbrand plot was used to determine a 1:1 binding ratio between **3.4** and Cu^{2+} ions, and an association constant of $1.06 \times 10^3\ M^{-1}$ was determined for the **3.4**-Cu^{2+} complex, which is indicative of relatively weak binding in aqueous solution at neutral pH. Lastly, absorbance and fluorescence titration data were used to determine detection limits of 2.6×10^{-8} M and 1.2×10^{-9} M, respectively.

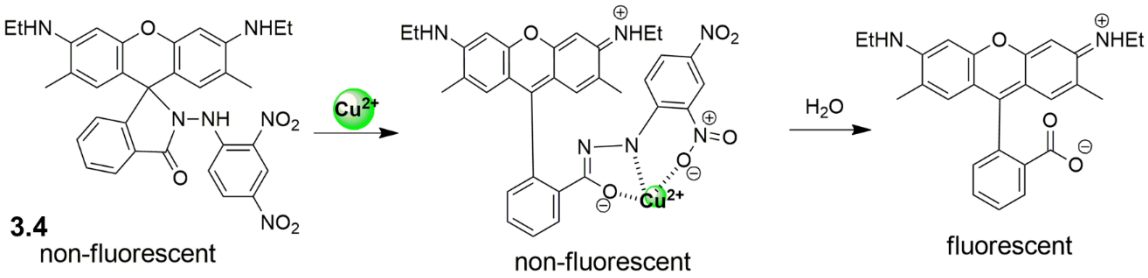

Scheme 3.5 *Proposed binding of **3.4** with Cu^{2+}, followed by imine hydrolysis upon the addition of water to the system.*

Xu et al. successfully designed a rhodamine-derived molecular probe (**3.5**) for fluorometric sensing of H^{+} between pH 2-4, and the colorimetric sensing of Cu^{2+} ions in a

mixture of neutral water and methanol (3:1, v/v).[134] A binary logic gate at monomolecular level with OR gate was then used to distinguish between pH less than or greater than 5, as well as concentrations of Cu^{2+} higher or lower than 0.5 μM. Sensor **3.5** displays an intense fluorescence signal at 579 nm in the pH range of 2-4. Upon increasing the pH up to 7, Xu et al. observed absorbed drastic hypochromic shifts in the fluorescence band, and above pH 7, virtually no fluorescence was observable in sensor **3.5**. In contrast to many of the rhodamine dyes reported in the literature, the addition of various metal ions, Ag^{+}, K^{+}, Na^{+}, Ba^{2+}, Ca^{2+}, Cd^{2+}, Co^{2+}, Cu^{2+}, Hg^{2+}, Mn^{2+}, Mg^{2+}, Ni^{2+}, Pb^{2+}, Zn^{2+}, Al^{3+}, Cr^{3+}, Fe^{3+}, and to the aqueous solution of sensor **3.5** did not result in a fluorescence turn on signal. Instead, the addition of the Cu^{2+} ion led to fluorescence quenching. Quenching is often used to monitor the concentration of analytes in solution, however, this method of quantification is sometimes unreliable due to different factors than can lead to quenching in complex matrixes, i.e. the presence molecular oxygen, chloride and iodide anions, and amine species in solution. Quenching may also be observed when the concentration of the chromophore in solution is too high, resulting in the formation of aggregates which are non-fluorescent. As an alternative, Xu et al. focused on the colorimetric response of **3.5** to Cu^{2+} in aqueous solvents. In acidic H_2O: MeOH (3:1), an absorbance band was observed at 564nm for [**3.5**-H]$^{+}$, whereas in neutral pH, upon coordinating to Cu^{2+}, an absorption band was instead observed at 570 nm. The coordination to copper is also accompanied by a solution change from colorless to pink, allowing for naked-eye detection. Job's plot analysis of **3.5** displayed a plot with a maximum at 0.33, corresponding to the 2:1 binding displayed in scheme 3.6. This stoichiometry was further validated through ESI-MS where a m/z signal of 1285.3 was

observed, which accounts for [Cu(**3.5**)$_2$ - H]$^+$. Lastly, a LoD of 0.0365 µM was determined from a plot of the absorbance at 570nm vs the concentrations of Cu^{2+} in solution. The proposed coordination environment between **3.5** Cu^{2+} ions is shown in scheme 3.6, however, no analyses were reported that verified that the mode of coordination was in fact through the oxygen atoms.

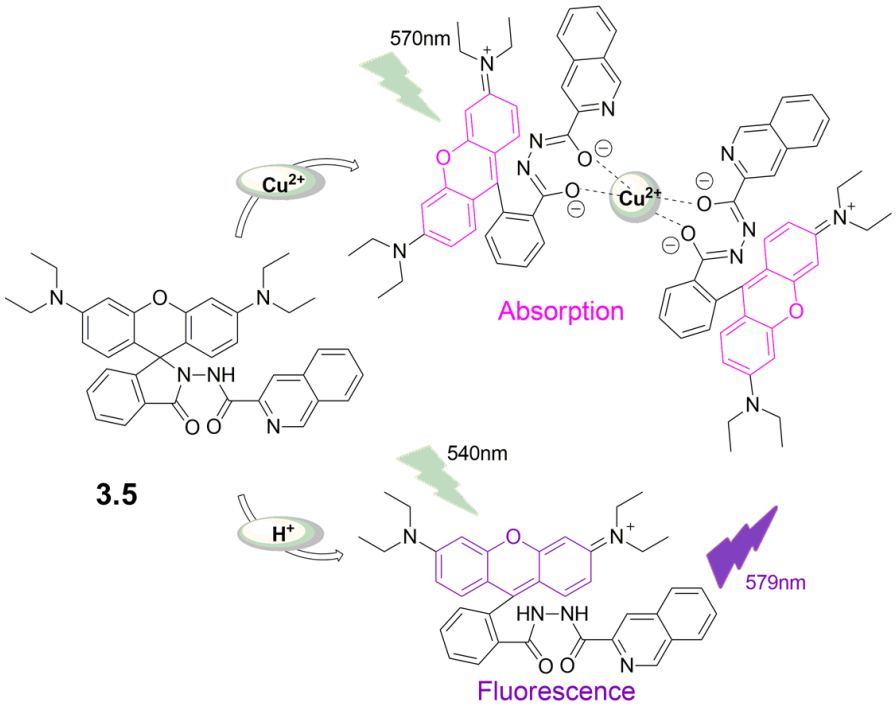

Scheme 3.6 *Dual nature of **3.5** for naked-eye detection of Cu^{2+} and fluorescence detection of pH < 4*

A rhodamine 6G-based bi-functional sensor was synthesized by Sinn and co-workers for the detection of Fe^{3+} and Cu^{2+} ions in solutions of 75% CH_3CN, 25% 0.01M Tris-HCl buffer at pH 7.0.[135] Compound **3.6** was designed to trap metal ions between the two rhodamine moieties, thereby acting as a tetradentate ligand with two carbonyl groups and two imine nitrogens serving as donor atoms. In the absence of metal ions and at pH > 4.5, no absorbance bands were observed above 400 nm for **3.6** in the solution of CH_3CN

and Tris-HCl buffer. The addition of Cu^{2+} to the solution of the sensor immediately resulted in a color change from colorless to pink and a hyperchromic shift was observed at 551 nm with a shoulder at 520 nm. The only other metal ion that resulted in a similar colorimetric response was the Fe^{3+} ion, which resulted in a new absorbance band at 562 nm. Upon comparison of the resultant absorbance bands, it was noted that the intensity of the band observed upon the addition of 40 equivalents of Cu^{2+} to **3.6** was greater than two times the signal observed when an equimolar concentration of Fe^{3+} was added to the solution of the sensor. This is likely due to the formation of Fe^{3+} hydrolysis products in the aqueous solution, as well as the tendency of Tris-HCl buffer to complex with Fe^{3+} ions.[136] Tris-HCl buffer is also notorious for coordinating to other metal ions such as, Cr^{3+}, Co^{2+}, Ni^{2+}, and Cu^{2+};[136] this metal binding behavior potentially offers an explanation for why such high concentration of the metals were needed to induce a significant turn on response in **3.6**.[136] By using the Benesi-Hildebrand method, a binding ratio of 1:1 was determined for the $[Cu(\mathbf{3.6})]^{2+}$ complex with a binding constant of $1.65 \times 10^3\ M^{-1}$. A limit of detection of 69 μM was calculated for Cu^{2+} ions, which is much lower than the 100 μM LoD determined for Fe^{3+} ions. On its own, sensor **3.6** displays a very weak fluorescence band at 570nm when excited at 520nm, however, the addition of Fe^{3+} to the solution of the sensor resulted in a bathochromic and hyperchromic shift observable at 580 nm. No other metal ions resulted in any notable emission enhancement. The data from the fluorescence titration of **3.6** with Fe^{3+} was then used to determine 1:1 complex formation as well as a binding constant of $9.75 \times 10^2\ M^{-1}$ which is indicative of very weak binding.

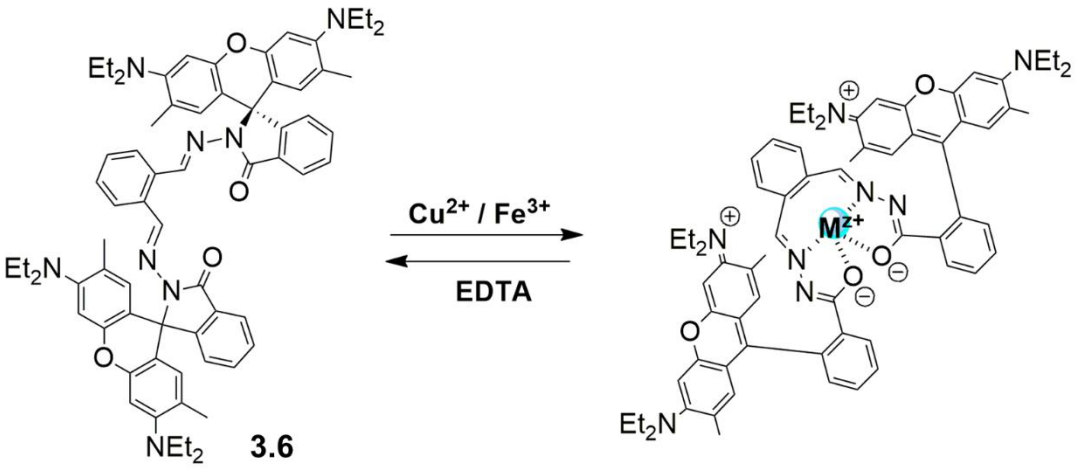

Scheme 3.7 *Proposed binding between **3.6** and metal ions as well as reversibility of the binding with EDTA. (z+ =+2 or +3)*

A CHEF induced molecular sensor (**3.7**) was synthesized by Goswami et al for detecting Fe^{3+} ions in aqueous solution at neutral pH.[137] In a solution of CH_3CN-H_2O (1:1, v/v, pH 7.2), the rhodamine-6G and 6-(hydroxymethyl) picolinohydrazide derivative is colorless, indicating that the structure mainly exists in the spirolactam form shown in scheme 3.8. This is further verified due to the absence of absorbance bands above 400 nm. Upon titrating two equivalents of Fe^{3+} to a 10 µM solution of **3.7**, a hyperchromic shift was observed at 530 nm, accounting for a 116-fold increase in the absorbance. From the absorbance titration data, the detection limit and association constant (K_{11}) were calculated to be 5.6×10^{-7} (31 ppb) and 1.0×10^4 M^{-1}, respectively. Additionally, very weak fluorescence was observed for compound **3.7** in the absence of Fe^{3+} ions, but the addition of Fe^{3+} to a solution of the sensor resulted in a 23-fold fluorescence enhancement observable at 550 nm. The detection limit and association constant were calculated to be 3.4×10^{-8} M (2 ppb) and 5.9×10^5 M^{-1}, respectively, for Fe^{3+} ions by fluorescence experiments. The effects of other relevant metal ions such as

K^+, Na^+, Cd^{2+}, Co^{2+}, Cu^{2+}, Fe^{2+}, Hg^{2+}, Mg^{2+}, Mn^{2+}, Ni^{2+}, Pb^{2+}, Zn^{2+}, Al^{3+}, Cr^{3+}, and In^{3+} were also studied but did no significant enhancement in fluorescence and absorption were absorbed. A small absorption band was observed for the Cu^{2+} ion, however this 7-fold increase was much lower than the 116-fold increase observed for Fe^{3+}.The coordination of compound **3.7** with the Fe^{3+} ion was investigated through TDDFT calculations which verifies the trigonal prismatic geometry shown in the [Fe(**3.7**)]$^+$ complex in scheme 3.8. Lastly, the authors prepared a 'dip-stick' test using TLC plates to demonstrate that the sensor could provide qualitative data in the solid phase. When the TLC plate coated with **3.7** was submerged into an aqueous solution containing Fe^{3+} ions, the silica surface change from white to pink. This simple approach is rather attractive as it allows for real-time, on-site metal analysis.

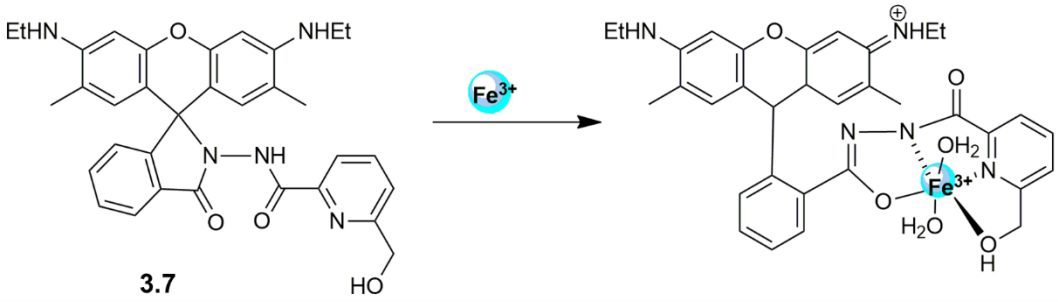

Scheme 3.8 *Proposed metal-ligand coordination between compound **3.7** and Fe^{3+} ions in aqueous solution.*

Chereddy and coworkers synthesized a naphthalimide-rhodamine 'FRET off-ON' sensor (**3.8**) for the selective ratiometric detection of Fe^{3+} ions in aqueous solutions and cellular environments (scheme 3.9).[138] The triazole appended quinoline-rhodamine conjugate serves two purposes, acting as the selective ionophore for Fe^{3+} ions, as well as

the FRET energy acceptor, while the 8-piperazone-naphthalimide moiety serves as the FRET energy donor. The intramolecular FRET mechanism is possible due to the overlap of the fluorescence emission of the naphthalimide moiety with the absorption spectrum of rhodamine B. Sensor **3.8** is observed as a pale-yellow color in aqueous CH_3CN (1:1. v/v 0.01 M Tris HCl-CH_3CN, pH 7.4) due to the naphthalimide moiety. Upon excitation of the naphthalimide unit at 415 nm, an electron transfer to the rhodamine moiety is not possible. However, the introduction of Fe^{3+} ions to the solution of **3.8** resulted in a linear increase in the absorbance band at 560 nm, and after the addition of two equivalents of Fe^{3+}, the absorbance at 560 nm had increased by 458-fold. This means that the FRET mechanism could only occur when the rhodamine had coordinated to Fe^{3+}. No other metals demonstrated this behavior, indicating the selective behavior of **3.8** for Fe^{3+}. The fluorescence studies of the **3.8** with Fe^{3+} displayed a hypochromic shift in the band at 532 nm, for the naphthalimide moiety, as well as a new hyperchromic band at 580 nm through and isoemissive point at 567 nm. The band at 580 nm corresponds to the ring opening mechanisms of the rhodamine. From the titration studies, the authors were able to determine 1:1 binding between the **3.8** and Fe^{3+} ions along with a dissociation constant of 1.04×10^{-6} M and a detection limit of

50 nM. Sensor **3.8** was also doped into mouse embryonic fibroblast (NIH 3T3), which is the most common type of connective tissue in mammals, to detect exogenous Fe^{3+} ions. In the absence of Fe^{3+}, a bright green fluorescence was observed, however, upon the addition of Fe^{3+} ions to the cells, an intense red color is observed with a decrease in the green fluorescence.

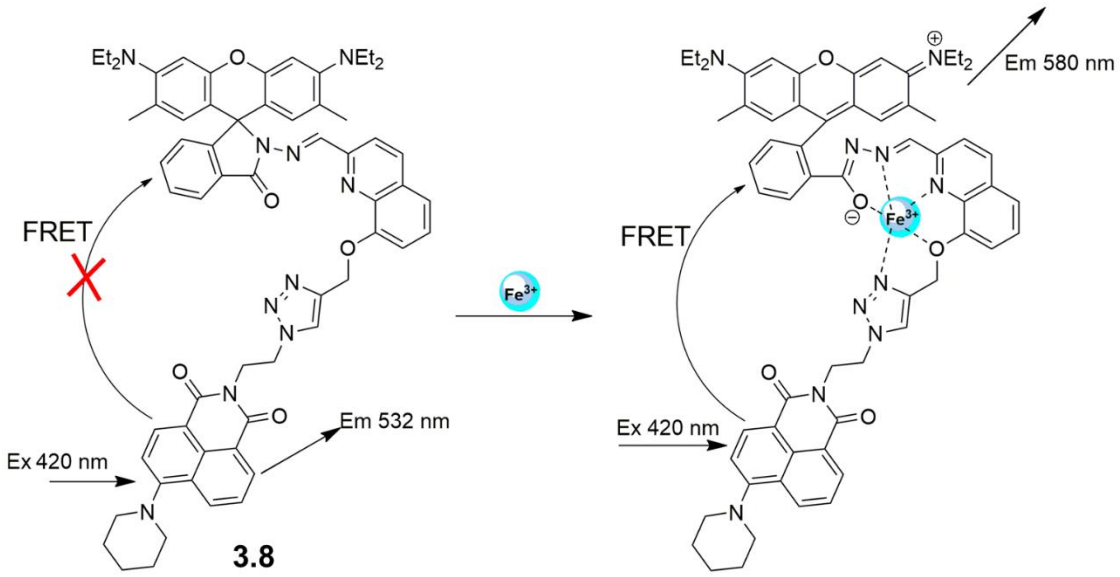

Scheme 3.9 *Proposed FRET based sensing observed in **3.8** upon binding Fe^{3+} ions.*

3.2.1 Concluding Remarks About Published Literature

Though the literature examples reviewed here report the selective binding of Cu^{2+} and/ or Fe^{3+} ions, it is important to note that many of these studies focused on only one solvent system and did not study the effect of varying the speciation of the metal ion, i.e., changing the counterion of the metal ion. Factors such as these cannot be ignored when determining the selectivity of a sensor. Moreover, the hydrolysis reactions of iron ions are often omitted. It would have been beneficial for the researchers to analyze the metal ions in a range of organic solvents to determine how the bulk solvent affected the binding between the receptor and the analyte. Many reported works use buffer solutions of Tris-HCl, however, this buffer system has been reported to coordinate to metal ions such as Cr^{3+}, Fe^{3+}, Co^{2+}, Ni^{2+} and Cu^{2+}.[136] It is possible that in Tris-HCl buffer, the receptors simply could not bind to other metal ions due to a higher binding affinity between the

bulk solvent and these ions. This means that under different aqueous conditions, sensor selectivity could possibly be diminished and often misrepresented.

Lastly, probes **3.4**, **3.5** and **3.6** all undergo fluorescence quenching upon coordination Cu^{2+} ions due to the paramagnetic nature of this metal ion. The +3 oxidation state of iron is also notorious for inducing the fluorescence quenching mechanism. While it is difficult to predict with certainty whether a sensor will undergo fluorescence amplification or quenching prior to conducting metal analysis, our goal is to carry out a fundamental investigation into rhodamine type molecular probes, and to determine the roles that different solvent systems and counterions play in affecting the binding interactions between the receptor and different analytes.

3.3 Sensor Design

The design principles of work previously carried out by members of the Wallace research group has produced a library of rhodamine based LMFPs. Within the last decade, there have been many published articles and reviews on rhodamine dyes and their ability to bind specific metal ions under aqueous conditions (some examples were discussed in section 3.2), however, much of this work is questionable. As a result, the work presented in this chapter analyzes a series of molecular probes with different coordination environments and their optical responses upon interacting with metal ions in different solvent systems.

Even though the rhodamine chromophore offers the advantage of better water solubility over the pyrene signaling discussed in chapter 2, there are still considerable challenges to overcome depending on the analyte of interest.[94,92] Sensor **3.10,** shown in

figure 3.2, was designed as a control to demonstrate how the chelate effect could alter the stability of the complexes formed between our sensors and metal ions. The chelate effect, by definition, enhances the affinity of chelating ligands for a metal ion compared to the affinity of a collection of similar nonchelating (monodentate) ligands. The chelate affect also results in more thermodynamically favored complexes which are more likely to form over complexes comprised of monodentate ligands. Sensor **3.11a** was synthesized to determine if the addition of a hard Lewis base, specifically an alcohol group, to the 9' position of the coordination environment would result in the formation of more stable complexes than would be observed for **3.10** with metal ions. The addition of an alcohol group to the coordination environment would result in the formation of both a five-membered and a six-membered ring upon coordination of receptor **3.11a** to a metal ion (figure 3.3), thus enhancing the stability of the complex. Furthermore, the addition of the alcohol group is also expected to improve the water solubility of the sensor, as the number of hydrogen bonding interactions between the sensor and water molecules would increase.

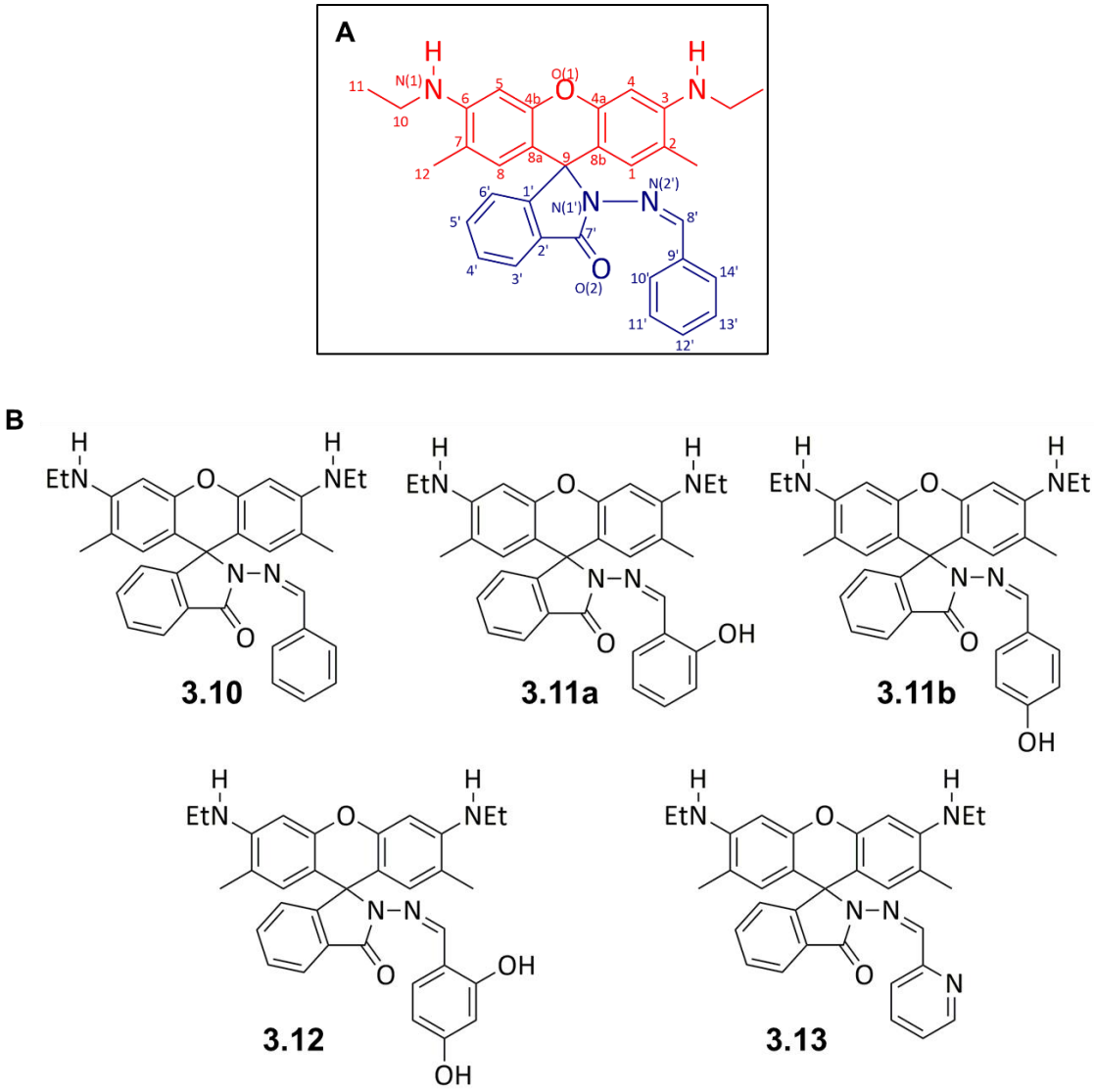

Figure 3.2 *(A) Numbering system used for rhodamine 6G dyes presented in this work. (B)Library of rhodamine dyes used for fundamental study to observe the chelate affect*

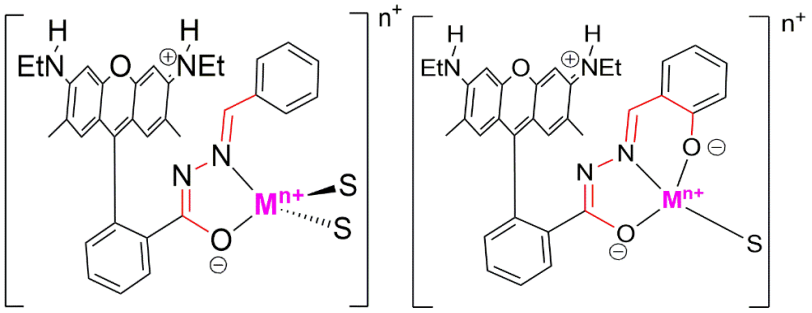

Figure 3.3 *Proposed coordination environments of* ***3.10*** *(left) and* ***3.11a*** *(right). The complex on the right is expected to be more thermodynamically stable than the complex on the left due to the chelate effect.*

By conducting an in-depth analysis of the sensors shown in figure 3.2, we hoped to better understand how factors such as different solvents and counterions would affect complex formation and stability in solution. Previous work by the Wallace et al. highlights that changing metal counterions can alter the binding ratios between receptors and metal ions.[94] With this knowledge in hand, we believe that it will be possible to design LMFPs with improved selectivity for target analytes in a range of aqueous environments.

3.4 Hypothesis

Low molecular weight fluorescent probes can be derivatized to serve as signaling probes for metal ions in biological and environmental systems. The addition of hard Lewis bases to the coordination environment will result in LMFPs that preferentially coordinate to hard Lewis acids, such as Al^{3+} and Fe^{3+} ions. It is however likely that some borderline metal ions such as Cu^{2+}, Fe^{2+}, and Zn^{2+} ions may also interact with the probes. To distinguish between the analytes, unique approaches, such as the use of a molecular logic gate can be used, as well as the introduction of chemical species that

will alter the binding between the metal ion and the molecular probe in a characteristic fashion The latter technique has been previously used by the Wallace group to distinguish between Fe^{3+} and Al^{3+} ions in organic solvent systems.[42]

3.5 Results and Discussion

3.5.1 General Synthesis and Characterization

Compounds **3.10**, **3.11a-b**, **3.12**, and **3.13** were all prepared in a two-step procedure, whereby the commercially available rhodamine 6G chloride was reacted with excess hydrazine hydrate for four hours and isolated as a pink solid (compound **3.9**) in 80-90% yields. Proton NMR was used to confirm the conversion of rhodamine 6G chloride to **3.9**, as the loss of the ethyl group from the ester ($CDCl_3$, triplet, 0.97 ppm) is easily observed as well as notable changes to the splitting patterns in the aromatic region. Compound **3.9** was then reacted with the appropriate aldehyde derivative via condensation reaction (scheme 3.10). The resulting rhodamine imines precipitated from the reaction solvent and were isolated in good yields between 80-90%. The loss of the two protons from N2' ($CDCl_3$, 3.57 ppm), as well as the emergence of an imine signal (8') between 8.50- 9.09 ppm in $CDCl_3$, verified the conversion from **3.9** to the desired rhodamine imine derivative. All compounds were fully characterized by means of ^{1}H-NMR ^{13}C-NMR, FT-IR, and ESI-MS, see section 3.6.5. Compounds **3.10**, **3.11a**, and **3.12** were characterized by the former techniques as well as X-ray crystallography.

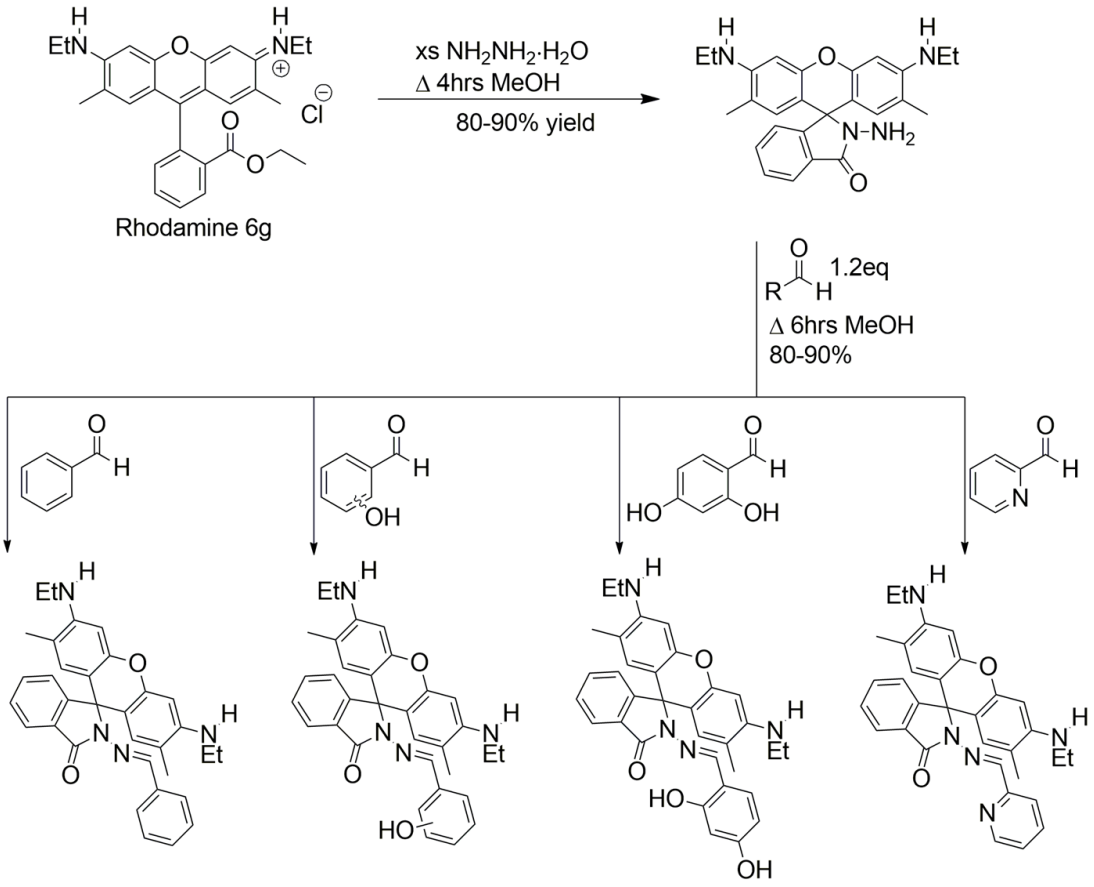

Scheme 3.10 *General synthesis of molecular probes **3.10**, **3.11a-b** (a = ortho, b = para), **3.12**, and **3.13**.*

3.5.2 X-ray Crystallography

X-ray quality crystals of compounds **3.10**, **3.11a** and **3.12** were obtained from slow evaporation of a concentration solution of methanol. All three compounds show the spriolactam ring formation, figures 3.4-3.6. The lactam and the xanthene group are orthogonal to one another. Compound **3.10** crystallizes in the centrosymmetric fashion, whereas compounds **3.11a** and **3.12** are both monoclinic crystal system (Table 3.1). Interestingly, the xanthene group adopts a sofa like conformation. Compound **3.12** has enclathrated methanol molecules in the crystal structure. Both **3.11a** and **3.12** have an

intramolecular hydrogen bonding interaction between the hydroxy group situated in the *ortho* position on the benzene core and the nitrogen atom in the hydrazine group. The crystal packing of all three compounds and that are stabilized via an array of CH···π interactions, this is clearly demonstrated in compound **3.10.**

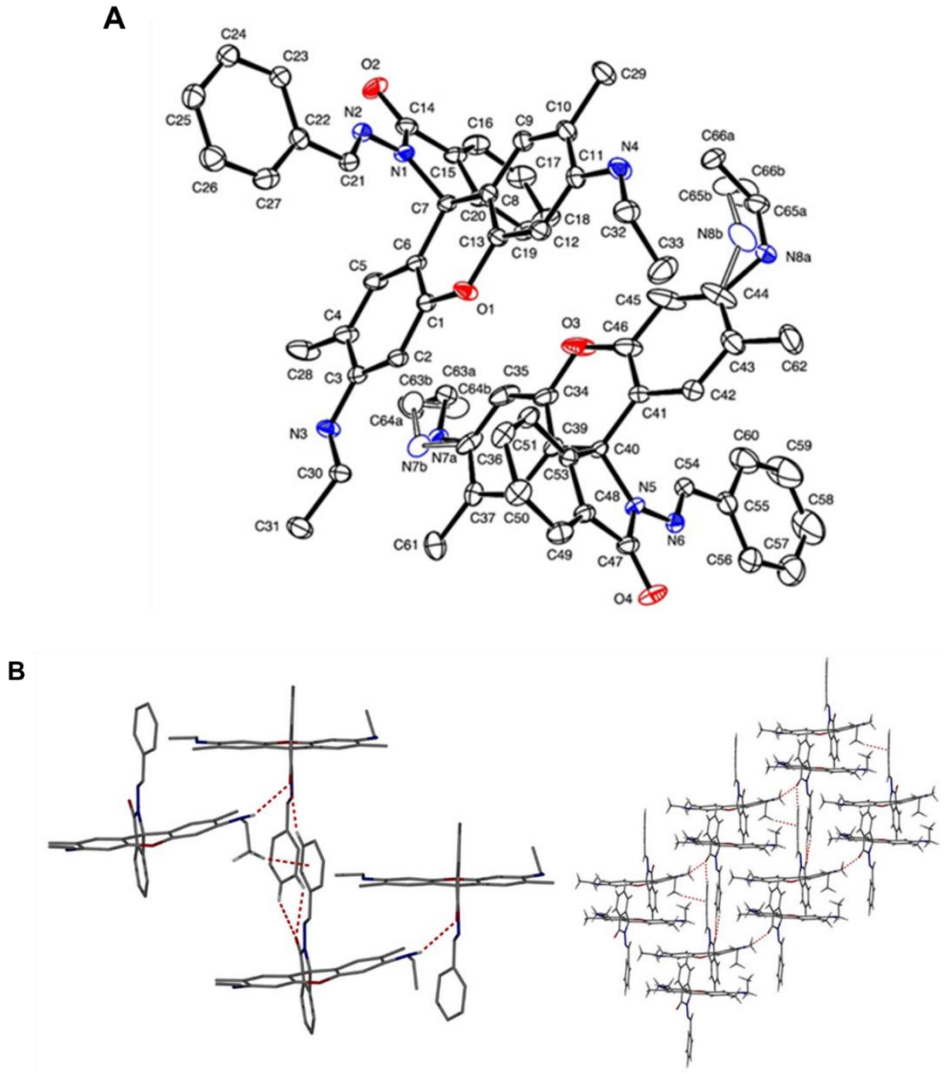

Figure 3.4 *(A) Compound **3.10** with displacement atomic ellipsoids at 50% probability and labeling. One of the ethyl groups is disordered and is represented as non-colored. (B) The molecular packing of compound **3.10** highlighting three distinctive hydrogen-bonding interactions (i) NH···O (ii) CH···π and (iii) a bifurcated CH···O*

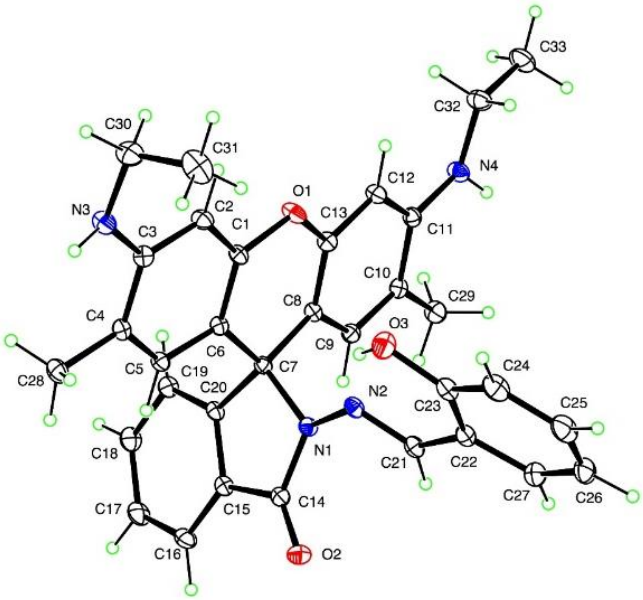

Figure 3.5 *Compound **3.11a** with displacement atomic ellipsoids at 50% probability and labeling.*

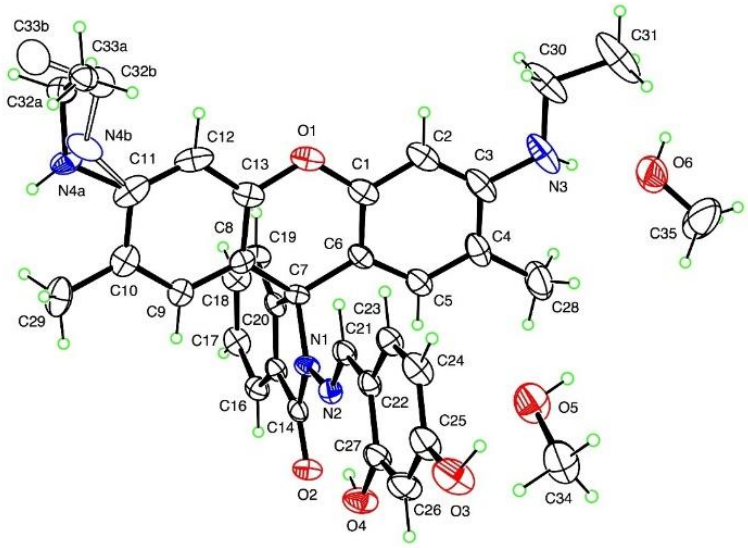

Figure 3.6 *) Compound **3.12** with displacement atomic ellipsoids at 50% probability and labeling. One of the ethyl groups is disordered and is represented as non-colored*

Table 3.1 *Summary of crystal data for compounds **3.10**, **3.11a** and **3.12.***

	Compound 3.10	**Compound 3.11a**	**Compound 3.12**
Formula	$C_{33}H_{32}N_4O_2$	$C_{33}H_{32}N_4O_3$	$C_{33}H_{32}N_4O_4$ $2CH_3OH$
M_r	516.63	532.62	612.71
Crystal color, habit	Colorless, tablet	Prism, light purple	Pink, Lath
Crystal system	Trinclinic	Monoclinic	Monoclinic
Space group	P1bar	$P_{21/c}$	$P_{21/c}$
a (Å)	11.3318(4)	10.6772(4)	15.3763(6)
b (Å)	13.1141(5)	20.5762(6)	13.9222(6)
c (Å)	18.3687(7)	12.3121(4)	15.2337(5)
α (°)	76.736(3)	-	-
β (°)	88.534(2)	101.6597(18)	105.726(2)
γ (°)	86.056(2)	-	-
V ($Å^3$)	2650.46(17)	2649.32	3139.0(2)
Z	4	4	4
F(000)	1096	1128	1304
Dx ($Mg·m^{-3}$)	1.296	1.335	1.296
Radiation type (λ)	(Mo) 0.71073	(Mo) 0.71073	(Cu) 1.54184
No. of unique reflections	35735	68931	24358
No. of observed reflections	16408	8525	4948
Parameters refined	777	372	456
R	0.069	0.046	0.038
R_w	0.202	0.119	0.143
S	1.03	1.01	1.06
Largest diffraction peak and hole (e $Å^{-3}$)	0.44 to -0.42	0.47 to – 0.26	0.22 to -0.32

Computer programs: APEX2 and SAINT (Bruker, 2009), SHELXS97 (Sheldrick, 2008) and SHELXL2014 (Sheldrick, 2015).

3.5.3 Gas Phase Studies (ESI-Mass Spectrometry)

The mass spectra for compounds **3.11a**, **3.12**, and **3.13** are highlighted in this section. The fragmentation patterns of these compounds were studied using collision induced dissociation (CID), which is a useful technique for gaining insight on the coordination environment of the receptor. We projected that the fragmentation pattern for the free molecular probe would be different from that of the complex.

CID of Free Probe **3.11a**

Depicted in figure 3.7a-b are the CID pattern and fragmentation pathway of sensor **3.11a**. It was necessary to spike the solution of **3.11a** with TFA because in its open form the sensor is more soluble in acetonitrile than it is in its closed form. The addition of TFA also served to amplify the signal of the positively charged species in positive mode. This observed decrease in solubility in organic solvents, going from **3.10** to **3.11a**, is a direct result of adding more polar groups to the sensor. The full mass spectra of compounds **3.10** and **3.11a** can be found in appendix A4. A MS/MS of the 533.3 m/z signal produces a 414.3 m/z, corresponding to a loss of 119 m/z. This 119 m/z charge difference was assigned to the alpha cleavage of 2-hydroxybenzonitrile from **3.11a**. This is a reasonable assignment however, high resolution mass spectrometry would offer further credence to this assignment.

Subsequent dissociation of the 414.3 m/z peak produces two unique daughter peaks. One of the daughter peaks corresponds to a difference of 73 m/z, while the other peak highlights the loss of 29 m/z. Alpha cleavage at one of the amines connected to the xanthene backbone accounts for the loss of 29 m/z and a fragment peak at 385.3 m/z,

while the loss of 73 m/z highlights alpha cleavage at the amine as well as the loss of the primary amide group, resulting in a 341.3 m/z signal. Fragmentation patterns of rhodamine dyes such as these have been cited by Ferreira et al. [139] Further fragmentation of the 341.3 m/z signal results in two daughter peaks with m/z 326.1 and 312.3, accounting for the loss of a methyl radical or an ethyl radical respectively from the remaining amine group. CID of the signal at 385.3 m/z follows the same fragmentation pattern as the 341.3 m/z peak. Attempts to perform CID on the 312.3 m/z signal produce signals too weak to confidently assign. From the fragmentation pattern, a reasonable fragmentation patters in highlighted in figure 3.7.

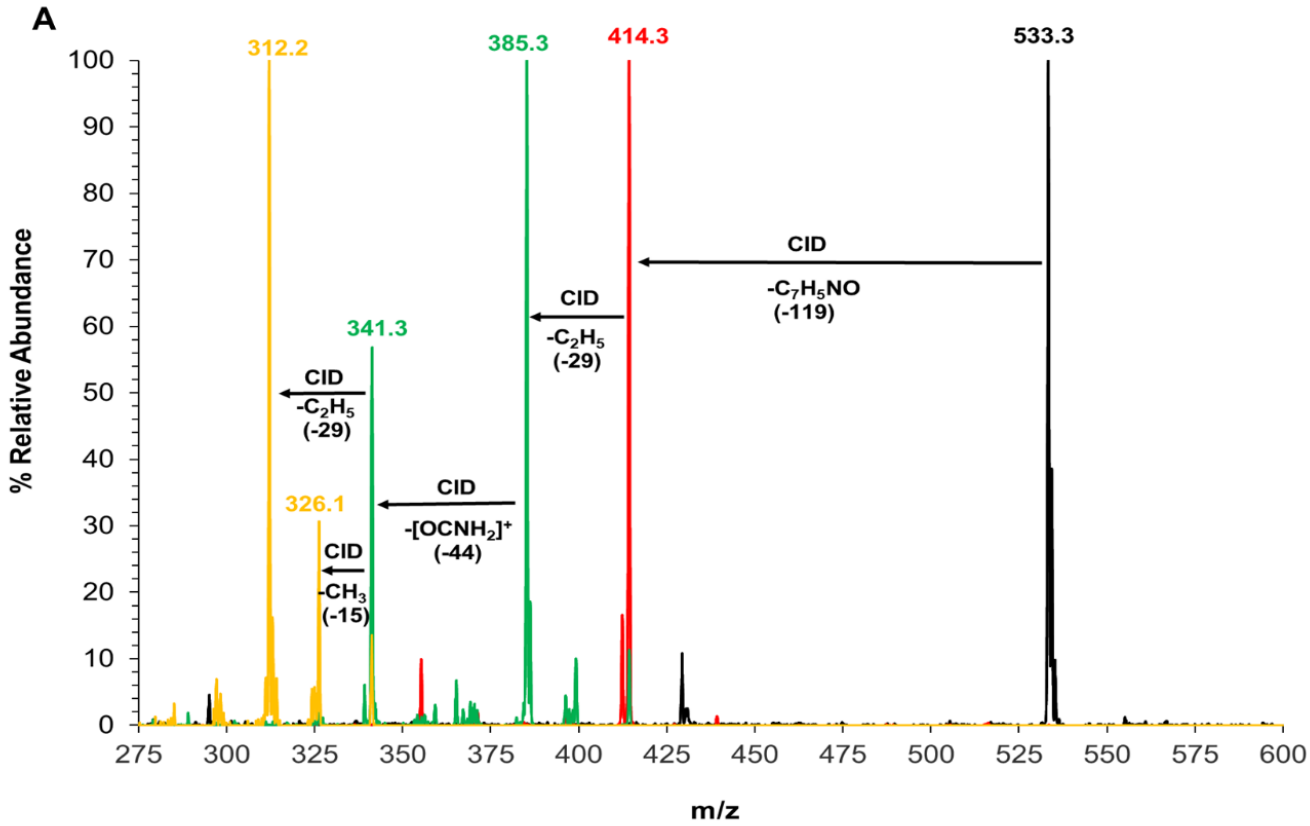
A
312.2
385.3
414.3
533.3
341.3
326.1
CID
-C7H5NO
(-119)
CID
-C2H5
(-29)
CID
-C2H5
(-29)
CID
-[OCNH2]+
(-44)
CID
-CH3
(-15)
% Relative Abundance
m/z
100
90
80
70
60
50
40
30
20
10
0
275
300
325
350
375
400
425
450
475
500
525
550
575
600

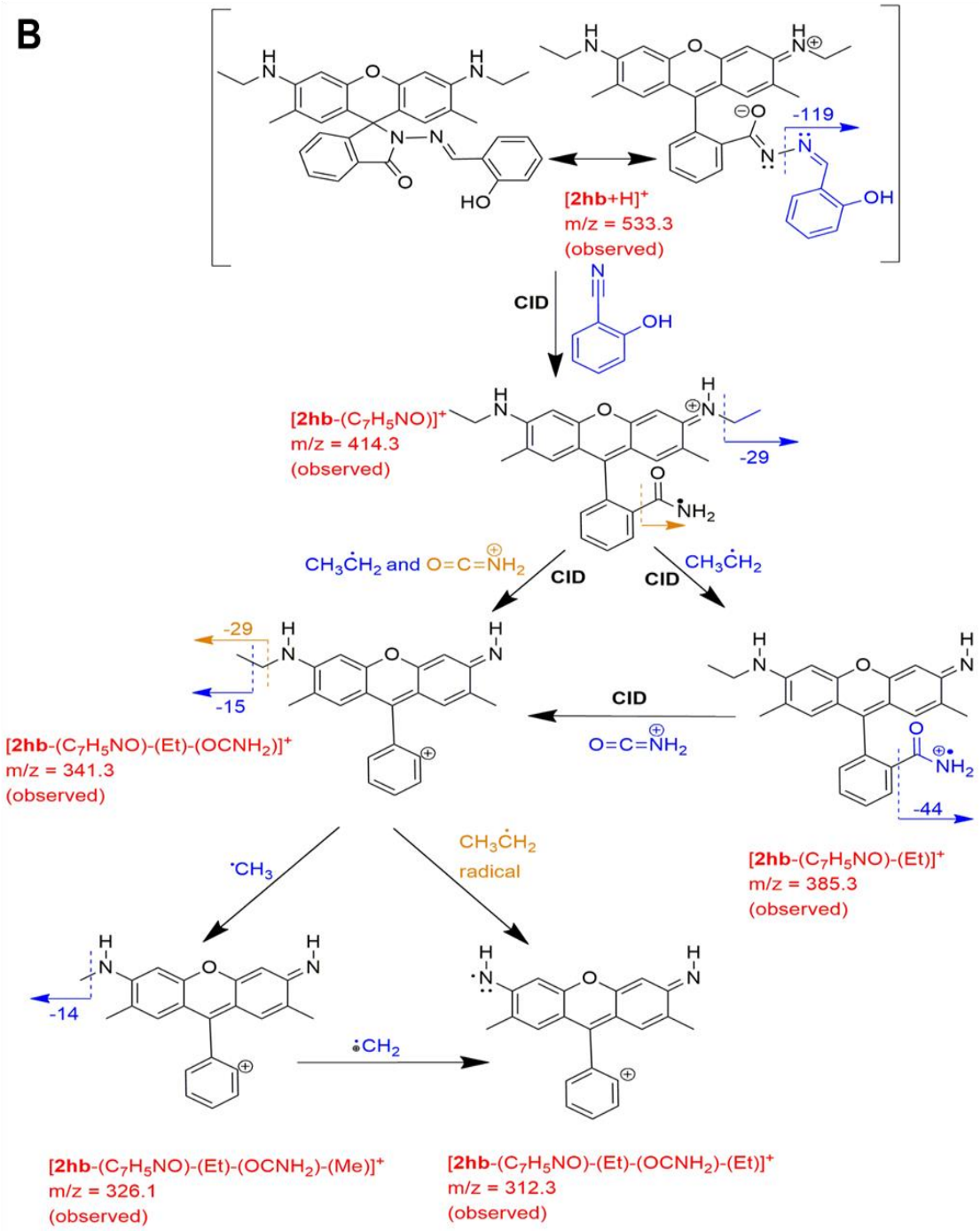

Figure 3.7 *(A) Normalized fragmentation pattern of **3.11a** in CH_3CN. (B) Fragmentation pathway of **3.11a** showing loss of fragments as well as resultant daughter peaks.*

Having gained an understanding of the fragmentation pattern of free molecular probe, we then wanted to determine if the fragmentation pattern of the metal complex would in fact differ from that of the "free" probe. The observation of a unique fragmentation pattern would offer further credence to the claim of the formation of coordination compounds between **3.11a** and metal ions in solution. Two different solutions were prepared and analyzed to determine how the ratio of the metal to the molecular probe would affect the resultant complexes that were formed.

Mass Spectrum of Probe **3.11a** with $Cu(NO_3)_2$ in a 1:2 Ratio

The addition of $Cu(NO_3)_2$ to a solution of molecular probe **3.11a** in acetonitrile resulted in the expected a pink solution, indicative of the ring opening mechanism. The sample was then allowed to equilibrate for two hours prior to being analyzed. When the sample was injected into the mass spectrometer, several signals were observed, at the following m/z values, 1252, 594, 531, and 503. These were assigned to the "free" molecular probe as well as the coordination compounds (figure 3.8a). High resolution mass spectrometry also highlighted the existence of the signal observed at 549.168612 m/z, accounting for $[Cu(\mathbf{3.11a})]^+$. Though some of these m/z values indicate the formation of a coordination compound; the signals alone do not provide information regarding the metal coordination environment.

Proposed species responsible for the m/z signals are shown in figure 3.8a. The signal at 1252m/z represents the positively charged, 2:1 $[Cu(\mathbf{3.11a})_2](NO_3)_2]^+$ species. This is contrary to the 1:1 $[Cu(\mathbf{3.11a})]^+$ complex observed at 594 m/z, which does not account for any counter ion species. The isotopic distributions for $[Cu(\mathbf{3.11a})]^+$ and

$[Cu(\mathbf{3.11a})_2](NO_3)_2]^+$ are shown in figures 3.9A-B. The experimental distributions, shown in black lines, are in good agreement with the theoretical isotopic distributions calculated for the complex (red lines).This distribution pattern appears to be unique to Cu^{2+} complexes as a similar pattern was observed for all of the Cu^{2+} coordination compounds discussed in this section.

Because the ESI-MS technique requires vaporization of the sample, it is possible that some species to dissociate prior to reaching the detector, as is likely the case for the 531 and 503 m/z signals.[140] The ring open form indicates that the sensor either was protonated by acidic species or was at one point coordinated to a metal ion. The signal observed at 531 m/z accounts for the loss of a proton, likely from the alcohol, whereas the signal at 503 m/z corresponds to alpha cleavage at one of the amines. This alpha cleavage is identical to the alpha cleavage observed in figure 3.7b. However, analysis of the fragmentation pattern of the probe-Cu^{2+} complex is notably different from that of the free probe.

CID of Probe **3.11a** with $Cu(NO_3)_2$ in a 1:2 Ratio

The CID analysis of the 1:2 solution of **3.11a** and $Cu(NO_3)_2$ is shown in figure 3.9. Fragmentation of the signal at 1252 m/z, results in the loss of two hydrogen atoms and a NO_3^- ion, forming a 1188 m/z daughter peak. Fragmentation of this daughter signal results in the loss of a proton from the alcohol and the generation of the positively charged 1:1 complex observed at 594 m/z. CID of the 1:1 complex produces signals too low to confidently assign. A MS/MS of the 531 m/z signal also resulted in signals too low to confidently assign. The species present in the 1:2 solution of **3.11a** with $Cu(NO_3)_2$

appear to follow a noticeably different fragmentation pattern from that of the free molecular probe. This is undoubtably a consequence of Cu^{2+} coordination. First, an ethyl group is cleaved from one of the amines next to the xanthene backbone, resulting in the signal observed at 503 m/z. This is in contrast to the free probe shown in figure 3.7, which first loses a 2-hydroxybenzonitrile group, resulting in a 414 m/z signal.

The result of CID on the 503 m/z signal was four daughter peaks with m/z signals at 488, 475, 459, and 445. These signals are highlighted in figure 3.9. The appearance of four daughter peaks is possibly due to an insufficient voltage being applied to the to the 503 m/z signal. This point is further validated due to the appearance of the strong 503 m/z signal in the CID spectrum. When conducting CID experiments, between 1-5% abundance of the fragmented species should be visible in the spectrum of the daughter peaks. However, in this case, the relative abundance of the 503 m/z signal was about 35%. Two possible species responsible for the daughter signals are observed at 488 and 475 m/z. These species account for the beta and alpha cleavage of a methyl group and an ethyl group, respectively, from the second amine next to the xanthene backbone. The structures of the remaining two daughter peaks, 459 and 445 m/z, are however not displayed, as there are several possible fragmentation pathways that may be responsible for the observed signals. Alpha cleavage of the methyl groups at positions 2 and 7 on the xanthene backbone could result in the observed m/z signals as well as cleavage of the amine groups. Cleavage of the amine groups is however the more likely fragmentation pathway as is suggested in work by Ferreira et al,.[139] This group displays the likelihood of this pathway and reproducibility of the results by conducting fragmentation studies on both rhodamine 6G and rhodamine B.

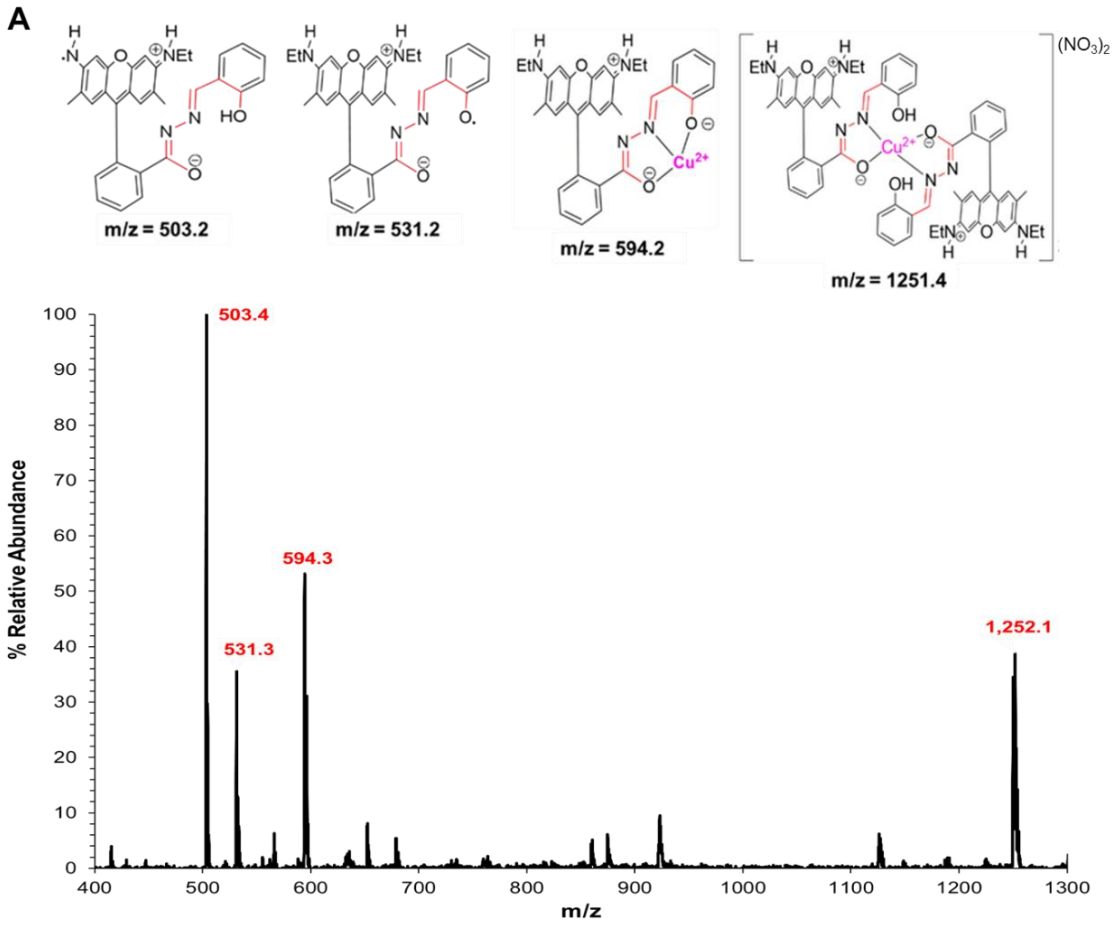
A
m/z = 503.2
m/z = 531.2
m/z = 594.2
m/z = 1251.4
(NO3)2
503.4
531.3
594.3
1,252.1
% Relative Abundance
m/z

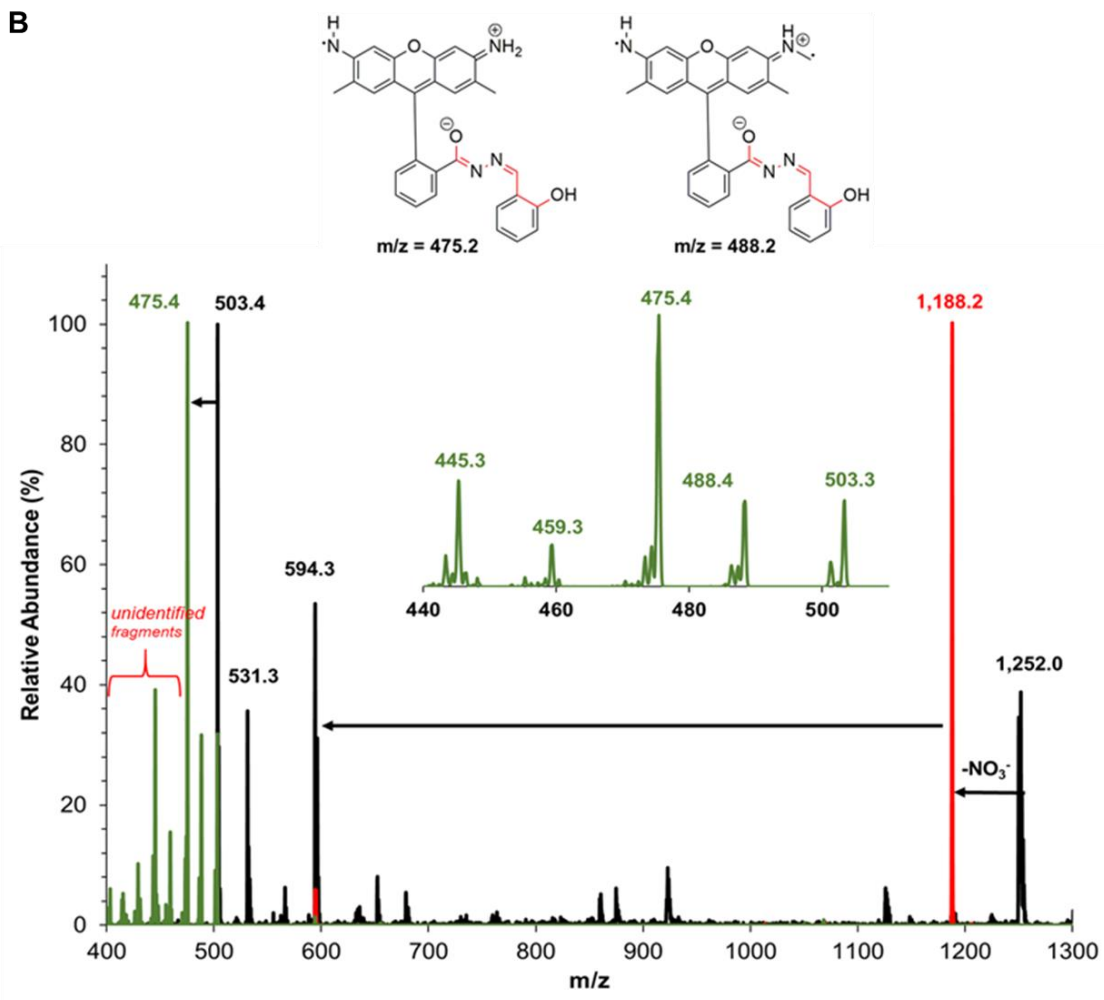

Figure 3.8 *(A) Full mass spectrum of* ***3.11a*** *with* $Cu(NO_3)_2$ *(1:2) in* CH_3CN *with proposed species shown for each m/z signal.(B) Fragmentation pattern of several of the major peaks highlighted in (A) along with two proposed daughter peaks resulting from the CID of 503 m/z.*

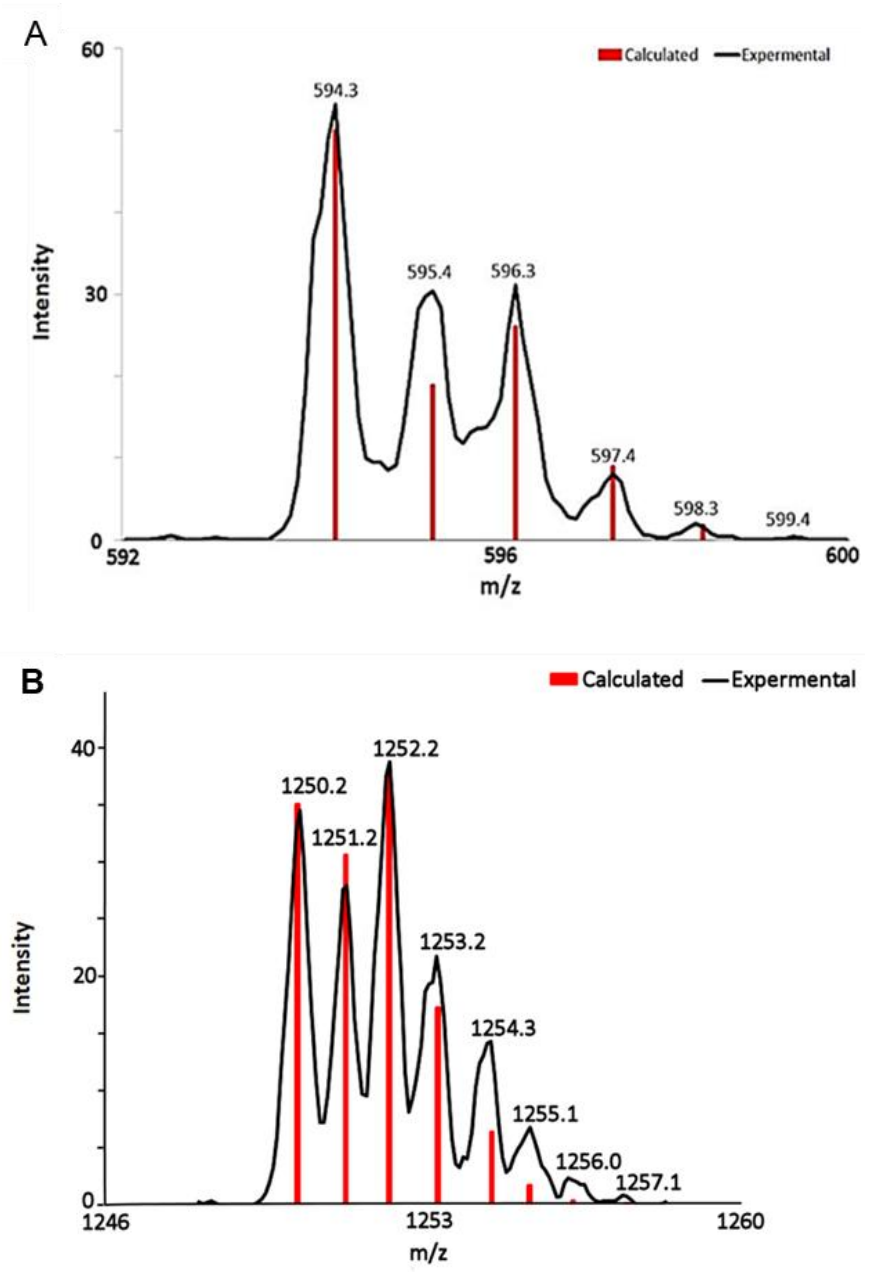

Figure 3.9 *(A) Isotopic distribution of [Cu(**3.11a**)]$^+$ in CH_3CN (B) Isotopic distribution of [Cu(**3.11a**)$_2$](NO$_3$)$_2$]$^+$ in CH_3CN*

Mass Spectrum of Probe **3.11a** with $Cu(NO_3)_2$ in a 1:1 Ratio

In contrast to the 1:2 solution of **3.11a** and $Cu(NO_3)_2$ solution, the 1:1 solution (figure 3.10) displays several signals not observed in the 1:2 solution. Furthermore, the

fragmentation pathway of several of the signals displayed in the 1:1 solution differ from those observed in the 1:2 solution. Present in both samples is the 1252 m/z signal, representative of $[Cu(\mathbf{3.11a})_2](NO_3)_2]^+$. The 1:1 solution also displays a signal at 1126 m/z, accounting for $[Cu(\mathbf{3.11a})_2] - H]^+$.

CID of Probe **3.11a** with $Cu(NO_3)_2$ in a 1:1 Ratio

A MS/MS of the 1126 m/z signal resulted in daughter peaks too weak to confidently assign. Upon CID of the 1:1 complex signal at 594 m/z the fragmentation pattern shown in figure 3.10b was observed. This fragmentation pattern is very different from that of the 1:2 solution and more closely resembles that of the free probe shown in figure 3.7a-b.

Fragmentation of the $[Cu(\mathbf{3.11a})]^+$ complex results in four daughter peaks at m/z = 531, 412, 369, and 355. The proposed species responsible for these daughter peaks are shown in figure 3.10b. The weak signal observed at m/z = 531 corresponds to the loss of the Cu^{2+} ion from the coordination environment of the receptor. This is the only daughter peak that does not account for the loss of functional groups from **3.11a**. All the other daughter peaks account for alpha cleavage of the 2-hydroxybenzonitrile groups and subsequent loss of additional functional groups. The fragmentation pattern for the remaining daughter peaks proceeds via initial loss of loss of the Cu^{2+} ion and alpha cleavage of the 2-hydroxybenzonitrile group, which accounts for the m/z signal centered at 412. The two other resultant species indicate the loss of the Cu^{2+} ion, alpha cleavage of 2-hydroxybenzonitrile, and additional cleavage of an ethyl group and a methyl group (369 m/z) or alpha cleavage of two ethyl groups (355 m/z). This further emphasizes that

the species in the 1:1 solution follows a fragmentation pathway similar to the one observed in figure 3.7.

By comparing the spectra and fragmentation patterns of the 1:2 and 1:1 solutions of **3.11a** with $Cu(NO_3)_2$, it appears that the 1:2 solution results in a higher concentration of complex formation i.e., shifts the equilibrium to the product side. This is likely due to the fact that a low concentration of 1:2 complexes form between compound **3.11a** and Cu^{2+} ions. The occurrence of these 1:2 receptor-metal complexes will be further emphasized in the optical studies section of this chapter. In the event of the formation of $[(Cu)_2(\mathbf{3.11a})]^{3+}$ in solution, this would mean that in the 1:1 solution, the concentration of Cu^{2+} ions is not high enough to form complexes with all of the sensor molecules that are present. As a result, much of the "free" probe remains in solution. Evidence of this is seen in the fragmentation pattern of the 1:1 solution which mirrors the fragmentation pattern of the "free" probe shown in figure 3.7, while the 1:2 solution demonstrates a unique fragmentation pattern.

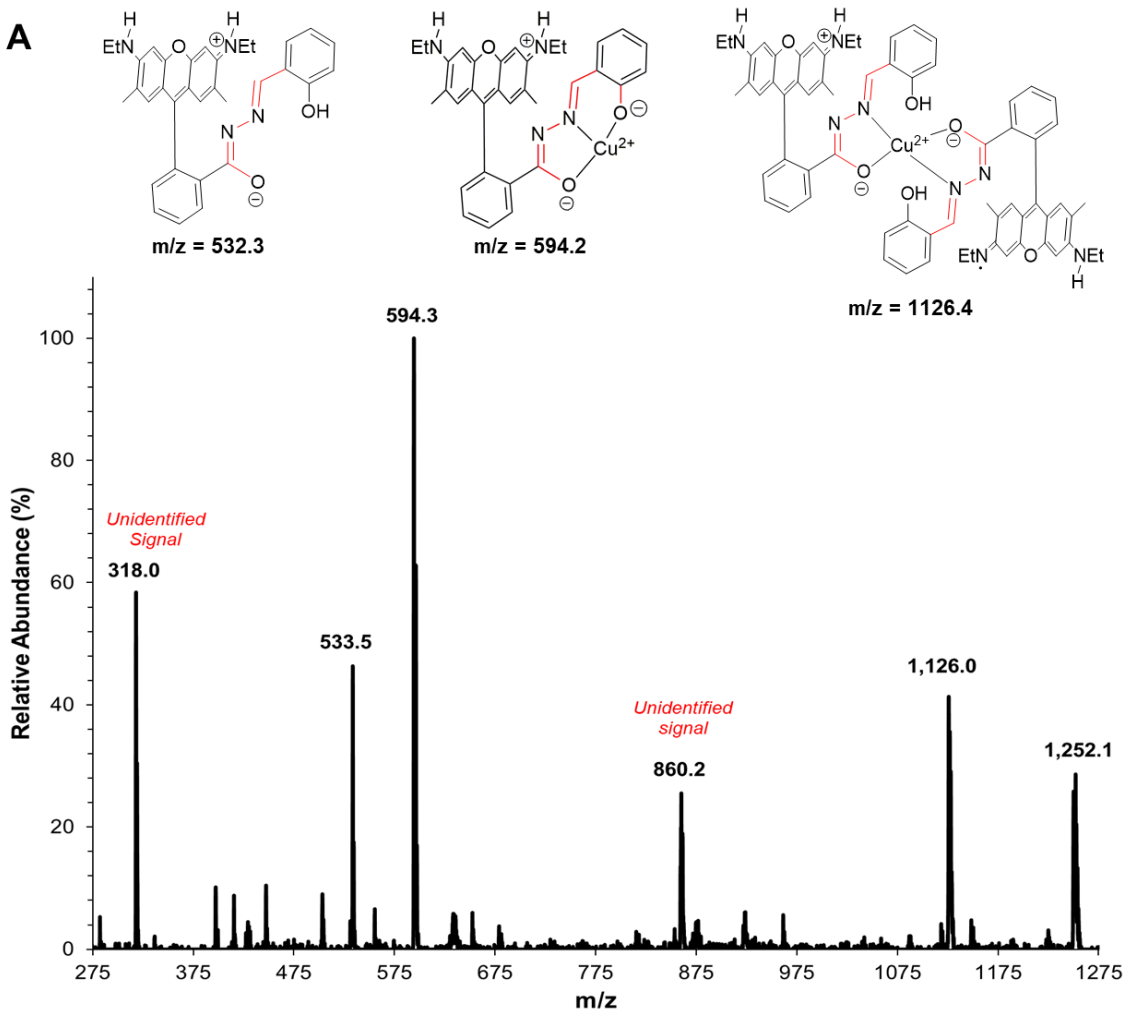
A
m/z = 532.3
m/z = 594.2
m/z = 1126.4
Relative Abundance (%)
m/z
Unidentified Signal
318.0
533.5
594.3
Unidentified signal
860.2
1,126.0
1,252.1

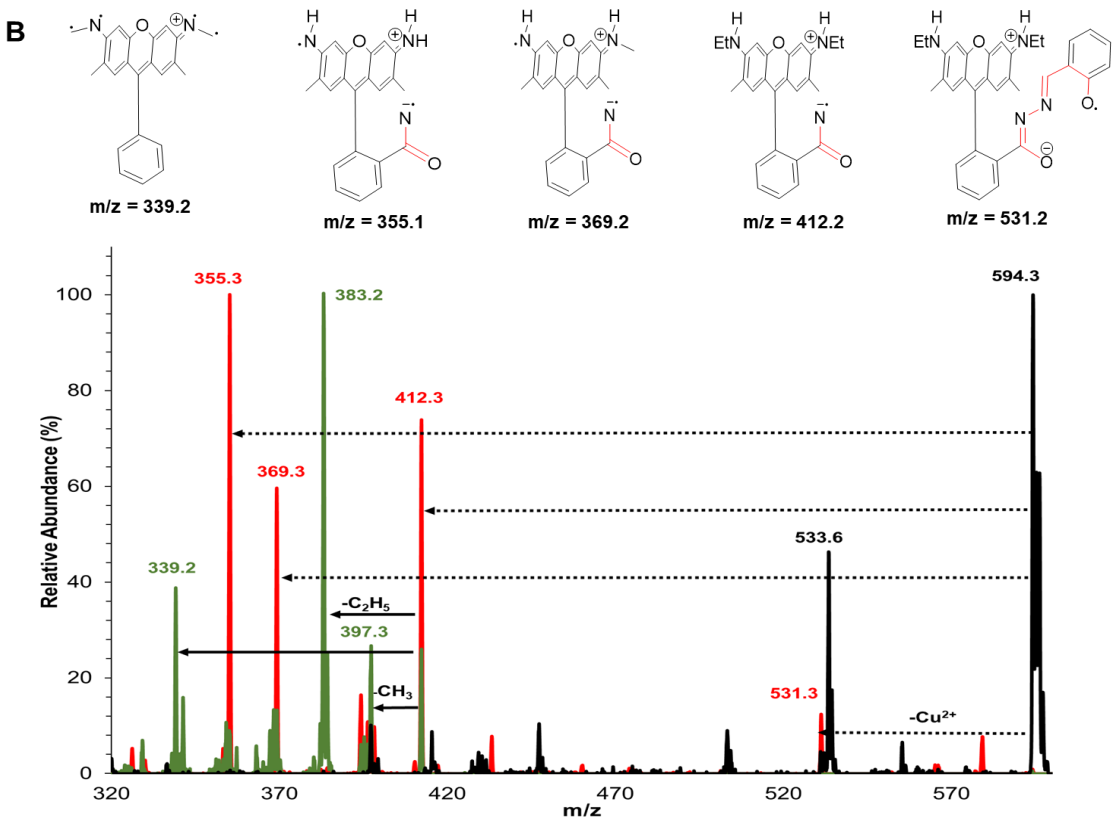

Figure 3.10 *(A) Full mass spectrum of **3.11a** with $Cu(NO_3)_2$ (1:1) in CH_3CN with proposed species shown for some m/z signals. (B) Fragmentation pattern of several of the major peaks highlighted in diagram A, along with proposed daughter peaks resulting from the CID of 594.3 m/z.*

ESI-MS Analysis of Probe **3.13** in CH_3CN

The mass spectrum of compound **3.13** is highlighted in figure 3.11a. The free probe has an exact mass of 517 amu, while the m/z signal in the spectrum accounts for [**3.13** + H]$^+$. Two dimer signals at 1035 m/z and 1057 m/z, account for [(**3.13**)$_2$ + H]$^+$ and [(**3.13**)$_2$ + Na]$^+$, respectively. The fragmentation pattern of this sensor is identical to that of the sensor **3.11a** and is shown in figure 3.11b. Upon the addition of a solution of $Cu(NO_3)_2$ to **3.13**, there is a notable color change from colorless to dark pink. Two solutions of the sensor with $Cu(NO_3)_2$ were prepared, in 1:1 and 1:2 ratios, however,

similar to sensor **3.11a**, the 1:2 solution proved to be more efficient at forming well defined complexes in solution. The 1:2 solution of **3.13** with $Cu(NO_3)_2$ displays the formation of a

$[Cu(\mathbf{3.13})NO_3]^+$ complex (figure 3.11c). The isotopic distributions for this complex is shown in figure 3.11 and displays distributions similar to those observed for $[Cu(\mathbf{3.11a})]^+$ and $[Cu(\mathbf{3.11a})_2](NO_3)_2]^+$ which were highlighted previously in this section. The experimental distributions, shown in black lines, are in good agreement with the theoretical isotopic distributions calculated for the complex (red lines). No other major complexes were observed, such as the 1:2 complex of the sensor with cupric ions. It is however possible that this is due to the extremely low concentrations of these complexes in solution. These will be further discussed in the optical studies section.

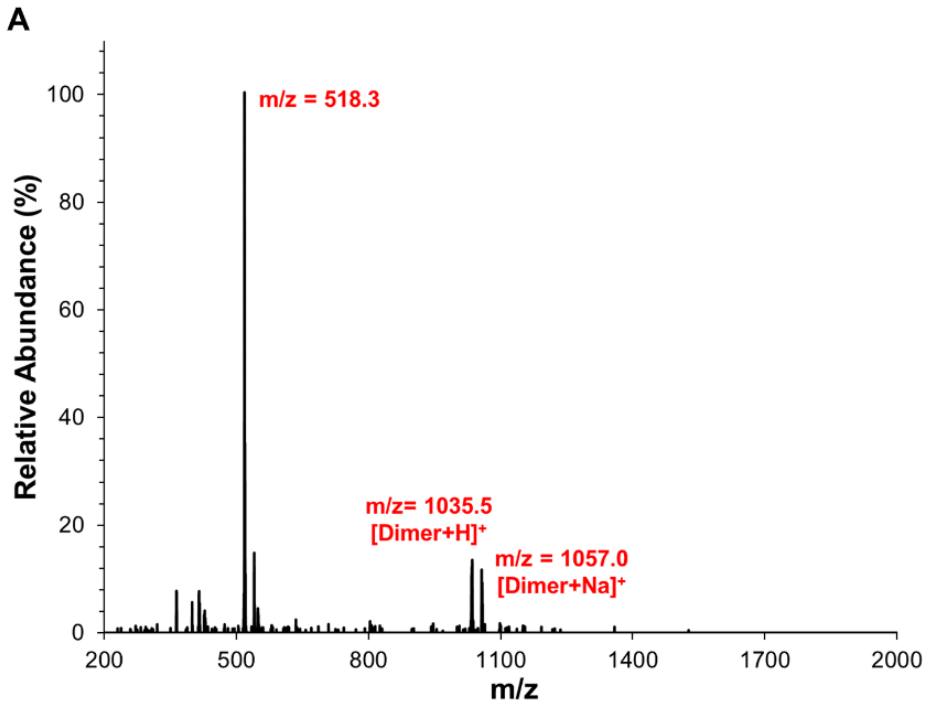

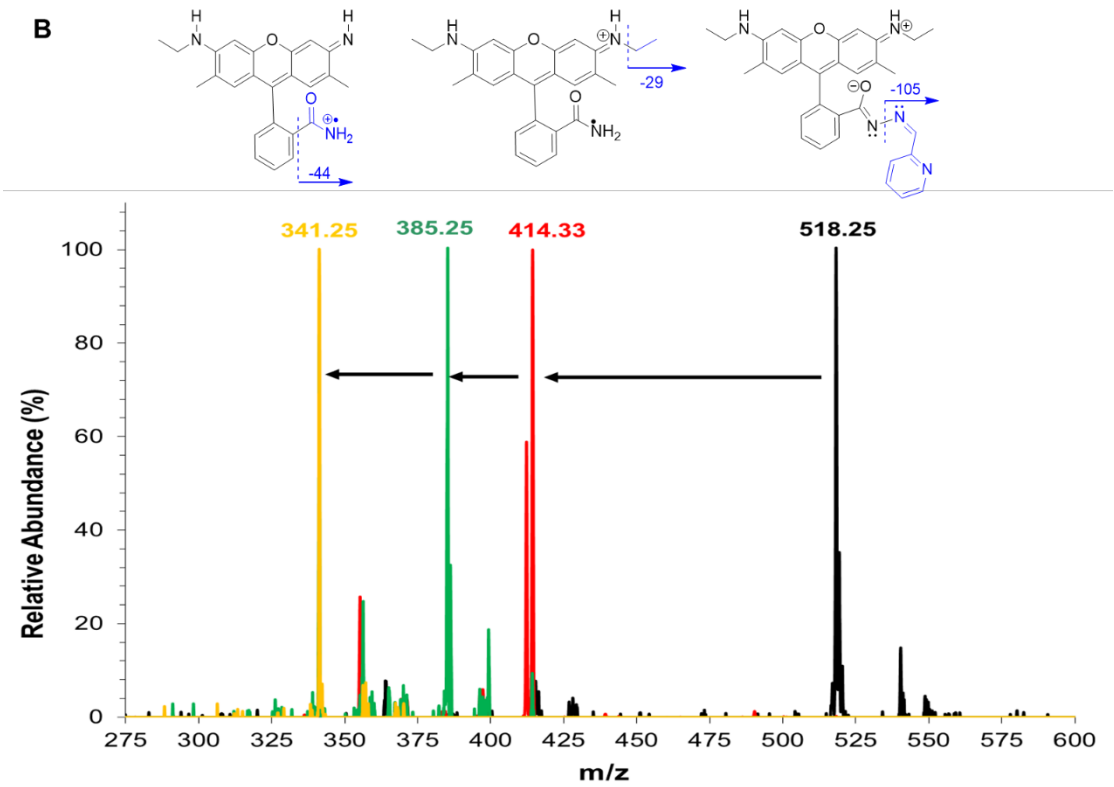
B
-44
-29
-105
341.25
385.25
414.33
518.25
Relative Abundance (%)
m/z

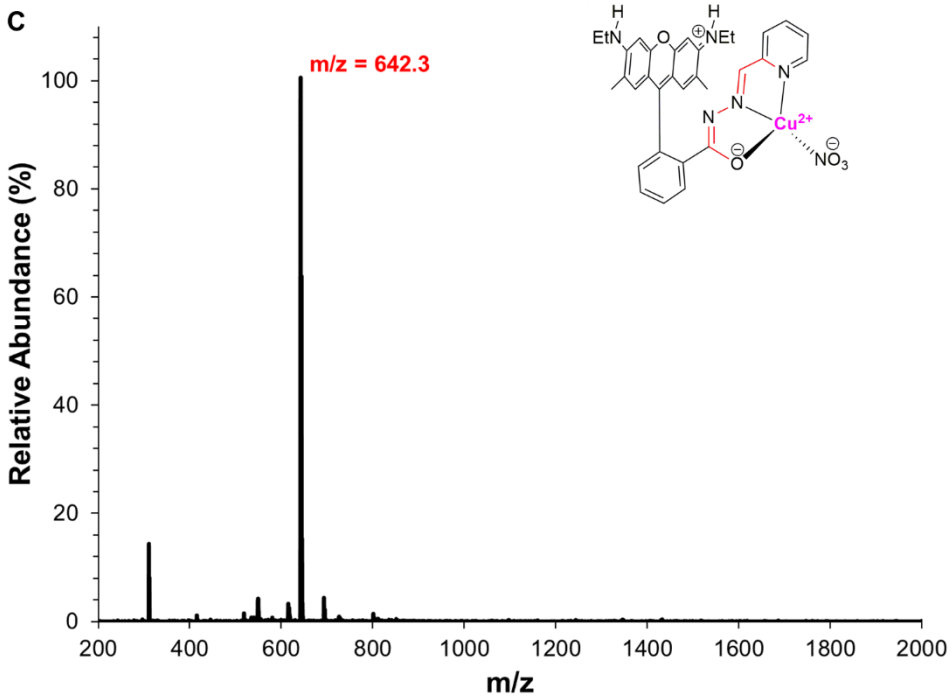
C
m/z = 642.3
Relative Abundance (%)
m/z

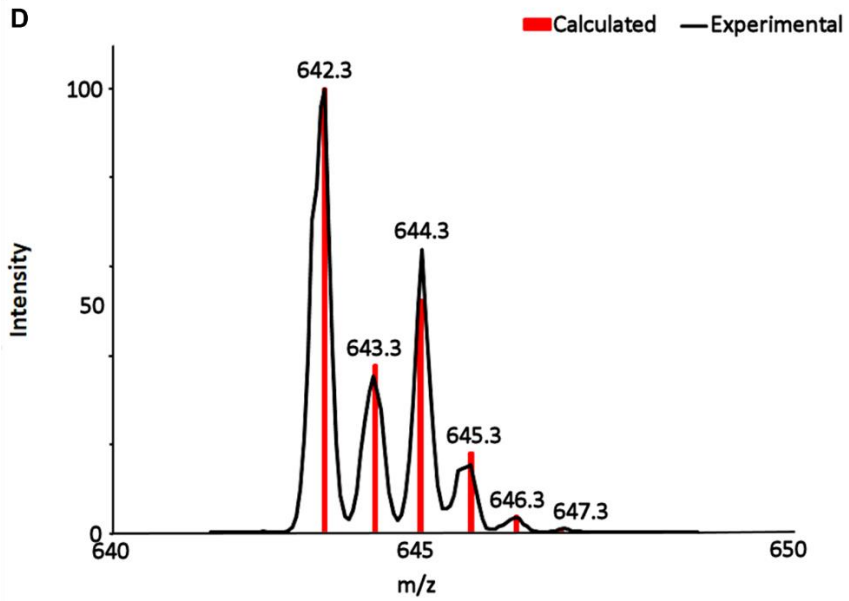

Figure 3.11 *(A) Mass spectrum of free probe **3.13**. (B) Fragmentation pattern of free probe **3.13** along with proposed species corresponding to each signal. (C) Mass spectrum of [Cu(**3.13**)NO_3)]$^+$ in CH_3CN. (D) Isotopic distribution of [Cu(**3.13**)NO_3)]$^+$ in CH_3CN.*

Summary

The Mass spectrum data of molecular probes **3.11a** and **3.13** with $Cu(NO_3)_2$ clearly shows the formation of metal-ligand complexes in the gas phase. By conducting an in-depth CID analysis of probe **3.11a**, we were able to validate our hypothesis statement that the fragmentation pattern of the coordination compound should be different than that of the "free" probe. We also observed the effects that altering metal-ligand ratios had on complex formation, from which we deduced that excess Cu^{2+} salt was needed for the reaction to favor the formation of [Cu(**3.11a**)] coordination compounds in solution. These studies, however, do not aid in definitively identifying which of the atoms in the coordination environment serve as donor ligands to the metal ion. NMR correlation spectroscopy is often used as an analytical technique for determining which chemical environments are affected by the coordination of a metal

ion, however, this method of analysis is typically limited to metal ions that are diamagnetic. Paramagnetic metals ions like Fe^{3+} and Cu^{2+} result in line broadening and poor spectral resolution. That said, FT-IR spectroscopy, which will be discussed in section 3.5.4, is a useful tool to aid in the structural elucidation of coordination compounds.

3.5.4 IR Study of Probe 3.11a with $Fe(CF_3SO_3)_3$

Based on our knowledge of rhodamine dyes, it is reasonable to assume that the carbonyl group, along with the alcohol and a nitrogen atom act as donor ligands to the metal ion. The coordination of the metal ion by the carbonyl group will be a useful handle to study in IR spectroscopy as a distinctive wavelength or intensity change will be observed between the free probe and the coordination compound. For compound **3.11a**, a change in either the intensity or shift in the stretching band of the carbonyl group of the γ-lactam group would indicate the involvement of this group in the coordination of the Fe^{3+} ion. Upon coordination to the Fe^{3+} ion, the ring opening mechanism alters the double bond character of the carbonyl group, resulting in a negatively charged oxygen (see section 3.1.1). Furthermore, the ring opening mechanism results in the generation of the azine functional group which is not observed in the spirolactam form of the receptor; instead, the hydrazine functional group is present in the spirolactam form.

The infrared spectrum of the free receptor **3.11a** was recorded as a solid using FT-IR, and displayed a characteristic IR stretch for the carbonyl of the γ-lactam at 1677 cm^{-1} (figure 3.12). The metal complex was prepared by grinding a 1:1 mix of sensor **3.11a** and $Fe(CF_3SO_3)_3$ with a mortar and pestle. Upon mixing, an extremely dark magenta solid

was observed. The IR analysis of the complex displayed almost a complete reduction in the carbonyl stretch 1677 cm^{-1} as well as the emergence of what appears to be an azine stretch at 1605 cm^{-1}. This assignment for the azine group is supported by the Spectral Database for Organic Compounds. Also observed in the spectrum are characteristic peaks of the triflate ion. Broad sulfonate stretches can be observed between 1250-1150cm^{-1}, while a sharp C-F stretch is present at 1025cm^{-1}. As was observed in the mass spectrum data, the metal salt can retain some of its counterions during complex formation, therefore the presence of these counterion peaks in the IR spectrum of the complex are to be expected.

$Fe(CF_3SO_3)_3$ 3.11a Complex

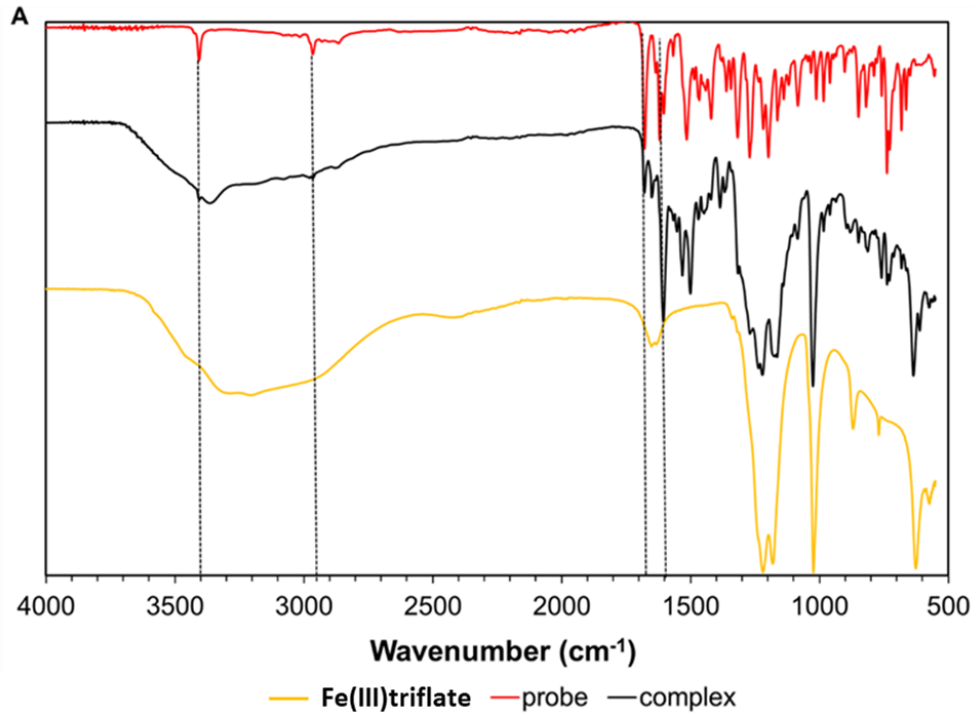

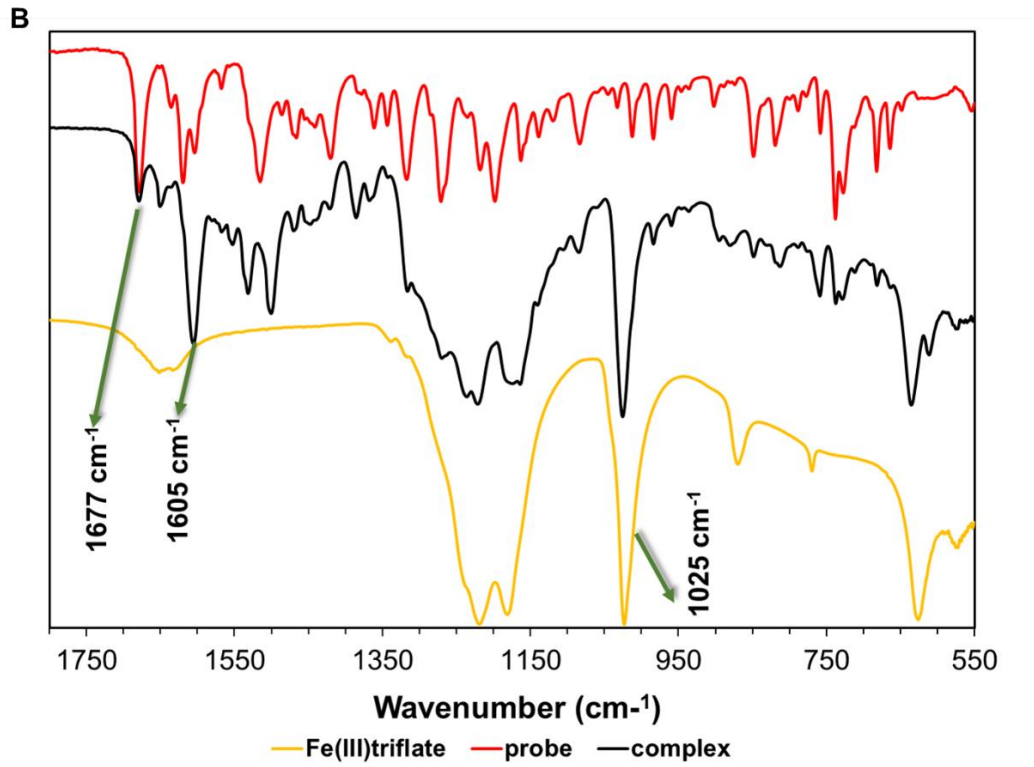

Figure 3.12 *(A) FT-IR spectra used to determine modes coordination between compound* ***3.11a*** *and* $Fe(CF_3SO_3)_3$*. (B) Expansion of diagram A*

3.5.5 Optical Spectroscopy – An Organic Solvent Study

In order to understand the metal binding behavior of our LMFPs in water, it is important to grasp the effects of organic solvents (protic and aprotic) first, as they are less complicated. This section highlights the interactions between sensors **3.10** and **3.11a** with Fe^{3+} ions in organic solvents. The organic solvent studies serve to highlight the interactions between the sensors and metal ions without the need to factor in the competitive nature of water and hydrolysis reactions that can interfere with complex formation and alter metal speciation. Once there is an understanding of the coordination environment in purely organic solvents, buffer systems can then be investigated. The

introduction of water will significantly complicate the binding environment, equilibria, and the spectroscopic response selectivity of the sensors.

The earliest report of a rhodamine dyes used as fluorescent sensor for a metal ion was reported by Czarnik et al., in 1997.[126] They utilized the rhodamine B hydrazide molecule to serve as a Cu^{2+} ion colorimetric and fluorescent sensor in a 8:2 mixture of 0.1M HEPES buffer and CH_3CN (scheme 3.2). Since this study was published, there have been many papers published on the use of rhodamine dyes in various systems for metal ion detection. Many of these reports claim that these LMFPs can sense metal species under certain conditions, however, these claims are however often misleading. This work brings into question the validity of some of the reports of Fe^{3+} ion detection with the use of rhodamine dyes in aqueous systems that we plan to address.

pH Studies of Compound **3.9**

When determining what applications an optical sensor can be used for, it is imperative to first observe the behavior of the sensors over a broad pH range to determine the optimal conditions over which metal analysis can occur. This is imperative if the probes are to be used in aqueous environments. The effect of acidic environments on the spirolactam rhodamine molecules was previously discussed in section 3.1.2. In the case of rhodamine-6G derivatives, this ring opening mechanism results in a color change from clear to pink and the emergence of an absorbance band near 530nm. This same mechanism, however, also occurs as a result of metal-ligand interactions between sensors and analytes. It is therefore important to be able to determine if the spectral changes observed in rhodamine-based sensors are the result of genuine metal coordination events

or simply due to protonation in aqueous media, as the aqueous chemistry is often overlooked.

As all of the compounds have the same spirolactam core as a part of the organic framework, only compound **3.9** will be discussed here. The pH study was performed in a 1:1 solution of DMSO and deionized water, as the sensor is not 100% water soluble. Hydrochloric acid (1.0 M) and sodium hydroxide (1.0 M) were used to adjust the pH as needed. The results of this pH study, shown in figure 3.13, indicate optimal pH ranges for sensor applications between pH 4-12, with the ability to work as low as pH 3 if necessary. This means that spectral and color changes that occur in this solvent system can be more confidently identified as the result of genuine metal-ligand interactions when hydrolysis reactions are not of concern. It is important to note however, that because these studies were conducted in a mixture of water and DMSO, these are not true pH values, as adding organic solvents shifts the pH window.

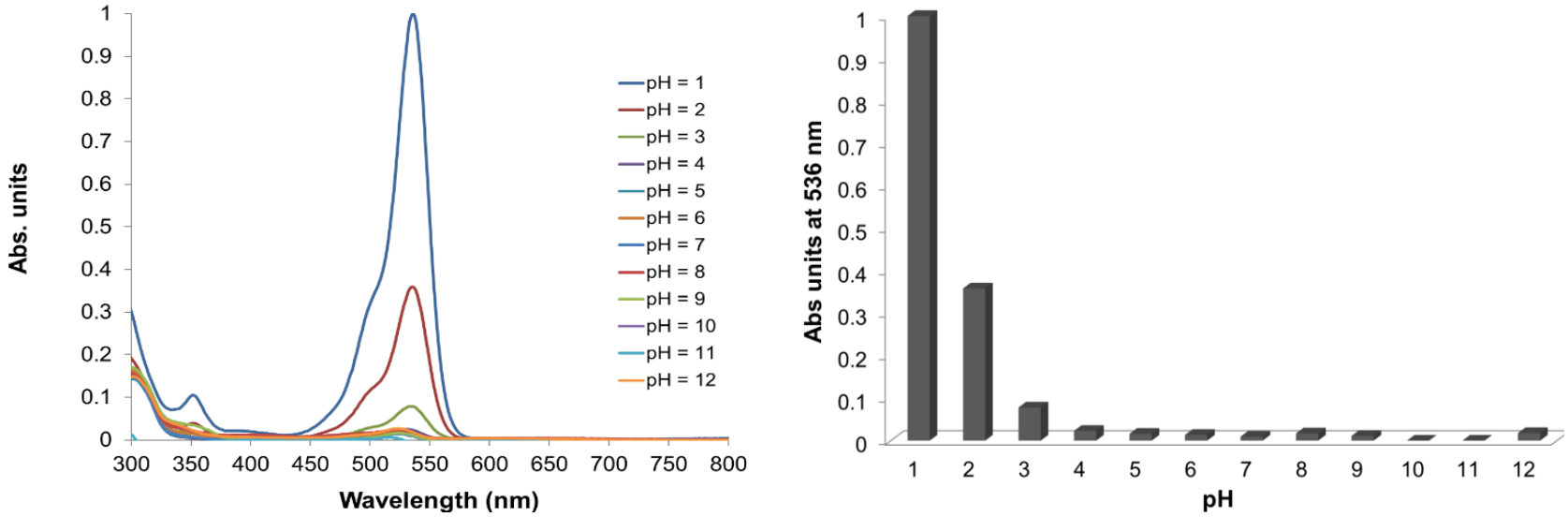

Figure 3.13 *pH study of compound* ***3.9*** *in 1:1 solution of DMSO and deionized water.*

Solvent Effects on Metal Coordination with Compound **3.10**

To obtain and understanding of the effect of solvent molecules on metal ion coordination and detection, a series of screening studies were performed. The metal ions that resulted in a spectroscopic response were then further analyzed. Metal screens were performed with control sensor **3.10** (25μM) in CH_3CN, DMSO, THF, and MeOH with two equivalents of the following metal ions; Ag^+, Na^+, K^+, Li^+, Ca^{2+}, Co^{2+}, Cu^{2+}, Fe^{2+}, Hg^{2+}, Mg^{2+}, Ni^{2+}, Pb^{2+}, Zn^{2+}, Al^{3+}, Cr^{3+}, and Fe^{3+}. The CH_3CN and THF were obtained from a solvent drying system to ensure that they contained little to no water. The MeOH was distilled and placed over size 4A molecular sieves overnight and the DMSO was placed over size 4A molecular sieves overnight as well to remove as much water as possible. The metal screen shows that coordinating solvents that contain oxygen donor atoms can inhibit the binding of metal ions. Due to the high concentration of this hard Lewis base in the bulk solvent, the solvent is able to saturate the metal center, thus prohibiting compound **3.10** from being able to coordinate to the metal ion. The only solvent that resulted in noticeable spectroscopic changes was CH_3CN. The addition of Fe^{3+} ions resulted in the largest spectral shift in the solution of sensor **3.10** in CH_3CN, no other metals resulted in comparable spectroscopic changes in the absorbance spectrum of compound **3.10**.

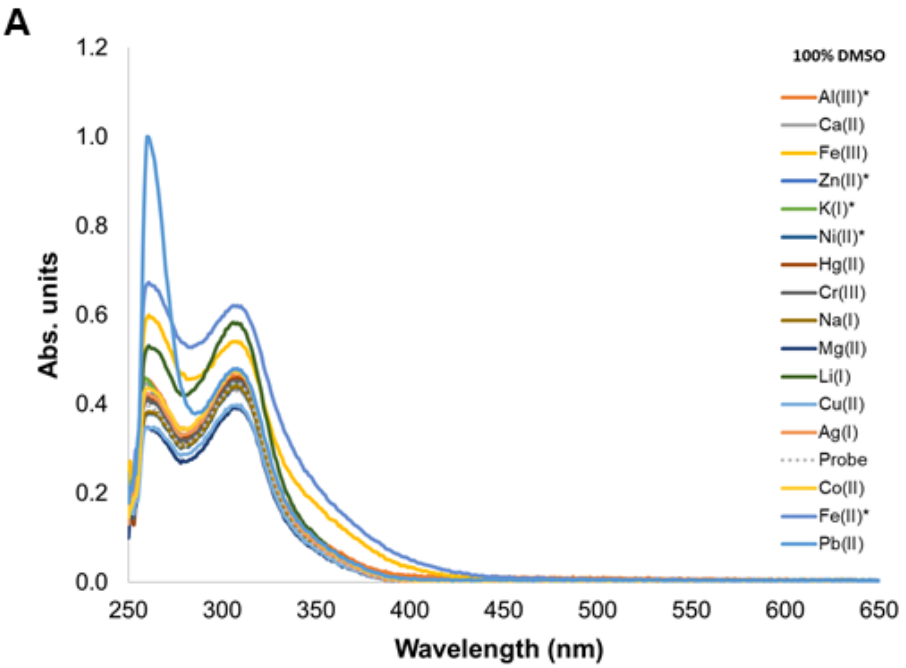
A
100% DMSO
Al(III)*
Ca(II)
Fe(III)
Zn(II)*
K(I)*
Ni(II)*
Hg(II)
Cr(III)
Na(I)
Mg(II)
Li(I)
Cu(II)
Ag(I)
Probe
Co(II)
Fe(II)*
Pb(II)
Abs. units
Wavelength (nm)

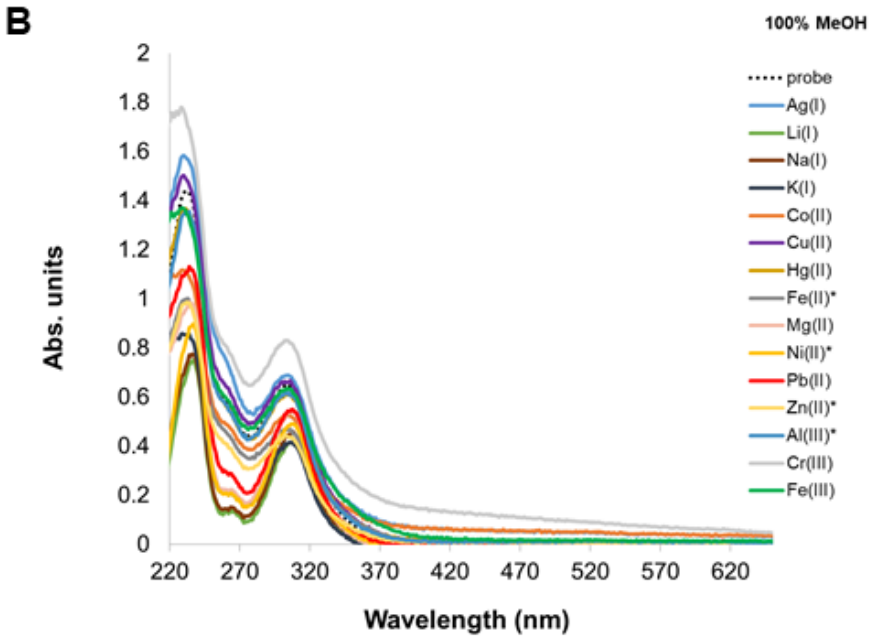
B
100% MeOH
probe
Ag(I)
Li(I)
Na(I)
K(I)
Co(II)
Cu(II)
Hg(II)
Fe(II)*
Mg(II)
Ni(II)*
Pb(II)
Zn(II)*
Al(III)*
Cr(III)
Fe(III)
Abs. units
Wavelength (nm)

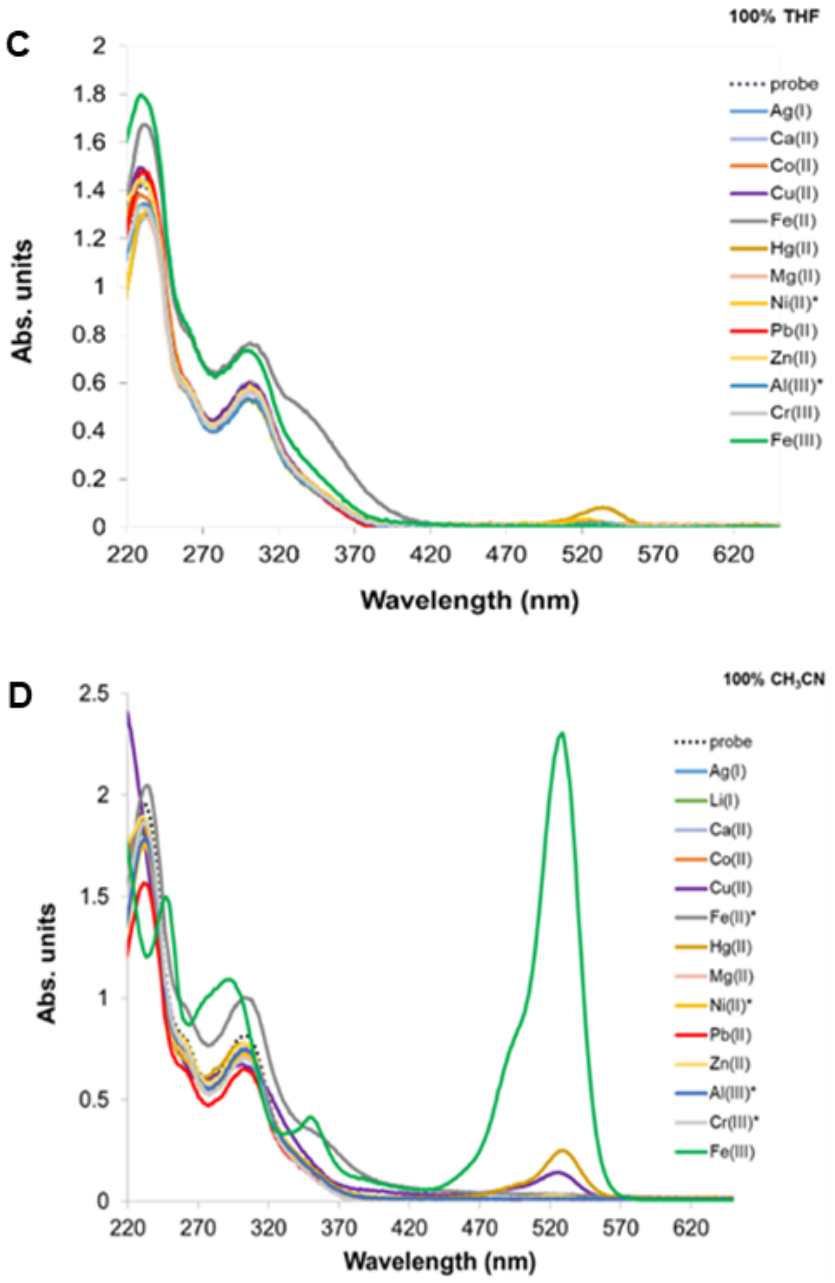
C
100% THF
Abs. units
Wavelength (nm)
probe
Ag(I)
Ca(II)
Co(II)
Cu(II)
Fe(II)
Hg(II)
Mg(II)
Ni(II)*
Pb(II)
Zn(II)
Al(III)*
Cr(III)
Fe(III)
D
100% CH3CN
Abs. units
Wavelength (nm)
probe
Ag(I)
Li(I)
Ca(II)
Co(II)
Cu(II)
Fe(II)*
Hg(II)
Mg(II)
Ni(II)*
Pb(II)
Zn(II)
Al(III)*
Cr(III)*
Fe(III)

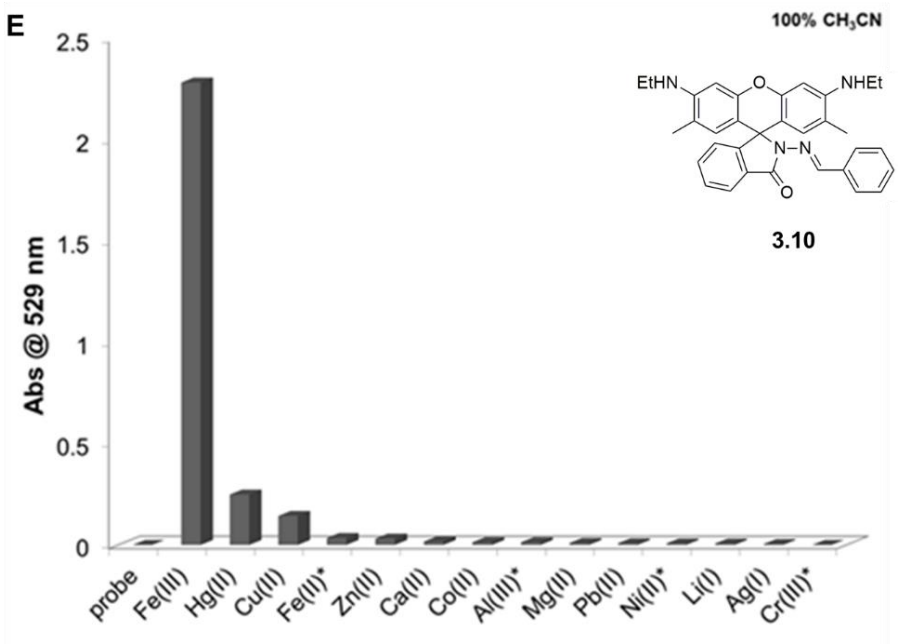

Figure 3.14 *Absorbance spectra of 25 μM solutions of compound **3.10** with two equivalents various metal ions in (A) DMSO, (B) MeOH, (C) THF, (D) CH_3CN. (E) Bar chart representation of the results of diagram D, whereby λ_{max} at 529 nm is plotted for each metal. Ions with asterisk in diagrams are chlorides, all others are nitrates.*

Job's Plot Analysis of Compound **3.10** with Fe^{3+} in CH_3CN

The stoichiometry between compound **3.10** and Fe^{3+} ions was confirmed by Job's plot analysis using absorbance data. A solution of compound **3.10** (5×10^{-5}M) was prepared in CH_3CN and the metal fraction was varied between 0 and 1 equivalent. Complexation between sensor **3.10** and two different Fe^{3+} salts were studied, $Fe(NO_3)_3$ and $Fe(CF_3SO_3)_3$ (figure 3.15).. This was done to determine if the counterion affected the stoichiometry of the complex formed. The effects of counterions on complex formation will be discussed later in this section. To ensure that equilibrium was reached, each of the solutions used for the analysis were run every hour for five hours to confirm that no drastic spectral changes had occurred. In the $Fe(NO_3)_3$ sample, detector saturation was observed at 528nm. As a result, the absorbance band at 346nm was instead used to

determine complex stoichiometry within the system. We postulate that the band at 346nm is evidence of the formation of a new species in solution, specifically, the **3.10**-Fe^{3+} complex, while the 528nm band simply signals that the ring opening mechanism has occurred. The Job's plot analysis of sensor **3.10** with $Fe(NO_3)_3$ and $Fe(CF_3SO_3)_3$ are shown in figure 3.15a-b. The minima of the curves lie at 0.54 and 0.50, respectively, corresponding to 1:1 (ligand: metal) stoichiometry under these conditions.

Care should be taken when interpreting Job's plot data as this type of analysis does not always reflect the true stoichiometry of the system under study. Computer programs and different software packages that can carry out non-linear regression calculations are now available. All other stoichiometric ratios highlighted in this work were calculated using non-linear regression analysis which was analyzed with Bindfit and Hypspec computer software.

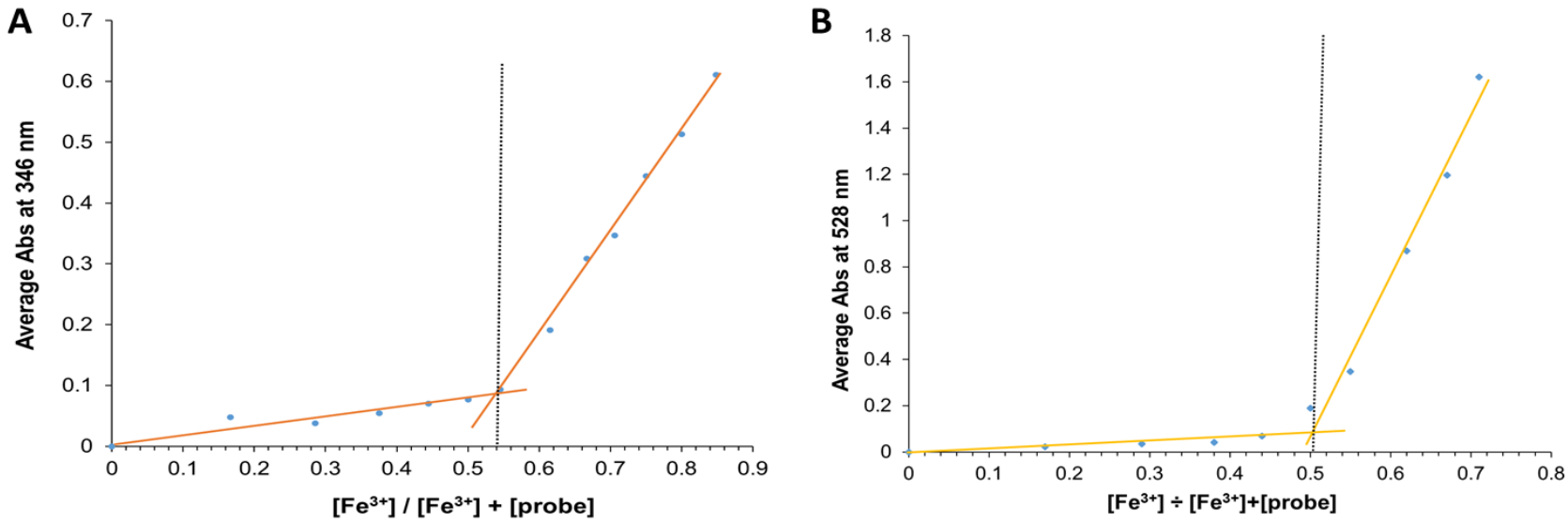

Figure 3.15 *Job's plot data for compound* ***3.10*** *with (A)* $Fe(NO_3)_3$ *and (B)* $Fe(CF_3SO_3)_3$ *in* CH_3CN

Absorbance Titration of Compound **3.10** with Fe^{3+} ions

Despite the similar binding ratios highlighted in the Job's plot analysis, inspection of the binding isotherms of the two Fe^{3+} salts with compound **3.10** yield strikingly different results. Upon initial inspection, the titration data for the two salts look identical, however, the binding isotherms are indicative of two possible ligand substitution pathways occurring. Furthermore, the sigmoidal nature of the binding curves suggests cooperative binding between the ligand and the Fe^{3+} ions.

The reaction **of 3.10** with $Fe(NO_3)_3$ appears to proceed via an associative ligand substitution in which the ligand groups on the sensor can approach iron complex before departure of the leaving group (NO_3^- ion). This pathway is especially likely because $Fe(NO_3)_3$ does not follow the 18 electron rule, and instead has fewer than 18 total electrons at the metal center. Conversely, the reaction of **3.10** with $Fe(CF_3SO_3)_3$ likely follows a dissociative ligand substitution pathway which would account for the initial lag time prior to an increase in the absorbance signal at 528nm (figure 3.17), as the loss of the triflate ion from the metal center is the rate determining step. Like $Fe(NO_3)_3$, $Fe(CF_3SO_3)$ also does not fulfill the 18 electron rule, however, the triflate ion is bulkier than the nitrate ion which makes it more difficult for an incoming ligand to approach the metal center prior to the loss of the triflate ion. As was observed in the mass spectrometry section (section 3.6.3), the complexes formed between sensors and metal ions typically maintain some of the initial counterions to balance the overall charge on the complex. This fact explains why the jobs plot mainly highlights 1:1 stoichiometry despite the bidentate coordination environment on sensor **3.10** which theoretically could allow for 2:1 and 3:1 complex formation between compound **3.10** and Fe^{3+} ions.

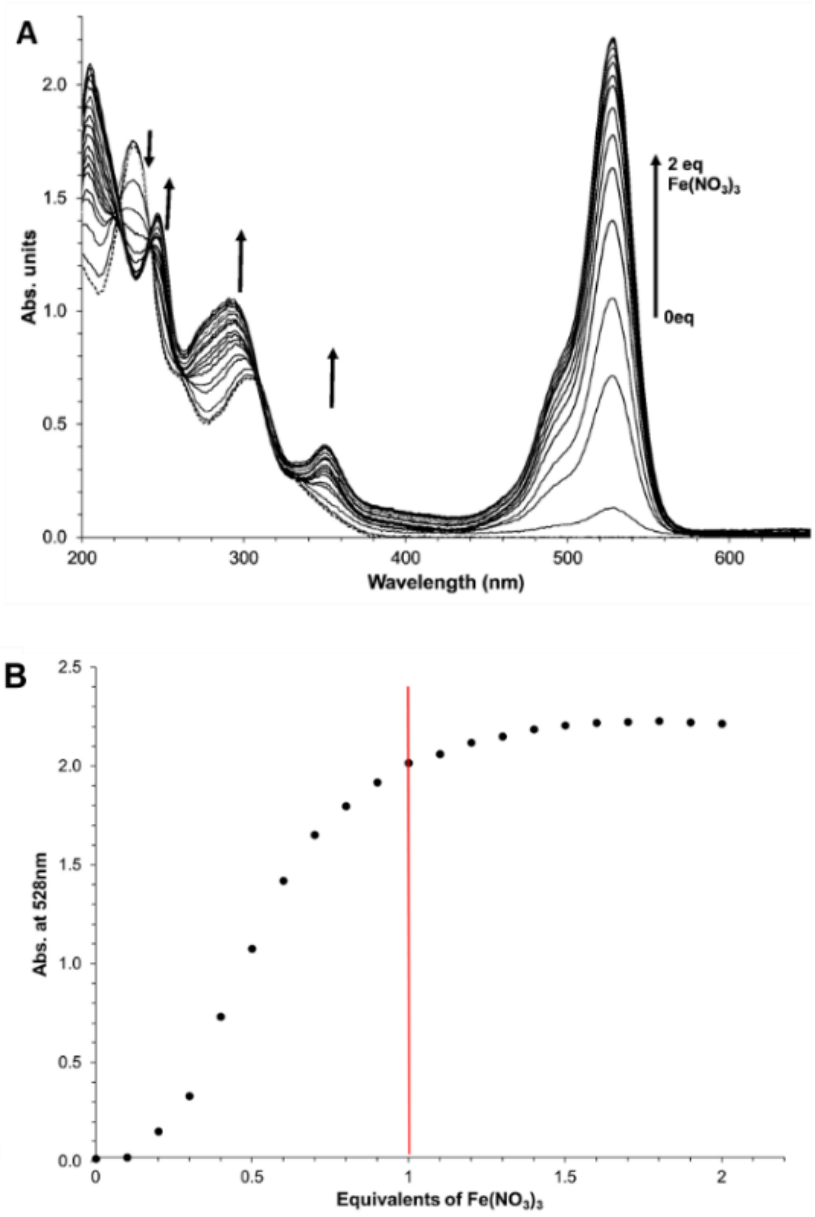

Figure 3.16 *(A) Absorbance spectra showing the titration from 0-2 equivalents of $Fe(NO_3)_3$ into a 25 μM solution of compound* ***3.10*** *in CH_3CN. (B) Binding isotherms from absorbance titration of* ***3.10*** *with $Fe(NO_3)_3$, whereby the λ_{max} at 528 nm is plotted versus the equivalents of $Fe(NO_3)_3$*

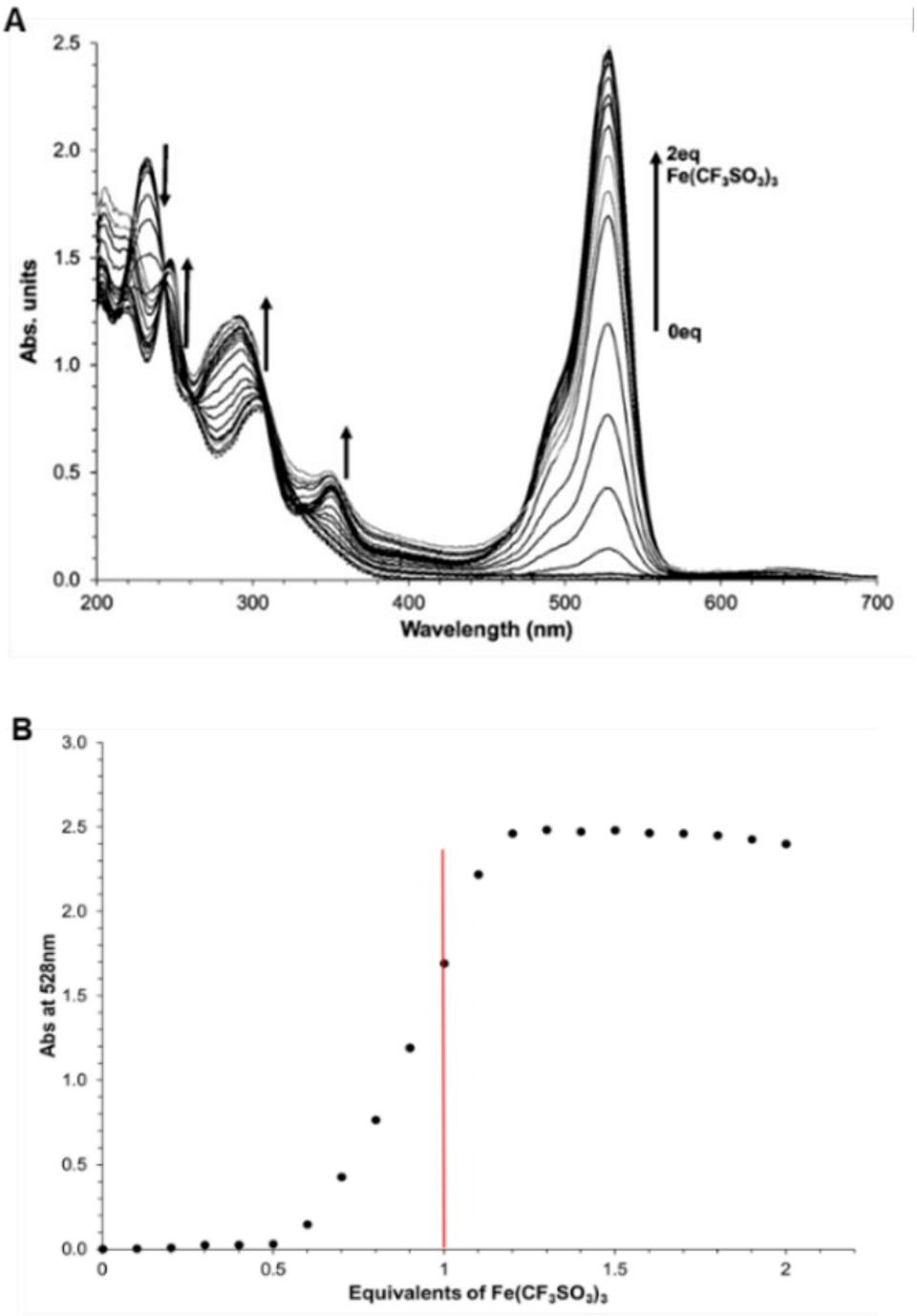

Figure 3.17 *(A) Absorbance spectra showing the titration from 0-2 equivalents of $Fe(CF_3SO_3)_3$ into a 25 µM solution of compound* ***3.10*** *in CH_3CN. (B) Binding isotherms from absorbance titration of* ***3.10*** *with $Fe(CF_3SO_3)_3$, whereby the λ_{max} at 528 nm is plotted versus the equivalents of $Fe(CF_3SO_3)_3$*

Decomplexation of [Fe(**3.10**)]$^{2+}$

To determine the binding constant (logβ) between our sensors and metal ions, non-linear regression analyses are carried out using HypSpec software. The Hypspec analysis gives insights into different species present in solution, such as other ratios i.e., 2:1 and 1:2 complexes, that may have formed. However, due to the complexation inhibition that was observed in oxygen containing solvents, no Hypspec analysis was performed on this system. This inhibition was proof enough that any complexes formed were not very stable. This point is further proven using figure 3.18, whereby the addition of THF to a solution of **3.10**-Fe^{3+} in CH_3CN results in a hypochromic shift in the absorbance band at 528nm. This spectral change indicates that the ligand groups on **3.10** are easily replaced by solvent molecules which have greater affinity for the Fe^{3+} ions. As a consequence of such weak complex formation, it would be impossible to use this sensor to detect metal ions in systems containing even very low concentrations of water. This observation was very significant, considering the similarity of the coordination environment between **3.10** and rhodamine B Hydrazide. Granted, Rhodamine B Hydrazide is expected to be more water soluble than **3.10** due to the hydrophobicity of benzyl group; however, the difference in metal ion selectivity of each of the sensors, as well as their dissimilar functionality in aqueous environments suggest that the degree of substitution of the amine atom has a direct effect on both the selectivity of the sensor and the stability of the complex formed. Unfortunately, no stability constants were reported by Czarnik et al., for their system.

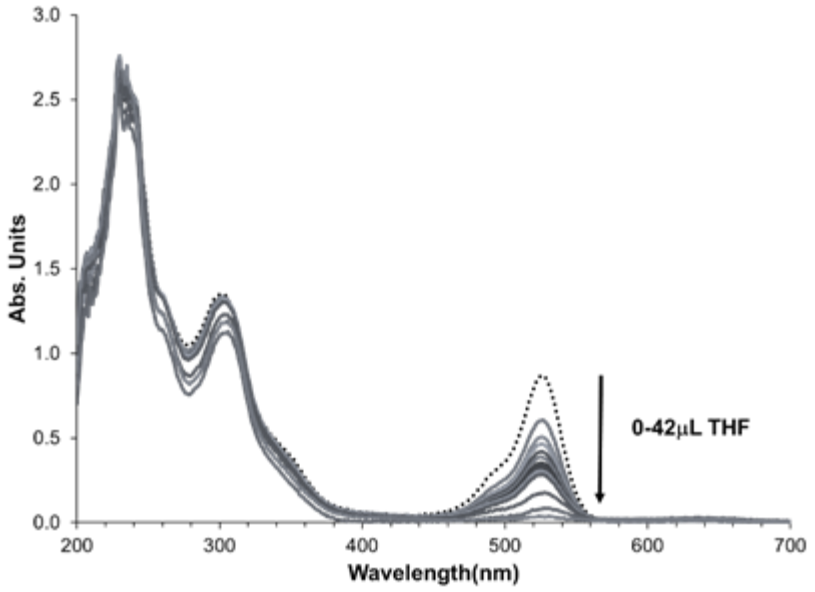

Figure 3.18 *Decomplexation observed as THF is titrated into a solution of compound* ***3.10*** *with 1eq* $Fe(CF_3SO3)_3$ *in* CH_3CN

Solvent Effects on Metal Coordination with Compound **3.11a**

The addition of a hard Lewis base to our receptor had a direct, and desirable effect on the stability of the complexes formed in various solvents, however, the selectivity was diminished. Metal screens were conducted with

25 μM solutions of compound **3.11a** and two equivalents the following metal salts, Ag^+, K^+, Li^+, Na^+, Ca^{2+}, Co^{2+}, Cr^{3+}, Cu^{2+}, Fe^{2+}, Hg^{2+}, Mg^{2+}, Ni^{2+}, Pb^{2+}, Zn^{2+}, Al^{3+}, and Fe^{3+}, in CH_3CN, MeOH, DMSO, and THF. For each of the solvents used, coordination between the sensor and several metal ions was observed (figure 3.19). A spectroscopic response was observed between **3.11a** and Fe^{3+}, Cu^{2+}, Fe^{2+} and Hg^{2+} ions in CH_3CN. As we previously observed, CH_3CN, does not appear to inhibit complex formation between our sensors and metal ions. However, inhibition is seen in the presence of oxygen containing solvents when Hg^{2+} was added to compound **3.11a**. In DMSO and MeOH, complexation

mainly occurs between compound **3.11a** and Cu^{2+} and Fe^{3+} ions, with minimal coordination observed to Fe^{2+}. Lastly, in THF, the species formed between Fe^{2+} ions and **3.11a** appears to be favored over all other metal-ligand species. The association constants for **3.11a** with Fe^{3+} ions in each of these solvent systems is shown in table 3.2. As we expected, the K_a values determined for the coordination compound in CH_3CN were much larger than when the complex was analyzed in oxygen containing solvents.

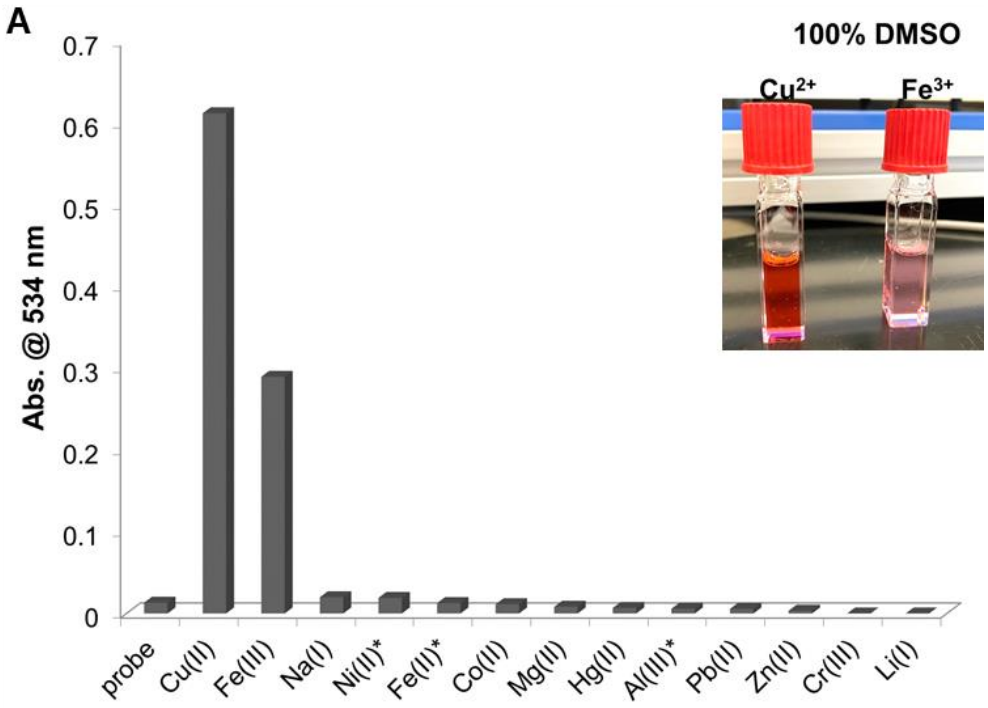

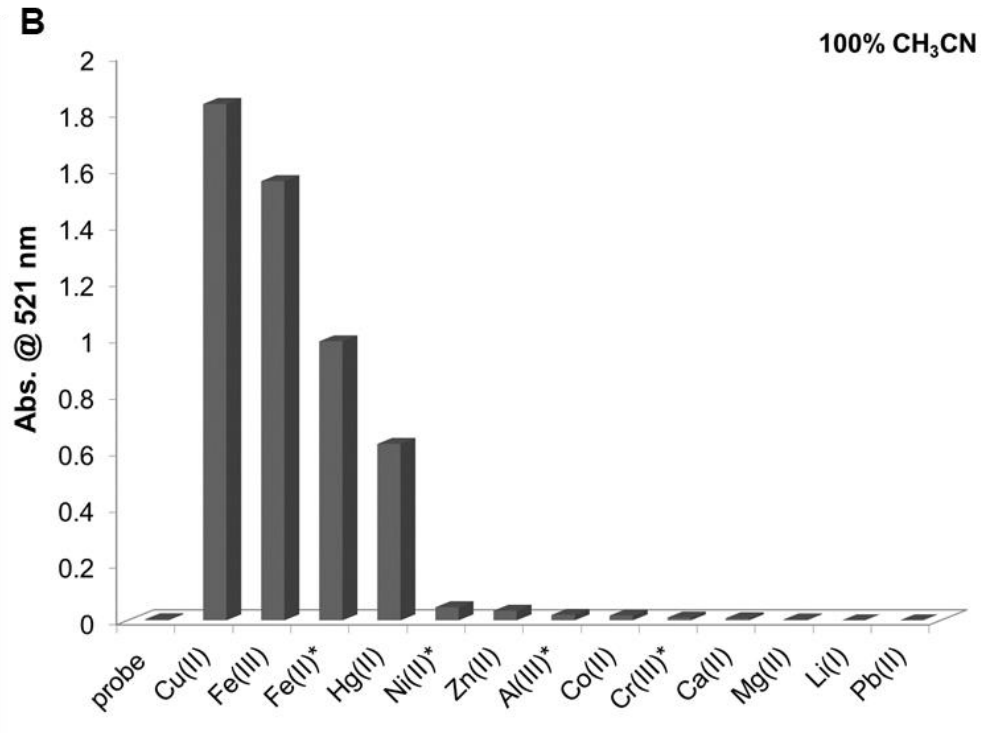
B
100% CH3CN
Abs. @ 521 nm
2
1.8
1.6
1.4
1.2
1
0.8
0.6
0.4
0.2
0
probe
Cu(II)
Fe(III)
Fe(II)*
Hg(II)
Ni(II)*
Zn(II)
Al(III)*
Co(II)
Cr(III)*
Ca(II)
Mg(II)
Li(I)
Pb(II)

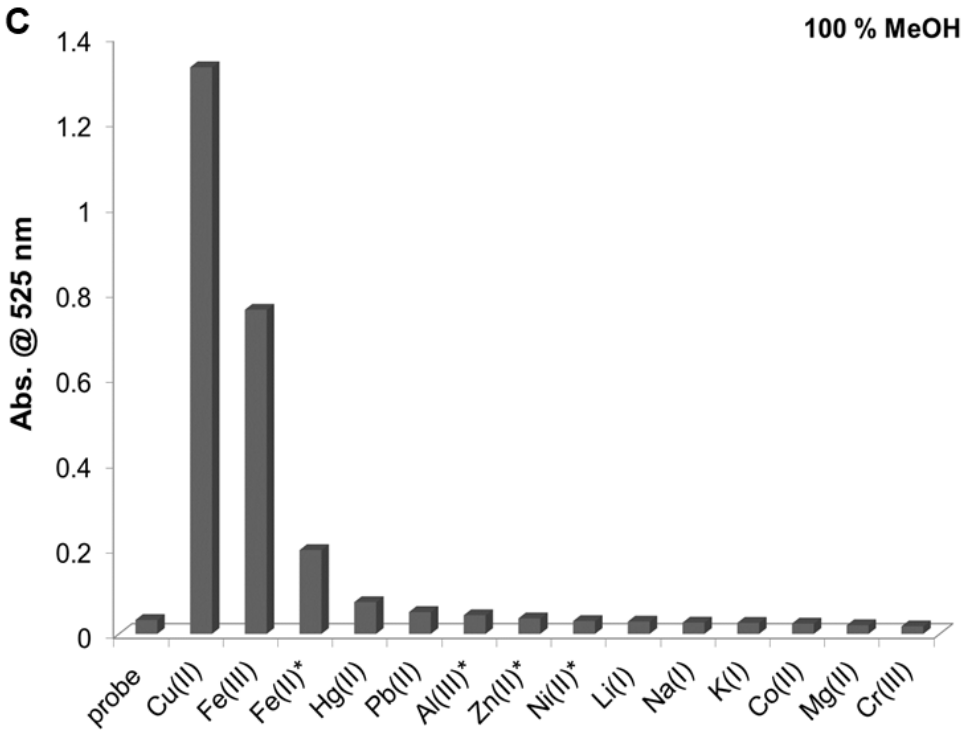
C
100 % MeOH
Abs. @ 525 nm
1.4
1.2
1
0.8
0.6
0.4
0.2
0
probe
Cu(II)
Fe(III)
Fe(II)*
Hg(II)
Pb(II)
Al(III)*
Zn(II)*
Ni(II)*
Li(I)
Na(I)
K(I)
Co(II)
Mg(II)
Cr(III)

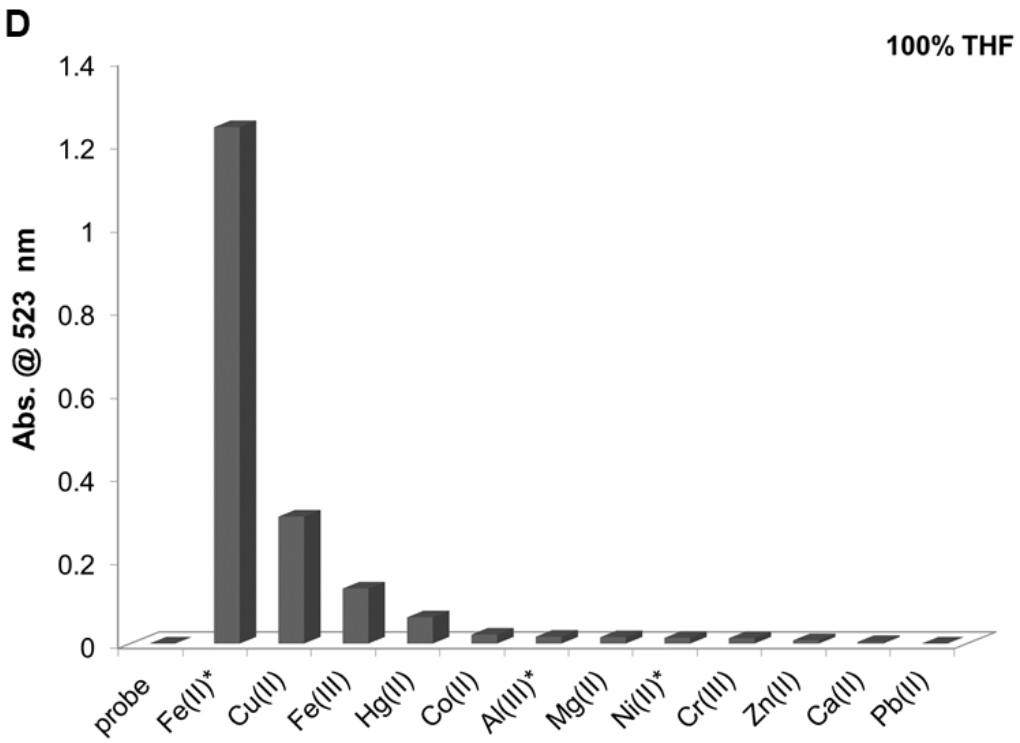

Figure 3.19 *Bar graph results of metal screens with 25 µM solutions of sensor* ***3.11a*** *with two equivalents of various metal ions in (A) DMSO (inset shows the color change immediately after adding* Cu^{2+} *and* Fe^{3+} *ions to the solution of the probe), (B)* CH_3CN *(C) MeOH, (D) THF. Ions with asterisk in diagrams are chlorides, all others are nitrates*

Table 3.2 *Association constants (K_a) for different species formed between compound* **3.11a** *and Fe^{3+} ions in various organic solvents.*
Note: All K_a values are within 10% error

$$[Fe(\mathbf{3.11a})_2]^+ \underset{\log K_{12}}{\rightleftharpoons} L + Fe^{3+} \underset{\log K_{11}}{\rightleftharpoons} [Fe(\mathbf{3.11a})]^{2+} \underset{\log K_{21}}{\rightleftharpoons} [Fe_2(\mathbf{3.11a})]^{5+}$$

[3.11a]	Solvent	K_a [Fe^{3+}:3.11a]
2.5×10^{-5} M	CH_3CN	$K_{11} = 1.1 \times 10^9$ $K_{12} = 8.8 \times 10^5$ $K_{21} = 1.4 \times 10^5$
	DMSO	$K_{11} = 1.3 \times 10^5$ $K_{21} = 2.5 \times 10^5$
	MeOH	$K_{11} = 4.4 \times 10^3$ $K_{21} = 1.1 \times 10^7$ $K_{12} = 7.1 \times 10^8$
	THF	$K_{11} = 1.4 \times 10^6$ $K_{21} = 1.9 \times 10^5$

Stoichiometric Analysis of Compound **3.11a** with Fe^{3+} ions

The majority of the optical studies with **3.11a** were conducted in CH_3CN, DMSO and mixtures of CH_3CN or DMSO with water or buffered solutions. In these solvent systems, changes to absorption spectra were consistently most notable for Fe^{3+} and Cu^{2+} ions. A Job's plot analysis was performed in anhydrous CH_3CN to determine the stoichiometry between **3.11a** and $Fe(CF_3SO_3)_3$. The concentration of the receptor was maintained at 5×10^{-5} M, while the mole fraction was varied from 0 to 1. Each solution was analyzed every hour for five hours to ensure that no additional changes to the spectra occurred. The jobs plot data in figure 3.20 displays a maximum at 0.6 which is indicative

of 1:2 binding between the sensor and Fe^{3+} ions. Evidence of this 1:2 binding is also evident in the sigmoidal nature of the curves shown in figure 3.21. However, non-linear regression analysis indicates the formation of several species in solution, including 1:1, 1:2, and 2:1, coordination compounds between **3.11a** and Fe^{3+} ions. The non-linear regression analysis was carried out using the isotherm data from the titration of **3.11a** with $Fe(CF_3SO_3)_3$ in CH_3CN, as this solvent system demonstrates the strongest metal ligand binding (figure 3.21). The association constants for this system are shown in table 3.3.

Each titration began with a 25 μM solution of **3.11a,** followed by the addition of 0 to five equivalents of $Fe(CF_3SO_3)_3$. In purely organic solvents, very steep binding curves are observed, all of which plateau after the addition of one or two equivalents of $Fe(CF_3SO_3)_3$. In contrast, mixtures of organic and aqueous solvents resulted in less pronounced changes to the shapes of the isotherms, reflecting a decrease in complex formation. This is due to the onset of iron hydrolysis which was discussed in chapter 1. These hydrolysis reactions inhibit the formation of coordination compounds between **3.11a** and Fe^{3+} ions, therefore only a small amount of the Fe^{3+} ions introduced to the solution of the LMFP are able to promote the ring opening mechanism which leads to an increase in the absorbance band near 530 nm. Furthermore, in the 1:1 mix of CH_3CN and 10 mM MES buffered solutions (pH 6.5), virtually no metal coordination was observed due to the strong binding between MES buffer and Fe^{3+} ions.[136]

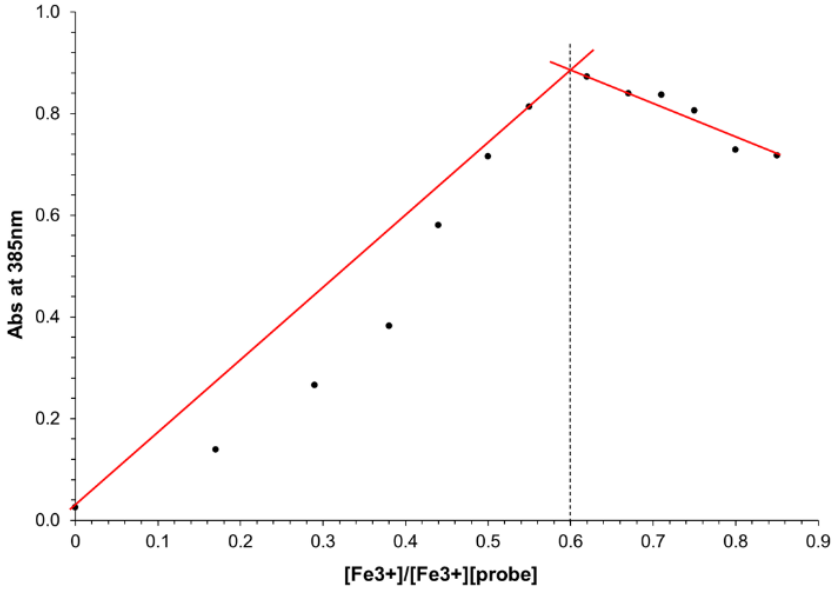

Figure 3.20 *Job's plot data for compound* ***3.11a*** *with* $Fe(CF_3SO_3)_3$ *in* CH_3CN

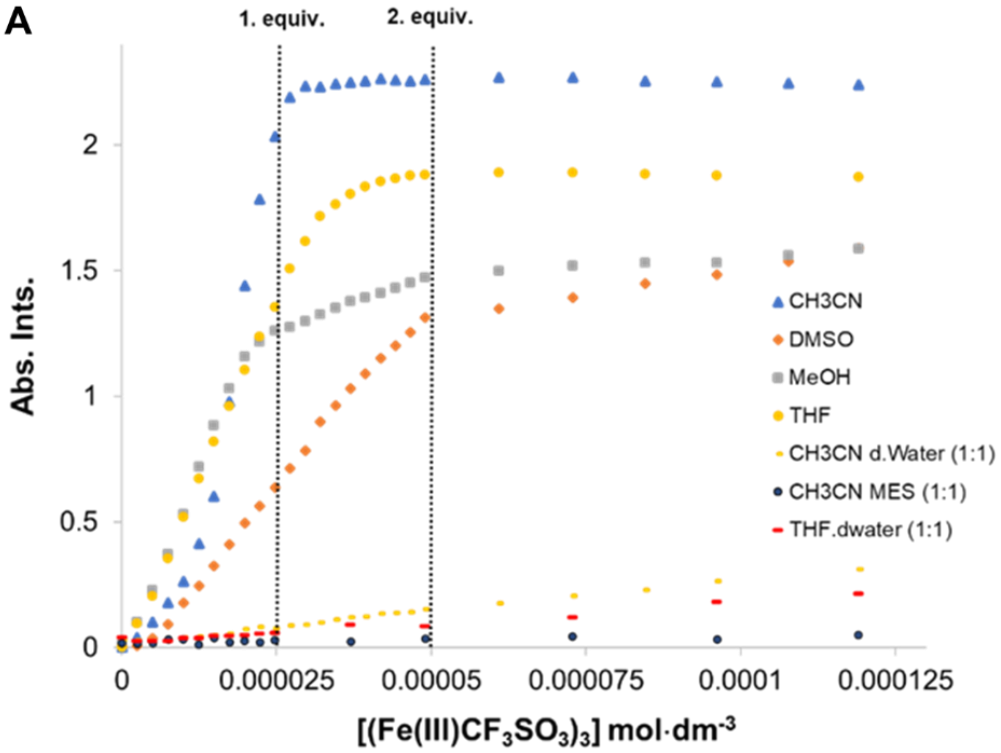

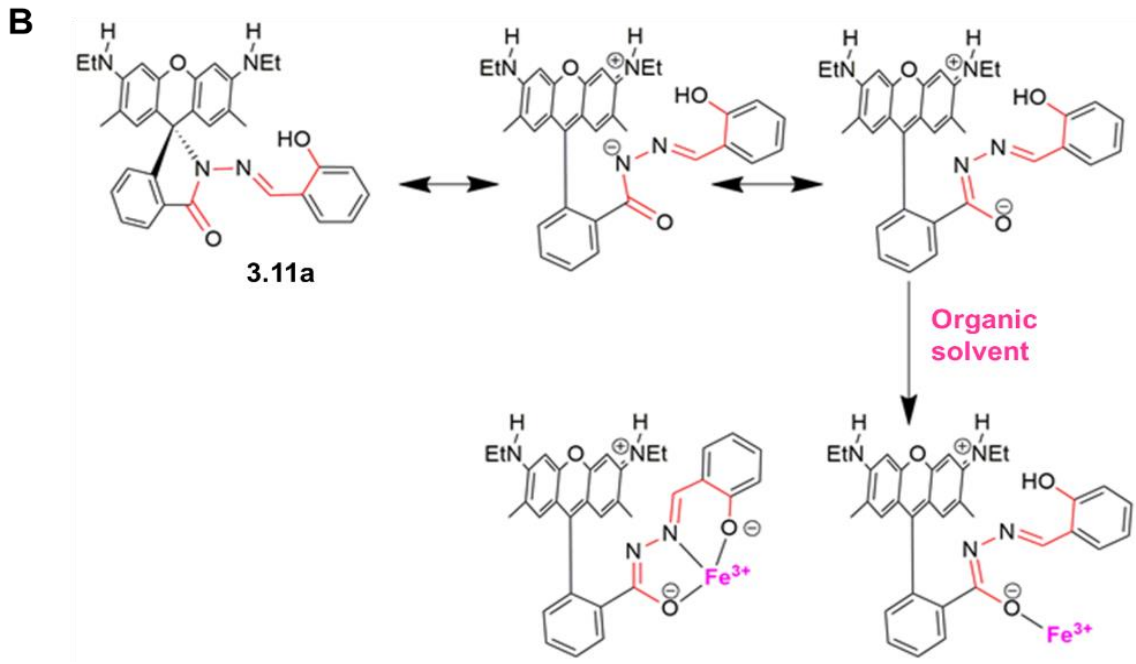

Figure 3.21 *(A)Isotherms plotted from the absorbance titrations between 25 µM solutions of compound **3.11a** and $Fe(CF_3SO_3)_3$ in a range of solvent systems. (B) Proposed cooperative binding between **3.11a** and Fe^{3+} ions in organic solvents*

The Onset of iron hydrolysis reactions can be further verified by analyzing the absorbance spectra of **3.11a** with $Fe(CF_3SO_3)_3$ in each of the solvent systems shown in figure 3.22. An iron hydrolysis study conducted by Andri Stefansson highlights the detection of two Fe^{3+} hydrolysis products, $FeOH^{2+}_{(aq)}$ and $Fe(OH)^{2+}_{(aq)}$, through UV-vis spectroscopy.[81] The absorption maxima for $FeOH^{2+}$ and $Fe(OH)_2^{+}$, which vary in intensity depending on the pH of the solution, are centered at 300nm and 350nm, respectively (see Appendix A.1). This work by Stefansson serves as a reference for identifying which absorption bands in the $[Fe(\mathbf{3.11a})]^{2+}$ complex correspond to the formation of new metal species in solution. As CH_3CN does not act as a coordinating solvent in our systems, we use this solvent as a baseline to which we compare all of the other analysis with compound **3.11a** in this section. Furthermore, no aggregation is

observed in CH_3CN. This likely explains why the absorbance signal for $[Fe(\mathbf{3.11a})]^{2+}$ was the most intense in CH_3CN, as aggregation has been proven to diminish the optical properties or LMFPs.[23, 95, 141]

In THF, DMSO, CH_3CN, and MEOH, ring opening is observed near 530nm. Hyperchromic shifts between 250-400nm are also observed and are likely the result of the formation of Fe^{3+} species in solution (figure 3.22). When water is introduced as a solvent, very little ring opening is observed, meaning that little-to-no complexation has occurred, however, notable absorbance bands are still observed between 250-400nm. The observation of these bands is indicative of Fe^{3+} hydrolysis product formation. As a result, of these hydrolysis reactions, it would be impossible to accurately monitor the concentration of Fe^{3+} ions in aqueous systems using this sensor.

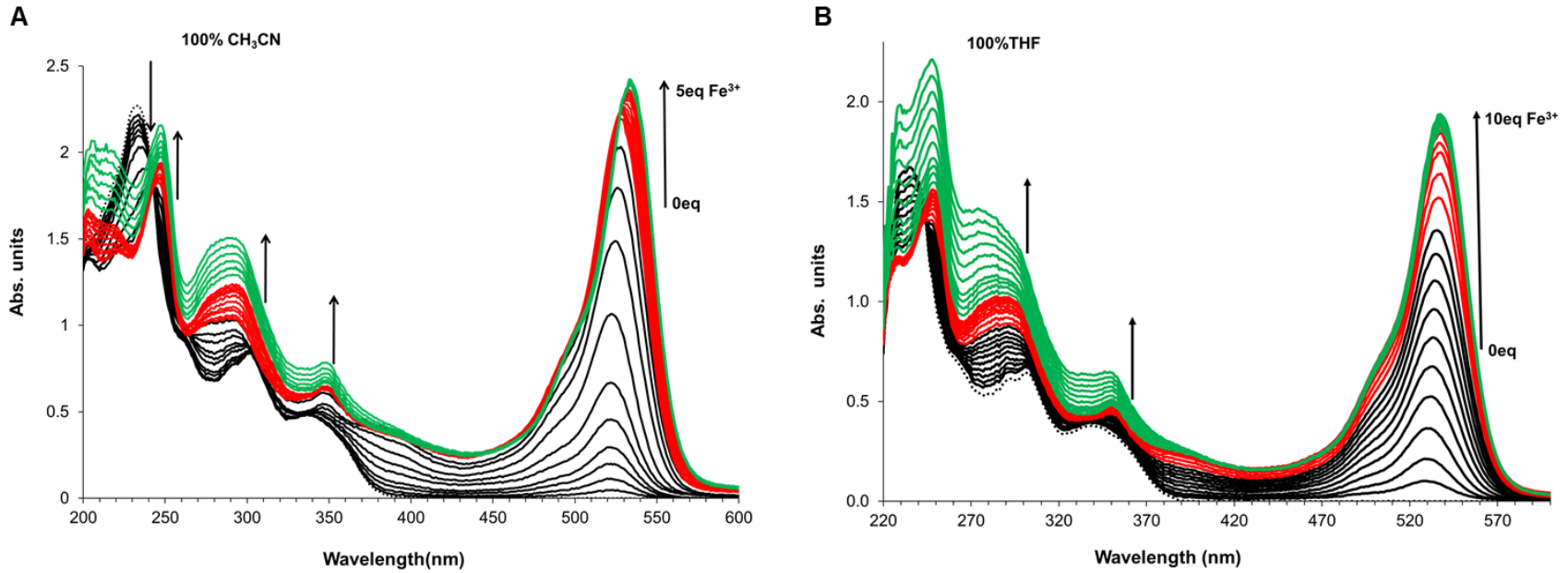
A
100% CH3CN
Abs. units
Wavelength(nm)
5eq Fe3+
0eq
B
100%THF
Abs. units
Wavelength (nm)
10eq Fe3+
0eq

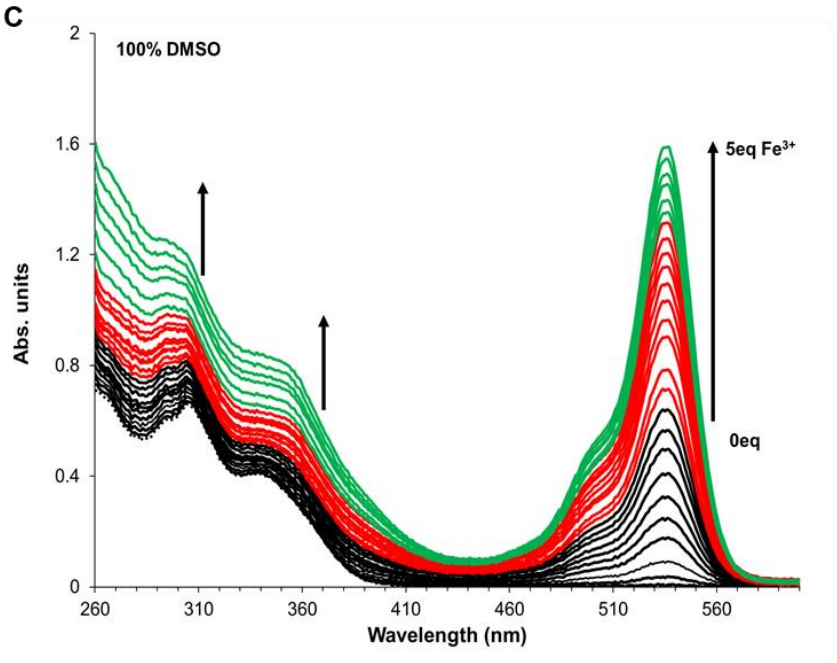
C
100% DMSO
Abs. units
Wavelength (nm)
5eq Fe3+
0eq
0
0.4
0.8
1.2
1.6
2
260
310
360
410
460
510
560

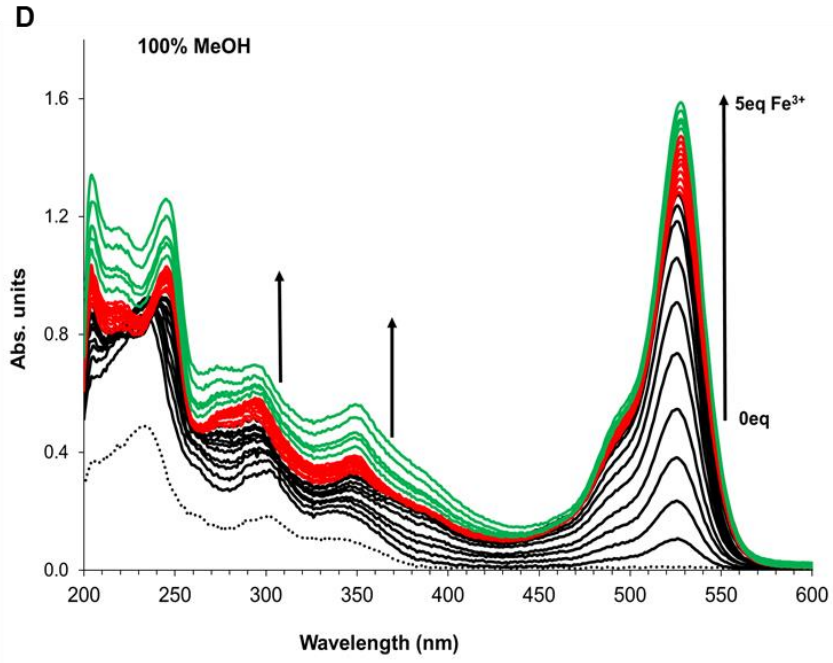
D
100% MeOH
Abs. units
Wavelength (nm)
5eq Fe3+
0eq
0.0
0.4
0.8
1.2
1.6
200
250
300
350
400
450
500
550
600

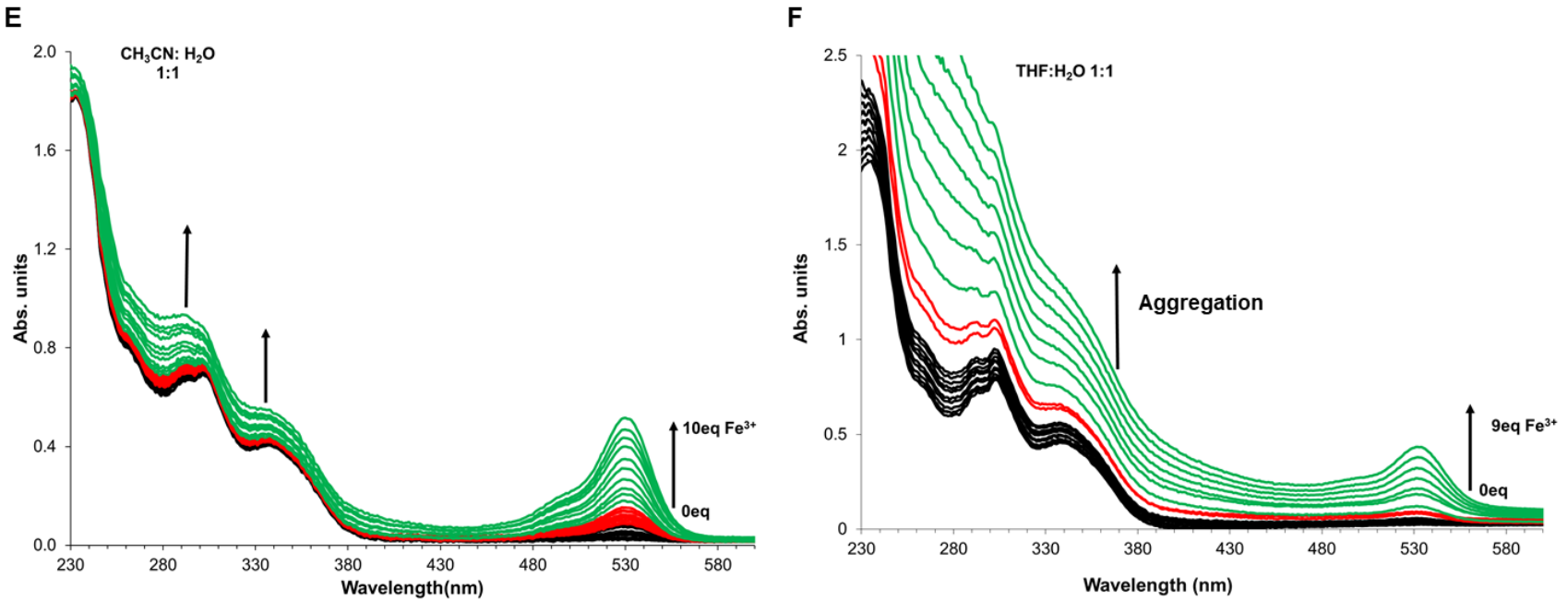

Figure 3.22 *Absorbance titrations between 25 µM solutions of compound* ***3.11a*** *and* $Fe(CF_3SO_3)_3$ *in (A)* CH_3CN*, (B) THF, (C)DMSO, (D) MeOH, (E)* CH_3CN*:*H_2O *(1:1), (F) THF:*H_2O *(1:1)*

Counterion Effects

The effects of the counterion is often ignored in the literature. However, we believe that it is imperative to address the influences that different counterions have on metal binding. In biological applications, the Cl^- anion is often used, whereas the ClO_4^- anion is prevalent in solid state studies. The Cl^- and ClO_4^- anions are also well known for acting as bridging species which affects the stoichiometry of coordination compounds. Additionally, the NO_3^- and $CF_3SO_3^-$ anions are typically used in solution studies due to their solubility in a broad range of organic and aqueous solvents.

Because each of these anions affect the extent of complex formation between LMFPs and metal ions, we conducted absorbance titration studies between each anion and **3.11a**. Titration studies were conducted in CH_3CN between 25 μM of compound **3.11a** and 0 to five equivalents of $Fe(CF_3SO_3)_3$ and $Fe(NO3)_3$, and 0 to ten equivalents of $Fe(ClO_4)_3$ and $FeCl_3$ (figure 3.23). The titration curves of the NO_3^- and $CF_3SO_3^-$ salts appear very similar and non-linear regression analysis revealed the formation of 1:1, 1:2, and 2:1 complexes in solution. The binding constants obtained for the two systems are however very different, as $Fe(CF_3SO_3)_3$ results in complexes that are more stable by two orders of magnitude than $Fe(NO_3)_3$ (table 3.3). The ClO_4^- salt displays binding constants identical to the 1:1 and 1:2 complexes of the $CF_3SO_3^-$ salt, however, no 2:1 complexes were observed. Lastly, the titration curve of the Cl^- salt is indicative of ill-defined complexes in solution. This observation was verified through non-linear regression analysis which identified $\log\beta$ values less than 1.

The larger NO_3^-, ClO_4^-, and $CF_3SO_3^-$ counterions appear to dissociate more readily in CH_3CN a than the smaller Cl^- ion. Evidence of this has been shown previously by the

Wallace group.[105] The readiness of the larger Fe^{3+} salts to dissociate appears to have a direct effect on the binding constant of the sensor-metal complexes being formed. The $CF_3SO_3^-$ and ClO_4^- ions are the largest counterions and are also very good leaving groups; this accounts for the large stability constants of the complexes that they form with compound **3.11a**. These results further emphasize the importance of taking metal speciation into consideration during analysis, as the speciation of the metal ion has a direct effect on the ability of the molecular sensor to accurately monitor the concentration of metal ions in solution. One reason that these counterion affects are often missed is that many literature reports simply concentrate on the fluorescence studies and omit the absorbance data.

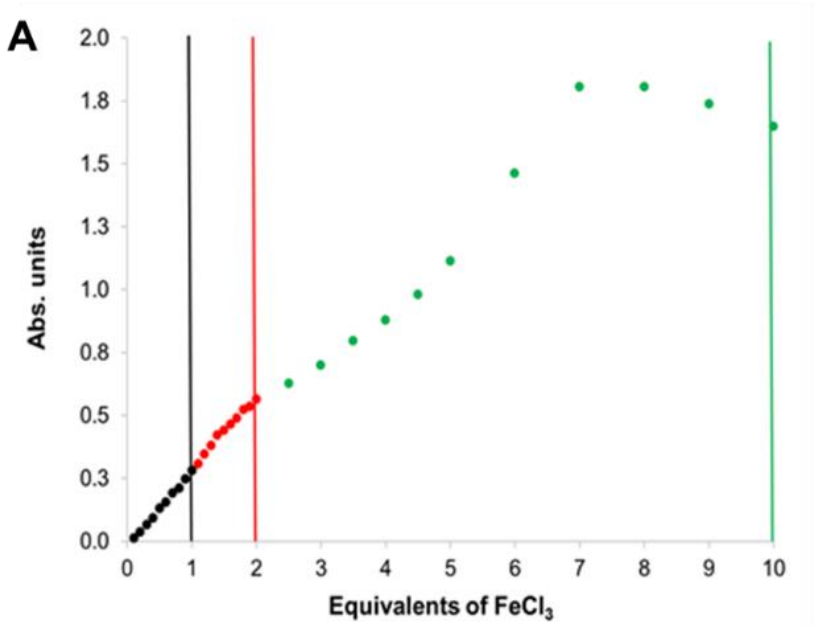
A
Abs. units
Equivalents of $FeCl_3$
0.0
0.3
0.5
0.8
1.0
1.3
1.5
1.8
2.0
0
1
2
3
4
5
6
7
8
9
10

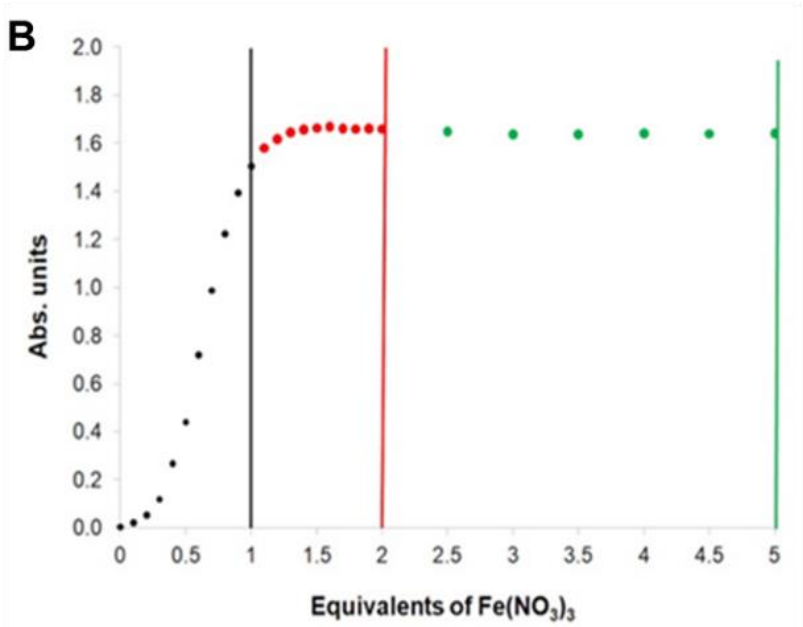
B
Abs. units
Equivalents of $Fe(NO_3)_3$
0.0
0.2
0.4
0.6
0.8
1.0
1.2
1.4
1.6
1.8
2.0
0
0.5
1
1.5
2
2.5
3
3.5
4
4.5
5

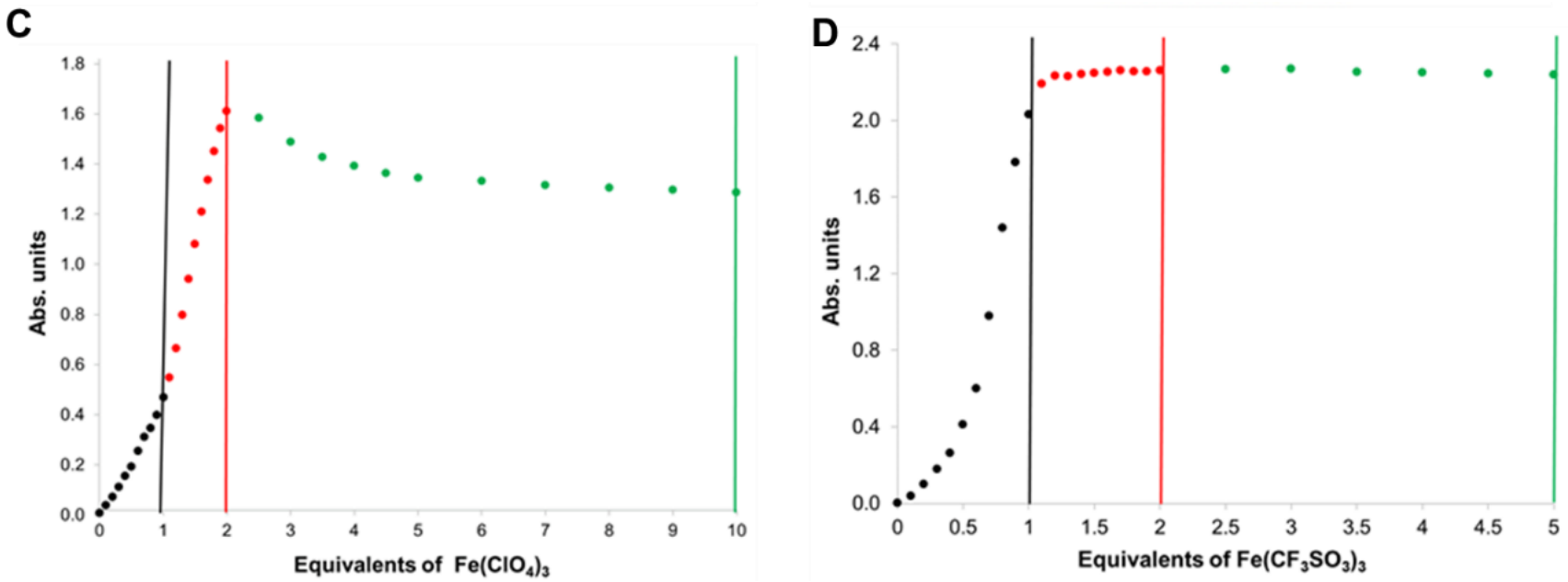

Figure 3.23 *Binding isotherms from the absorbance titrations of 25 μM solutions of* ***3.11a*** *with four different* Fe^{3+} *salts in* CH_3CN *(A)* Cl^- *(B)* NO_3^- *(C)* ClO_4^- *(D)* $CF_3SO_3^-$

Table 3.3 *Association constants calculated for compound* ***3.11a*** *with various* Fe^{3+} *salts in* CH_3CN *using the data in figure 3.23.*

All K_a values are within 10% error

Iron Salt	K_a [Fe^{3+}:3.11a]
$Fe(NO_3)_3$	$K_{11} = 3.2 \times 10^7$ $K_{12} = 6.7 \times 10^5$ $K_{21} = 4.5 \times 10^3$
$Fe(CF_3SO_3)_3$	$K_{11} = 1.4 \times 10^9$ $K_{12} = 1.1 \times 10^6$ $K_{21} = 1.7 \times 10^5$
$Fe(ClO_4)_3$	$K_{11} = 1.4 \times 10^9$ $K_{21} = 1.7 \times 10^5$
$FeCl_3$	$K < 1$

Fluorescence Studies Between **3.11a** and Fe^{3+} ions

The Fe^{3+} ion is notorious for forming non-fluorescent coordination compounds with LMFPs due to the paramagnetic nature of the ion. [130,142] As a result of this, we wanted to determine whether the fluorescence of **3.11a** would be quenched or enhanced upon the addition of Fe^{3+} ions to a solution of the sensor. Fluorescent off-ON sensors offer the benefit of improved sensitivity over colorimetric sensors as fluorescence spectroscopy is much more sensitive than absorbance spectroscopy.[32] Fluorescence spectroscopy also offers the advantage of utilizing different fluorescence mechanisms such as FRET, CHEF, PET, and TICT.[138,143,144]

A fluorescence metal screen was conducted in CH_3CN between compound **3.11a** and a range of metal ions, namely, Ag^{+}, Al^{3+}, Co^{2+}, Cu^{2+}, Fe^{2+}, Hg^{2+}, Ni^{2+}, Pb^{2+}, Zn^{2+}, and Fe^{3+}. The concentration of the probe was 1.25×10^{-7} M, to which 40 equivalents of each metal ion was added. This large concentration of metal ions was used because we have observed that at very low concentrations of LMFPs, such as 10^{-7} M, larger amounts of metal ions are needed to produce a fluorescence turn-on signal. The results of the metal screen showed that only Fe^{3+}, Cu^{2+}, and Hg^{2+} ions resulted in an increase in the fluorescence band at 545nm (figure 3.24). In the presence of Fe^{3+} ions, a 73-fold fluorescence enhancement was observed. This is much larger than the 28-fold and 16.7-fold fluorescence enhancement observed for Cu^{2+}, and Hg^{2+} ions, respectively. No other metals resulted in a notable change in the fluorescence spectra of compound **3.11a**.

These observations are in alignment with the results of the absorbance metal screen reported earlier in the section. Based on those studies, the introduction of oxygen containing solvents would likely inhibit the fluorescence mechanism from occurring between the probe and Hg^{2+} ions. Because Fe^{3+} ions resulted in the largest fluorescence enhancement, this section will focus mainly on studies with the Fe^{3+} ion. Section 3.5.6 will highlight the fluorescent behavior of compound **3.11a** in the presence of Cu^{2+} ions

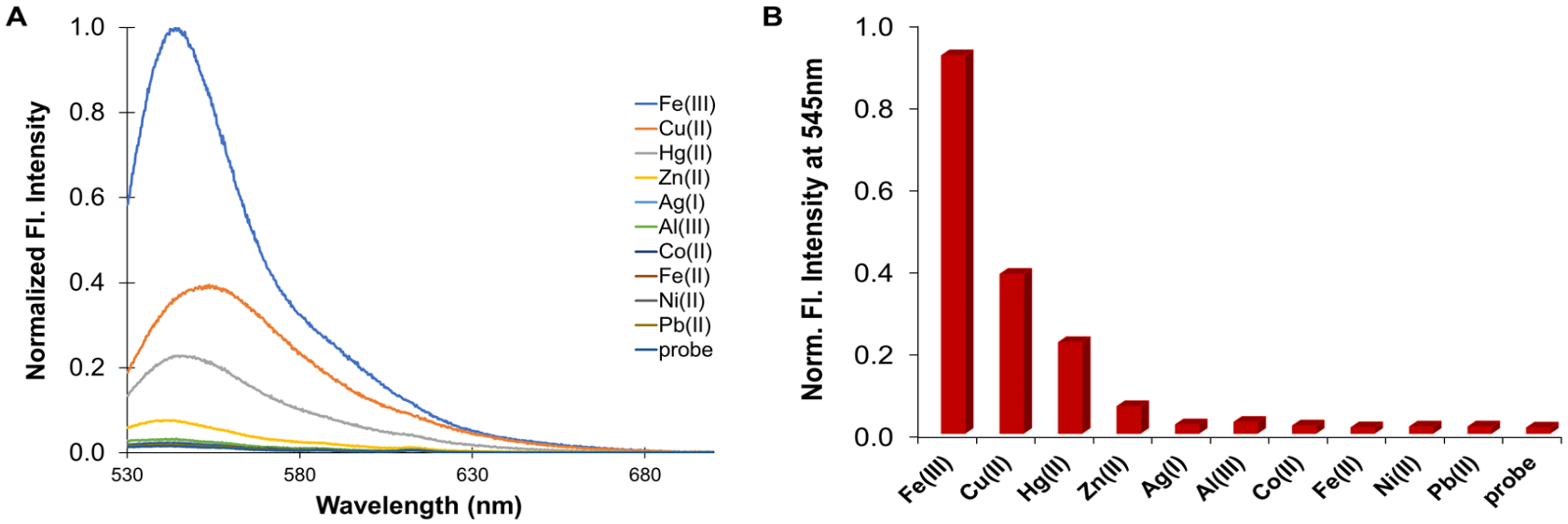

Figure 3.24 *Fluorescence metal screen between 0.125 μM solutions of compound* ***3.11a*** *and 40 equivalents of various metal ions in* CH_3CN. λ_{Ex} = *520 nm*

Fluorescence titration studies were conducted in DMSO, CH_3CN, MeOH, and THF to determine how each of the solvents would affect the fluorescence of the $[Fe(\mathbf{3.11a})]^{2+}$ coordination compound. We expected that that largest fluorescence enhancement would be observed in CH_3CN, a non-coordinating solvent. The titrations were carried out by first adding 2 mL of a 0.125 μM solution of **3.11a** to a quartz cuvette. A very low intensity emission band is observed between 550 to 565 nm for the unbound sensor, depending on the solvent used. The addition of up to 8 equivalents of $Fe(CF_3SO_3)_3$ resulted in a noticeable fluorescence enhancement in each of the spectra shown in figure 3.25. The largest increase in the fluorescence is observed when CH_3CN is used as a solvent- resulting in a 6-fold increase in the fluorescence of compound **3.11a**. In DMSO and MeOH, 2.3-fold and 3-fold fluorescence enhancements were observed, respectively, while the solution of THF displayed a very weak fluorescence signal. This weak fluorescence intensity is likely related to the low solubility of **3.11a** in THF. We have observed that the ring open form of **3.11a** is much more soluble in weakly polar organic solvents, like THF, than the spirolactam form. Because of the low concentration of the receptor and Fe^{3+} ions in solution, it is likely that the THF solvent molecules disrupt the interactions between the Fe^{3+} ions and the receptor. Increasing the time between each addition of Fe^{3+} salt may lead to larger increases in the observed emission as the system would be allowed to stir for longer and possibly reach equilibrium.

From the results of these titrations, it is clear that compound **3.11a** serves as an efficient off-ON fluorescent sensor for Fe^{3+} ions in strong polar protic and aprotic organic solvents, as the receptor is very soluble in these types of solvents. Unfortunately, compound **3.11a** cannot be as a fluorescent sensor for Fe^{3+} ions in aqueous solutions. The

binding between this receptor and Fe^{3+} ions is not strong enough for **3.11a** to solubilize the Fe^{3+} hydrolysis products like siderophore molecules are able to. Siderophore molecules form extremely stable complexes with Fe^{3+} ions, demonstrating K_a values up to 10^{52} M^{-1}. These molecules are able to solubilize Fe^{3+} precipitates in solution and bind to the metal centers in purely aqueous solutions. Siderophore-inspired LMFPs will be discussed in chapter 5 of this work.

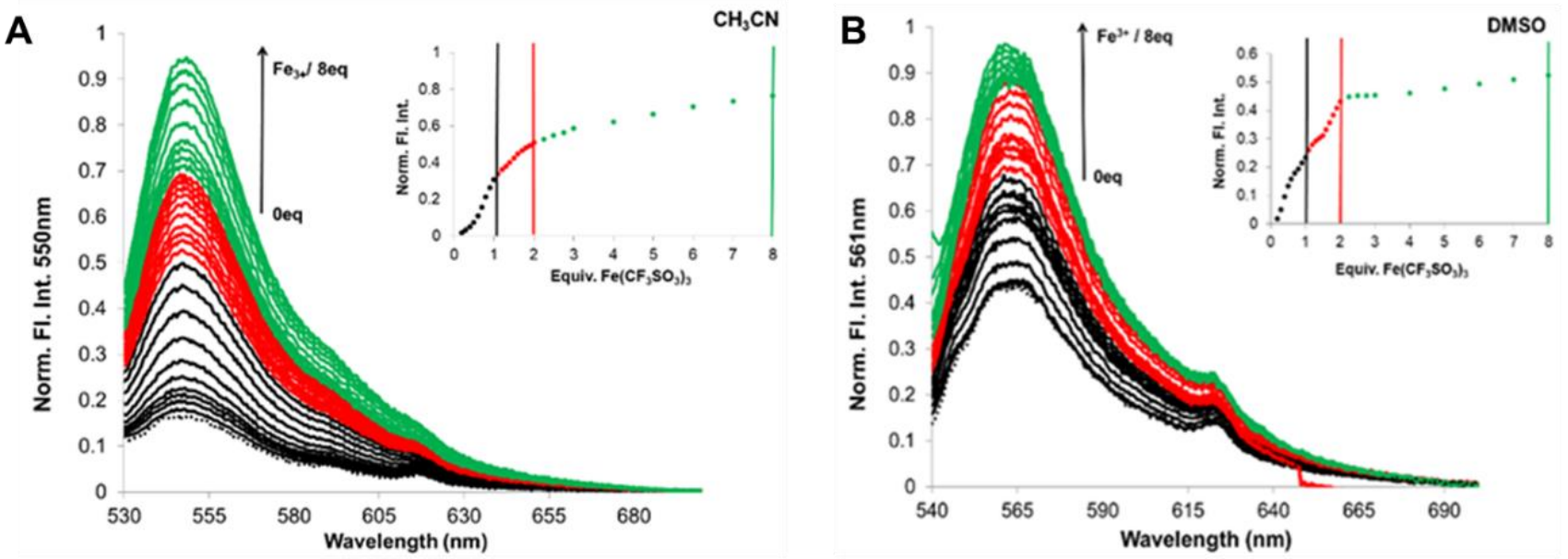
A
CH3CN
Fe3+/ 8eq
0eq
Norm. Fl. Int. 550nm
Wavelength (nm)
Norm. Fl. Int.
Equiv. Fe(CF3SO3)3
B
DMSO
Fe3+ / 8eq
0eq
Norm. Fl. Int. 561nm
Wavelength (nm)
Norm. Fl. Int.
Equiv. Fe(CF3SO3)3

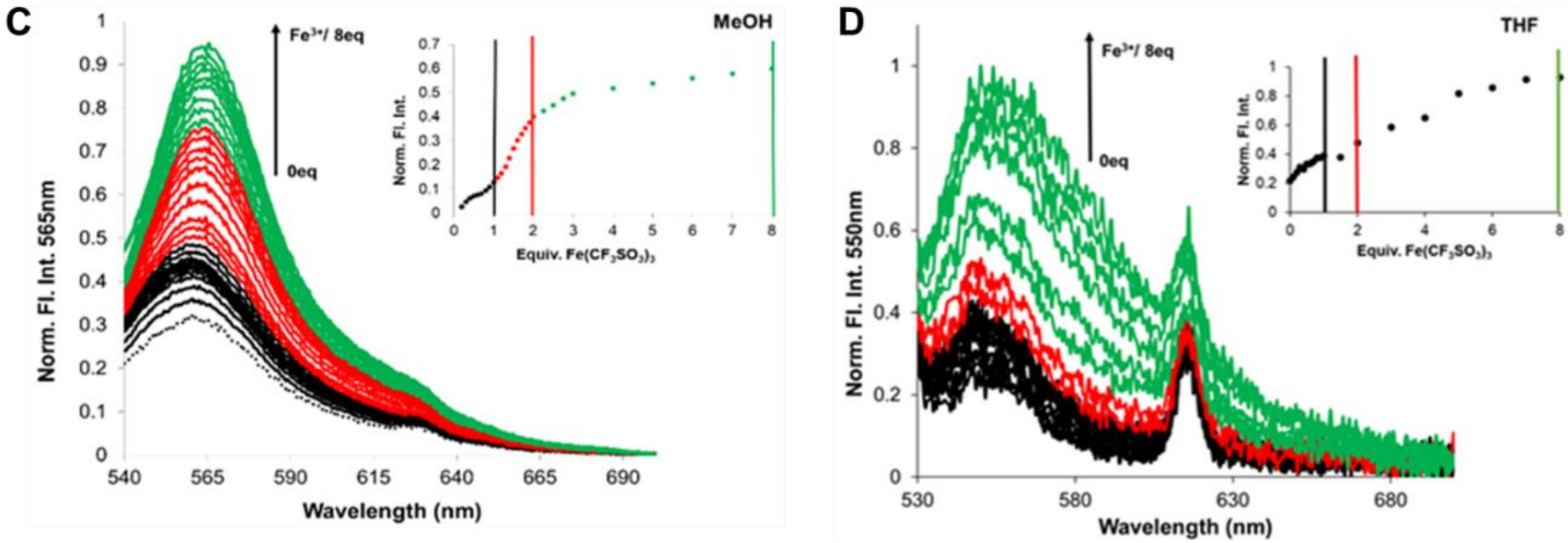

Figure 3.25 *Fluorescence plots and binding isotherms (inset) resulting from the titration of* $Fe(CF_3SO_3)_3$ *into 0.125 µM solutions of* ***3.11a*** *in (A)* CH_3CN, λ_{Ex} = 520 nm (B)DMSO, λ_{Ex} = 530 nm (C) MeOH, λ_{Ex} = 530 nm (D) THF, λ_{Ex} = 520 nm

Detection Limit of Compound **3.11a** for Fe^{3+} Ions in Organic Solvents

Fluorescence titration data can also be used to determine how sensitive a LMFP is for a specific analyte. The sensitivity of a molecular probe is very significant because it is important to be able to detect trace amounts (μM to nM) of metal ions in different systems. The limit of detection (LoD) is defined as the analyte concentration resulting in a signal equal to the blank signal plus three standard deviations from the blank, i.e., $y = b+3\sigma$. The limit of detection was determined by titrating a 250 μM solution of $Fe(ClO_4)_3$ into a 0.25 μM solution of **3.11a** in CH_3CN. The perchlorate salt was chosen because the addition of up to one equivalent of the salt into **3.11a** results in a linear plot rather than a sigmoidal plot. Evidence of this is observable in the isotherms in shown in figure 3.23.

To determine limit of detection (LoD), the change in the intensity of emission band at 550 nm versus the concentration of Fe^{3+} was plotted. The method of least squares was then used to give a line of regression (figure 3.26). Using a 95% confidence level, the LoD of **3.11a** for Fe^{3+} ions was determined to be 51.4nM (2.87 ppb). A similar limit of detection of 54.3nM, was calculated when DMSO was instead used as the solvent. These detection limits are comparable to the LoDs reported by Goswami et al., and Chereddy et al., in section 3.2. Goswami et al., reported a LoD of 2.0 ppb for Fe^{3+} ions in a mix of CH_3CN-water (1:1, v/v, pH 7.2), while Chereddy et al., reported a LoD of 2.79 ppb for Fe^{3+} ions in 0.01 M Tris-HCl buffer and CH_3CN (1:1, v/v, pH 7.4). Each of these reported LoDs are much lower that the allowable concentration of Fe^{3+} ions in drinking water of 0.3 ppm, as defined by WHO.[50] However, none of these LMFPs were able to demonstrate Fe^{3+} ion detection in 100% aqueous solution.

Even though compound **3.11a** is not capable of accurately determining the concentration of Fe^{3+} ions in aqueous environments (due to iron hydrolysis), the low LoD for Fe^{3+} ions in different organic solvent systems, and the small size of **3.11a** makes it a viable candidate for use in bioimaging applications.

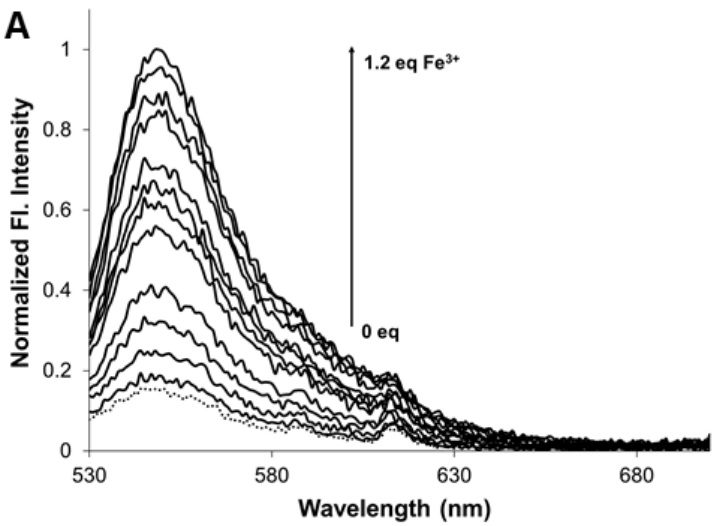
A
Normalized Fl. Intensity
1
0.8
0.6
0.4
0.2
0
530
580
630
680
Wavelength (nm)
1.2 eq Fe3+
0 eq

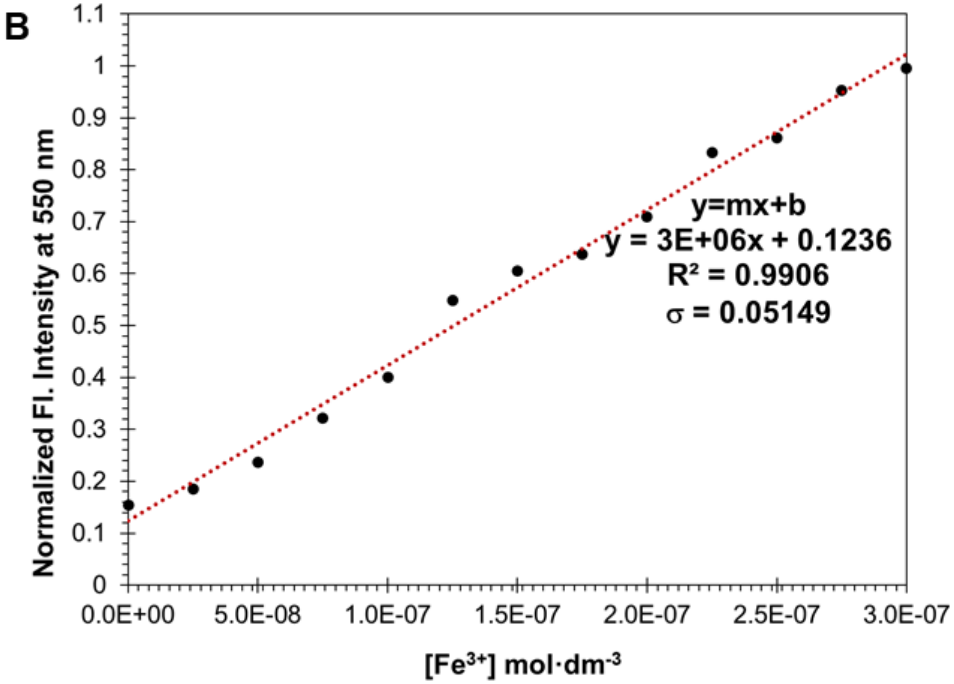
B
Normalized Fl. Intensity at 550 nm
1.1
1
0.9
0.8
0.7
0.6
0.5
0.4
0.3
0.2
0.1
0
0.0E+00
5.0E-08
1.0E-07
1.5E-07
2.0E-07
2.5E-07
3.0E-07
[Fe3+] mol·dm-3
y=mx+b
y = 3E+06x + 0.1236
R² = 0.9906
σ = 0.05149

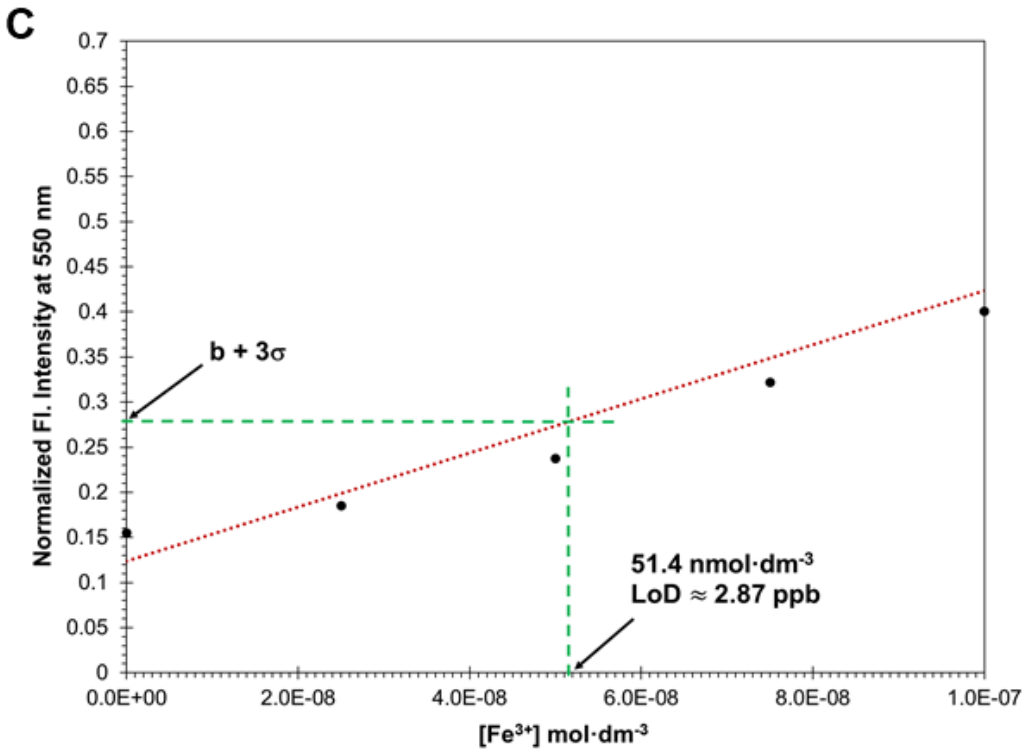

Figure 3.26 *(A) Fluorescence data used for LoD calculation with compound* ***3.11a*** *(B) Calibration curve used to calculate the LoD for* $Fe(ClO_4)_3$ *with compound* ***3.11a*** *in* CH_3CN *(C) Expansion of diagram B.*

Fluorescence Lifetime Studies for Compound **3.11a** with Fe^{3+} ions

The advantages of measuring the fluorescence lifetimes (τ_0) of different chemical species were discussed in depth in chapter 2.3.2. Based on this information, we expect that the fluorescence decay profile of the free probe, **3.11a**, will be different from that of the [Fe(**3.11a**)]$^{2+}$ coordination compound.[112, 145] The fluorescence lifetime of the ring-open form of **3.11a** in DMSO-0.01% HCl was compared to that of the [Fe(**3.11a**)]$^{2+}$ complex in DMSO. The fluorescence lifetime of the ring-open form of **3.11a** in EtOH-0.01% HCl was also observed to determine the how this lifetime would compare to that of rhodamine 6G.

The concentration of the receptor was maintained at 25 μM for each sample and the ratio of **3.11a** with $Fe(CF_3SO_3)_3$ was 1:2. The fluorescence decay profiles and random distribution of weighed residuals of [**3.11a** + H]$^+$ and [Fe(**3.11a**)]$^{2+}$ are shown in figure 3.27. The fluorescence decay plots are fitted to a single exponential with excellent χ^2 values very close to 1. All trials were repeated three times to ensure reproducibility of the results. The protonated form of **3.11a** in DMSO displayed a fluorescence lifetime of 4.35 ± 0.0625 ns, while the [Fe(**3.11a**)]$^{2+}$ complex remained in the excited state for 3.37 ± 0.0167 ns. Both of these lifetimes differ from that of rhodamine-6G in a solution of EtOH-0.01% HCl, which has a reported fluorescence lifetime of 3.7 ± 0.4 ns.[146] The lifetime of **3.11a** in EtOH-0.01% was found to be 3.98±0.0308 ns.

Because the lifetimes observed for the free probe in DMSO and EtOH differ, it is imperative to analyze the lifetimes of LMFPs and the coordination compounds that they form in a variety of solvents. Fluorescence lifetimes are not only dependent upon the solvent system, but the concentration of the LMFP as well as the presence of dissolved

oxygen in solution affect the fluorescence decay profiles of different chemical species. This means that we can expect the fluorescence lifetime of [Fe(**3.11a**)]$^{2+}$ to vary when slightly moving from one solvent system to another. We can however always expect to observe a decrease in the fluorescence lifetimes of compound **3.11a** in the presence of Fe^{3+} ions. Similar behavior to this has been reported in the literature for rhodamine coordination compounds and has also been observed in this work between **3.11a** and Cu^{2+} ions as well as with compound **4.6** which will be discussed in chapter 4.[147,148] The reason for the observed decrease in the fluorescence lifetime as we move from the free probe to the coordination compound was also explained in chapter 2. As the number of radiative decay (Γ) pathways increases, which is observed by an increase in the fluorescence intensity, the fluorescence lifetime decreases as a consequence.

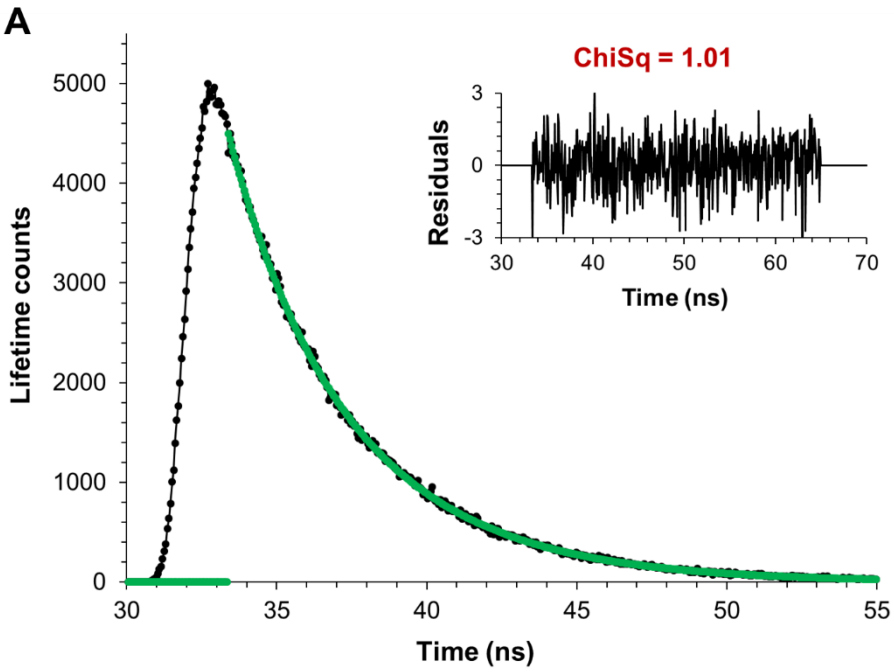

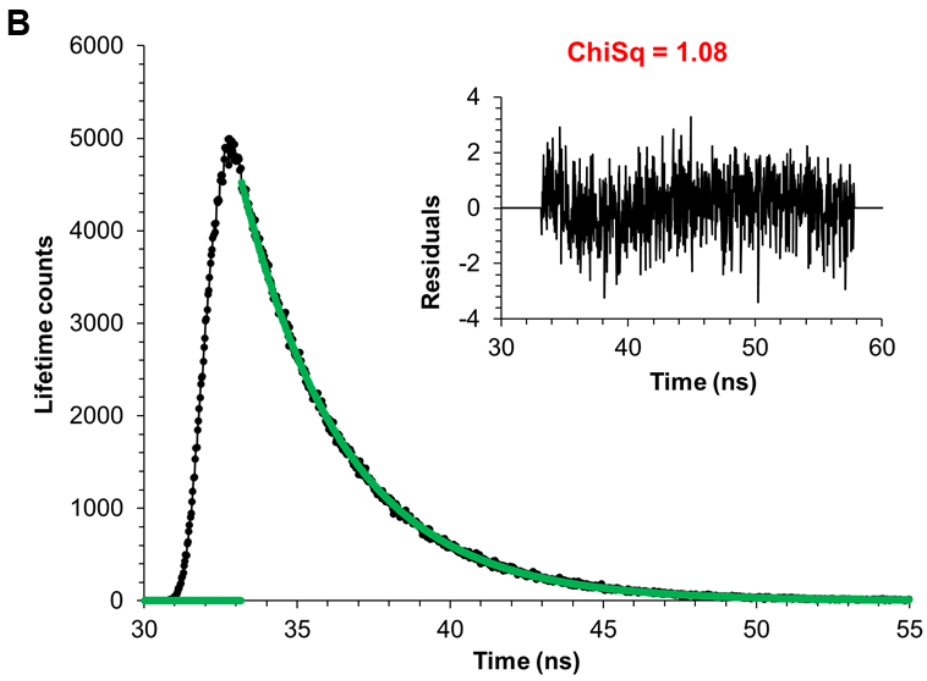

Figure 3.27 *(A) Fluorescence decay of free probe **3.11a** in DMSO-0.01% HCl with residuals shown in inset. (B) Fluorescence decay of [Fe(**3.11a**)]$^{2+}$ in DMSO with residuals shown in inset*

3.5.6 Toward Aqueous Solubility-Optical Spectroscopy

Now that we have a better understanding of the binding in organic solvents, the attention is turned to aqueous systems. This section focuses on the three LMFPs, **3.11a**, **3.12** and **3.13**, and their ability to detect metal ions in aqueous solutions. Under aqueous conditions, these LMFPs display improved selectivity for Cu^{2+} ions over other metal ions.

Stoichiometric Analysis of Compounds **3.11a** and **3.12** with Cu^{2+} Ions in Various Solvent Systems

A series of optical titration studies were carried out between compound **3.11a** and $Cu(NO_3)_2$ ions in a range of solvent systems (figure 3.28). For each of the titrations, the

starting concentration of the receptor was 2.5×10^{-5} M and up to five equivalents of $Cu(NO_3)_2$ salt was then introduced incrementally to the solution of the receptor. Contrasting the Fe^{3+} ion studies displayed in figure 3.21, the introduction of water and buffer solutions, specifically, 2-(N-morpholino)ethanesulfonic acid (MES), did not appear to greatly inhibit the formation of coordination compounds between compound **3.11a** and Cu^{2+} ions. The varying solvent systems do however display different stoichiometric ratios as well as binding constants. The binding isotherms in figure 3.29 correspond to the absorbance spectra shown in figure 3.28. The sharp increases observed in these binding isotherms are indicative of very strong binding between compound **3.11a** and Cu^{2+} ions in organic, and aqueous systems.

In addition to the absorbance band near 530 nm, which corresponds to ring opening, an absorbance band centered near 400 nm is also observable in each of the spectra in figure 3.28. This absorbance band is representative of the formation of a copper coordination complex, similar to the coordination bands explained in section 3.5.5 for Fe^{3+} complexes, and is observed in a number of rhodamine-based Cu^{2+} ions probes. [149,150] The appearance of a similar absorbance band in the titration studies between compounds **3.12** and **3.13** and two different Cu^{2+} salts verified that this band is indeed unique to the formation of Cu^{2+} coordination compounds with our probes (see appendix A5). The Cu^{2+} coordination band, however, appears to be much more pronounced and more consistent when switching between solvent systems than those observed for the Fe^{3+} ion studies. This indicates that the solvent molecules interfere less in the formation of coordination compounds between Cu^{2+} ions and **3.11a** than they do between Fe^{3+} ions and **3.11a**.

Also important to note is the isobestic point at 350 nm in figure 3.28, diagrams B, C, and E. This isobestic point indicates that the addition of Cu^{2+} ions does not affect the absorbance of **3.11a** at 350 nm. An isobestic point is, however, absent is Figure 3.28, diagrams A, D, and F. In diagram A, the isobestic point was initially visible, however, as the concentration of Cu^{2+} salt increased beyond 50 μM, the absorbance band at 350 nm gradually increased. In diagrams D and F the isobestic point is likely absent due to the high concentration of water molecules present in the samples. As the concentration of water increased, the samples required longer mixing times between sample analysis to reach equilibrium, and aggregation was also observed. A number of literature examples demonstrate the increased aggregation observed in LMFPs as the ratio of water in the system increases.[151,141]

Despite the differences observed in the spectra in figure 3.28, it is clear that compound **3.11a** is capable of coordinating to Cu^{2+} ions in systems containing high concentrations of water. Furthermore, the use of MES buffer (10 mM, pH 6.5) which was chosen due to its minimal binding to Cu^{2+} ions (when the concentration of the buffer is less than 30 mM), verifies that the ring opening mechanism is due to genuine metal coordination, and not protonation of the sensor in aqueous media.[136] A comparison of diagrams E and F in figure 3.28 shows that in DMSO and water (1:9, v/v, pH 7.0), some of the receptor molecules are present in the open form prior to the addition of the Cu^{2+} salt. In contrast, the solution of DMSO and MES buffer (1:9, v/v, pH 6.5) displays a negligible absorbance band at 530 nm prior to the addition of Cu^{2+} ions.

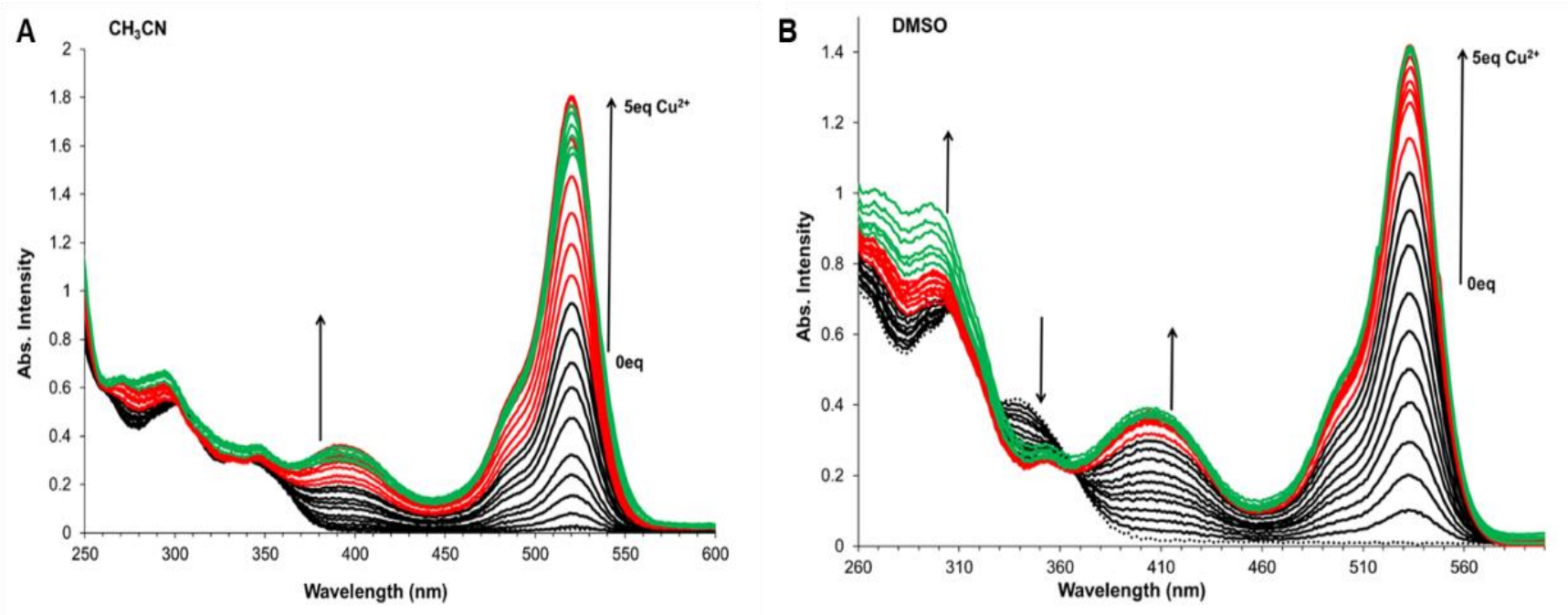
A
CH3CN
Abs. Intensity
Wavelength (nm)
5eq Cu2+
0eq
B
DMSO
Abs. Intensity
Wavelength (nm)
5eq Cu2+
0eq

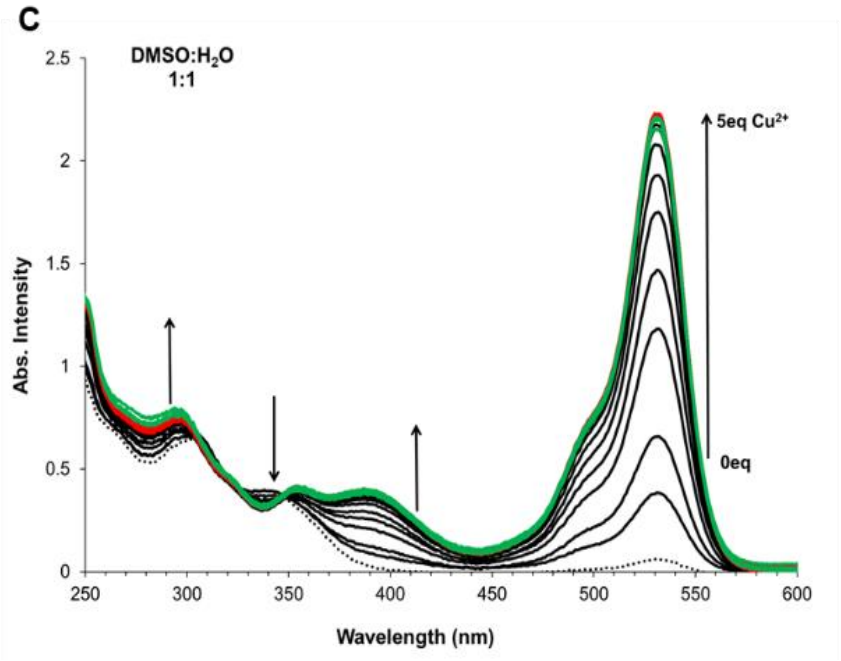
C
DMSO:H2O
1:1
5eq Cu2+
0eq
Abs. Intensity
Wavelength (nm)
2.5
2
1.5
1
0.5
0
250
300
350
400
450
500
550
600

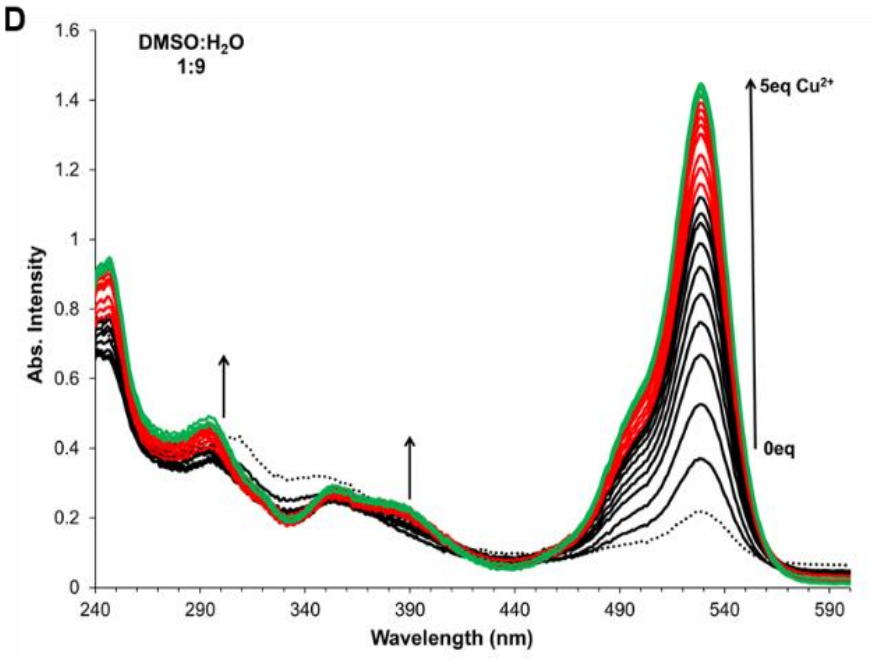
D
DMSO:H2O
1:9
5eq Cu2+
0eq
Abs. Intensity
Wavelength (nm)
1.6
1.4
1.2
1
0.8
0.6
0.4
0.2
0
240
290
340
390
440
490
540
590

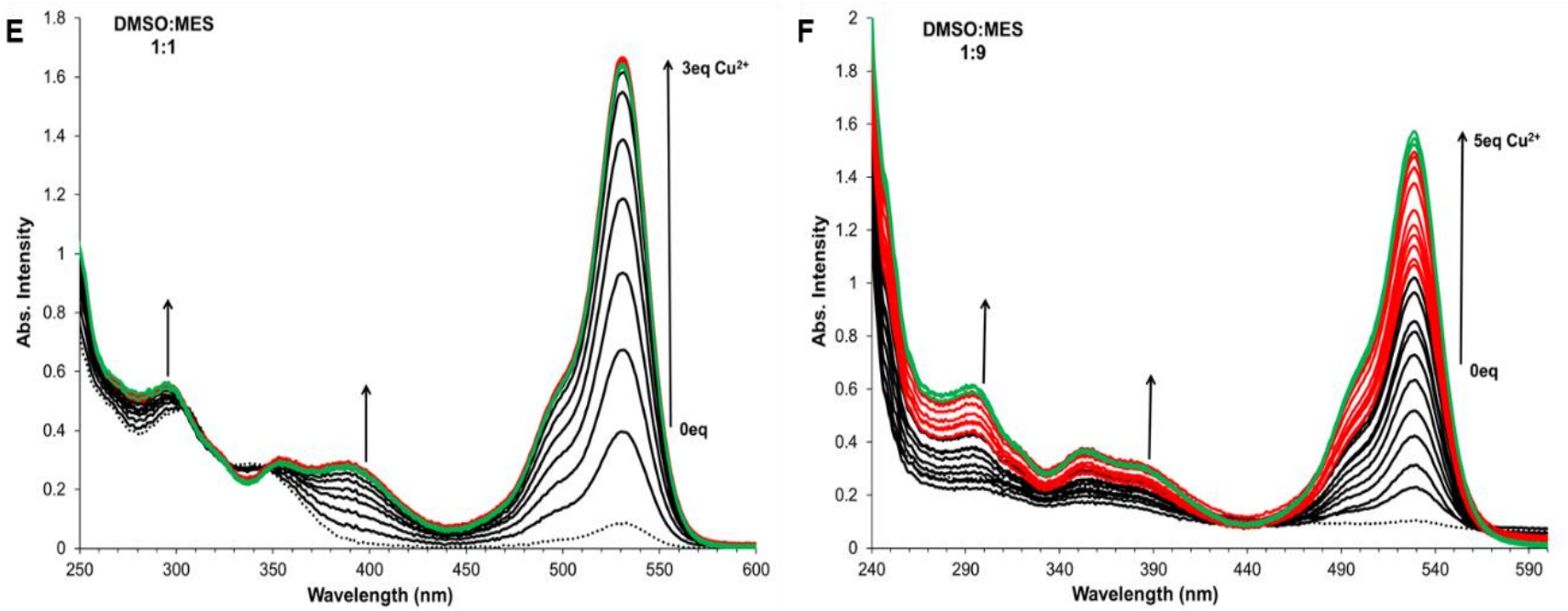

Figure 3.28 *Absorbance titrations between 25μM solutions of compound* ***3.11a*** *and* $Cu(NO_3)_2$ *in (A)* CH_3CN*, (B) DMSO, (C)DMSO: water (1:1, v/v, pH ≈7.), (D) DMSO: water (1:9,v/v pH ≈7.0), (E) DMSO: MES (1:1, v/v, pH=6.5), (F) DMSO: MES (1:9, v/v, pH=6.5)*

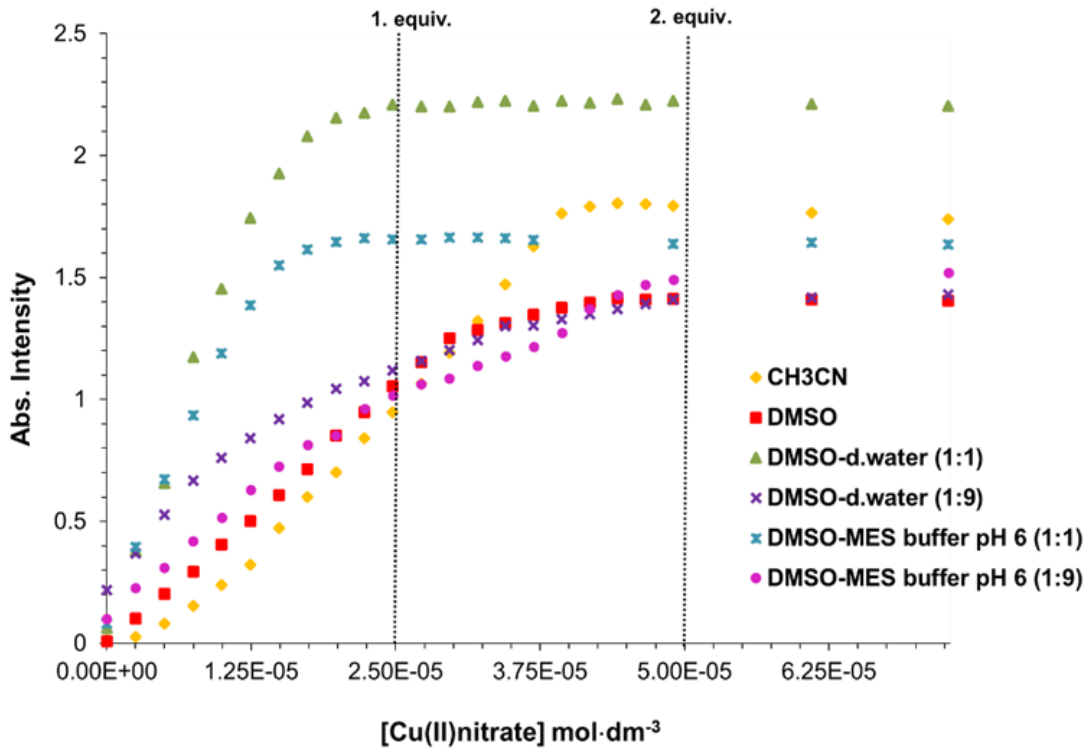

Figure 3.29 *Binding Isotherms plotted from the absorbance titrations between 25μM solutions of compound* ***3.11a*** *and* $Cu(NO_3)_2$ *in a range of solvent systems*

Due to the strong binding interactions observed in the 25 μM solutions of compound **3.11a** with Cu^{2+} ions (figure 3.29), non-linear regression analysis was performed at lower concentrations in some of the systems. The binding isotherms plotted for the systems at lower concentrations are very different from those of the 25 μM solutions (see figure 3.30). For example, in figure 3.29, the 1:1 aqueous solutions show sharp increases up to one equivalent of Cu^{2+} salt, followed by flattening of the curves. However, the dilute 1:1 aqueous solutions (12.5 μM of compound **3.11a**) display more gradual increases in the absorbance bands at 533nm. The 25 μM solution of compound **3.11a** in DMSO and water (1:1, v/v) suggests predominantly 1:1 binding whereas the

12.5 µM solution demonstrates 1:2 binding between the receptor and Cu^{2+} ions. Based on the stability constants (table 3.4), both 1:1 and 1:2 stoichiometry exists between compound **3.11a** and Cu^{2+} in the 1:1 solution of DMSO and water. However, once the ratio of water was increased to nine times the amount of DMSO, mainly 1:1 stoichiometry was observed. Another solvent that is important to note is the behavior of **3.11a** towards Cu^{2+} ions in CH_3CN. When CH_3CN is used as a solvent, compound **3.11a** displays cooperative binding towards Cu^{2+} ions, resulting in a sigmoidal curve. This behavior is observed in the concentrated (25 µM) and dilute (10 µM) solutions of **3.11a**. This sigmoidal curve is only observed in CH_3CN and is a clear indication of the 1:2 binding between **3.11a** and Cu^{2+} ions (scheme 3.11). This stoichiometry was verified using non-linear regression analysis (table 3.4).

A comparison of the stability constants observed in purely organic solvents versus those observed in the 1:1 aqueous solutions, indicates that the introduction of water does not greatly inhibit the ability of compound **3.11a** to efficiently bind to Cu^{2+} ions. As the concentration of water was increased, up to nine times the amount of DMSO, the stability of the complexes did decrease , however, the stability constants still point to the formation of very stable complexes between compound **3.11a** and Cu^{2+} ions in the 1:9 organic: aqueous solutions. When compared to the stability constants highlighted for compounds **3.4** and **3.6** in section 3.2, compound **3.11a** demonstrates much stronger binding (greater than two magnitudes) toward Cu^{2+} ions in a range of solvent systems.

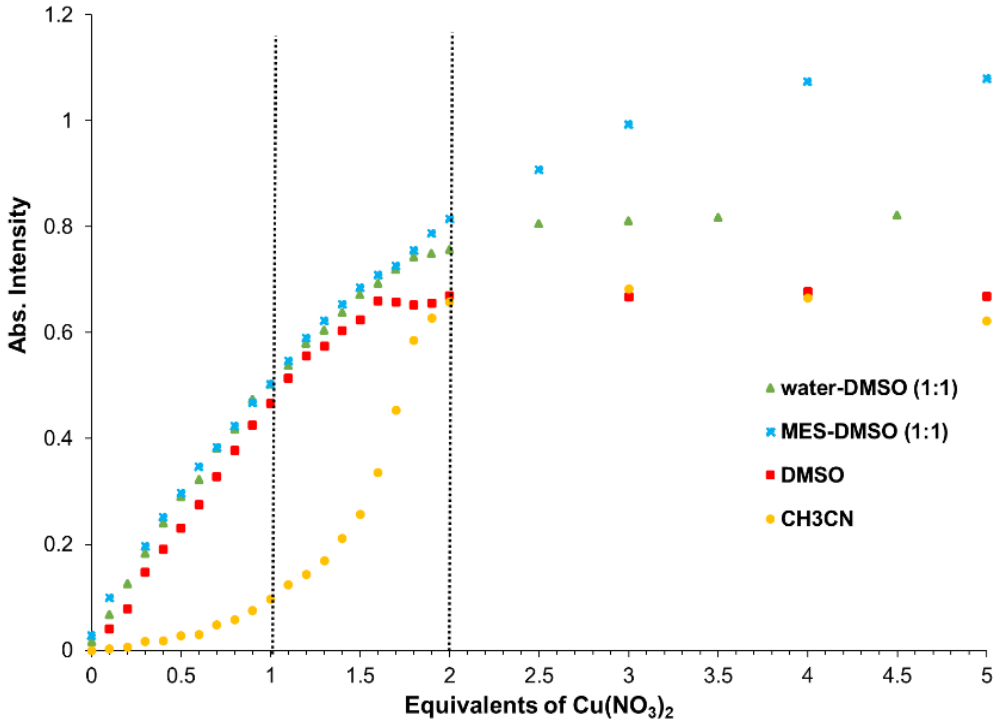

Figure 3.30 *Isotherms plotted from the absorbance titrations between compound* ***3.11a*** *and* $Cu(NO_3)_2$ *in a range of solvent systems. See table 3.4 for the concentrations of compound* ***3.11a*** *used for each solvent system.*

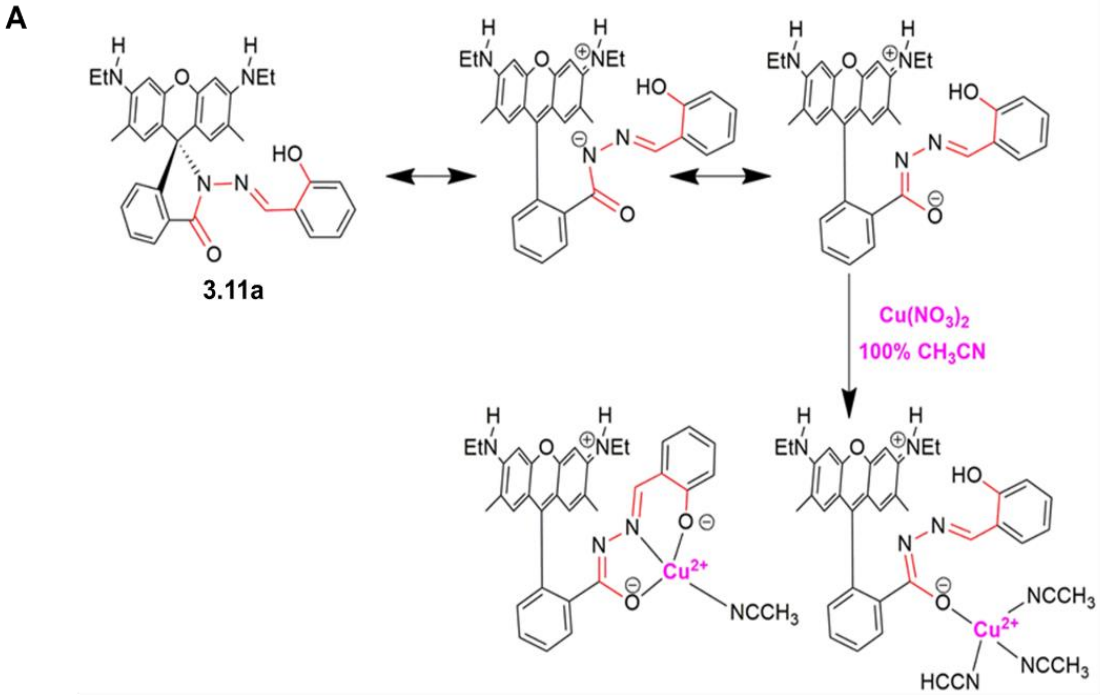

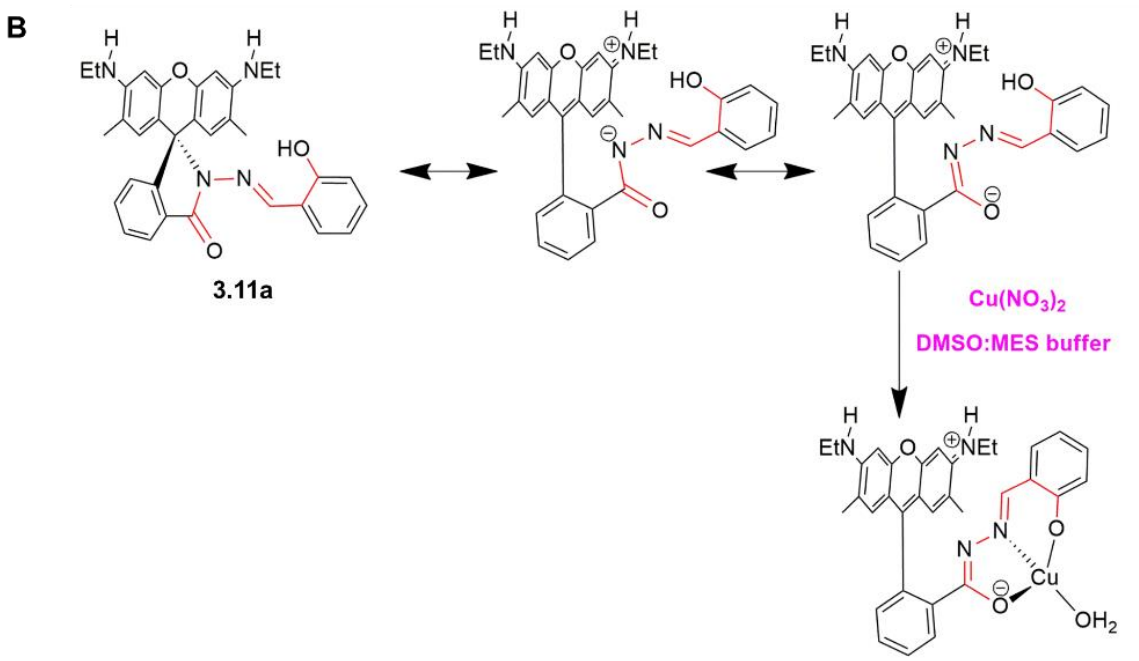

Scheme 3.11 *(A) Proposed cooperative bonding between **3.11a** and Cu^{2+} ions in CH_3CN (B) Proposed bonding between **3.11a** and Cu^{2+} ions in DMSO: 10 mM MES (1:1, v/v, pH 6.5).*

Table 3.4 *Binding constants calculated for compound* ***3.11a*** *with* $Cu(NO_3)_2$ *in various solvent systems. Note: The concentration of MES buffer was 10 mM for each solution with pH= 6.5*

Note: All K_a values are within 10% error

[3.11a]	Solvent	K_a [Cu^{2+}: 3.11a]
1.0×10^{-5} M	CH_3CN	$K_{11} = 1.7 \times 10^6$ $K_{21} = 1.4 \times 10^7$
1.0×10^{-5} M	DMSO	$K_{11} = 2.1 \times 10^7$ $K_{21} = 4.4 \times 10^5$
1.25×10^{-5} M	DMSO: H_2O 1:1	$K_{11} = 6.5 \times 10^7$ $K_{12} = 1.0 \times 10^6$
2.5×10^{-5} M	DMSO: H_2O 1:9	$K_{11} = 3.3 \times 10^5$
1.0×10^{-5} M	DMSO: MES 1:1	$K_{11} = 7.1 \times 10^6$
2.5×10^{-5} M	DMSO: MES 1:9	$K_{11} = 3.3 \times 10^5$

As it is our goal to improve sensor function in aqueous environments, the interactions between compound **3.12** and $CuCl_2$ were studied. In addition to the hydroxyl group at the 10' position, compound **3.12** also contains a hydroxyl group at the 12' position (refer to numbering system in section 3.3). Control studies between sensor **3.11b** and cupric ions verified that the hydroxyl group at the 12' position is not a part of the coordination environment. Compound **3.11b** instead behaves like compound **3.10** and does not display metal coordination in oxygen containing solvents (scheme 3.12). The hydroxyl group at the 12' position on compound **3.12** therefore serves to improve the

water solubility of the sensor. The improved sensor function under aqueous conditions was verified through a series of titration studies. In contrast to the drastic decreases in stability constants for compound **3.11a** with Cu^{2+} ions as we moved from the 1:1 to 1:9 (v/v) organic-aqueous systems, the stability constants for compound **3.12** with Cu^{2+} ions in aqueous systems remains fairly constant (table 3.5). In fact, the stability constants for the 1:1 $[Cu(\mathbf{3.12})]^{+}$ complexes in aqueous solutions were higher than the stability constant observed for the 1:1 complex in the solution of DMSO.

It is also important to note that the use of the Cl^{-} anion instead of the NO_3^{-} anion did not seem to hinder the calculation of stability constants and complex stoichiometry the way it did between compound **3.11a** and $FeCl_3$ in section 3.5.5. The absorbance spectra and titration curves corresponding to the systems highlighted in table 3.5 can be found in appendix A5. The titration curves are in agreement with the results of the linear regression analysis, which indicates mainly 1:1 binding between **3.12** and Cu^{2+} ions in aqueous media. The proposed non-cooperative binding between these two species is shown in scheme 3.13.

Absorbance studies were also performed on compound **3.13** which contains a nitrogen atom at the 10' prime position. As expected, the decreased solubility of compound **3.13** in aqueous solutions when compared to compounds **3.11a** and **3.12**, resulted in lower stability constants observed for the $[Cu(\mathbf{3.13})]^{2+}$ complexes (appendix A5).

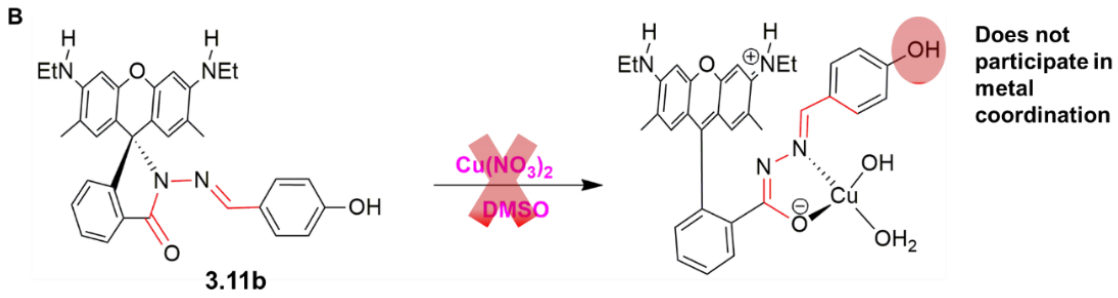

Scheme 3.12 *Lack of binding between compound* ***3.11b*** *and metal ions in oxygen containing solvents*

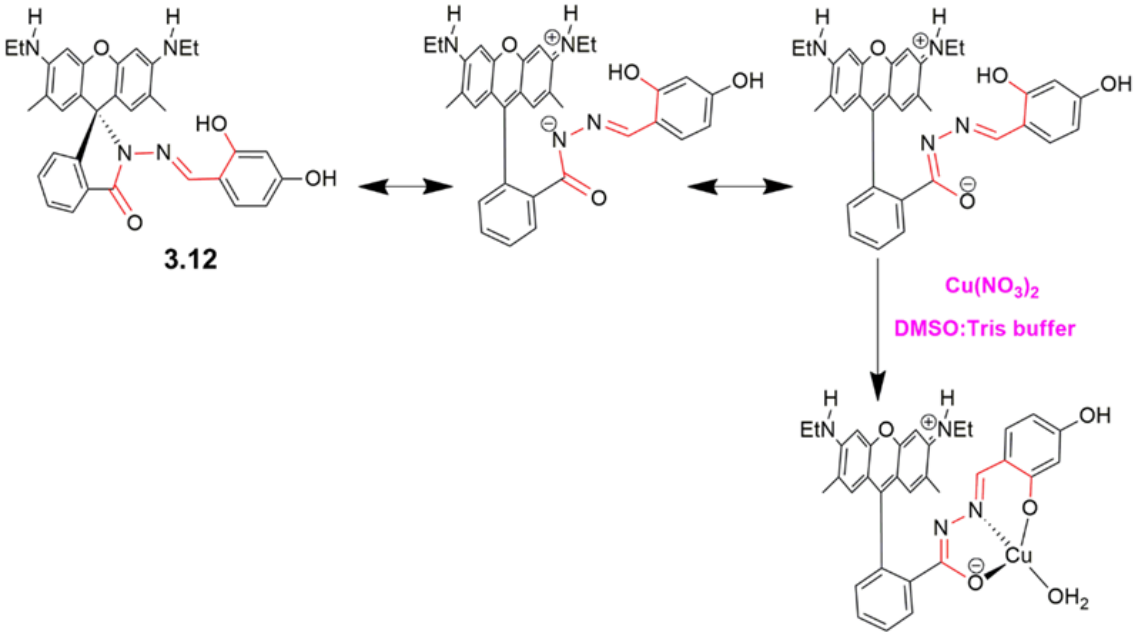

Scheme 3.13 *Proposed binding between* ***3.12*** *and* Cu^{2+} *ions in aqueous solution.*

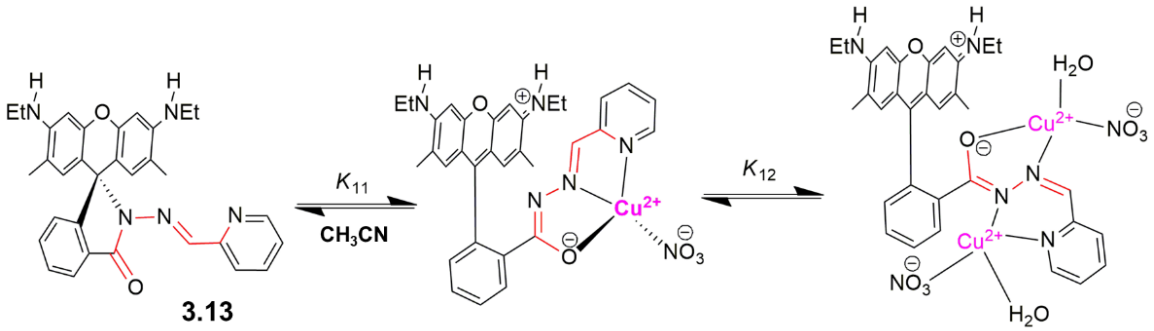

Scheme 3.14 *Proposed binding between* ***3.13*** *and* Cu^{2+} *ions in* CH_3CN

Table 3.5 *Binding constants calculated for compound* ***3.12*** *with* $CuCl_2$ *in various solvent systems. The concentration of the Tris Buffer was 30 mM for each aqueous solution with pH = 7.5.*

Note: All Ka values are within 10% error

[3.12]	Solvent	K_a [Cu^{2+}:3.12]
2.5×10^{-5} M	DMSO	$K_{11} = 4.4 \times 10^5$
	DMSO: Tris 1:1	$K_{11} = 8.1 \times 10^5$ $K_{21} = 1.6 \times 10^4$
	DMSO: Tris 15:85	$K_{11} = 1.6 \times 10^6$
	DMSO: Tris 1:9	$K_{11} = 1.1 \times 10^6$

Competition Study Conducted with Compound **3.11a** in DMSO

The interference of competing metal ions was investigated by a competition experiment conducted with a series of 10μM solutions of compound **3.11a** in DMSO. Two equivalents of $Cu(NO_3)_2$ in DMSO were then added to each of the solutions of the probe followed by the addition of four equivalents of a competing metal ion. The only metals that result in a decrease in the absorbance band at 533nm are, Fe^{3+}, Fe^{2+}, Al^{3+} and Cr^{3+}

ions (figure 3.31). Interferences from iron species were to be expected as we have previously demonstrated that compound **3.11a** also forms coordination compounds with these metal ions (section 3.5.5). We postulate that interferences from these metal ions would be less pronounced under aqueous conditions due to hydrolysis reactions.

Even though the metal screens discussed in section 3.5.5 (figure 3.19) did not display any interactions between compound **3.11a** and Al^{3+} and Cr^{3+} ions, it is likely that due to the high concentration of these hard lewis acids, in comparison to the concentration of the receptor molecules and Cu^{2+} ions, they were able to displace some of the Cu^{2+} ions from the receptor. It is also likely that the addition of these hard Lewis acids to the solutions of compound **3.11a** affected the pH of the solutions. Special attention should therefore be paid to ensure that the pH of the solution remains neutral. Despite the slight decreases observed in the absorbance intensity at 535nm, a notable absorbance band is still present, proving that compound **3.11a** functions efficiently for Cu^{2+} ion detection, even in the presence of competing metal ions**.**

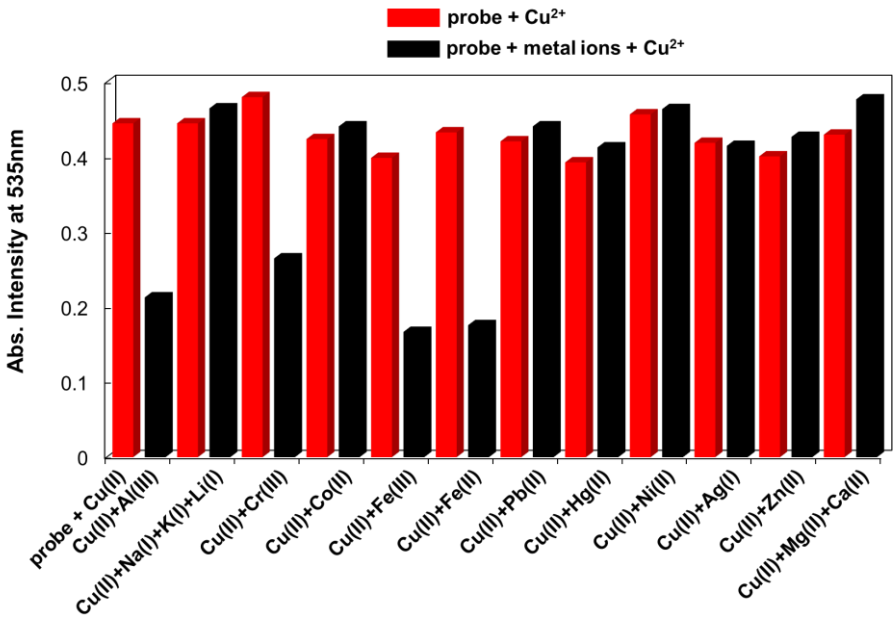

Figure 3.31 *Absorbance response of compound **3.11a** toward Cu^{2+} ions in the presence of various metal ions.*

Detection Limit of Compound **3.11a** for Cu^{2+} Ions

The limit of detection was determined by titrating a 10 mM solution of $Cu(NO_3)_2$ into a 10 µM solution of **3.11a** in DMSO. To determine limit of detection (LoD), the change in the intensity of absorbance band at 533 nm versus the concentration of Cu^{2+} was plotted. The method of least squares was then used to produce a line of regression (figure 3.32). Using a 95% confidence level, the LoD of **3.11a** for Cu^{2+} ions in DMSO was determined to be 3.0×10^{-7} M (19 ppb). In a solution of MES buffer-DMSO (1:1, v/v) , the LoD was found to be 1.65×10^{-6} M (0.1048 ppm) which is much lower than the allowable concentration of Cu^{2+} ions in drinking water of 1.3 ppm as outlined by the Environmental Protection Agency (see appendix A5 for spectra).[152]

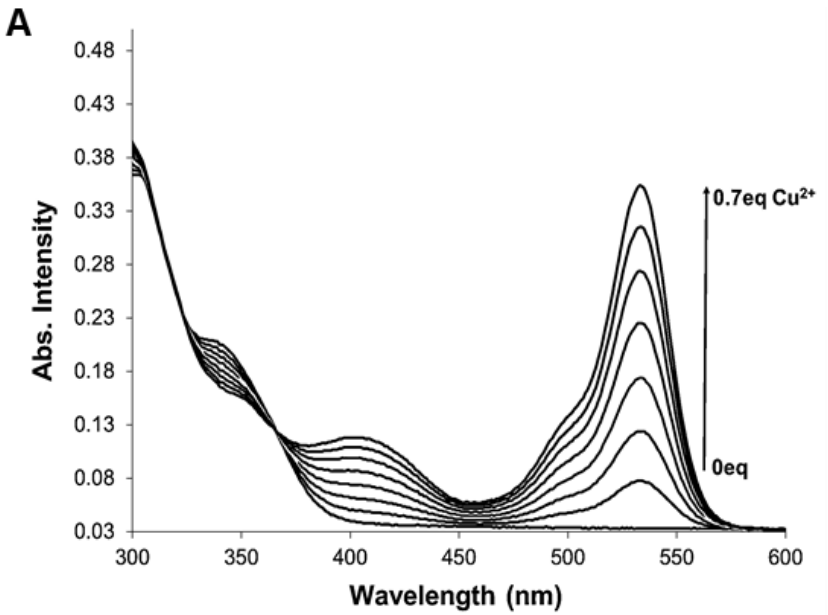
A
Abs. Intensity
Wavelength (nm)
0.7eq Cu2+
0eq
0.48
0.43
0.38
0.33
0.28
0.23
0.18
0.13
0.08
0.03
300
350
400
450
500
550
600

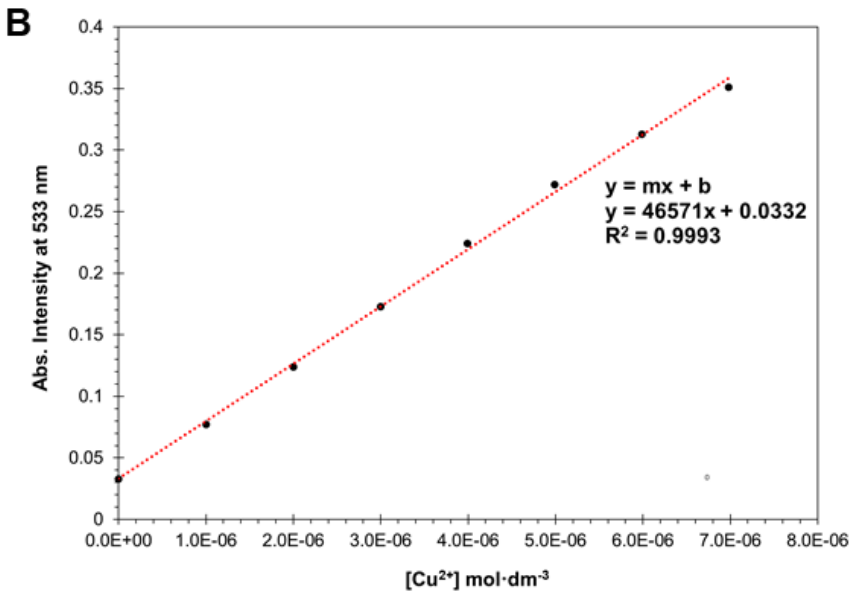
B
Abs. Intensity at 533 nm
[Cu2+] mol·dm-3
y = mx + b
y = 46571x + 0.0332
R2 = 0.9993
0.4
0.35
0.3
0.25
0.2
0.15
0.1
0.05
0
0.0E+00
1.0E-06
2.0E-06
3.0E-06
4.0E-06
5.0E-06
6.0E-06
7.0E-06
8.0E-06

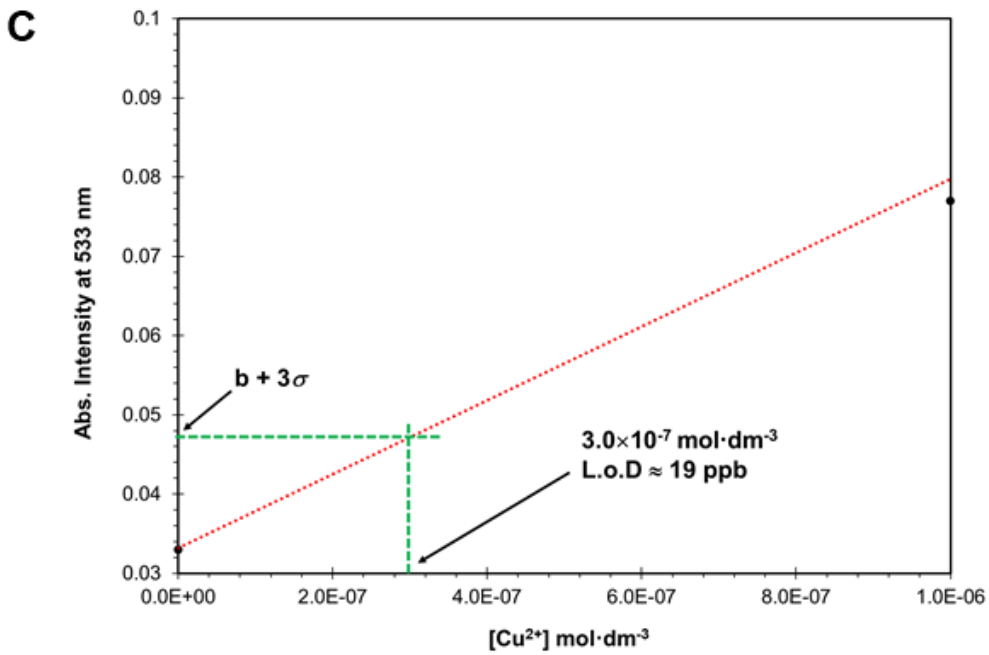

Figure 3.32 *(A) Absorbance data used for LoD calculation with compound **3.11a** (B) Calibration curve used to calculate the LoD for $Cu(NO_3)_2$ with **3.11a** in DMSO (C) Expansion of diagram B.*

Fluorescence Studies of Compound **3.11a** with $Cu(NO_3)_2$

The Cu^{2+} ion is notorious for forming non-fluorescent complexes with LMFPs in organic and aqueous solvents; this was demonstrated in compounds **3.4**, **3.5**, and **3.6** in section 3.2. Unfortunately, there is no way to guarantee what type of fluorescence mechanism will occur when a metal ion coordinates to a receptor. As a result of this, we conducted fluorescence studies to determine how the fluorescence of compound **3.11a** would be affected upon the addition of Cu^{2+} ions to a solution of the LMFP.

Initial fluorescence studies with 1.25×10^{-7} M solutions of compound **3.11a** displayed no fluorescence enhancements upon the addition of up to ten equivalents of Cu^{2+} ions to the solution of the receptor in CH_3CN. This led us to believe that compound **3.11a** would not be useful as a fluorescent sensor for Cu^{2+} ions. However, upon increasing the concentration of compound **3.11a** to 2.5×10^{-7} M, a 25-fold increase in the emission band centered at 548 nm was observed as up to 70 equivalents of $Cu(NO_3)_2$ were added to the solution (figure 3.33A-B). Further increasing the concentration of compound **3.11a** to 6.25×10^{-7} M resulted in more desirable results (figure 3.33C-D). At this concentration, a bathochromic shift from 548 nm to 563 nm was observed as well as 2,400-fold increase in the fluorescence of compound **3.11a**.

A comparison of the spectral data in figure 3.33 verifies that at lower concentrations of compound **3.11a**, a larger difference in the metal-ligand ratio is required to observe a fluorescence enhancement. This explains why no fluorescence enhancement was observed in the 1.25×10^{-7} M solution of compound **3.11a**, as a higher concentration of Cu^{2+} ions would have been required to induce the fluorescence turn on

mechanism. The association constants of the complexes formed in the 2.5×10^{-7} M solution of **3.11a** with Cu^{2+} ions were determined using non-linear regression analysis with bindfit software. The association constants for $[Cu(\mathbf{3.11a})]^{+}$ and $[Cu_2(\mathbf{3.11a})]^{3+}$ were 1.70×10^{5} M^{-1} and 3.59×10^{8} M^{-2}, respectively. The larger binding constant for the 1:2 probe-metal species is in agreement with the K_a values shown in table 3.4 and is the result of excess Cu^{2+} ions in solution as well as the ability of all four of the Lewis bases on the compound to participate in metal coordination

The ability of compound **3.11a** to serve as an off-ON fluorescence sensor was unexpected, as the formation of Cu^{2+} complexes often results in decreases in the fluorescence of otherwise fluorescent compounds (see section 3.1). As we have demonstrated thus far, compound **3.11a** is not entirely soluble in water. Because of this, we chose to limit the fluorescence studies to CH_3CN which serves as our solvent baseline. With the knowledge that we have gained regarding the selectivity, coordination environment, and optical behavior of **3.11a** towards Cu^{2+} ions, we plan to improve the water solubility of this LMFP up to 100%. In doing this we hope that we will be able to confidently perform fluorescence analysis in aqueous solutions with less concerns of interferences from aggregation.

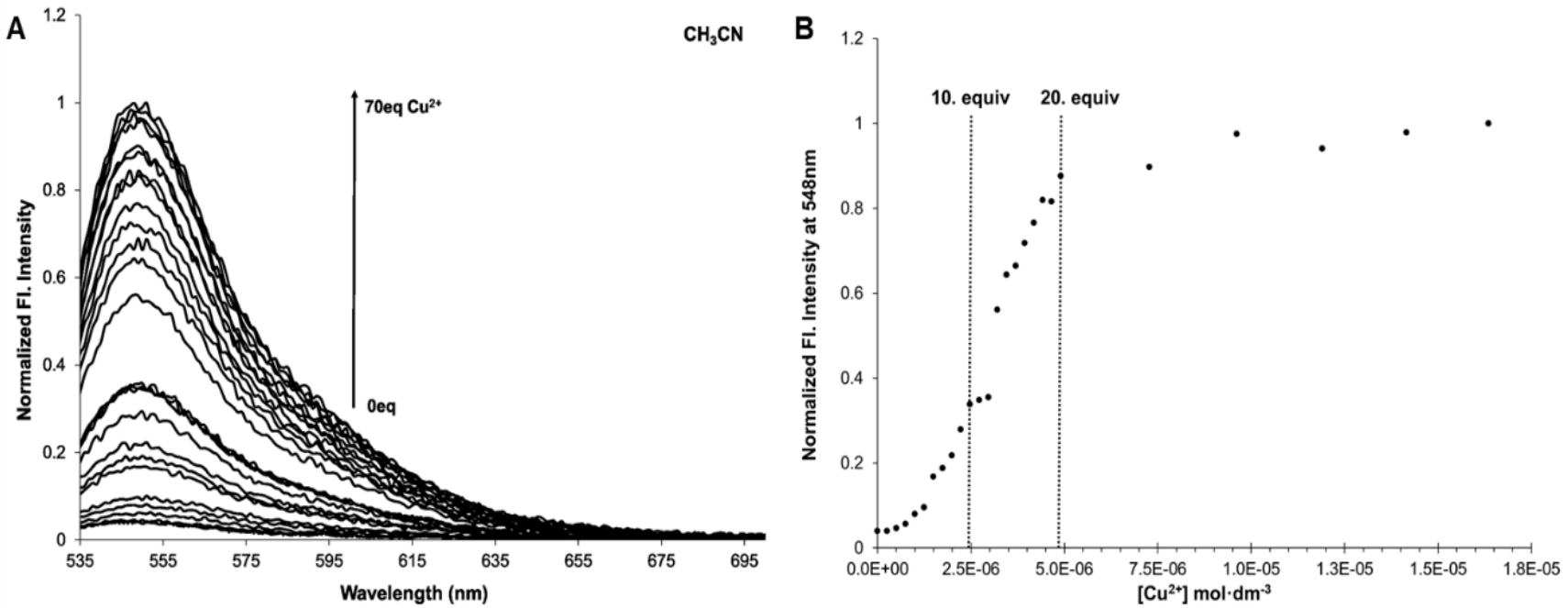
A
CH3CN
70eq Cu2+
0eq
Normalized Fl. Intensity
Wavelength (nm)
1.2
1
0.8
0.6
0.4
0.2
0
535
555
575
595
615
635
655
675
695
B
10. equiv
20. equiv
Normalized Fl. Intensity at 548nm
[Cu2+] mol·dm-3
0.0E+00
2.5E-06
5.0E-06
7.5E-06
1.0E-05
1.3E-05
1.5E-05
1.8E-05

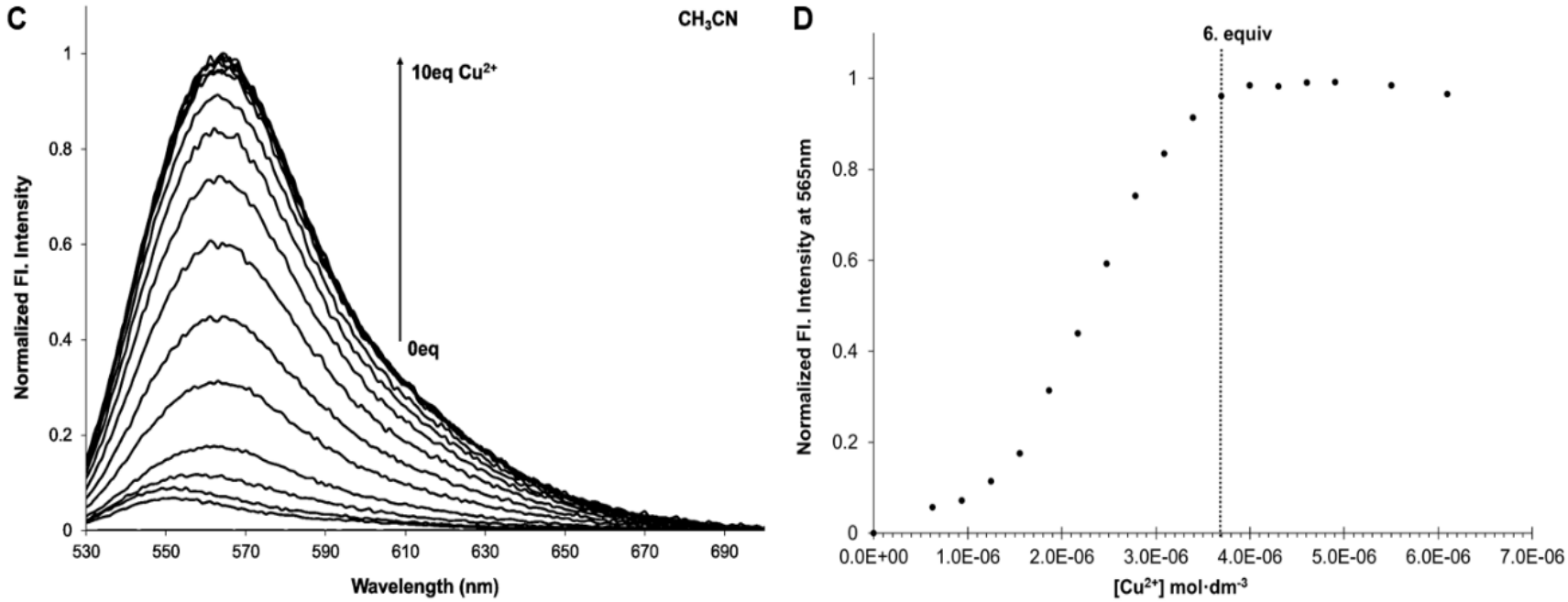

Figure 3.33 *Fluorescence plots and binding isotherms resulting from the titration of $Cu(NO_3)_2$ into (A) a 2.5×10^{-7} M solution of* ***3.11a*** *and (B) a 6.25×10^{-7} M solution of* ***3.11a*** *in CH_3CN*

Fluorescence Lifetime Study for Compound **3.11a** with Cu^{2+} Ions

The fluorescence decay profile of $[Cu(\mathbf{3.11a})]^{+}$ was analyzed to determine how the decay of this complex compared to the $[Fe(\mathbf{3.11a})]^{2+}$ complex discussed in section 3.5.5. We expected that the fluorescence lifetime of the Cu^{2+} complex would be notable different from that of the free probe and the Fe^{3+} complex.

To ensure that the results were as reliable as possible, all three samples were analyzed on the same day and at the same concentrations. The concentration of the receptor was maintained at 25 μM and the ratio of **3.11a** with $Cu(NO_3)_2$ was 1:2 The fluorescence decay plot was fitted to a single exponential with an excellent χ^2 value of 1.09. The sample was analyzed three times over the course of an hour to ensure reproducibility of the results. As stated in section 3.5.5, the protonated form of **3.11a** displays a fluorescence lifetime of 4.35 ± 0.063 ns, and the $[Fe(\mathbf{3.11a})]^{2+}$ complex remains in the excited state for 3.37±0.017 ns. In contrast, the coordination compound formed between **3.11a** and Cu^{2+} ions displays a fluorescence lifetime of 3.23±0.029 ns. As was previously stated, the formation of coordination compounds between compound **3.11a** and Fe^{3+} and Cu^{2+} ions decreases the fluorescence lifetime of the excited state of the probe. Furthermore, because both of the coordination complexes exhibit different fluorescence lifetimes, compound **3.11a** could be used to distinguish between the two metal ions in organic solvents. In aqueous solvents, only the Cu^{2+} complexes would be expected to display notable fluorescence lifetimes due to the hydrolysis reactions of Fe^{3+} ions.

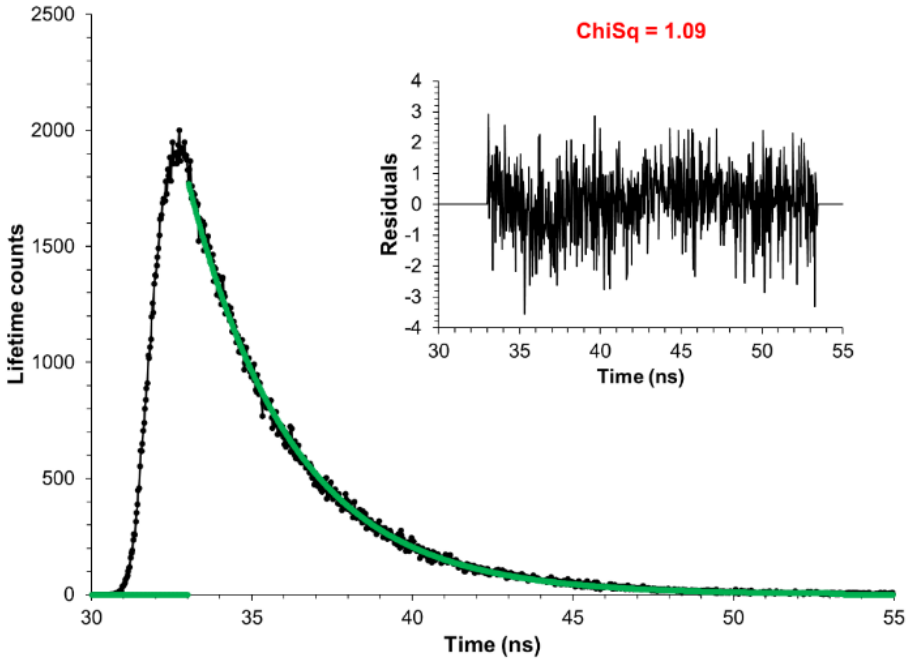

Figure 3.34 *Fluorescence decay of [**3.11a**-Cu^{2+}] in DMSO with residuals shown in inset*

3.6 Summary

Molecular probes **3.10**, **3.11a**, **3.12**, and **3.13** were synthesized as a small library of rhodamine 6G dyes for screening and detecting metal ions in a variety of solvent systems. Solid state, gas phase and solution- based techniques were investigated. The solution studies of compound **3.10** highlight the ability of oxygen containing solvents to inhibit the formation of coordination compounds. The weak binding between compound **3.10** and metal ions can be attributed to the coordination environment of the probe which acts as a bidentate ligand. By utilizing the chelate effect and adding an additional hard Lewis base to the coordination environment, the stability constants of the complexes formed improved drastically, allowing for metal analysis in a broad range of solvent systems.

The ESI-MS data verifies the formation of Cu^{2+} complexes between compounds **3.11a** and **3.13**. Analysis of the fragmentation patterns of the free receptor, **3.11a**, versus that of the coordination compound, highlights a change in the fragmentation pattern of the receptor once metal coordination has occurred. Furthermore, the ESI-MS highlights the retention of some counterions by the metal ion upon formation of the coordination compound. This observation can be attributed to the nature of the Cu^{2+} ion which typically coordinates to four donor ligands; coordination to six donor ligands is also common. Compound **3.11a** serves as a tridentate ligand, therefore the counterion serves as the fourth donor ligand.

Due to the paramagnetic nature of the Cu^{2+} and Fe^{3+} ions, FT-IR spectroscopy was used as a means of partially identifying which ligands were participating in metal coordination. The IR spectra of compound **3.11a** with $Fe(CF_3SO_3)_3$ served as a means of verifying that the oxygen of the lactam group is in fact involved in metal coordination. This was concluded due to the decrease in characteristic carbonyl peak at 1677 cm^{-1} upon the addition of the Fe^{3+} salt. Unfortunately, metal coordination to the other donor ligands could not be verified due to the triflate anion which displays very strong, broad peaks in the regions where additional metal coordination would be observed.

The optical studies of compounds **3.11a**, **3.12**, and **3.13** were integral in determining optimal conditions necessary for metal ion detection to occur. The absorbance and fluorescence studies between compound **3.11a** and Fe^{3+} ions supported our claims that Fe^{3+} ion detection is limited in aqueous environments due the hydrolysis reactions that these ions undergo. As a result, compound **3.11a** cannot be used for the detection of Fe^{3+} ions in solutions with high concentrations of water. We also determined

that the metal counterion has a direct effect on complex stability. Even though a color change was observed for all Fe^{3+} salts, no quantitative data was obtained for the chloride salt due to the presence of ill-defined species in solution. Despite this drawback, compound **3.11a** still shows promise as a useful molecular probe for detecting Fe^{3+} ions. The strong binding observed between various Fe^{3+} salts and **3.11a**, with K_a values as high as 1.37×10^9 M^{-1} for the 1:1 complex, the detection limits of 51.4 nM and 54.3 nM in CH_3CN and DMSO, respectively, and the bright fluorescence of the complex formed indicate that compound **3.11a** would be a useful candidate for bioimaging techniques involving the detection of Fe^{3+} ions.

As it was our goal, we were able to successfully demonstrate the aqueous applications of compounds **3.11a**, **3.12** and **3.13**. The presence of the alcohol group (**3.11a**) instead of a nitrogen group (**3.13**) at the 10' position demonstrated stronger binding interactions to Cu^{2+} ions in a range of aqueous solvent systems. Under aqueous conditions (DMSO-water, 1:1, v/v, pH 7), [Cu(**3.11a**)]$^+$ demonstrates a $K_a = 6.53 \times 10^7$ M^{-1}, which is larger than the K_a observed in 100% DMSO ($K_a = 2.05 \times 10^7$ M^{-1}). The LoD calculated was 19ppb in DMSO and 104.8 ppb in a solution of DMSO-MES buffer (1:1, v/v, pH = 6.5), both of which are much lower than the allowable concentration of Cu^{2+} ions in drinking water of 1.3ppm.[50] Furthermore, we proved that the addition of an alcohol group at the 12' position (**3.12**) would improve sensor function under aqueous conditions. The [Cu(**3.12**)]$^+$ complex demonstrated consistent stability constants of $\log\beta \approx 6$ in organic and aqueous solutions containing up to 90% water, whereas the stability of [Cu(**3.11a**)]$^+$ decreased notably under similar conditions. Lastly, we demonstrated the fluorescence capabilities of **3.11a** toward Cu^{2+} ions, as the addition of the metal salt to a

solution of the probe in CH_3CN resulted in a a 2,400-fold fluorescence increase. We then determined the fluorescence lifetime of [Cu(**3.11a**)]$^+$ to be 3.23±0.0293 ns which is easily distinguishable from the lifetime of the free probe.

3.7 Experimental Methods

3.7.1 General Experimental Conditions

All spectra reported in this text were collected at ambient temperature, unless otherwise stated. All reagents and chemicals, unless otherwise stated, were utilized as purchased from Sigma-Aldrich or Alfa Aesar. Proton and carbon-13 1D NMR spectra were recorded on a Bruker Ultrashield Plus 400MHz spectrometer in the appropriate deuterated solvents. Chemical shifts are reported in parts per million (ppm), relative to tetramethylsilane (0 ppm), which is the internal standard. Mass spectrometry studies were conducted using a Thermo Fisher LXQ quadruple mass spectrometer. Infrared spectra were recorded on a Nicolet Nexus 470 FT-IR spectrometer. The fluorescence emission spectra were collected on a Horiba PTI QuantaMaster 400 with slit widths set to 0.50 mm, unless otherwise stated, and the UV-vis spectra were recorded on a Thermo Scientific Evolution 220 spectrometer. The pH of the solutions used in optical studies were recorded using a Fisherbrand accumet XL150 pH benchtop meter. Fluorescence lifetime studies were carried out using a Horiba Deltaflex time correlated single photon counting (TCSPC) system fitted with picosecond detection modules.

3.7.2 Mass Spectrometry Methods

Samples were prepared in HPLC grade acetonitrile at 1.0 $mg \cdot mL^{-1}$. Solutions of the free ligand were spiked with 0.1% trifluoroacetic acid prior to injection of the sample into the instrument. The coordination compounds of **3.11a** and **3.13** were prepared in 1:1 and 2:1 ratios of the metal to ligand and allowed to equilibrate for two hours prior sample to analysis. Data was acquired in both the positive and negative ion mode.

3.7.3 UV-Vis and Fluorescence Methods

For the absorbance titration studies, 2.5 mM stock solutions of compounds **3.10**, **3.11a-b**, **3.12**, and **3.13** were prepared by dissolving the appropriate mg amount of each compound in 4 mL of the selected solvent system. Equimolar stock solutions (2.5 mM) of each metal salt were also prepared. To prepare the 25 µM solutions of the receptor, a 20 µL aliquot of the stock solution was added to a quartz cuvette containing 1.98 mL of solvent. During the titration, aliquots of 2 µL of the stock solutions of Cu^{2+} or Fe^{3+} salts were then added to the cuvette containing the receptor. The samples were stirred using a vortex for 1 minute between each addition of metal salt and the spectra were recorded after each addition.

For the metal screens, a series of 25 µM solutions of the compounds **3.10**, **3.11a-b**, **3.12**, and **3.13** were prepared exactly as was mentioned above. To these solutions were added aliquots of 40 µL of the 2.5 mM stock solutions of the metal salts. Each of the samples were allowed to equilibrate for 30 minutes prior to analysis of the absorbance spectra.

For the fluorescence emission studies, 12.5 µM stock solutions of compound **3.11a** were prepared by diluting 20 µL of the 2.5 mM stock solutions used in the absorbance studies, with 3.98 mL of the selected solvent system. To prepare the 0.125 µM solutions of the receptor, a 20 µL aliquot of the stock solution was added to a quartz cuvette containing 1.98 mL of solvent. During the titrations, aliquots of 2 µL of the stock solutions of Fe^{3+} salts were then added to the cuvette containing the receptor. The samples were stirred using a vortex for 2-3 minute between each addition of metal salt and the spectra were recorded after each addition. Longer stirring times were required due to the extremely low concentration of the receptor molecules and metal ions in solution which require longer time to reach equilibrium. The metal screens were carried out by adding 40 equivalents of each metal salt to a 0.125 µM solution of compound **3.11a** in the appropriate solvent system. The solutions were allowed to equilibrate for 1 hour prior to being analyzed.

3.7.4 Synthetic Methods

*Preparation of rhodamine 6G hydrazide (compound **3.9**)* [149]

Compound **3.9** was synthesized by a process similar to work published by Xiang et al.[149] Rhodamine 6G (1.0 g, 2 mmol) was added to a 100 ml round bottom flask followed by the addition of 25 mL of methanol. Excess hydrazine hydrate (64%, 1.53g, 30 mmol) was then added dropwise to the solution of rhodamine 6G over a ten-minute period while the solution stirred. The solution was allowed to reflux for 4 hours, after which a pink precipitate formed. The solvent was then removed under reduced pressure and the resultant precipitate was filtered and washed with cold water then dried in a

desiccator overnight, yielding rhodamine 6G hydrazide as a light pink powder (0.8586 g, yield 85%). The results of the NMR analysis are in agreement with literature values.[1]H NMR (400 MHz, $CDCl_3$) δ (ppm): 7.98 - 7.95 (1H, m), 7.46 (2H, td, J=2.4, 3.9 Hz), 7.08 - 7.05 (1H, m), 6.39 (2H, s), 6.26 (2H, d, J=0.5 Hz), 3.58 (2H, s), 3.52 (2H, t, J=4.5 Hz), 3.22 (4H, td, J=6.8, 10.9 Hz), 1.92 (6H, s), 1.32 (6H, t, J=7.1 Hz). ^{13}C NMR (100 MHz, $CDCl_3$) 166.2, 152.2, 151.8 ,147.5, 132.6, 129.9, 128.,1 127.7, 123.8, 123.0, 118.0, 104.9, 96.8, 77.4, 77.3, 77.1, 76.8, 66.0, 38.4, 16.7, 14.8.

*General procedure for preparation of compounds **3.10**, **3.11a**, **3.12**, **3.13***

To a solution of compound **3.9** (0.125g, 0.29 mmol) in methanol (15ml) was added 2 equivalents of the appropriate aldehyde (0.58 mmol). The mixture was then refluxed for 6 hours. The solvent was reduced to ≈ 20% under reduced pressure and the resultant solid was filtered and washed with diethyl ether (3 × 20 mL). The precipitate was dried in a desiccator overnight to afford the desired LMFPs in 80-90% yields

Characterization of **3.10**

Lavender powder. ^{1}H NMR (400 MHz, DMSO) δ (ppm): 8.67 (1H, s), 7.90 (1H, d, J=7.0 Hz), 7.62 - 7.54 (2H, m), 7.39 (2H, m), 7.34 (3H, m), 7.04 (1H, d, J=7.5 Hz), 6.33 (2H, s), 6.17 (2H, s), 5.06 (2H, t, J=5.3 Hz), 3.17 - 3.08 (4H, m), 1.83 (6H, s), 1.20 (6H, t, J=7.0 Hz). ^{13}C NMR (100 MHz, $CDCl_3$) δ (ppm): 165.2, 152.3, 151.3, 147.6, 146.5, 135.2, 133.4, 129.6, 128.7, 128.2, 127.7, 127.5, 123.7, 123.4, 118.0, 106.3, 96.7, 77.4, 77.0, 76.7, 65.8, 38.4, 16.7, 14.8. IR(ATR solid) 3440 ν_{N-H} (m), 3024, 2968, 2865 ν_{C-H} (m), 1718 $\nu_{C=O}$ lactam (vs). ESI mass spectrometry: m/z 517.0 $([M + H]^+)$; M^+ calculated 516.2. See appendix for spectra.

Characterization of **3.11a**

Light pink powder ^{1}H NMR (400 MHz, $CDCl_3$) δ (ppm): 10.88 (1H, s), 9.11 (1H, s), 8.01 - 7.99 (1H, m), 7.54 - 7.50 (2H, m), 7.18 - 7.11 (2H, m), 7.07 (1H, dd, J=1.5, 7.6 Hz), 6.85 (1H, d, J=8.2 Hz), 6.77 (1H, dt, J=0.9, 11.3 Hz), 6.43 (2H, s), 6.29 (2H, s), 3.50 (2H, s), 3.21 (4H, q, J=7.1 Hz), 1.88 (6H, s), 1.31 (6H, t, J=7.1 Hz). ^{13}C NMR (100 MHz, $CDCl_3$) δ (ppm): 164.3, 158.6, 152.3, 151.8, 151.2, 147.7, 133.6, 131.4, 131.2, 129.7, 128.6, 127.8, 124.1, 123.3, 118.9, 118.5, 118.1, 117.0, 105.6, 96.8, 66.4, 38.3, 16.6, 14.73. IR(ATR solid) 3405 ν_{N-H} (m), 2955 ν_{C-H} (m), 1678 $\nu_{C=O}$ (vs) lactam. ESI mass spectrometry: m/z 533.3 ($[M + H]^+$); M^+ calculated 532.3.

Characterization of **3.12**

Light pink powder. ^{1}H NMR (400 MHz, DMSO): δ, ppm 10.68 (1H, s), 9.94 (1H, s), 8.86 (1H, s), 7.87 (1H, dd, J = 2.2, 6.6 Hz), 7.56 (2H, dtd, J = 7.5, 7.9, 6.2 Hz), 7.04 - 7.01 (2H, m), 6.28 (2H, s), 6.24 (1H, dd, J = 2.2, 8.4 Hz), 6.15 (2H, s), 6.13 (1H, d, J = 2.4 Hz), 5.07 (2H, t, J = 5.4 Hz), 3.11 (4H, td, J = 6.2, 14.1 Hz), 1.83 (6H, s), 1.18 (6H, t, J= 7.2 Hz). ^{13}C NMR (100 MHz, DMSO) 163.6, 161.5, 159.9, 151.9, 151.7, 151.5, 148.3, 134.1, 132.2, 129.3, 129.2, 127.4, 124.2, 123.4, 118.8, 111.0, 108.3, 104.8, 103.1, 96.2, 66.0, 37.9, 17.5, 14.6 IR(ATR solid) 3405 ν_{N-H} (m), 3336 ν_{O-H} (m), 2972, 2888 ν_{C-H} (m), 1671 $\nu_{C=O}$ (vs) lactam. HRMS: m/z 549.248982 ($[M + H]^+$); M^+ calculated 548.2.

Characterization of **3.13**

Light pink solid. ^{1}H NMR (400 MHz, $CDCl_3$) δ (ppm): 8.45 (1H, qd, J=1.0, 4.7 Hz), 8.24 (1H, s), 8.05 - 8.03 (1H, m), 8.01 (1H, td, J=1.0, 8.1 Hz), 7.59 (1H, dt, J=1.2, 8.0 Hz), 7.47 (2H, qd, J=2.1, 6.4 Hz), 7.12 (1H, qd, J=2.0, 7.4 Hz), 7.07 - 7.04 (1H, m), 6.41 (2H, s), 6.35 (2H, s), 3.48 (2H, s), 3.21 (4H, dd, J=3.3, 6.8 Hz), 1.87 (6H, s), 1.31 (6H, t, J=7.1

Hz). ^{13}C NMR (100 MHz, $CDCl_3$) δ (ppm): 165.6, 154.5, 152.8, 151.1, 149.0, 147.6, 145.4, 136.1, 133.9, 128.3, 127.7, 127.3, 123.7, 123.6, 120.6, 118.0, 105.8, 97., 65.7, 38.3, 16.7, 14.8. IR(ATR solid) 3442 ν_{N-H} (m), 3010 ν_{C-H} (w), 2967 ν_{C-H} (m), 1719 $\nu_{C=O}$ (vs) lactam. ESI mass spectrometry: m/z 518.3 ($[M + H]^+$); M^+ calculated 517.3

CHAPTER IV – Water soluble Cu^{2+} probe

4.1 Introduction

A significant disadvantage of the probes discussed in chapters 2 and 3 are their low water solubility. All of the studies performed with compound **2.4** were carried out exclusively in CH_3CN due to the poor probe solubility as well as an inability to measure Fe^{3+} ion concentrations in aqueous solvent systems. In order to utilize our probes in biological and environmental systems, it is important to design sensors that function well in aqueous environments. Another disadvantage of the pyrene-based sensor is that its absorption and emission bands are in the UV- region, and even though the excimer band occurs at a longer wavelength (420- 490 nm), the excitation wavelength used to view the excimer band is still very low (350 nm) and is therefore harmful to cells. Molecular probes used in different cell studies should have high excitation wavelengths in the visible to near infrared region (>600 nm) to minimize photodamage to biological samples as well as interference from the background autofluorescence of biomolecules in living systems.[131]

The transition to rhodamine-based chromophores resulted in the ability to precisely measure dilute concentrations (ppm) of Cu^{2+} ions in solutions comprised of up to 90% water. However, as the concentration of water in the systems increased, the probe functions were adversely affected. Furthermore, organic solvents, which can be toxic to biological samples, were still required to dissolve the probes prior to carrying out solution studies. Because rhodamine dyes display fluorescence signals in the visible range, we have decided to continue to utilize this family of chromophores in our molecular probe design. This section will focus on the synthesis of a water-soluble molecular probe that is

selective for Cu^{2+} ions. The importance of Cu^{2+} ions ion living organisms was highlighted in chapter 1. These ions play several key roles in enzymes along with functions in redox reactions, and are also incorporated into a number of metalloenzymes involved in hemoglobin formation, carbohydrate metabolism, and cross-linking of collagen, elastin, and hair keratin.[44] However, an excess of Cu^{2+} ions can lead to the generation of reactive oxygen species (ROS) which are harmful to organs. Prolonged exposure to these ROS can result in hemolysis and jaundice, convulsions, hypotension, cirrhosis of the liver, Wilson's disease, and Alzheimer's disease.[50]. It is therefore important to synthesize molecular probes that are capable of selectively detecting Cu^{2+} ions, without causing harm to cells.

4.2 Literature Examples of Water Soluble LMFPs for Cu^{2+} ion Detection

There are many examples of Cu^{2+} optical probes in the literature, however the vast majority of these compounds must initially be dissolved in organic solvent prior to the introduction of water to the solution and many of these probes are often not selective for Cu^{2+} ions alone. Furthermore, many of the sensors reported in the literature only serve as colorimetric sensors for Cu^{2+} ions due to the paramagnetic nature of the metal ion which leads to fluorescence quenching. This t limits the sensitivity of the molecular probes as steady state fluorescence techniques typically allow for lower analyte concentration analysis and quantification.

Raju and coworkers synthesized a rhodamine 6G- dihydroeruginoic acid derivative capable of detecting Cu^{2+} and Zn^{2+} ions via colorimetric and fluorescence techniques, respectively, in 100% HEPES buffer at pH 7.4 (scheme 4.1).[153] The addition

of Cu^{2+} ions to a HEPES buffered solution of compound **4.1** displayed a color change from colorless to pink along with a hyperchromic shift at 525 nm. No other metal ions that were analyzed in this solvent system resulted in any observable color change nor a change in the absorbance band at 525 nm. Jobs plot analysis was used to verify a 1:1 binding stoichiometry between compound **4.1** and Cu^{2+} ions, and an association constant of $0.6 \times 10^5\ M^{-1}$ was determined using a non-linear fit of the absorbance intensity versus the ratio equivalents of [Cu^{2+}] to [**4.1**].

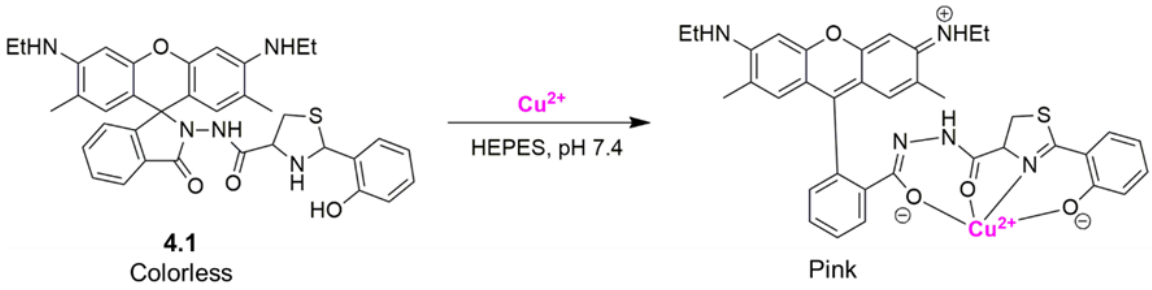

Scheme 4.1 *The proposed binding between **4.1** and Cu^{2+} ions in 100% HEPES buffer (pH 7.4)*

The limit of detection of compound **4.1** for Cu^{2+} ions was calculated as 37 nM (2.35 ppb), which is much lower than the allowable Cu^{2+} ion concentration in drinking water of 1.3 ppm.[152] Electrospray ionization mass spectrometry was also used to verify the formation of the [Cu(**4.1**)(H_2O) + Na^+] adduct, m/z = 737.2, which supports the 1:1 stoichiometry observed in the absorbance titration data. Additionally, FTIR-ATR analysis displayed a shift in wavenumber from 1703 cm^{-1} to 1637 cm^{-1} was observed upon the formation of the [Cu(**4.1**)]$^+$ complex. An observation similar to this was reported in section 3.5.4 to highlight the formation of a coordination compound between compound **3.11a** and $Fe(CF_3SO_3)_3$, whereby a noticeable decrease in the IR stretch attributed to the

carbonyl of the lactam group was observed. Like many of the Cu^{2+} ion sensors reported in the literature, no notable fluorescence was observed in compound **4.1** in the presence of Cu^{2+} ions. A fluorescence enhancement was however observed for Zn^{2+} ions due to the acid induced, amide bond cleavage, resulting in the ring open rhodamine 6G hydrazide moiety. Due to the water solubility and dual metal detection capabilities of compound **4.1**, Raju and coworkers were able to use this molecular probe to analyze the concentrations of Cu^{2+} and Zn^{2+} in various water samples with high accuracy as well as monitor Zn^{2+} ions in live shrimp.

A rhodamine B- thiosemicarbazide derivative (compound **4.2**) was synthesized by Zhao et al. for the selective detection of Cu^{2+} ions in aqueous solution via colorimetric and fluorometric methods.[150] In a mixture of MeOH-water (30:70, v/v), compound **4.2** appears clear in solution and does not exhibit any fluorescence or absorbance in the visible region. The addition of Cu^{2+} ions to a solution of the sensor resulted in a hyperchromic shifts in the absorbance band at 565 nm, owing to the ring opening mechanism which occurs when the probe coordinates to a target analyte. None of the other metals that were analyzed resulted in any notable spectroscopic changes. It is however important to note that the only other metal ions that were Ag^{+}, Cd^{2+}, Mg^{2+}, Mn^{2+}, Ni^{2+}, Pb^{2+}, Zn^{2+}, and Cr^{3+}. It is likely that iron species were not explored due to the possibility of the onset of hydrolysis reactions in aqueous media, however, sensors that bind Cu^{2+} ions often also bind to Hg^{2+} ions, depending on the solvent system; this dual nature of LMFPs was demonstrated in chapter 3 of this work. Therefore, we cannot rule out the possibility that compound **4.2** might also bind to other metals such as Hg^{2+} ions.

This is reasonable as the molecular probe does contain a sulfur atom which is well known for binding Hg^{2+} ions.

Scheme 4.2 *The proposed binding between* ***4.2*** *and* Cu^{2+} *ions in a solution of* CH_3CN *and water (30:70, v/v, pH 7.0).*

Job's plot analysis was used by the researchers to determine the stoichiometry between compound **4.2** and Cu^{2+} ions, which was found to be 1:1. It is however possible that there are 1:2 ligand-metal complexes present in solution as the nitrogen atoms in the coordination environment of **4.2** are also capable on binding to Cu^{2+} ions (see chapter 3). A non-linear fitting of the absorbance titration curve was used to calculate a binding constant of 2.7×10^5 M^{-1}, which is about one magnitude lower than the binding constant highlighted in table 3.4 for the [Cu(**3.12**)]$^+$ complex in solution of Tris (30mM)-DMSO (90:10, v/v, pH 7.5). From the absorbance titration data, a LoD of 0.078 µM was calculated in the 30% MeOH solution. The fluorescence capabilities of compound **4.2** were also explored. In contrast to many other literature examples, the spectroscopic analysis of compound **4.2** were carried out in a range of solvent systems, namely, water (70%), MeOH, EtOH, $(CH_3)_2CO$, CH_3CN, and DMF, to determine how each of the solvents affected the absorbance and fluorescence spectra of the molecular probe in the presence of Cu^{2+} ions. In each of the abovementioned solvent systems a notable

spectroscopic change was observed, however, the most drastic increases in the absorbance and fluorescence spectra were observed in CH_3CN and MeOH. In the absorbance studies, MeOH proved to be the best solvent, whereas the fluorescence enhancement in CH_3CN was greater than two times the fluorescence increase observed when MeOH was used as the solvent. As a result, the fluorescence analyses were carried out in a mix of CH_3CN-water (30:70, v/v, pH 7.0). The addition of Cu^{2+} ions to a solution of compound **4.2** resulted in a hyperchromic shift at 578 nm, which accounts for a relatively narrow stokes shift of 13 nm. None of the other metals that were screened resulted in a florescence enhancement. From the fluorescence titration data, a LoD of 0.041 µM was determined for Cu^{2+} ions. Despite the high selectivity of this compound **4.2** towards Cu^{2+} ions in aqueous media, the need to initially dissolve the probe in organic solvent prior to analysis limits the use of the probe. Furthermore, a more thorough metal screen should be performed to verify that no other biologically relevant metal ions induce spectroscopic changes within the molecular probe.

Two boronic acid containing molecular probes were synthesized by Swamy et al. for Cu^{2+} ion detection in aqueous solution.[154] Compound **4.3** is a rhodamine B-monoboronic acid derivate, whereas compound **4.4** utilizes the fluorescein chromophore and two boronic acid groups. Despite the similarities between the fluorescein and rhodamine B chromophores, the fluorescence responses observed in the two molecular probes are very different. Compound **4.3** serves as an off-ON colorimetric and fluorescent sensor for Cu^{2+} ions in 20mM HEPES buffer at pH 7.4 (0.5% CH_3CN), whereas the coordination of Cu^{2+} ions to compound **4.4** induces a photoinduced electron

transfer (PET) mechanism through the lone pair of electrons on the tertiary amine, resulting in fluorescence quenching.

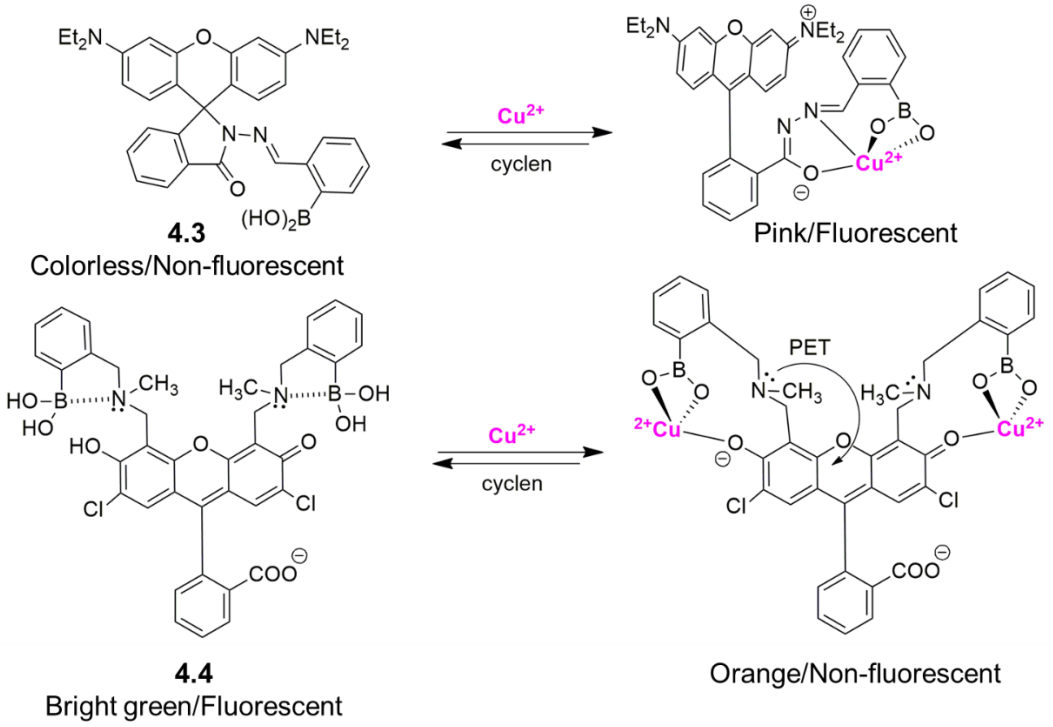

Scheme 4.3 *The Proposed binding between two different boronic acid derivatives (**4.3** and **4.4**) and Cu^{2+} ions in 95% HEPES buffer (20mM).*

The addition of Cu^{2+} ions to the solution of compound **4.3** resulted in the appearance of a new absorbance band at 556 nm and an emission band at 572 nm. The stoichiometry of the complex was determined by a Job's plot to be 1:1 and the association constant was calculated to be 2.8×10^3 M^{-1} based on the results of the fluorescence titration experiment. This K_a value is relatively weak when compared to the other association constants for Cu^{2+} ion probes highlighted in this work. Other metals such as Ag^+, K^+, Li^+, Na^+, Rb^+, Ca^{2+}, Cd^{2+}, Co^{2+}, Cs^{2+}, Mg^{2+}, Mn^{2+}, Ni^{2+}, Hg^{2+}, Sr^{2+}, and Zn^{2+} did not result in any colorimetric or fluorescence changes in compound **4.3**. It is unclear why Al^{3+} and Pb^{2+} ions were not investigated as they are also biologically and

environmentally relevant metals. The hydroxyl groups serve as hard Lewis base which could potentially coordinate to the hard Al^{3+} ion and the borderline Pb^{2+} ion.

A control study with pyrene boronic acid was performed to determine the role of the boronic acid moiety in metal binding. The introduction of Cu^{2+} ions to the pyrene sensor displayed a strong excimer band due to the stacking between pyrene rings as a result of coordination to Cu^{2+} ions. This verified that the coordination to Cu^{2+} ions does in fact occur through the boronic acid groups. In contrast to compound **4.3**, compound **4.4** displays 1:2 binding between the probe and Cu^{2+} ions in the 20mM HEPES buffer solution. No colorimetric analysis of was carried out on compound **4.4** to determine how different metal ions affect the absorbance of the free probe ,however, a fluorescence metal screen was performed and highlights a hypochromic shift around 525 nm when Cu^{2+} ions are introduced to the solution of the sensor. No other metal ions displayed this behavior.

From the fluorescence titration of Cu^{2+} ions into compound **4.4,** an association constant of 8.4×10^6 M^{-2} was determined. It is interesting that the K_a reported for compound **4.3** was lower the association constant for compound **4.4** with Cu^{2+} ions. Compound **4.3** is postulated to behave as a tetradentate ligand which should result in a more stable complex than compound **4.4** which behaves as a tridentate ligand. It is possible that the coordination environment of compound **4.4** adopts a more optimal geometry than **4.3**, which minimizes bond angle strain and yields a more stable complex. Despite the higher complex stability observed in **4.4**, compound **4.3** was used as a fluorescent sensor to image Cu^{2+} ions in zebrafish. Compound **4.3** was able to detect the

presence of Cu^{2+} ions in zebrafish that were incubated with external Cu^{2+} ions as well as those that were not exposed to external Cu^{2+} ions.

An off-ON colorimetric and fluorescent molecular probe capable of detecting Cu^{2+} ions in aqueous environments was synthesized by Yu at al.[155] Compound **4.5** was synthesized for use in solutions composed of mostly water, however, when the content of water in the solution of the sample exceeded 20% (v/v), the fluorescence and colorimetric responses of the sensor towards Cu^{2+} ions decreased drastically. In solutions containing greater than 50% water (v/v) virtually no optical responses were observed. As a result, all of the metal studies conducted with **4.5** were performed in solutions of 20mM HEPES-MeOH (20:80, v/v, pH 6). Of the metals that were screened via colorimetric analysis, namely, Ag^{+}, Na^{+}, Cd^{2+}, Cu^{2+}, Ni^{2+}, Pb^{2+}, Zn^{2+}, and Fe^{3+} ions, only the Cu^{2+} ion resulted in a color change from colorless to pink, which was accompanied by a hyperchromic shift in the absorbance spectrum at 550 nm. The metal screen should however be extended to include metals ions such as Al^{3+}, Cr^{3+} ions as well as group 1 and 2 metals to rule out any interactions that may occur between these ions and compound **4.5**.

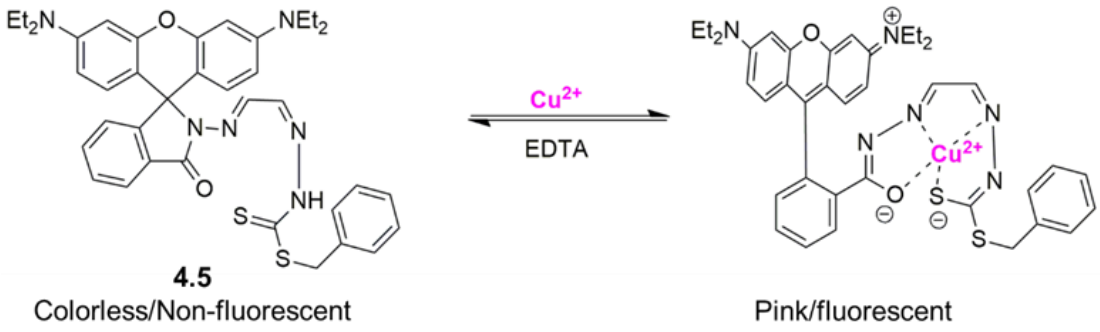

Scheme 4.4 *Proposed binding between compound* ***4.5*** *and* Cu^{2+} *ions in aqueous media*

The method of continuous variation was used to determine the stoichiometry between **4.5** and Cu^{2+} ions, which was found to be 1:1. The formation of the 1:1 complex was also verified using the Benesi Hildebrand method as well as ESI-MS in which a strong signal accounting for the $[Cu(\mathbf{4.5})\text{-}H]^+$ was observed. Additionally, an association constant of $1.7 \times 10^5\ M^{-1}$ was calculated. This value is comparable to some of the other rhodamine sensors referenced in this chapter, however, it is important to note that the other sensors were analyzed in solutions containing much higher concentrations of water. Fluorometric analysis was also carried out which supports the observation that compound **4.5** is selective for Cu^{2+} ions. A 100-fold fluorescence enhancement was observed when 10 µM of Cu^{2+} ions were added to a 1.0 µM solution of **4.5**. No other metal ions displayed this large of an increase in the fluorescence spectra. Finally, competitions experiments were also carried out to determine if the addition of competing ions to a solution of the $[Cu(\mathbf{4.}5)]^+$ complex would affect the fluorescence of the complex. The results revealed that the Cu^{2+} induced fluorescence response was unaffected by the introduction of other metal ions. Though compound **4.5** is able to serve and a colorimetric and fluorescence molecular probe for Cu^{2+} ions, the low water solubility of the probe limits its applications in biological and environmental studies. The addition of more hydrophilic groups to the **4.5** may assist with improving the probes function in aqueous solutions.

4.2.2 Summary

Though the aforementioned LMFPs were able to demonstrate selectivity for Cu^{2+} ions in aqueous solutions, compounds **4.1** and **4.4** were still limited to use as colorimetric

sensors due to the fluorescence quenching abilities of the Cu^{2+} ion. Furthermore, compound **4.1** was the only sensor that was able to achieve 100% water solubility. All of the other Cu^{2+} probes required the use of an organic co-solvent to dissolve the compounds prior to spectroscopic analysis. The use of some organic solvents can be harmful to biological organisms; therefore, limits the applications of some of these probes. Another shortcoming of a number of the probes in the literature is the lack of a thorough metal screen which would prove if the sensor is in fact selective for one metal ion over others. Chapter 3 highlighted the multi-metal ion detection capabilities of molecular probes in various solvent systems. As a result of this, it is imperative to conduct thorough metal screen experiments in a range of solvent systems.

4.3 Hypothesis

The addition of a water solubilizing sulfonate group to molecular probe 3.11a can be used to improve the spectroscopic functions of the probe in aqueous environments as well as reduce the need to use harmful organic co-solvents when analyzing biological samples. The coordination environment of compound **3.11a** has already proven to be efficient for binding Cu^{2+} in a broad range of aqueous and organic systems. We want to determine whether the addition of the sulfonate group will alter the stoichiometry and stability of the complexes formed, as metal ions can also coordinate to the oxygen atoms on the sulfonate group. Additionally, we will need to study the fluorescence behavior of the probe to determine whether the compound will be able to maintain its fluorescence capabilities in aqueous systems. Lastly, we will analyze the

fluorescence decay profile of the water soluble LMFP and compare it to the decays of the other LMFPs reported in chapters 2 and 3 of this work.

4.4 Results and Discussion

4.4.1 General Synthesis and Characterization

Compound **4.6** was prepared by first synthesizing sodium 3-formyl-4-hydroxybenzenesulfonate via a multistep reaction between salicylaldehyde, aniline, and H_2SO_4. The product was isolated as a light tan solid in 50-60% yield. Proton NMR and FT-IR spectroscopy were used to confirm the conversion of salicylaldehyde to the sulfonate derivative. The FT-IR spectrum showed clear changes to the single bond region between 3100 cm^{-1} and 3400 cm^{-1}, accounting for the sulfonate group which is readily protonated. This IR spectrum is in agreement with reports of sodium hydroxybenzene sulfonate derivatives found in the spectral database for organic compounds (SDBS). Additionally, changes in the splitting patterns of the ^{1}H-NMR spectra were observed as well as the disappearance of one of the signals in the benzene region due to the position being occupied by the sulfonate group. In the salicylaldehyde molecule, two triplets appear at 6.94 and 7.50 ppm, respectively, and a doublet and doublet of doublets can be seen at 7.00 and 7.67 ppm, respectively. In contrast, the sulfonate derivative does not display any triplets and instead a doublet, is observed at 6.33 ppm and a doublet of doublets and doublet are observed at 7.28 and 7.57 ppm, respectively

A condensation reaction between the amine group (N2') on **3.9** and the aldehyde group of sodium 3-formyl-4-hydroxybenzenesulfonate was then carried out in a mixture of water and MeOH(20:80) and the desired molecular probe, **4.6,** was isolated as an

orange precipitate in 75% yield (scheme 4.5). The loss of the two protons from N2' around 4.23 ppm as well as the emergence of an imine signal (8') at 8.52 ppm in the ^{1}H-NMR spectrum verified the conversion from **3.9** to **4.6**. Probe **4.6** was then further analyzed via ^{13}C-NMR, FT-IR, and ESI-MS.

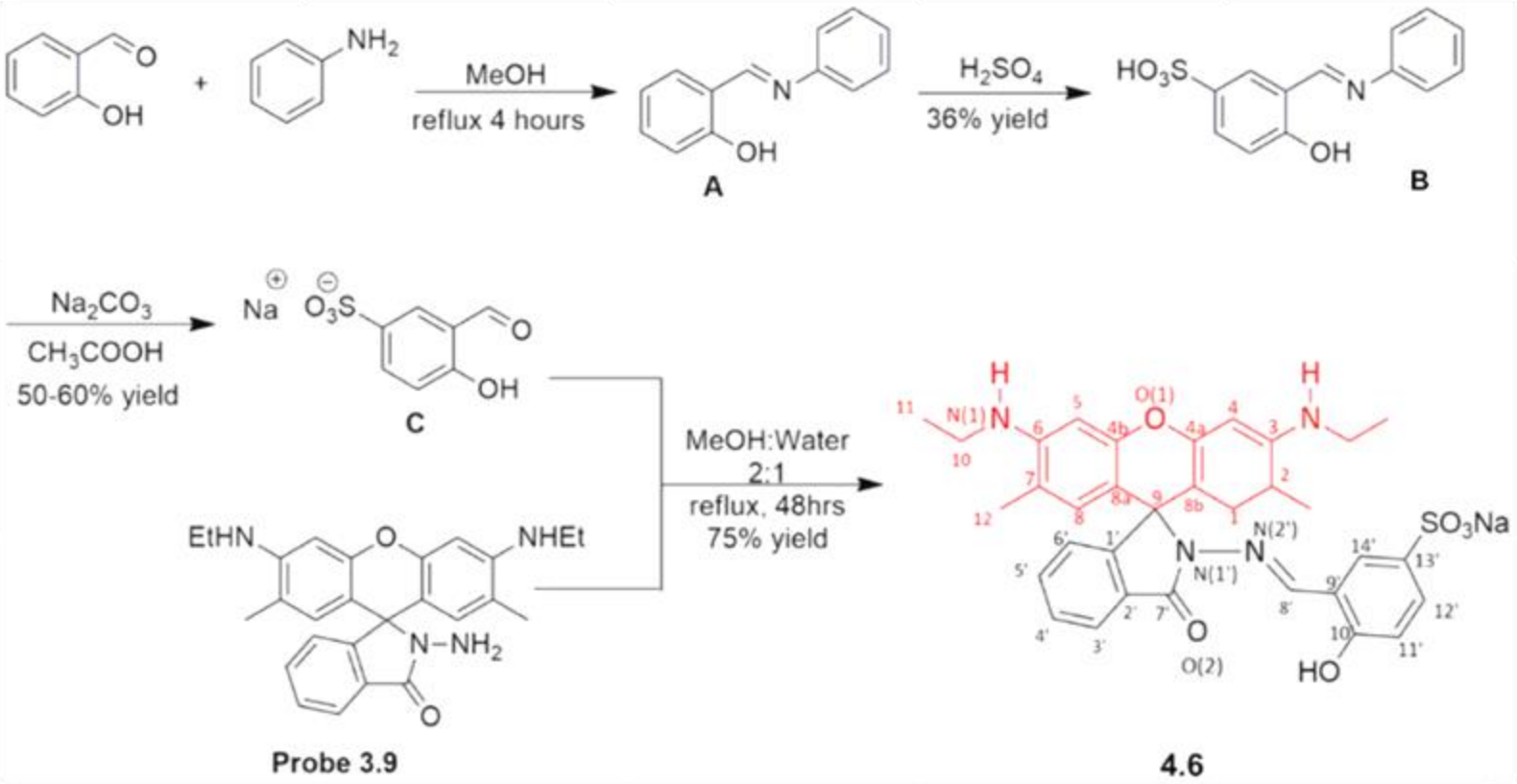

Scheme 4.5 *General synthesis of molecular probe* ***4.6***

4.4.2 Gas Phase Studies (ESI-MS)

The ESI-MS of compound **4.6** was obtained by dissolving the probe in HPLC grade MeOH. The signal observed at m/z = 611.0 in figure 4.1A accounts for the [**4.6** - Na]$^-$ species and was recorded in the negative mode, while the dimeric species [(**4.6**)$_2$ + Na + H]$^+$ is observed at m/z = 1246. The addition of one equivalent of $Cu(NO_3)_2$ to the solution of **4.6** resulted in the signal observed at m/z = 697.0 in figure 4.1B. The proposed species responsible for the m/z signal at 697.0 is [Cu(**4.6**) + H+ Na]$^+$. The species responsible for the m/z signals observed at 360.4 and 1033.0 have not been identified. The fragmentation pattern of the [Cu(**4.6**)] complex is shown in figure 4.1C and follows a pattern similar to [Cu(**3.11a**)]$^+$ (section 3.5.3). The fragmentation proceeds via the formation of two major daughter peaks at m/z = 681.2 and 412.2. The signal at m/z = 412.2 accounts for the initial loss of the Na^+ and Cu^{2+} cations as well as the phenylmethanimine group from [Cu(**4.6**) + H+ Na]$^+$. A similar fragmentation pattern was also observed for [Cu(**3.11a**)]$^+$ (see figure 3.10 in section 3.5.3). Further fragmentation of the followed a pathway identical to that of [Cu(**3.11a**)]$^+$.

In contrast to the daughter signal at m/z = 412.2, the signal at m/z = 681.2 is the result of beta cleavage of a methyl group from [Cu(**4.6**) + H+ Na]$^+$, as well as the loss of a hydrogen atom. Cleavage of the methyl and ethyl groups from the N1 nitrogen (see numbering in scheme 4.5) atoms has been shown in chapter 3 and was also proven by Ferreira et al.[139] CID of the m/z charge signal at 681.2 resulted in three daughter peaks at m/z = 601.2, 398.3, and 380.3., for which the proposed structures as shown in figure 4.1C. The daughter peak at 601.2, corresponds to the loss of the Na^+ and Cu^{2+} ions and the addition of six protons. The signal observed at m/z = 398.2 represents the loss of both

metal cations, a hydrogen atom, and the phenylmethanimine group, as well as beta cleavage of a methyl group from N1. Lastly, the signal at m/z = 380 follows the same pattern as the signal at m/z = 398.2 but accounts for an additional beta cleavage of a methyl group as well as the loss of three hydrogen atoms.

The mass spectrum data of **4.6** with $Cu(NO_3)_2$ clearly shows the formation of a metal-ligand complex in the gas phase. By conducting a CID analysis of the coordination compound formed between **4.6** and Cu^{2+} ions we were able to show that the complex follows a fragmentation pattern similar to $[Cu(\mathbf{3.11a})]^+$, which was discussed in depth in chapter 3. As this study does not identify specifically which donor groups are involved in Cu^{2+} ion coordination, FT-IR spectroscopy will be used to provide information on the coordination environment of the metal.

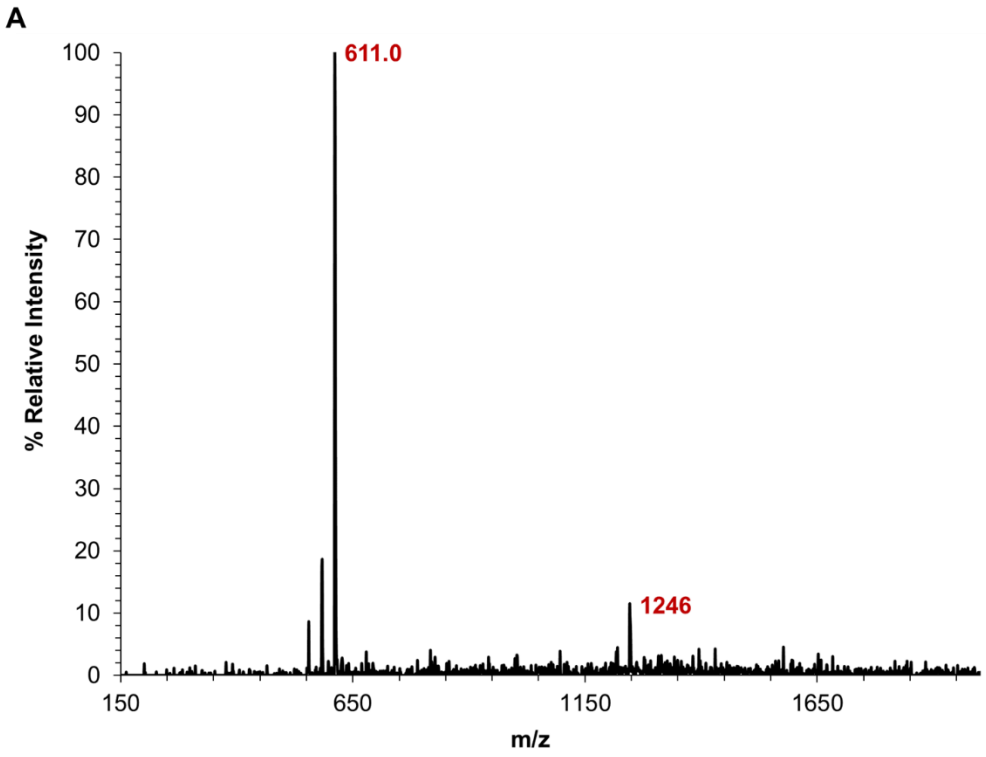

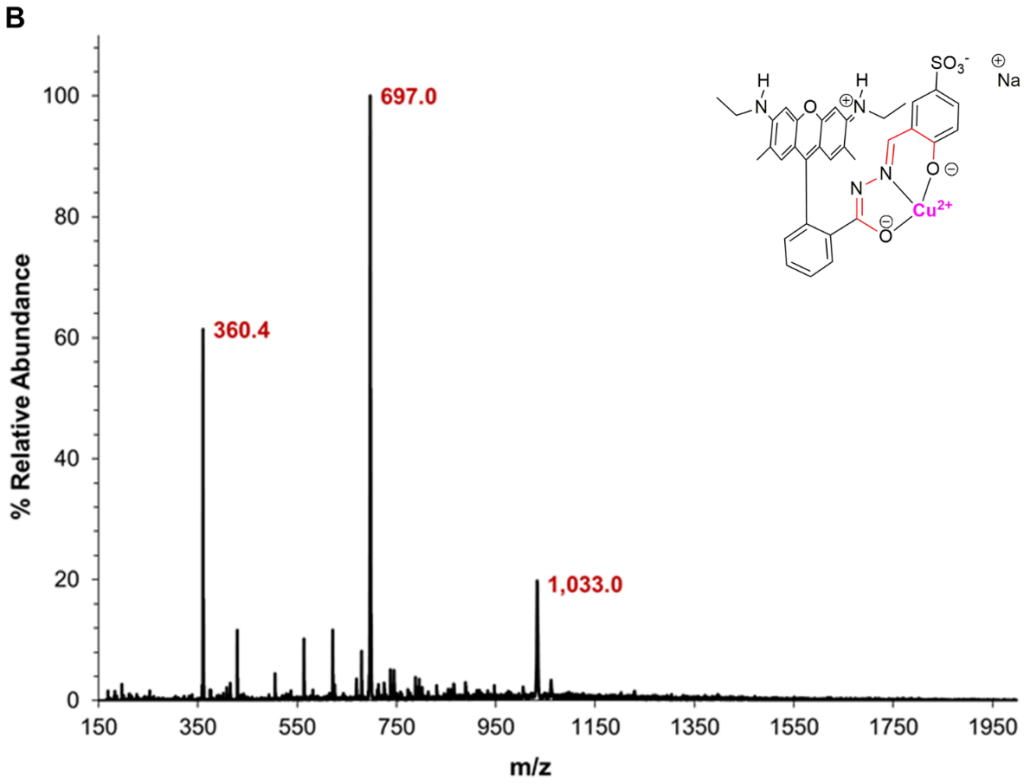
B
% Relative Abundance
100
80
60
40
20
0
697.0
360.4
1,033.0
150
350
550
750
950
1150
1350
1550
1750
1950
m/z
H
N
O
H
N
SO3-
Na
N
N
O
Cu2+
O

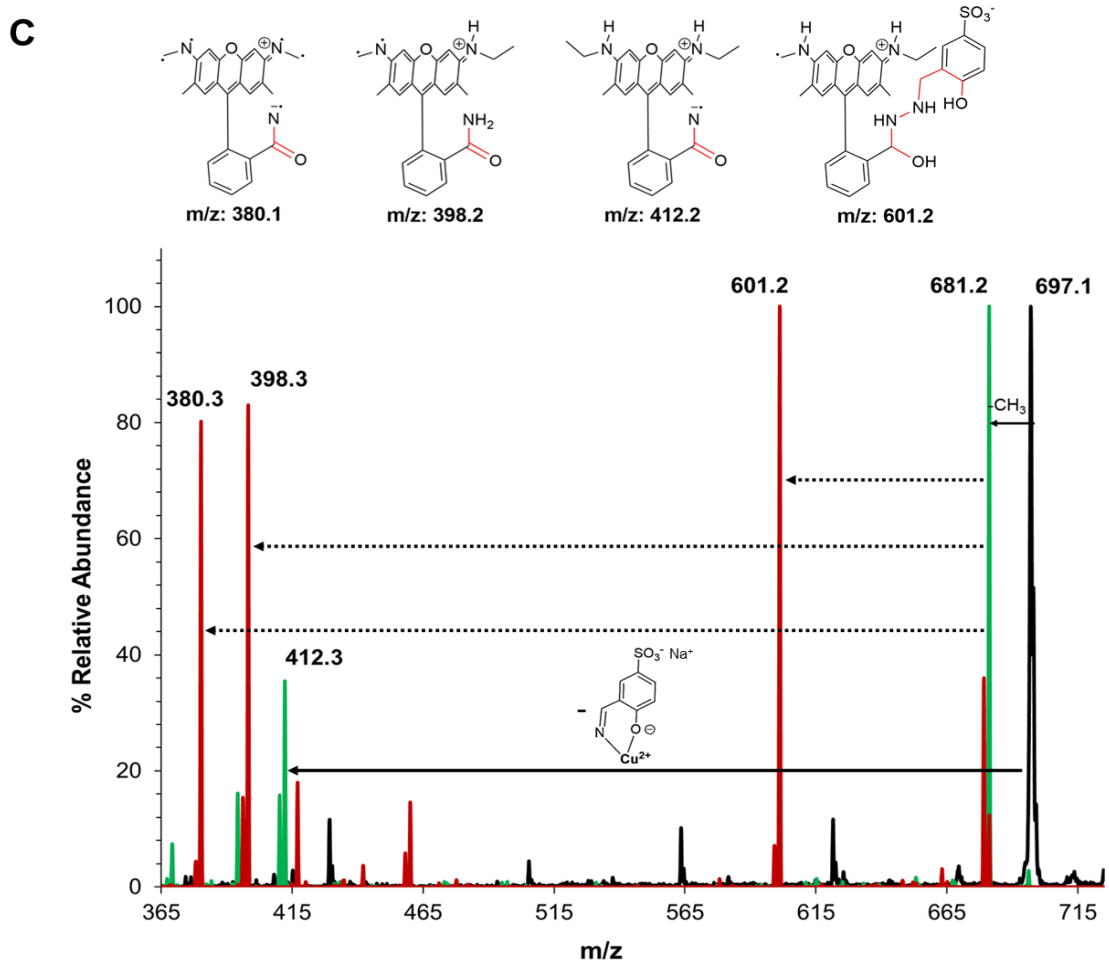

Figure 4.1 *(A) ESI-MS of **4.6** in MeOH (B) ESI-MS of [Cu(**4.6**) + Na]$^+$ in MeOH (C) Fragmentation pattern of [Cu(**4.6**) + Na]$^+$*

4.4.3 Solid State Study (FT-IR spectroscopy)

The [Cu(**4.6**)$_2$] complex was prepared by grinding a 2:1 ratio of **4.6** and Cu(NO$_3$)$_2$ with a mortar and pestle. Upon mixing the two compounds, an extremely dark solid was observed. The coordination environment was confirmed by analyzing changes to the carbonyl stretch of the γ-lactam. The IR spectrum of the complex displayed a complete reduction in the carbonyl stretch at 1701 cm^{-1} and the emergence of a strong IR stretch at 1600 cm^{-1} (figure 4.2). We postulate that this change is due to the coordination of **4.6** to

the Cu^{2+} ion. The appearance of the stretch at 1600 cm^{-1} is likely due to the generation of the azine functional group upon the change in conformation from the spirolactam to the ring open form of the probe. This mode of coordination was also reported by Raju et al. and was discussed in section 4.2 of this chapter.[153] There are also notable changes in the hydrogen bonding region which could account for Cu^{2+} ion coordination to the hydroxyl group at the 10' position of **4.6**. These changes could however also be due to coordination of the metal to the sulfonate group.

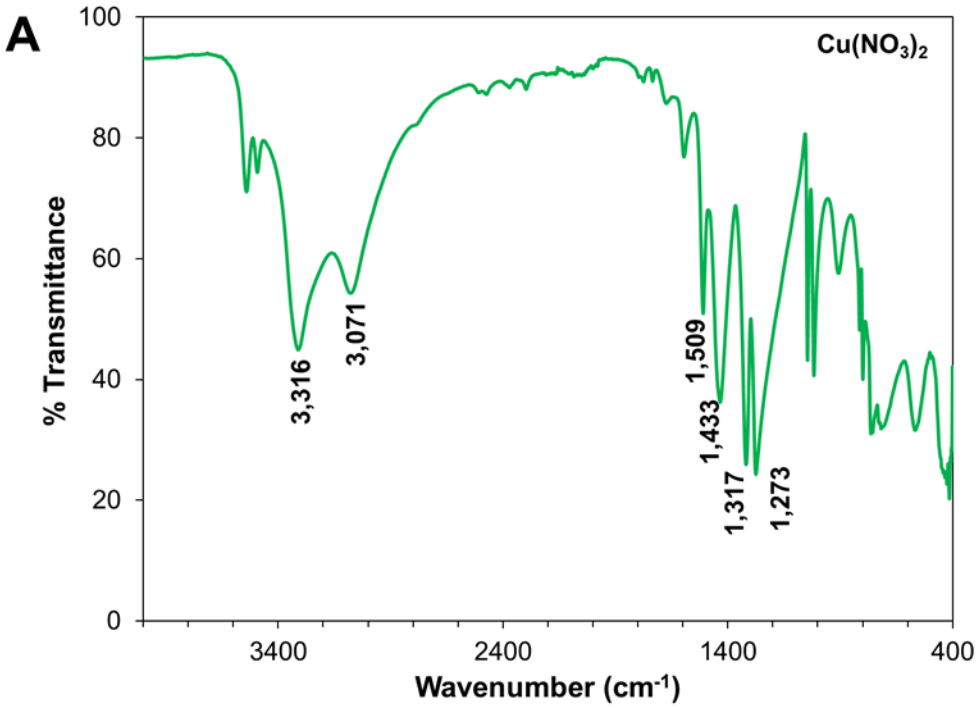

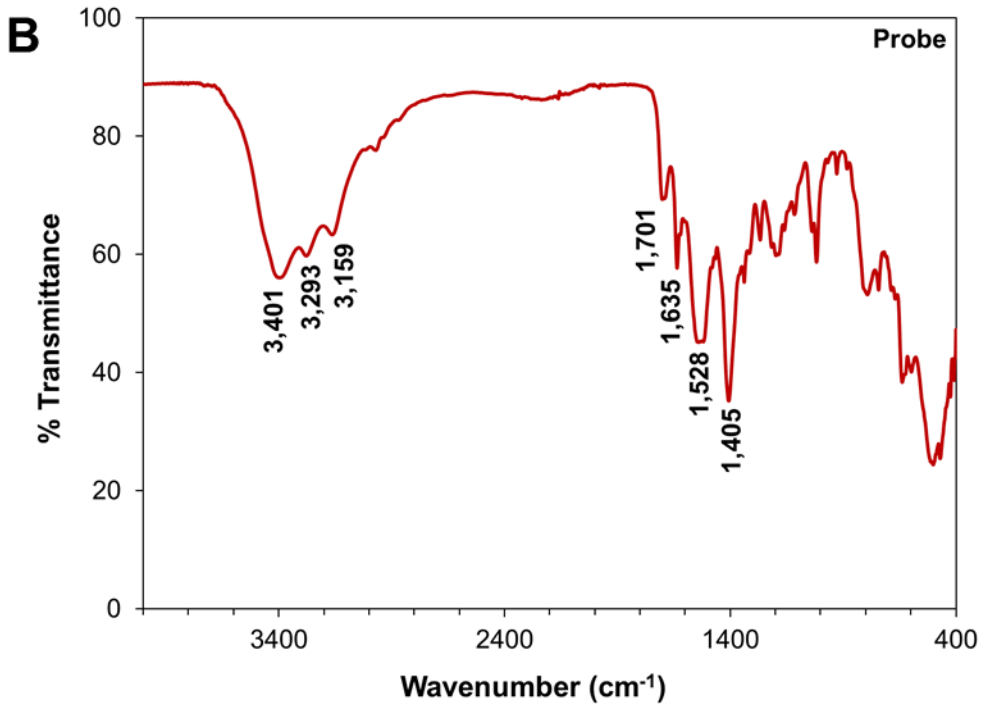
B
Probe
100
80
60
40
20
0
% Transmittance
3,401
3,293
3,159
1,701
1,635
1,528
1,405
3400
2400
1400
400
Wavenumber (cm-1)

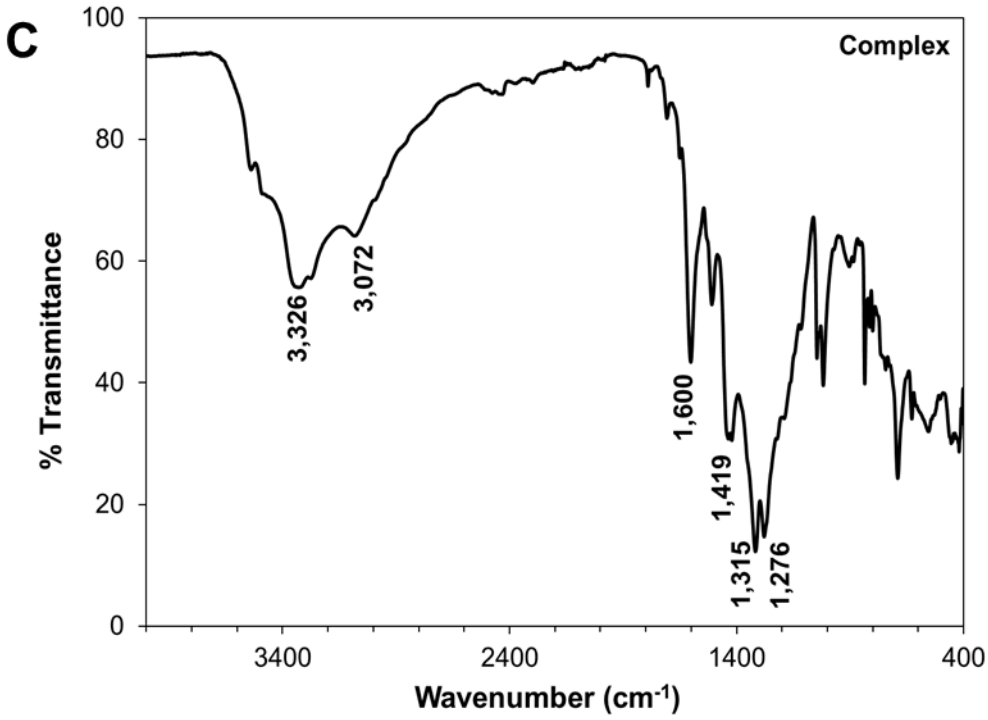
C
Complex
100
80
60
40
20
0
% Transmittance
3,326
3,072
1,600
1,419
1,315
1,276
3400
2400
1400
400
Wavenumber (cm-1)

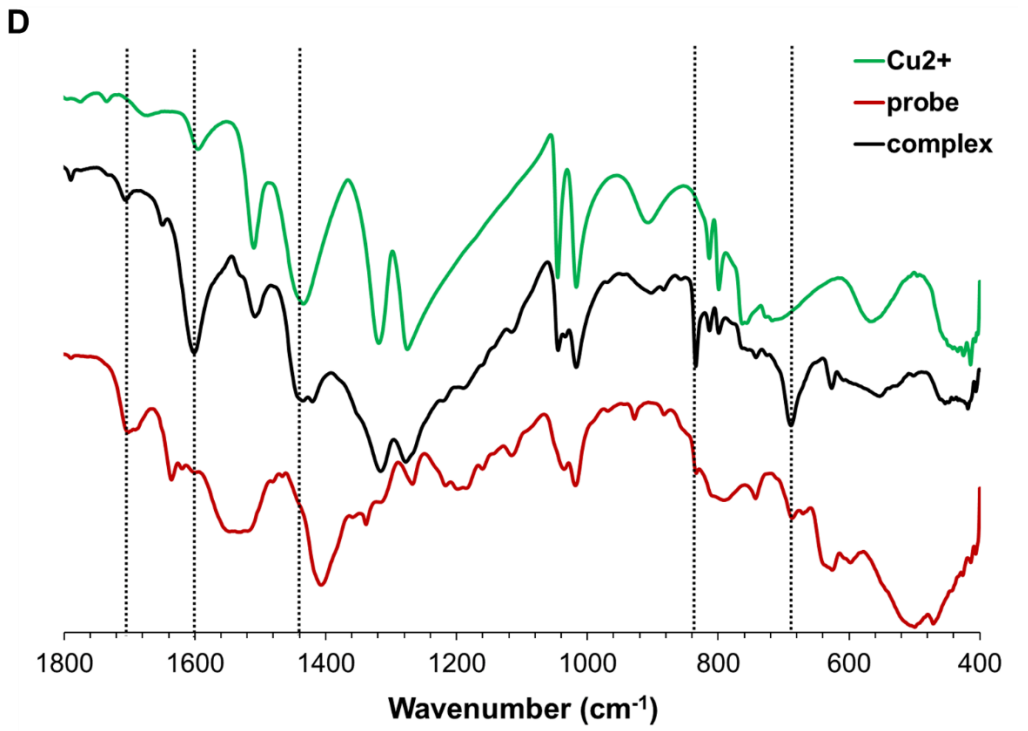

Figure 4.2 *FT-IR spectra used to determine modes of coordination between $Cu(NO_3)_2$ and* ***4.6*** *(A) $Cu(NO_3)_2$, (B) compound* ***4.6*** *(C) [Cu(****4.6****)$_2$] complex (D) stacked spectra of diagrams A, B, and C.*

4.4.4 Optical Studies

pH studies of compound **4.6**

Understanding the optimal pH ranges over which a molecular probe can be used to accurately monitor analyte concentrations is imperative. This is especially important for probes that will be used in biological and environmental systems. The effect of acidic environments on spirolactam rhodamine compounds was discussed in section 3.1. Because the opening of the rhodamine 6G spirolactam ring can occur as a result of metal coordination or protonation of the species in aqueous media, it is imperative to be able to discern between which of the two events are actually responsible for the colorimetric and fluorometric changes in the compound. A pH study was therefore conducted on

compound **4.6** in a solution of DMSO-water (2:98, v/v) to determine optimal ranges over which metal analysis could occur (figure 4.3). Hydrochloric acid (1.0) and sodium hydroxide (1.0 M) were used to adjust the pH as needed. The results of the pH study indicate the optimal pH ranges for compound **4.6** between pH ≈ 8 to 10.5. This pH window is much narrower than that of compound **3.9** which was discussed earlier in this work (see section 3.5.5). This is likely due to the negatively charged sulfonate group which is readily protonated in mildly acidic solution. Even though minimal ring opening is observed at pH 7.5, we decided that our analysis could be conducted between pH 7.5-10.4 as this ring opening does not interfere with our metal analysis. This is because we do not merely focus on the ring opening mechanism to identify when metal coordination has occurred, but we also analyze other unique absorbance bands, like the Fe^{3+} coordination bands highlighted in chapter 3.5.5, to signify the formation of coordination complexes in solution.

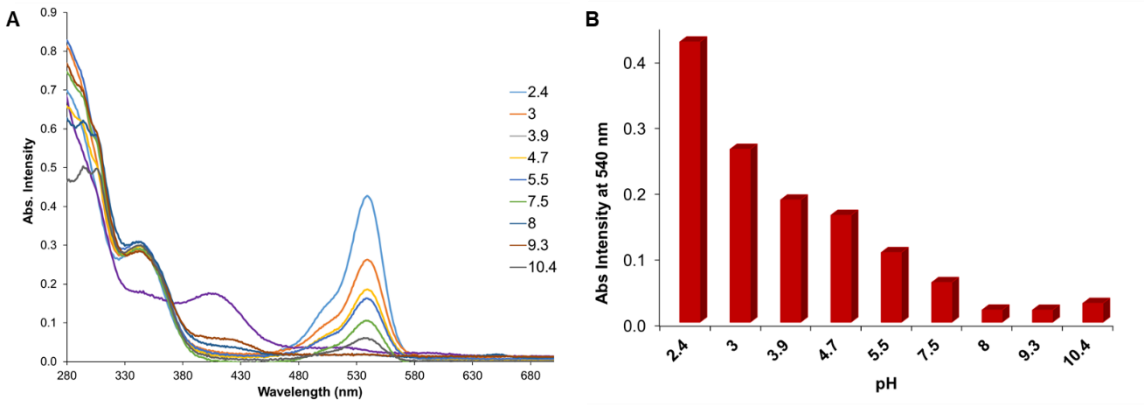

Figure 4.3 *pH study of 5.0 ×10^{-5} M solution of compound **4.6** in DMSO-deionized water (2:98 v/v).*

Metal Screen of Compound **4.6** in DMSO

A colorimetric metal screen was screen was conducted in DMSO to determine which metal ions would induce the ring opening mechanism in compound **4.6** (figure 4.4). It was expected that compound **4.6** would display similar metal ion selectivity to compounds **3.11a** and **3.12**, as these compounds all have the same coordination environment. The metal screen was conducted in DMSO due to the low solubility of compound **4.6** in CH_3CN and less polar solvents such as THF. Compound **4.6** is very soluble in DMSO, MeOH, EtOH and 99.5% aqueous solutions. Two equivalents of each of the metal ions shown in figure 4.3 (Ag^+, K^+, Na^+, Ca^{2+}, Co^{2+}, Cu^{2+}, Fe^{2+}, Hg^{2+}, Mg^{2+}, Ni^{2+}, Pb^{2+}, Zn^{2+}, Al^{3+}, Cr^{3+}, and Fe^{3+} ions) were added to 25 µM solutions of compound **4.6** in DMSO. The only metal ion that resulted in a significant color change was the Cu^{2+} ion. Very little ring opening was observed in the presence of iron ions and we expect that this response will be further minimized at this pH due to hydrolysis reactions. The Al^{3+} ion also resulted in a very small hyperchromic shift at 530 nm, however the Cu^{2+} signal was 17-times larger than the signal observed for the Al^{3+} ion. Furthermore, the Cu^{2+} ion coordination band between 380-450 nm was also apparent in the spectra. Coordination of compound **4.6** to Fe^{3+}, Fe^{2+}, and Al^{3+} ions does not result in the emergence of this coordination band.

The results of the metal screen indicate that **4.6** is more selective, via colorimetric methods, for Cu^{2+} ions than compounds **3.11a** and **3.12** despite all three molecules exhibiting the same coordination environments. It is possible that the oxygen atoms on the sulfonate group coordinate to the iron ions and inhibit the metal ions from interacting

with the donor ligands in the coordination environment which would explain why very little ring opening was observed for the iron species.

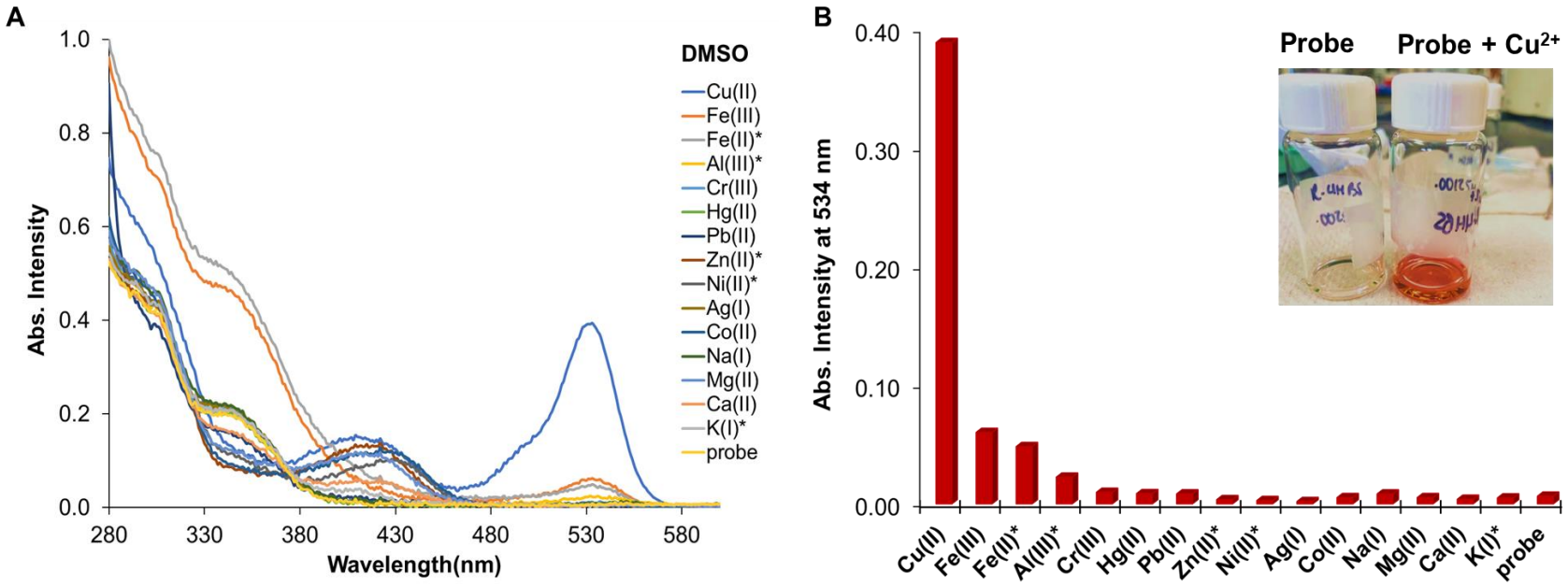

Figure 4.4 *(A) Absorbance spectra of a 25 μM solution of compound* ***4.6*** *with 2 equivalents of various metal ions in DMSO. (B) Bar chart representation of the results of diagram A, whereby* λ_{max} *at 534 nm is plotted for each metal ion (inset shows the color change immediately after adding* Cu^{2+} *the solution of the probe). Note: Ions with asterisk are chloride salts, all others are nitrate salts.*

Stoichiometric Analysis of Compound **4.6** for Cu^{2+} Ions

A series of titration studies were carried out between compound **4.6** and $Cu(NO_3)_2$ in DMSO to determine how changing the concentration of the **4.6** would affect the binding ratio between the molecular probe and Cu^{2+} ions. The isotherms of the titration studies are shown in figure 4.5 for three solutions of compound **4.6** at 10, 15, and 150 µM concentrations. The isotherm for the 10 µM solution of **4.6** plateaus after the addition of one equivalent of Cu^{2+} ions, whereas the isotherms of the more concentrated samples begin to plateau when the ratio of the probe to Cu^{2+} ions is 2:1. Job's plot analysis was used to confirm that the 2:1 complex, $[Cu(\mathbf{4.6})_2]^{2-}$, was in fact the predominant species in solution (figure 4.6). This is demonstrated in the convergence point at 0.3 $[Cu^{2+}]/[Cu^{2+}]$ + [**4.6**]. Non-linear regression analysis was performed using Bindfit software to verify the occurrence of the $[Cu(\mathbf{4.6})_2]$ complex as well as determine the how stable the complex is in various solvent systems. The association constants for the different species formed between **4.6** and Cu^{2+} ions in DMSO are shown in table 4.1.

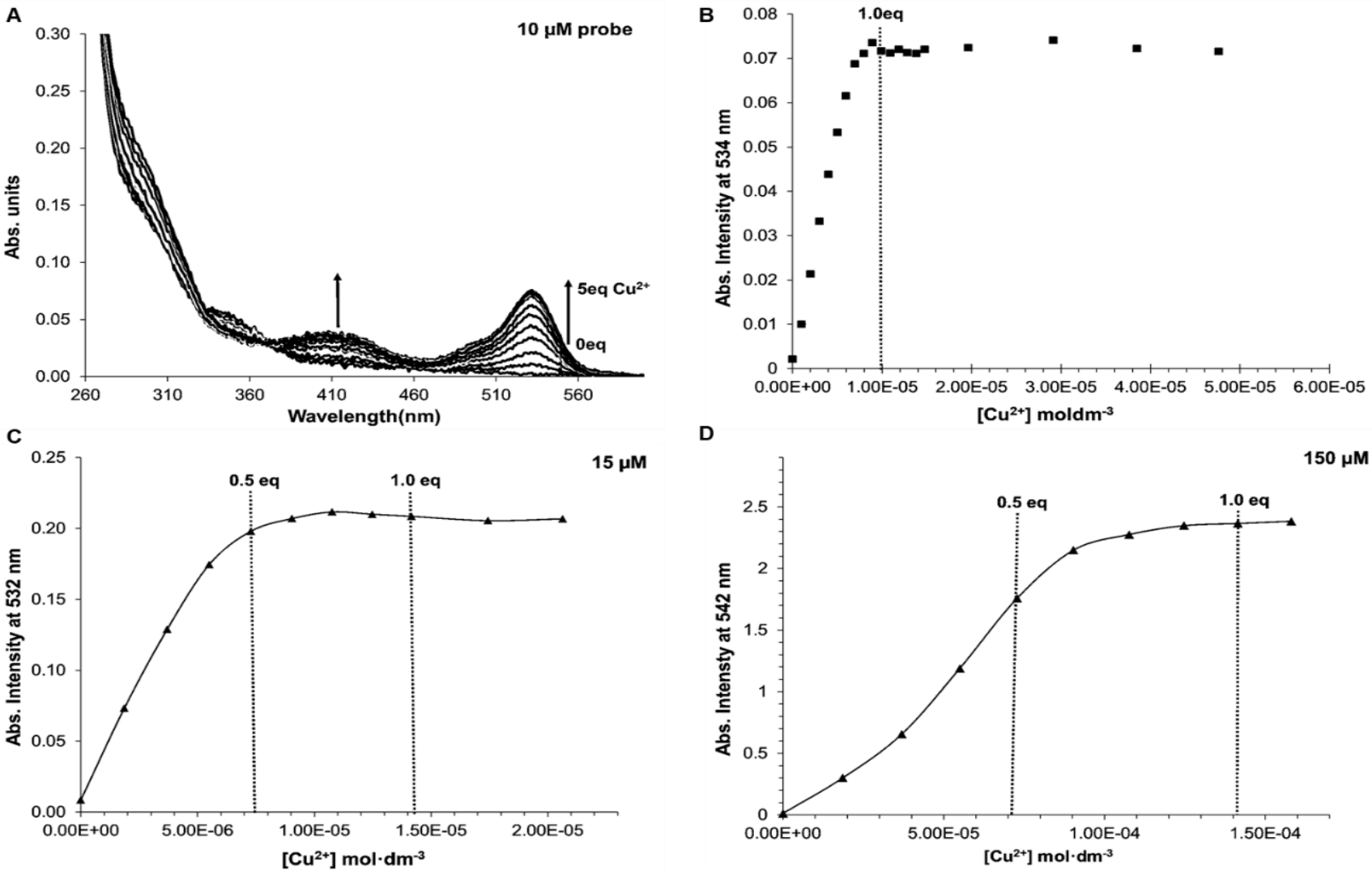
A
10 μM probe
Abs. units
Wavelength(nm)
5eq Cu2+
0eq
B
1.0eq
Abs. Intensity at 534 nm
[Cu2+] moldm-3
C
15 μM
0.5 eq
1.0 eq
Abs. Intensity at 532 nm
[Cu2+] mol·dm-3
D
150 μM
0.5 eq
1.0 eq
Abs. Intensty at 542 nm
[Cu2+] mol·dm-3

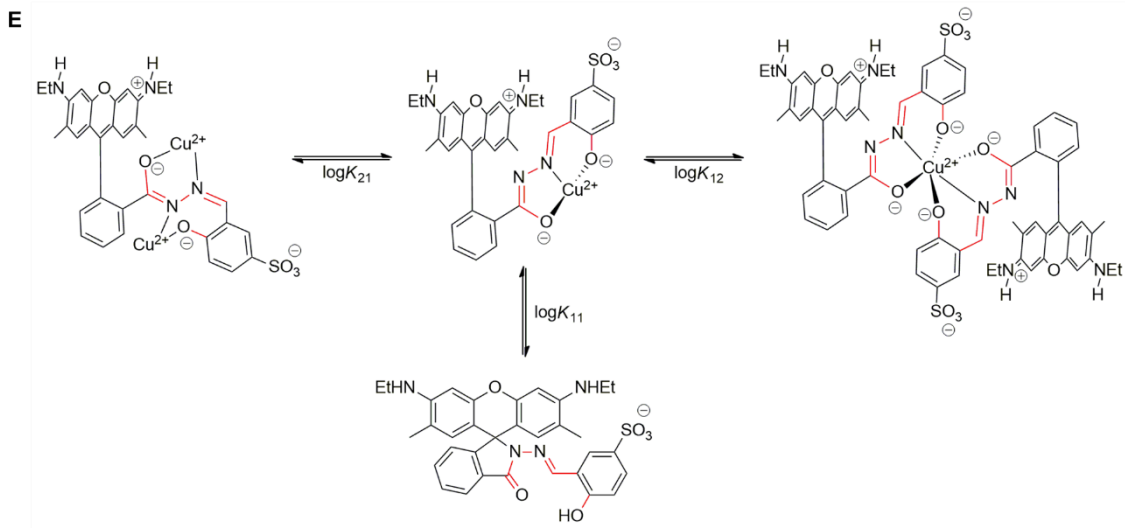

Figure 4.5 *Results of the titration of Cu^{2+} ions into various solutions of compound* ***4.6*** *in DMSO. (A-B) 10 µM (C) 15 µM (D) 150 µM (E) Proposed binding between* ***4.6*** *and Cu^{2+} ions responsible for observed K_a values.*

Table 4.1 *Ka values for coordination compounds formed in a 15 µM solution of* ***4.6*** *with Cu^{2+} ions in DMSO.*

K_a [Cu^{2+}: 4.6]
$\log K_{11} = 5.3 \times 10^5 \pm 16.3$
$\log K_{21} = 2.2 \times 10^7 \pm 18.1$
$\log K_{12} = 5.6 \times 10^6 \pm 5.1$

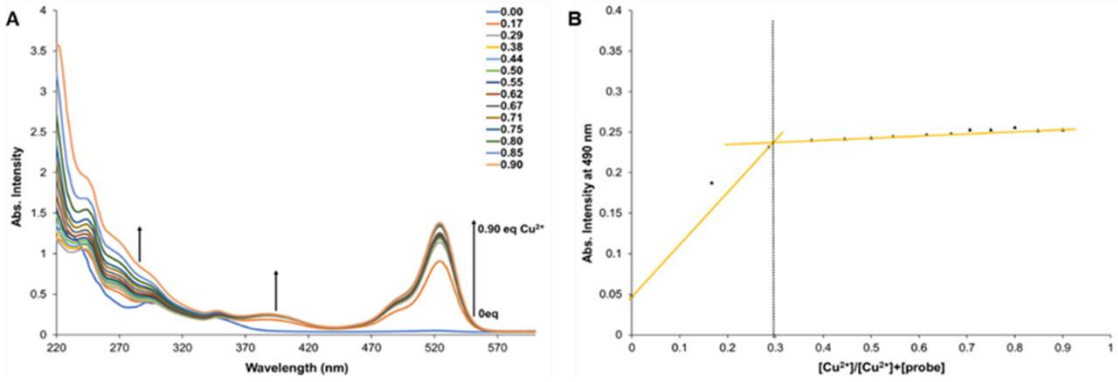

Figure 4.6 *Job's plot data for a 50 µM solution of compound* ***4.6*** *with $Cu(NO_3)_2$ in DMSO.*

Buffer Studies with Compound **4.6**

Attempts to analyze the binding ratios between compound **4.6** and Cu^{2+} ions in 98% aqueous solutions proved to be challenging as the probe quickly becomes saturated and minimal changes in the absorbance bands at 530 nm and 410 nm are observed after 0.3 equivalences of Cu^{2+} ions have been added to the solution (figure 4.7). This is a reasonable observation when considering the 2:1 stoichiometric ratio between **4.6** and Cu^{2+} ions. Upon the introduction of Cu^{2+} ions to the solution of the sensor, two molecules of **4.6** immediately coordinate to the metal ion. Once all of the sensor molecules have coordinated to the Cu^{2+} ions no further changes to the absorbance bands at 530 nm and 410 nm are observed aside from negligible deviations from the baseline due to the onset of aggregation, likely resulting from the high concentration of water molecules in solution.

Of the four buffer solutions that were analyzed, EPPS and PBS buffer proved to be the most efficient buffers for use in our metal sensing applications. The bicine buffer likely serves as a tetradentate ligand and forms very stable coordination compounds with the Cu^{2+} ions, which would account for the negligible absorbance enhancements in figure 4.7A. On the other hand, in the CHES buffer, the majority of **4.6** in solution appears to exist in the ring open form despite the pH of the solution being in the optimal range (pH $\approx$8-10.5) for metal analysis with this probe. As a result, only minimal increases in the absorbance spectra were observed once Cu^{2+} ions were introduced to the solution. Even though compound **4.6** is soluble in purely aqueous solutions, this buffer study led us to the conclusion that it may be more beneficial if we incorporated higher concentrations of

polar protic organic solvents, such as MeOH and EtOH, into our solutions to obtain more quantitative results.

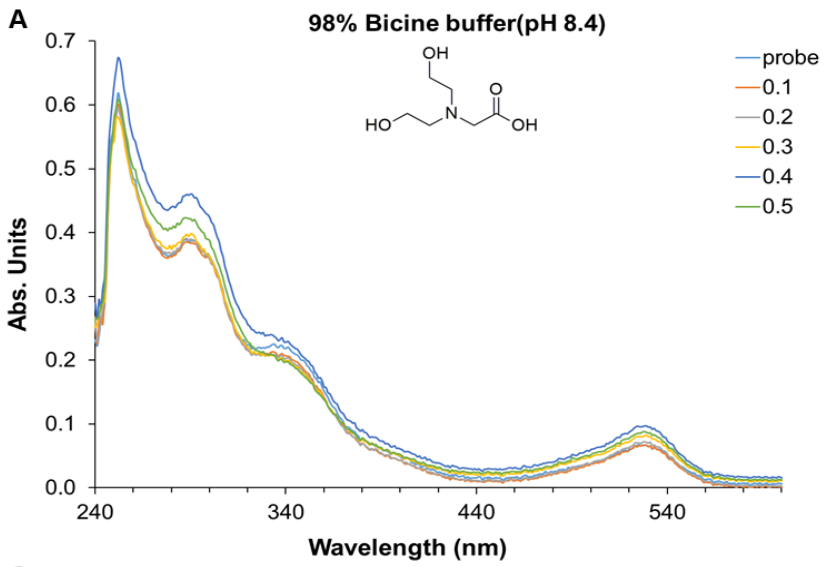
A
98% Bicine buffer(pH 8.4)
OH
HO
N
O
OH
probe
0.1
0.2
0.3
0.4
0.5
Abs. Units
0.0
0.1
0.2
0.3
0.4
0.5
0.6
0.7
240
340
440
540
Wavelength (nm)

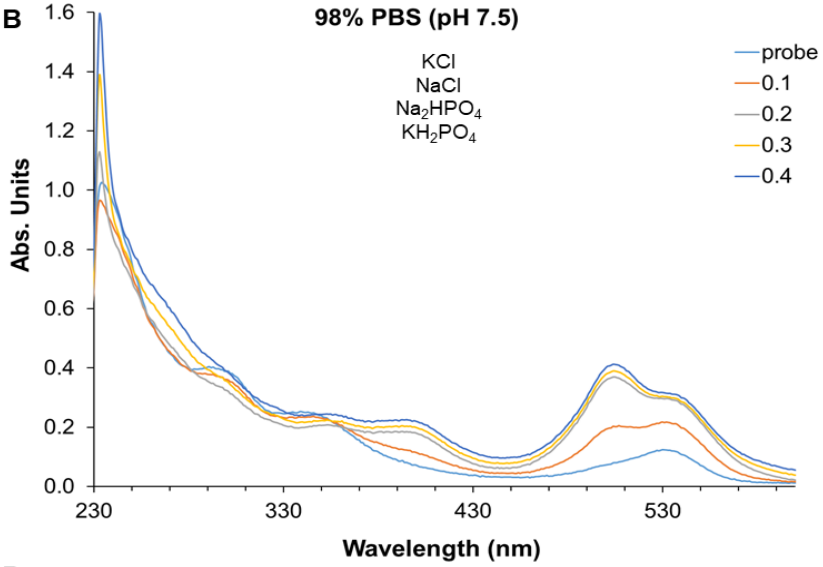
B
98% PBS (pH 7.5)
KCl
NaCl
Na_2HPO_4
KH_2PO_4
probe
0.1
0.2
0.3
0.4
Abs. Units
0.0
0.2
0.4
0.6
0.8
1.0
1.2
1.4
1.6
230
330
430
530
Wavelength (nm)

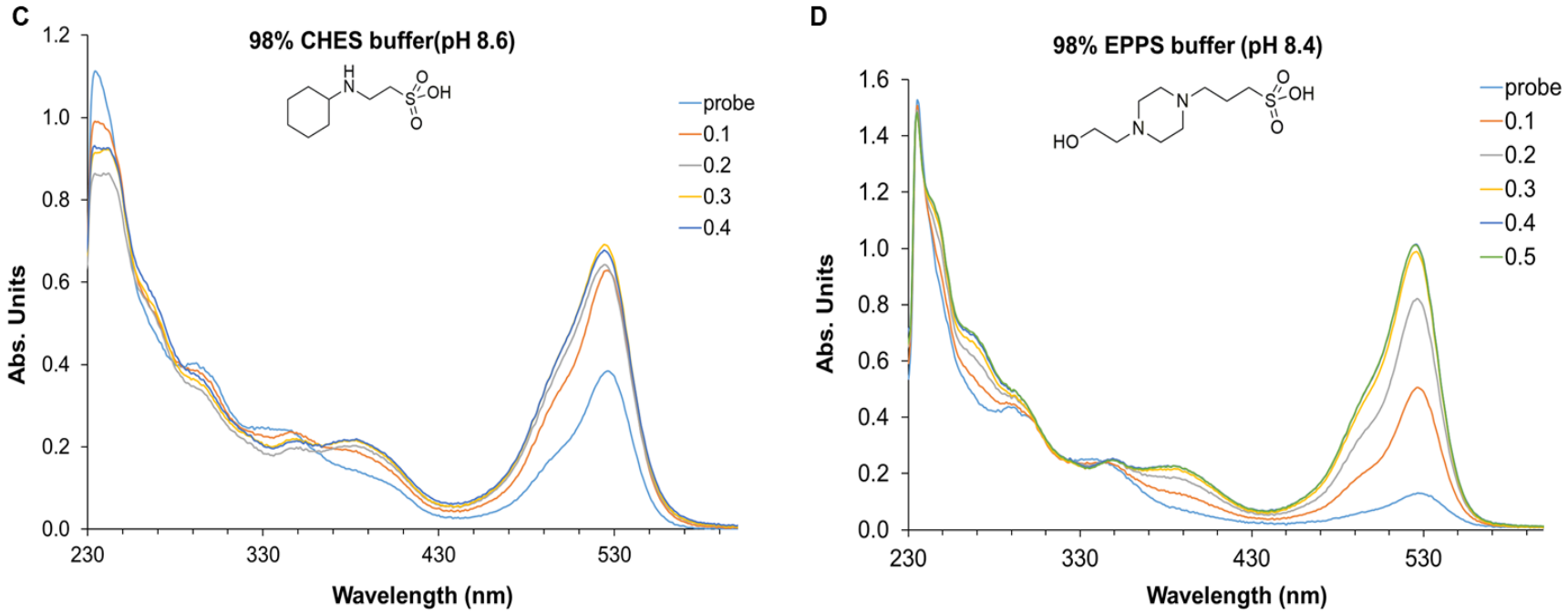

Figure 4.7 *Absorbance spectra of 50 µM solutions of compound* ***4.6*** *with increasing equivalents if* Cu^{2+} *ions in DMSO: buffer (2:98, v/v) (A) Bicine buffer (B) PBS buffer (C) CHES buffer (D) EPPS buffer*

Detection Limit of Compound **4.6** for Cu^{2+} Ions

The LoD was determined by titrating a 1×10^{-3} M solution of $Cu(NO_3)_2$ solution into a 1×10^{-5} M solution of **4.6** in DMSO. To determine LoD, the change in the intensity of absorbance band at 532 nm versus the concentration of Cu^{2+} solution was plotted. The method of least squares was then used to produce a line of regression (figure 4.8). Using a 95% confidence level, the LoD of **4.6** for Cu^{2+} ions in DMSO was determined to be 8.65×10^{-7} M (54.9 ppb). This is not as low as the LoD calculated for compound **3.11a** however, this can be explained by comparing the solubility of the two compounds in organic solvents. Despite both probes being soluble in DMSO, compound **3.11a** is much more soluble in organic solvents than **4.6** which may account for this observation. A LoD was also calculated for the sensor in EtOH and was found to be 7.5×10^{-6} M (0.47 ppm) which is much higher than the LoD calculated for DMSO (see appendix). It is possible that in other solvents such as MeOH and aqueous solutions of MeOH and EPPS buffer (figure 4.9) compound **4.6** is capable of detecting lower concentrations of Cu^{2+} ions, however, this method of analysis is restricted by the need for linear regression analysis. In systems where the stoichiometry between the probe and analyte is not 1:1, as is the case here, it can be difficult or even impossible to plot linear graphs as a sigmoidal shape is characteristic of systems where the stoichiometry is predominantly 2:1.

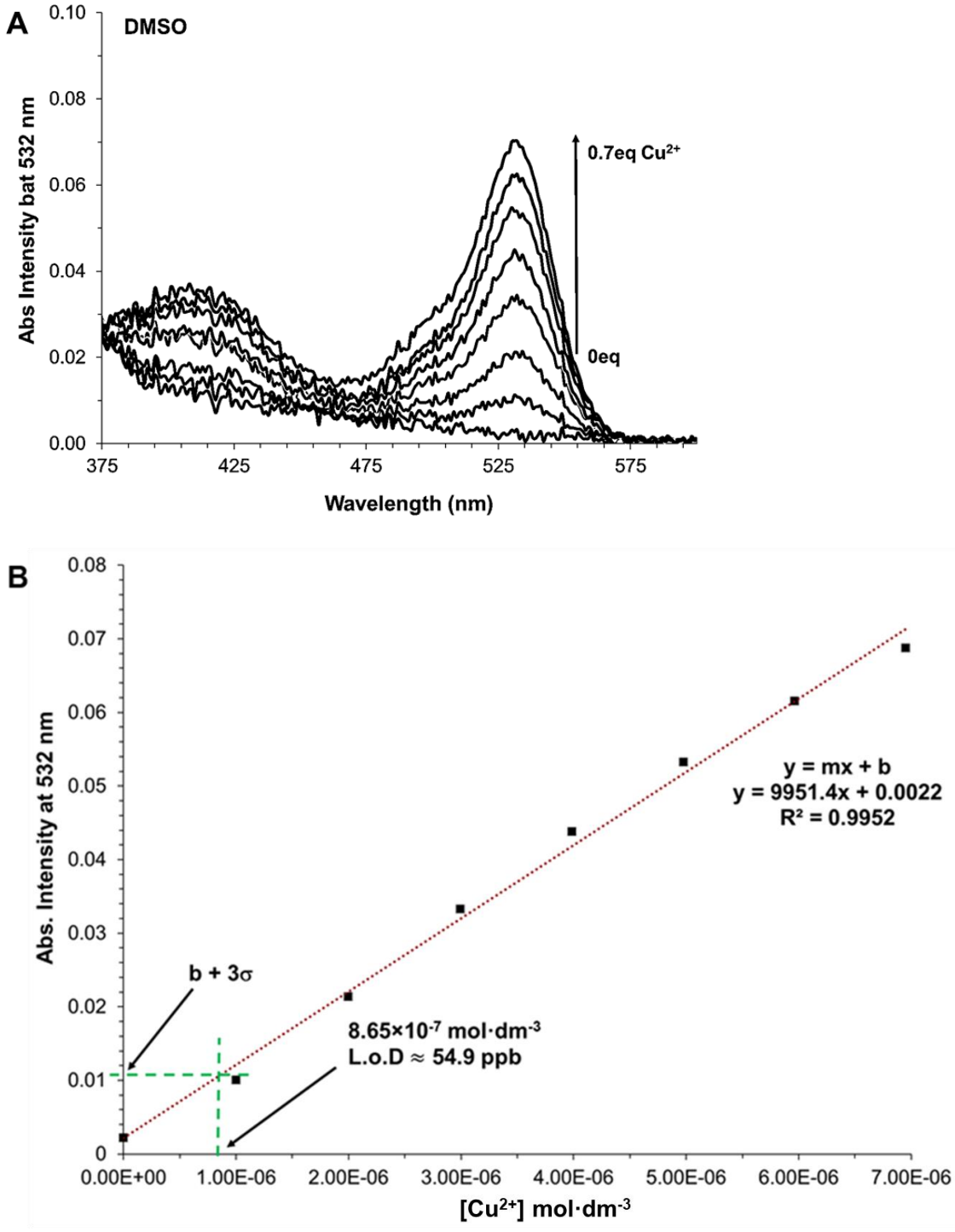

Figure 4.8 *(A) Absorbance data used for LoD calculation with compound* ***4.6****.(B) Calibration curve used to calculate the LoD for* $Cu(NO_3)_2$ *with compound* ***4.6*** *in DMSO.*

Fluorescence Studies of Compound **4.6** with $Cu(NO_3)_2$

The fluorescence capabilities of compound **4.6** were analyzed in several different solvent systems (figure 4.9).Titration studies were performed with 5×10^{-6} M solutions of **4.6** in DMSO, EtOH, MeOH, and MeOH: EPPS (1:1, v/v, 10mM, pH 8.0) to determine if the molecular probe would exhibit a fluorescence enhancement or decrease upon the addition of Cu^{2+} ions to each of the solvent systems. For each of the solvents used, a notable fluorescence enhancement was observed near 550 nm, though the largest increases were observed in DMSO and MeOH. In the DMSO solution, a 15-fold fluorescence enhancement was observed in the band at 563 nm, whereas a 7-fold enhancement was observed in MeOH. For the solutions of EtOH and MeOH: EPPS buffer, 4-2-fold and 3-fold fluorescence enhancements were observed, respectively. In EtOH a hypsochromic shift was also observed from 540-553 nm as Cu^{2+} ions were added to the solution. The Fe^{3+} ion was also investigated in DMSO, however the addition of 20 equivalents of the metal ion to the solution of **4.6** led to a very small decrease in the fluorescence signal at 560 nm. This minor decrease in fluorescence was however not enough of a difference to be considered as an efficient quenching mechanism and is more likely associated with a decrease in the concentration of the probe.

A comparison of the fluorescence spectra and binding isotherms in figure 4.9 shows that, in DMSO, the addition of low concentrations of Cu^{2+} ions to the solution immediately results in a drastic change in the fluorescence of **4.6**, whereas larger concentrations of the metal ion were required to produce notable changes in the other solvent systems. Non-linear regression analyses were performed using Bindfit software to compare the stability constants of the [Cu(**4.6**)$_2$] complex in 100% organic solvents to

those in aqueous solutions. Despite the ability of the complex to fluoresce in 98% aqueous solutions (figure 4.9A), correlating the concentration of the complex in solution to the fluorescence signal proved challenging as the samples require long mixing times (>5 minutes) to reach equilibrium and the data points still often deviated from the expected pattern. As a result, compound **4.6** could be useful for qualitative fluorescence analysis of Cu^{2+} ions in solutions containing high concentrations of water (up to 100%), however, quantitative analysis would be less reliable. Because it is our goal to apply our sensors to different biological systems, we chose to analyze the K_a of the complex in EtOH as this solvent is less toxic to cells than MeOH and DMSO. In EtOH, a K_a of 5.94×10^7 M^{-2} was determined for [Cu(**4.6**)$_2$]. For the 1:1 solution of MeOH-EPPS buffer (pH 8.0), a K_a of 1.6×10^8 M^{-2} was determined. These are both considerably large binding constants, especially when compared to the literature examples highlighted earlier in this chapter. This improvement in complex stability in aqueous solution was expected based on the observations in table 3.4, whereby the [Cu(**3.12**)]$^+$ complex demonstrated greater stability as the aqueous content of the solvent system was increased.

DMSO

2:98
DMSO:EPPS

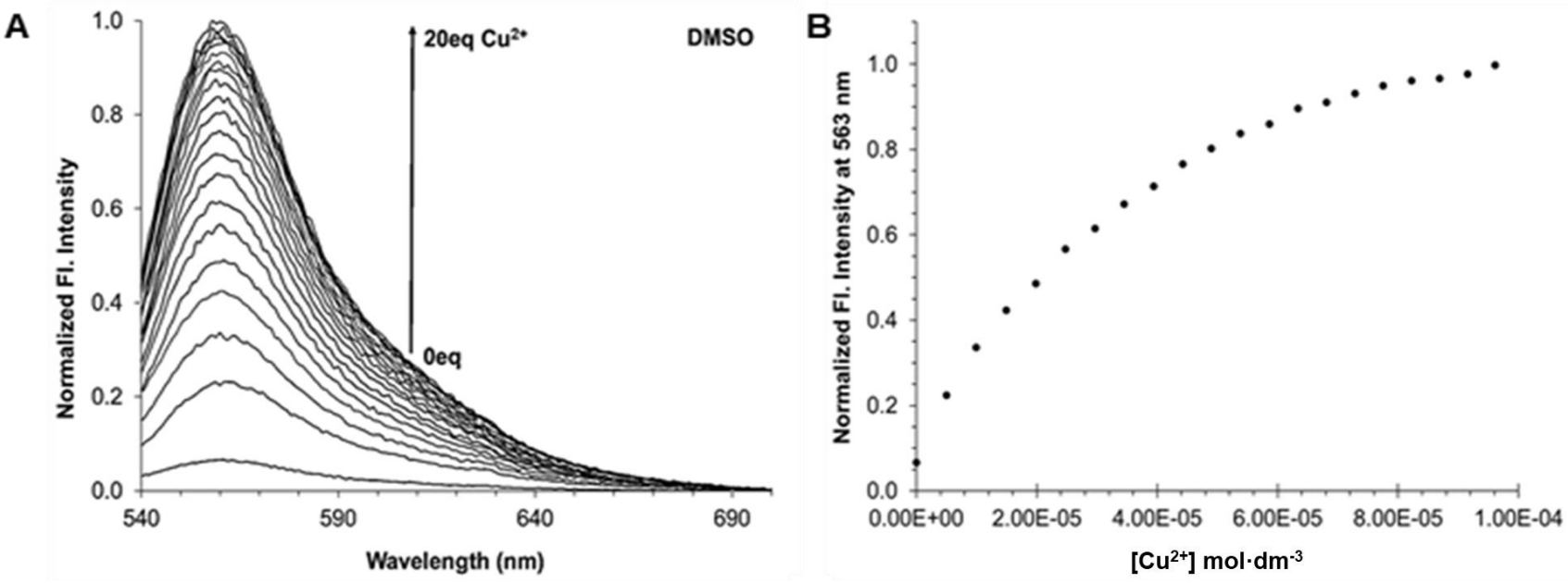

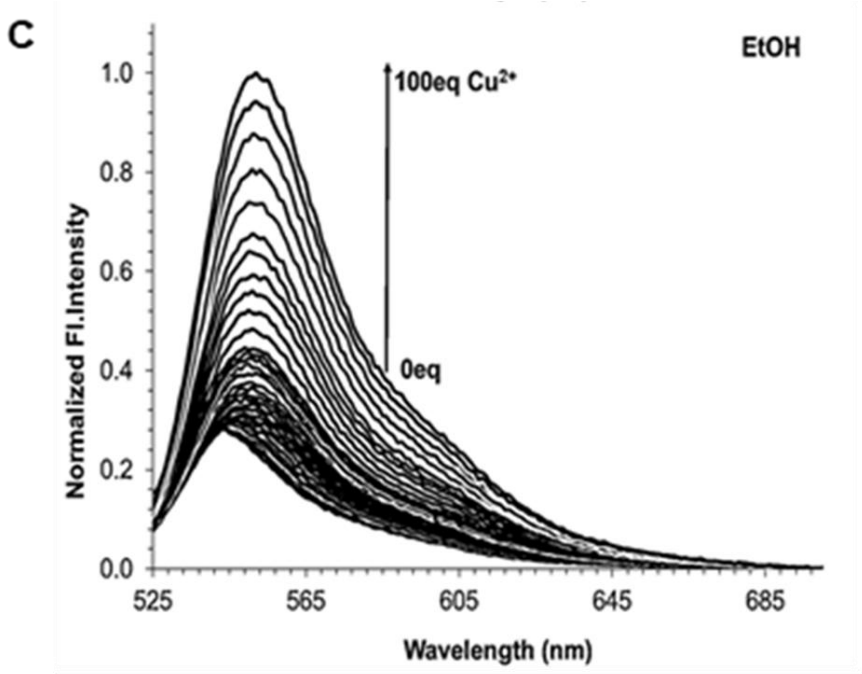
C
EtOH
100eq Cu2+
0eq
Normalized Fl.Intensity
1.0
0.8
0.6
0.4
0.2
0.0
525
565
605
645
685
Wavelength (nm)

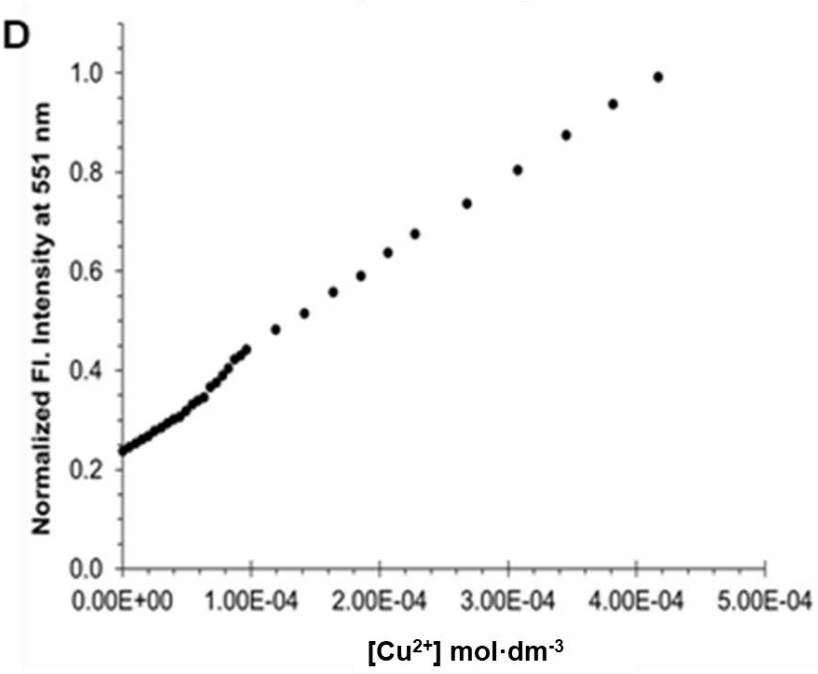
D
Normalized Fl. Intensity at 551 nm
1.0
0.8
0.6
0.4
0.2
0.0
0.00E+00
1.00E-04
2.00E-04
3.00E-04
4.00E-04
5.00E-04
[Cu2+] mol·dm-3

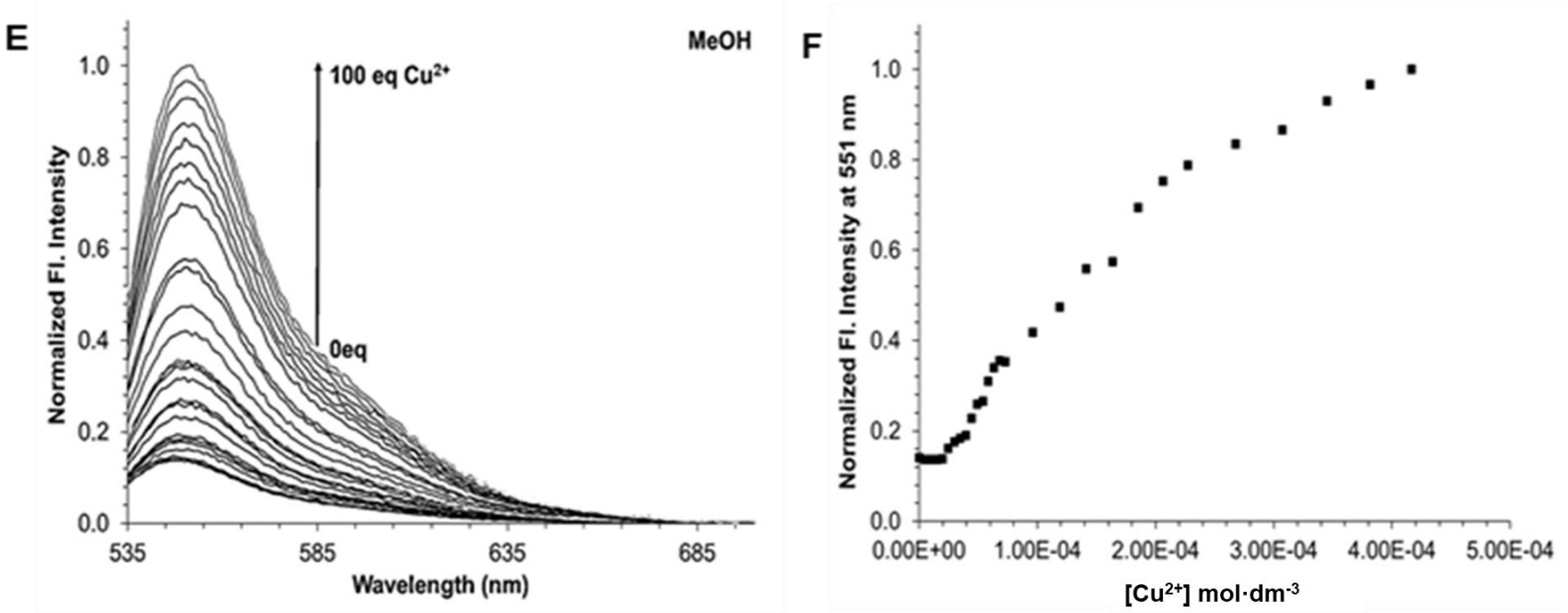
E
MeOH
100 eq Cu2+
0eq
Normalized Fl. Intensity
1.0
0.8
0.6
0.4
0.2
0.0
535
585
635
685
Wavelength (nm)
F
Normalized Fl. Intensity at 551 nm
1.0
0.8
0.6
0.4
0.2
0.0
0.00E+00
1.00E-04
2.00E-04
3.00E-04
4.00E-04
5.00E-04
[Cu2+] mol·dm-3

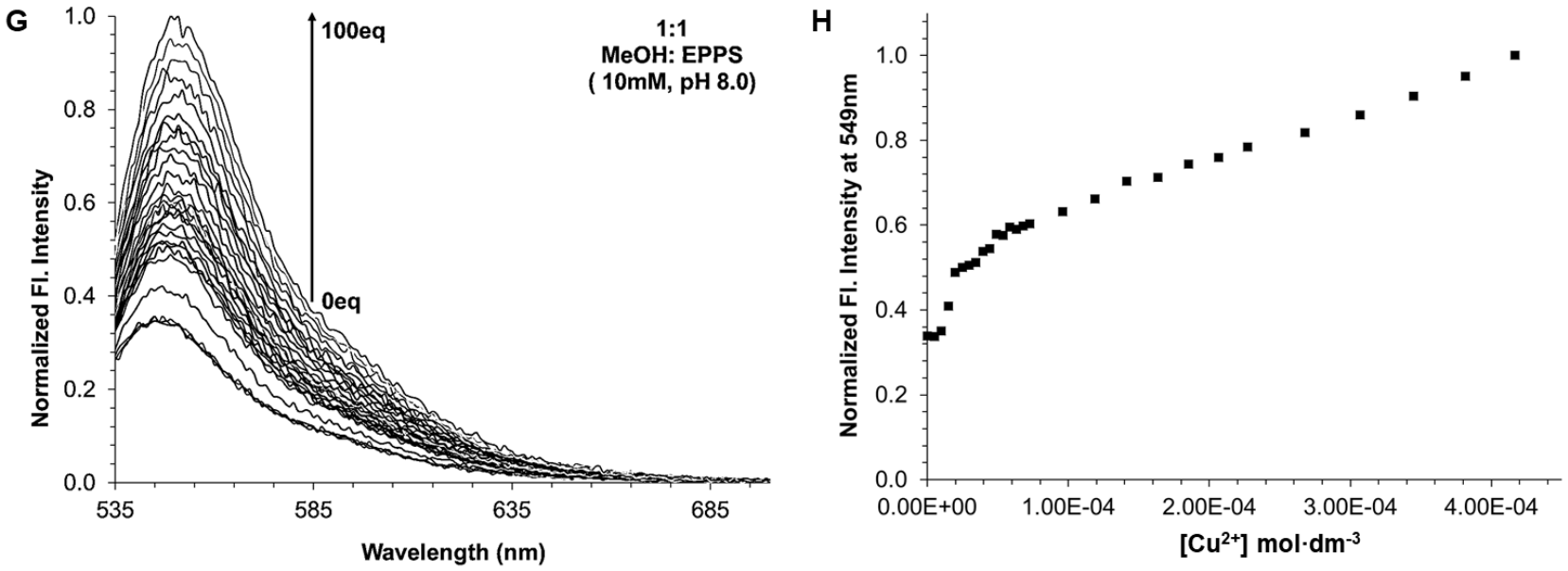

Figure 4.9 *Fluorescence plots and binding isotherms resulting from the titration of* $Cu(NO_3)_2$ *into 5 µM solutions of* ***4.6*** *in (A-B) DMSO ,* λ_{ex} *= 530 nm, (C-D) EtOH ,* λ_{ex} *= 514 nm, (E-F) MeOH ,* λ_{ex} *= 525 nm, (G-H) MeOH: EPPS (1:1, v/v, 10mM, pH 8.0) ,* λ_{ex} *= 525 nm*

Fluorescence Lifetime Study for Compound **4.6** with Cu^{2+} Ions

The fluorescence decay profiles and random distribution of weighed residuals of **4.6** and [Cu(**4.6**)$_2$] in DMSO are shown in figure 4.10. The concentration of the receptor on its own was 2.5×10^{-5} M and the ratio of **4.6** with $Cu(NO_3)_2$ was 2:1. The fluorescence decay plots are fitted to double exponentials with excellent χ^2 values of 1.03 and 1.04 for the free probe and the complex, respectively. This differs from the lifetime studies in chapter 3, whereby the data was fitted with single exponentials. Each of the samples were analyzed three times to ensure reproducibility of the results and the solution of the complex was allowed to equilibrate for 1 hour prior to analyzing the sample. For the unbound probe, two fluorescence lifetimes were observed of $\tau_1 = 1.70 \pm 0.147$ ns and $\tau_2 = 4.10 \pm 0.0618$ ns, whereas the lifetimes of the complex were found to be $\tau_1 = 1.68 \pm 0.282$ and $\tau_2 = 3.54 \pm 0.0412$. Though the τ_1 value for the unbound probe and the complex were almost identical, the values for τ_2 showed a larger difference between the fluorescence decays of the free and coordinated probe. The decrease in the lifetime of **4.6** upon complex formation is consistent with the data presented in chapter 3 for compound **3.11a** with Cu^{2+} and Fe^{3+} ions. Decreases in the fluorescence lifetime of rhodamine derivatives upon complex formation have also been reported throughout the literature and have been attributed to different fluorescence mechanisms such as PET, CHEF, FRET, and fluorescence quenching.[156-144]

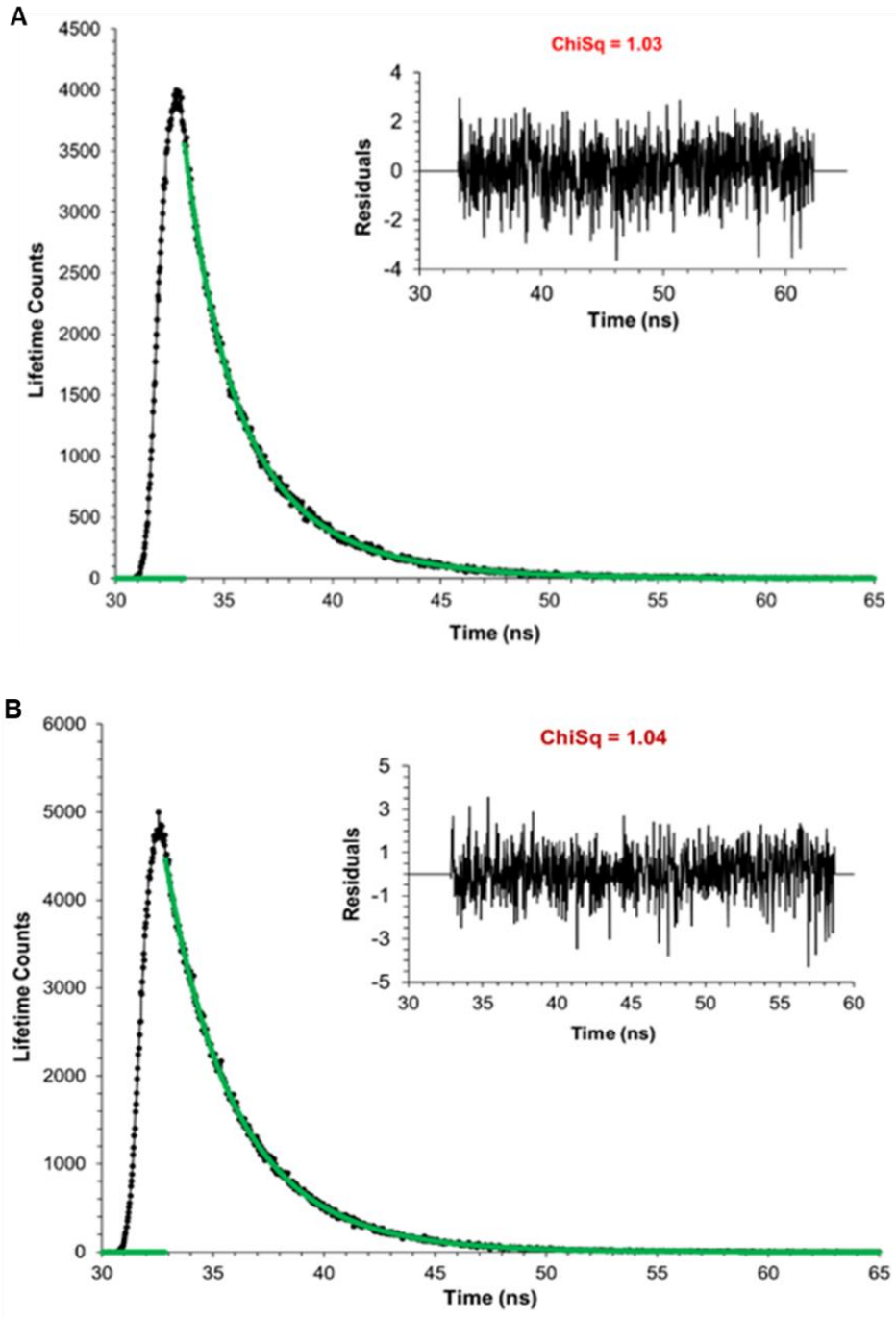

Figure 4.10 *Fluorescence decay profiles of (A)* ***4.6*** *and (B) [Cu(****4.6****)$_2$] in DMSO with residuals shown in inset.*

4.5 Summary

We have successfully prepared a water-soluble rhodamine 6G derivative that demonstrates improved selectivity for Cu^{2+} ions in organic and aqueous solvent over other metal ions. The structure of compound **4.6** was confirmed through elemental analysis, ^{1}H-NMR, ESI-MS and FT-IR spectroscopy. UV-Vis, steady state fluorescence and fluorescence lifetime studies were all performed to gain an understanding of how compound **4.6** interacts with Cu^{2+} ions. From the UV-Vis and Fluorescence studies we were able to determine optimal pH ranges between 8 and 10.5 for metal analysis as well as 2:1 binding stoichiometry between the probe and Cu^{2+} ions. Unfortunately, we were not able to conduct quantitative analysis in 100% aqueous solutions due to the probe becoming saturated very quickly- a consequence of the probes 2:1 binding with Cu^{2+} ions. We were, however, able to demonstrate a range of solvents systems in which **4.6** can be used to detect Cu^{2+} ions. We also proved that the [Cu(**4.6**)$_2$] complex is more stable in aqueous systems than it is in organic systems. Despite the lack of quantitative data in solutions comprised of mostly water, the high selectivity of compound **4.6** for Cu^{2+} and its ability to serve as a off-ON colorimetric and fluorescent sensor makes this probe a viable candidate for use in biological applications.

4.6 Experimental Methods

4.6.1 General Experimental Conditions

The same conditions that were applied to chapter 3 apply to this study. Refer to the general experimental conditions in chapter 3.7.1 for the conditions used in this study.

4.6.2 Mass Spectrometry Methods

Samples were prepared in HPLC grade MeOH at 1.0 $mg \cdot mL^{-1}$. The solutions of the free probe was spiked with 0.1% TFA prior to injecting the samples into the instrument. Data was acquired in both positive and negative mode.

4.6.3 Uv-Vis and Fluorescence Methods

For the absorbance titration studies, 2.5×10^{-3} M stock solutions of compound **4.6** were prepared by dissolving the appropriate 6.1 mg of the compound in 4mL of the selected solvent system. An Equimolar stock solution (2.5×10^{-3} M) of $Cu(NO_3)_2$ was also prepared from which a 1.0×10^{-3} M diluted solution of **4.6** was made. To prepare the 10 µM solution of the receptor, an 8 µL aliquot of the stock solution was added to a. quartz cuvette containing 1.992 mL of DMSO. During the titration, aliquots of 2.0 µL of the 1.0×10^{-3} M solution of Cu^{2+} were then added to the cuvette containing the receptor. The samples were stirred using a vortex for one minute between each addition of metal salt and the spectra were recorded after each addition.

The metal screen with compound **4.6** was performed by preparing a series of 25 µM solutions of compound **4.6** using the 2.5×10^{-3} M stock solution of the receptor. This

equates to dissolving 20 µL of the stock solution of the probe in 1.98 mL of solvent in a quartz cuvette. To these solutions were added aliquots of 40 µL of 2.5×10^{-3} M stock solutions of the metal salts. Each of the samples were allowed to equilibrate for 30 minutes prior to analysis of the absorbance spectra.

The fluorescence titration studies were performed by diluting 4.0 µL of the 2.5×10^{-3} M stock solution of the receptor up to 2 mL with the appropriate solvent in a quartz cuvette. During the titrations, aliquots of 4.0 µL of the 2.5×10^{-3} M stock solutions of $Cu(NO_3)_2$ were then added to the cuvette containing the receptor. The samples were stirred using a vortex for 2-3 minutes between each addition of the metal salt and the spectra were recorded after each addition.

4.6.4 Synthetic Methods

Preparation of sodium 3-formyl-4-hydroxybenzenesulfonate[157]

The title compound was prepared by a process similar to work published by Liu et al. Salicylaldehyde (2.65 mL, 25.0 mmol) was dissolved in 100 mL of MeOH in a 250 mL round bottom flask followed by the addition of aniline (2.28 ml, 25.0 mmol) to the flask. The solution was stirred under reflux conditions for 4 hours and monitored via TLC analysis to determine when all of the starting material had been used up. The solution was then cooled to room temperature and the solvent was removed under reduced pressure, yielding a pale-yellow liquid, N-phenyl-salicylaldimine (Intermediate **A**). Concentrated H_2SO_4 (15 mL, 98 wt %, density = 1.84 $g \cdot mL^{-1}$) was then added dropwise into the above liquid and the solution was stirred at 105 ˚C for 6 hours. At the end of this time, the contents of the flask were cooled and poured slowly into ice water with vigorous stirring,

resulting in a bright yellow solid precipitate which was then filtered and washed with ice water. The solid was then dissolved in boiling water and then allowed to cool. The yellow N-phenyl-5-sulfonato-salicylaldimine (Intermediate **B**) was filtered and washed with cold methanol and dried under vacuum (crude yield 2.48 g, 36%). Intermediate **B** and Na_2CO_3 (1.0g, 9.0 mmol) were then boiled in an open flask containing 20 mL deionized water for 2 hours. At the end of this time, glacial acetic was added to the cooled solution and the pH was adjusted to 5. The mixture was then cooled to 0 degrees and pale-yellow colored sodium 3-formyl-4-hydroxybenzenesulfonate was filtered off and washed 3 times with 15 mL aliquots of cold methanol followed by drying of the solid under vacuum. Yield 1.21g, 60%. ^{1}H NMR (400 MHz, DMSO): δ, ppm 9.98 (1H, s), 7.56 (1H, d, *J* = 2.6 Hz), 7.27 (1H, dd, *J* = 2.6, 9.2 Hz), 6.33 (1H, d, *J* = 9.2 Hz). ^{13}C NMR (100 MHz, DMSO) δ (ppm): 191.6, 176.2, 133.7, 130.34, 126.6, 123.4, 122.3. IR(ATR solid) 3403, 3293 $\nu_{O\text{-}H}$ sulfonate (m), 3153 $\nu_{O\text{-}H}$ alcohol (m), 1636 $\nu_{C=O}$ aldehyde (m).

*Preparation of Compound **4.6***

Sodium 3-formyl-4-hydroxybenzenesulfonate (0.5g, 2.2 mmol) was dissolved in 5.0 mL of deionized water and added to a solution of **3.9** (0.19g, 0.44 mmol) in 20 mL of methanol while stirring to ensure that both reagents dissolved completely. The mixture was refluxed at 80 ̊C for 72 hours after which time the solvent was reduced by ≈ 80% and the solid was filtered and washed with diethyl ether. The crude product was then purified by silica gel column chromatography (MeOH: DCM:TEA 80:18:2). Compound **4.6** was isolated as a light orange powder (0.21 g, 75%). ^{1}H NMR (400 MHz, MeOD): δ, ppm 8.55 (1H, d, *J* = 10.1 Hz), 8.01 (1H, d, *J* = 7.2 Hz), 7.65 (2H, t, *J* = 6.9 Hz), 7.59

(1H, t, J = 6.9 Hz), 7.51 (1H, d, J = 1.9 Hz), 7.11 (1H, d, J = 7.2 Hz), 6.85 (1H, d, J = 8.7 Hz), 6.45 (2H, s), 6.26 (2H, s), 3.25 (4H, q, J = 7.1 Hz), 1.89 (1H, s), 1.31 (6H, t, J = 7.2 Hz). ^{13}C NMR (100 MHz, DMSO) δ (ppm): 179.0, 165.1, 152.3, 151.4, 150.9, 148.9, 148.4, 134.0, 128.9, 128.5, 127.9, 126.7, 123.7, 122.9, 118.9, 117.4, 116.4, 104.2, 96.3, 66.3, 37.9, 15.6, 13.2. IR(ATR solid) 3401, 3293 $\nu_{O\text{-}H}$ sulfonate (m), 3159 $\nu_{O\text{-}H}$ alcohol (m), 1701 $\nu_{C=O}$ lactam, 1635 $\nu_{C=O}$ aldehyde (m). ESI mass spectrometry: m/z 611.0 ($[M]^+$); M^+ calculated 611.2.

CHAPTER V – Synthesis of an Artificial Siderophore

5.1 Natural Siderophores

The term siderophore is used to describe the low -molecular weight iron-binding agents secreted by bacteria and fungi under iron deficient conditions.[158] As expressed in chapter one of this work, iron regulation is central to the survival and function of almost all living organisms. Iron deficiency can compromise vital cellular processes such as respiration, gene regulation, photosynthesis, and the synthesis of amino acids, whereas an excess of unbound iron species can cause toxicity through the production of damaging radicals generated via Fenton chemistry.[159]

Whilst mammals typically obtain iron through their diets, bacteria and other microorganisms must acquire iron directly from their environment. Due to the scarcity of Fe^{2+} ions in aerobic environments (see chapter 1.4), Fe^{3+} ions must be utilized by bacteria to maintain sufficient cellular iron concentrations needed for survival.[160] Because Fe^{3+} species form insoluble hydroxides under aqueous conditions (except for in highly acidic environments with pH less than 3), solubilizing chelating ligands are required to mediate the uptake or Fe^{3+} ions by microorganisms.[160] Siderophores therefore contain chelating units that are optimized for binding to Fe^{3+} ions in aerobic and aqueous environments.

Bacterial siderophores generally contain catecholate ligands, while fungal siderophores exhibit hydroxamate iron binding units. Other common binding motifs observed in siderophores include carboxylates and α-hydroxycarboxylate (citrate) groups (figure 5.1).[161] The most efficient siderophores are those that are capable of adopting an octahedral coordination geometry upon binding to Fe^{3+} ions.[162] One example of this is Enterobactin. Enterobactin is a hexadentate catecholate siderophore produced by bacterial

species such as *Escherichia coli* and forms extremely stable 1:1 complexes with Fe^{3+} ions- displaying K_a values as high as 10^{49} M^{-1} (figure 5.2).[162] This compound is one of the strongest natural Fe^{3+} ion-binding motifs known at physiological pH (pH 7.4).

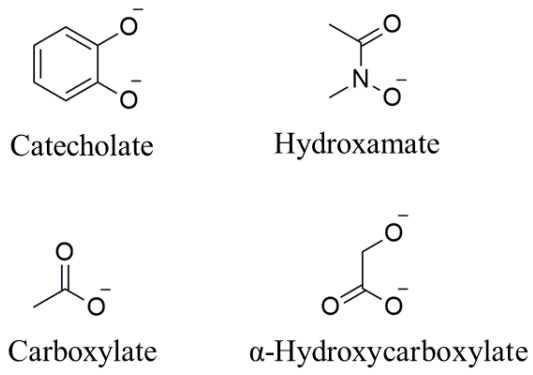

Figure 5.1 *Common siderophore chelating motifs*

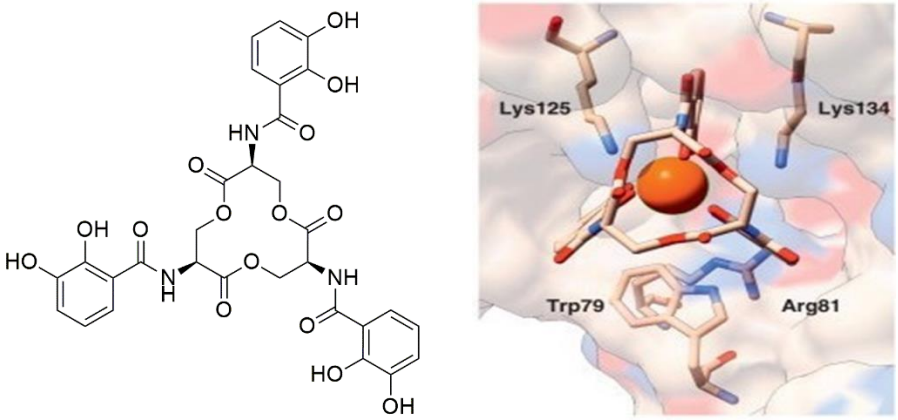

Figure 5.2 *Enterobactin-Fe^{3+} complex showing coordination through the catecholate groups to form an octahedral environment around the metal center. "Reprinted from Current Opinion in Chemical Biology, 17 (2), Sia, A. K.; Allred, B. E.; Raymond, K. N., Siderocalins: Siderophore binding proteins evolved for primary pathogen host defense, 150-157., Copyright (2013), with permission from Elsevier.*

5.2 Synthetic Siderophores

The ability to form stable iron complexes is often linked to two features of siderophores: denticity and lack of conformational flexibility.[160] By synthesizing

siderophores in the lab it is possible to derivatize these compounds to contain different signaling motifs that allow for the quantitative analysis of Fe^{3+} ions in different environments. Furthermore, the synthesis of siderophores allows for the production of gram to kg amounts of these compounds and eliminates the need to isolate siderophores from the growth medium of microorganisms which is often tedious and requires highly trained personnel.[163]

The synthesis of siderophore mimics has been reported extensively throughout the literature. However, the synthetic methods have proven to be challenging due to the need for chiral selectivity, whilst maintaining a hydrolyzable backbone.[160] The water-soluble nature of these compounds also complicates the isolation process. Rather than attempting synthesize siderophores that can be found in nature, scientists often design siderophore inspired LMFPs. These probes benefit from the selectivity of naturally occurring siderophores as well as their water-soluble nature, but do not to bind to metal ions as strongly naturally occurring siderophores. Furthermore, many siderophore inspired LMFPs serve as on-OFF fluorescence sensors (see chapter 1) which limits their sensitivity.

A siderophore-inspired nanoparticle-based biosensor was synthesized by Phillips at al., for the selective detection of Fe^{3+} ions in saline solution.[164] The water soluble gold nanoparticles utilize catechol binding motifs which form aggregates upon binding Fe^{3+} and produce a notable color change from red to purple (scheme 5.1). This color change corresponds to an absorbance enhancement at 700 nm, which is a much longer wavelength than any of the molecular probes that have been discussed in this work thus

far. The optical properties of **5.1** are owed to the size of the nanoparticles which were analyzed using tunneling electron microscopy and found to be ~40 nm.

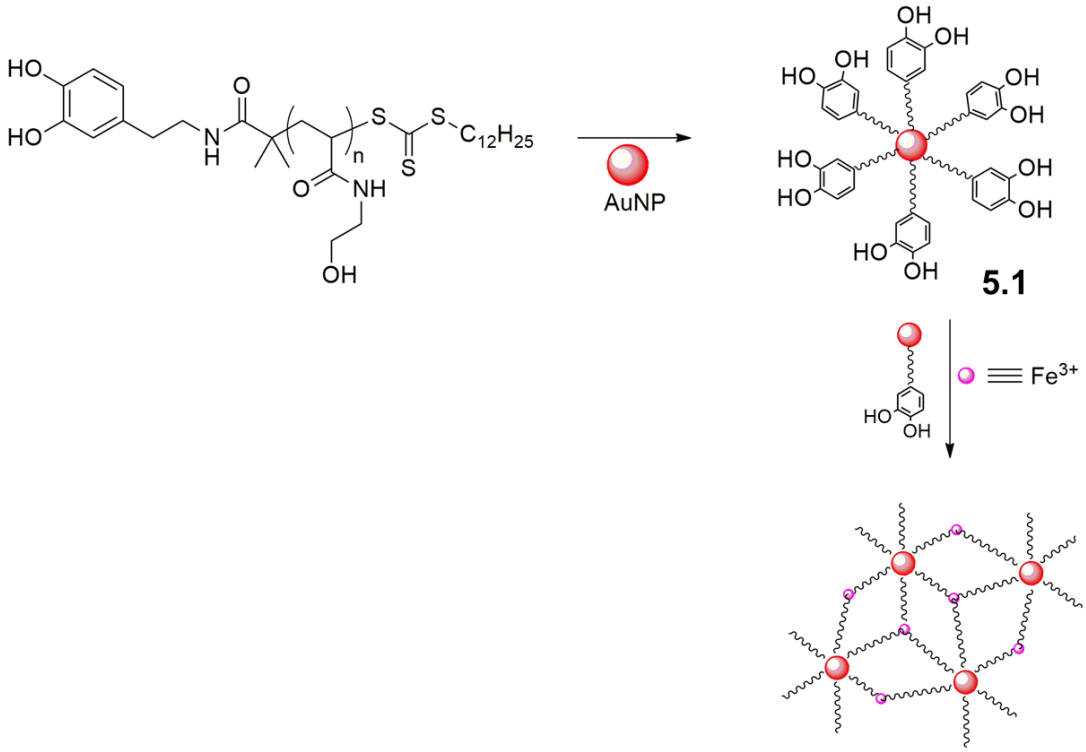

Scheme 5.1 *Proposed binding between **5.1** and Fe^{3+} ions in saline solution.*

Titration studies between **5.1** and Fe^{3+} ions were used to determine a LoD of 0.45 ppm which is slightly above the allowable concentration of Fe^{3+} ions in drinking water of 0.3 ppm, outlined by WHO.[50] Small absorbance enhancements were also observed in the Fe^{2+} ions and Cu^{2+} ions, however these were to a much lesser extent than was observed for Fe^{3+} ions. It is likely that in the oxygen-rich aqueous environment, Fe^{2+} ions were oxidized to Fe^{3+} ions which explains why a colorimetric response was observed in the presence of Fe^{2+} ions. Additionally, as we have shown in chapter 3 of this work, LMFPs that bind Fe^{3+} ions often also bind Cu^{2+} ions, therefore this response was to be expected.

The ability to tune the optical properties **5.1** by altering the particle size makes this system ideal for use in bioimaging applications which require long wavelength molecular probes (see chapter 4). Unfortunately, like many of the iron binding molecular probes reported in the literature, compound **5.1** serves solely as a colorimetric sensor due to the paramagnetic nature of Fe^{3+} ions. No fluorescence studies were reported by Phillips et al., therefore it remains unclear how effectively the fluorescence of **5.1** was quenched in the presence of Fe^{3+} ions.

An artificial ferrichrome-type siderophore, compound **5.2**, was synthesized by Ouchetto et al for selectively binding to Fe^{3+} ions in aqueous solution.[165] The fluorescent ferrichrome derivative was prepared by coupling the siderophore motif with a hydroxysuccinimidyl ester fluorescent probe. No absorbance studies were reported for **5.2**, however, the addition of Fe^{3+} ions to a solution **5.2** in MeOH and aqueous sodium acetate (80:20, v/v) resulted in a hypochromic shift at 538 nm in the fluorescence spectrum. Ouchetto et al., determined that the decrease in the fluorescence of **5.2** was the result of static quenching upon complex formation between **5.2** and the paramagnetic Fe^{3+} ion, however, no quenching constant was reported. Additionally, no binding constants nor LoDs were reported for this work which is unfortunate.

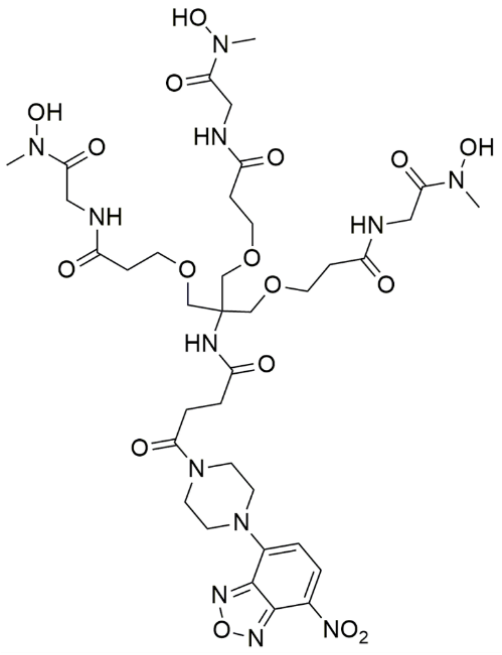

5.2

Figure 5.3 *Fluorescent ferrichrome mimic: compound* ***5.2***

Several other metal ions were analyzed to determine how interactions between the ions and **5.2** would affect the optical properties of the probe. The metals included Ca^{2+}, Mg^{2+} and Cu^{2+} ions. As expected, the addition of Cu^{2+} ions to the solution of **5.2** also significantly reduced the fluorescence signal observed at 538 nm. It would have been beneficial for the authors of this work to analyze other hard and borderline Lewis acids such as Al^{3+}, Fe^{2+} ions, which are known to form stable coordination compounds with hard Lewis bases and are also biologically relevant metal ions. The authors did however demonstrate the ability of compound **5.2** to mimic the behavior of naturally occurring ferrichrome toward Fe^{3+} ions as well as the ability of the probe to permeate S. cerevisiae, C. albicans, and T. foetus cellular membranes without adversely affecting the fluorescent properties of the probe.

Two pyochelin-based LMFPs, **5.3** and **5.4**,were synthesized by Noël et al., for the detection of Fe^{3+} ions in aqueous media as well as in cellular matrices.[166] Pyochelin is a siderophore produced by *Pseudomonas aeruginosa* and *Burkholderia cepacian*- these are Gram negative bacteria that rely on iron uptake for growth. The 4-nitro-benzo[1,2,5]oxadiazole (NBD) fluorophore was chosen due to its size and photophysical properties in aqueous media. No absorbance data or metal screens were reported for **5.3** and **5.4**, therefore it is unclear whether these probes are in fact selective for Fe^{3+} ions over other metal ions.

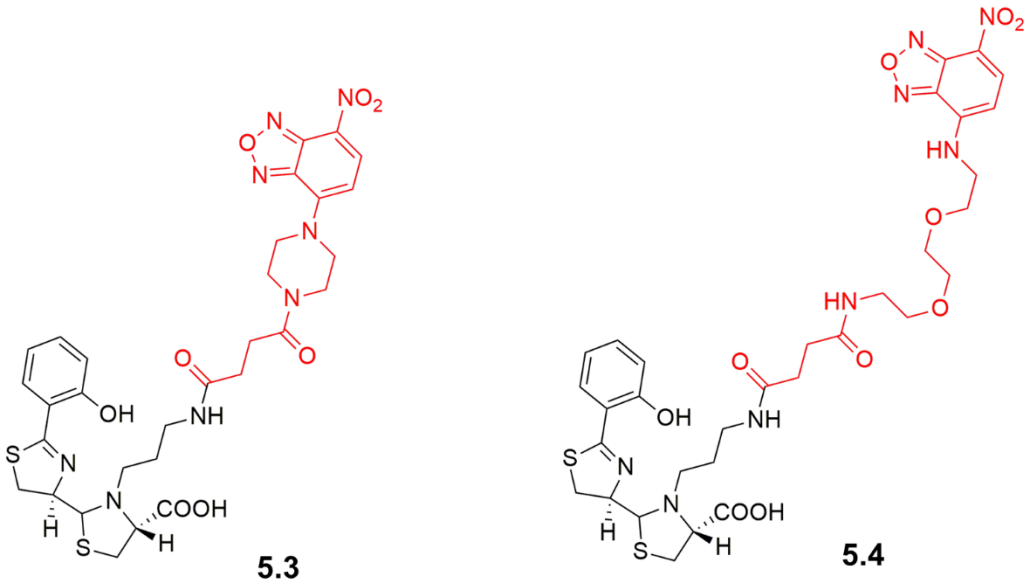

Figure 5.4 *Pyochelin- based LMFPs: compounds **5.3** and **5.4***

Unexpectedly, the addition of Fe^{3+} ions to solutions of **5.3** and **5.4** in Tris-HCl buffer (pH 8.0) resulted in notable fluorescent enhancements at 545 nm. A 320% fluorescence enhancement was observed in **5.4**, while a 290% enhancement was observed for **5.3**. The ability of **5.3** and **5.4** to detect Fe^{3+} ions in basic aqueous solution is unique for two reasons. Firstly, the formation of iron hydroxide precipitates in solution means

that compounds **5.3** and **5.4** are able to solubilize these precipitates in solution and form very stable complexes with Fe^{3+} ions. Secondly, the paramagnetic nature of the Fe^{3+} ions often quench the fluorescence of otherwise fluorescent compounds, which limits the use of many molecular probes. Fluorescence titration data was used to determine binding ratios as well as association constants between the probes Fe^{3+} ions using the Method of Continuous Variation. Job's plot data indicated 1:2 stoichiometry and an association constant of $K_{12} = 6.3 \times 10^{10}$ M^{-2} between Fe^{3+} ions and **5.3**, while 1:3 stoichiometry was observed between Fe^{3+} ions and **5.4** and an association constant of $K_{13} = 2.6 \times 10^{19}$ M^{-3}. These association constants are much larger than those reported for the iron binding motifs discussed in chapters 2 and 3 which is owed to the strong affinity of siderophores for Fe^{3+} ions.

Quantum yield analysis was carried out whereby the quantum yields of the building blocks of **5.3** and **5.4** (see regions highlighted in red in scheme 5.3) were set to 1 and all other compounds were cross references to these standards. The quantum yield of free probe **5.3** was found to be 0.19, while the Fe^{3+}-**5.3** complex was found to have a quantum yield of 0.32. It is proposed that in the absence of the metal ion the pyochelin moiety is able to quench the fluorescence of the NBD group, whereas the introduction of Fe^{3+} ions inhibits quenching of the NBD group by coordinating to the pyochelin moiety. The same behavior was observed for **5.4**, whereby the quantum yield of the free probe was found to be 0.39 while the coordination compound displayed a quantum yield of 0.58. It is likely that the increased distance between the pyochelin and NBD groups is responsible for the decrease in the fluorescence quenching of the NBD. No limit of detection values were reported for probes **5.3** and **5.4**, however, Noël et al., were able to

demonstrate the ability of both probes to permeate cellular membranes and detect as low as 1 μM concentrations of Fe^{3+} ions in *P. aeruginose* PAD07 cells.

Probes **5.1-5.4** all demonstrated the unique abilities of siderophore mimics to detect Fe^{3+} ions in aqueous media which can be challenging due to the formation of iron hydroxides at pH > 4 (see chapter 1). Each of these studies however highlight the some of the drawbacks of working with siderophore mimics. Compounds **5.1** and **5.2** were only able to be utilized as colorimetric probes and both reports lacked critical information such as binding constant, detection limits, and thorough metal screening to determine the selectivity of the probes. Noël et al., also failed to demonstrate. the selectivity of compounds **5.3** and **5.4** for Fe^{3+} ions as no metal screens were performed and no absorbance data was reported. Furthermore, the quantum yield data reported in the study was relative to the building blocks of the **5.3** and **5.4** and should have instead been crossed referenced to the quantum yields of well-known chromophores (See section 3.5.5).

5.3 Sensor Design

Based on the knowledge that we have gained regarding the role of solvents, counterions and coordination environments in metal ion selectivity, we have chosen to design a siderophore-inspired rhodamine-based LMFP (compound **5.13**). As we have shown in chapters 2 and 3, rhodamine dyes can be modified to improve the water solubility of the probes without compromising the optical properties of the chromophore. These chromophores also allow for analyte detection in broad range of organic and aqueous solvent systems. In contrast to many of the probes highlighted in our literature

searches, the rhodamine-based LMFPs that we have designed (chapters 3 and 4)do not undergo fluorescence quenching in the presence of paramagnetic Cu^{2+} and Fe^{3+} ions. As a result, we have chosen to incorporate a similar core structure in the design of compound **5.13**.

As it is our goal to synthesize a siderophore mimic, compound **5.13** contains two catechol groups as well as the lactam moiety which will allow the probe to behave as a hexadentate ligand. By increasing the number of binding sites on the molecular probe we expect to form an extremely stable and thermodynamically favored coordination compound that will be unlikely to undergo decomplexation in the presence of oxygen containing solvents (see section 3.5.5). Furthermore, we postulate that the use of catechol groups, which serve as hard Lewis bases, will improve the selectivity of the probe for Fe^{3+} over other competing metal ions in aqueous media.

The full synthesis of compound **5.13** is still underway. We have however successfully synthesized compounds **5.11** and **5.12** and are exploring methods that will improve the reaction time as well as increase the product yield as we move forward to the desired product.

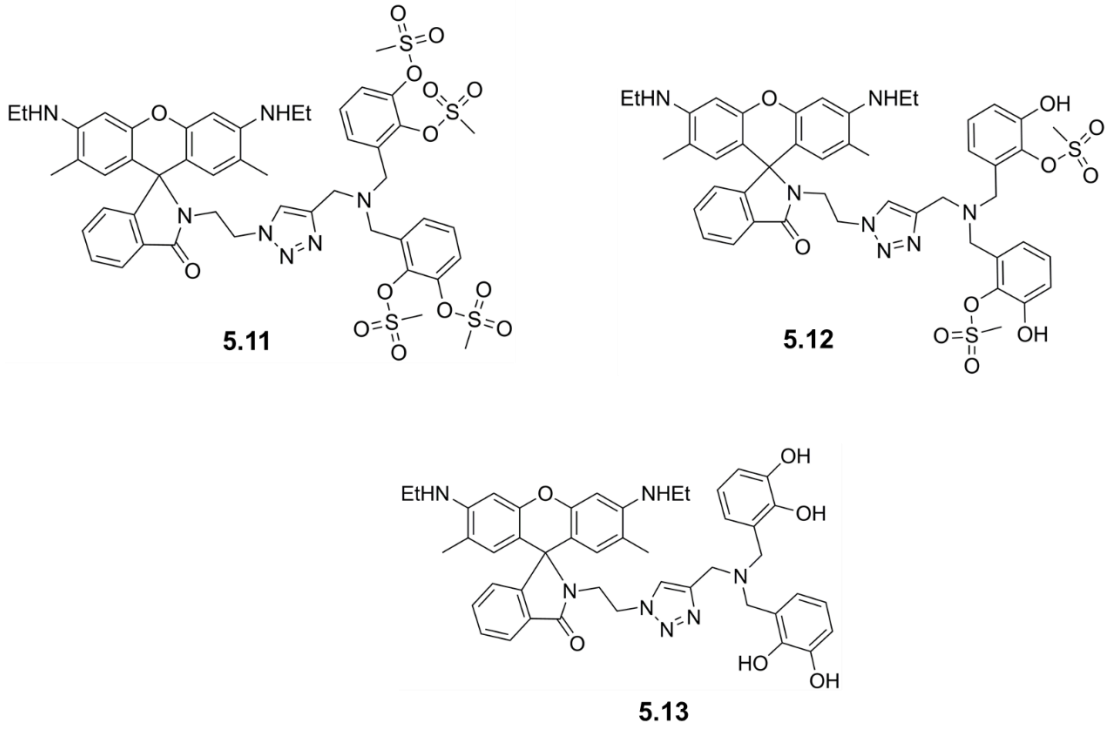

5.11

5.12

5.13

Figure 5.5 *Compounds* ***5.11****,* ***5.12****, and* ***5.13****.*

5.4 General Synthesis and Characterization

Compound **5.11** was prepared by first synthesizing rhodamine 6G azide (compound **5.6**) via a condensation reaction between 2-azidoethylamine and rhodamine 6G. The product was isolated as a dark pink solid in 85-95% yield. Conversion of the ester group of rhodamine 6G to the azide was confirmed via ESI-MS, proton NMR spectroscopy and FT-IR spectroscopy. The emergence of a strong azide band at 2100 cm^{-1} in the FT-IR spectrum as well as the disappearance of the methyl signal of the ester ~1.00 ppm, verified complete conversion to **5.6**.

Compound **5.6** was then reacted with compound **5.10** via a copper catalyzed click reaction to afford compound **5.11** as a light orange glassy solid (scheme 5.4). Conversion of the starting material to products was confirmed by the disappearance of the terminal

alkyne proton signal ~2.33 ppm which appears as a triplet due to long range coupling with the CH_2 protons adjacent to the alkyne. The disappearance of the terminal alkyne signal is indicative that the alkyne group on compound **5.10** had completely reacted with compound **5.6**, forming the triazole moiety. Formation of the triazole was also confirmed by the appearance of a singlet at 7.43 ppm, corresponding to the proton on the triazole moiety.

Deprotection of the catechol groups was attempted using lithium aluminum hydride at room temperature. Deprotection of two of the alcohols was verified using ESI-MS as well as proton NMR spectroscopy. The m/z signal of compound **5.11** appears at mz/ =1094.3, accounting for [**5.11** + H]$^+$. In contrast, the m/z signal for **5.12** appears at m/z = 938.4, corresponding to [**5.12** + H]$^+$. Furthermore, the ^{1}H-NMR spectrum of **5.12** only displays one siglet at 3.19 ppm accounting for six methyl protons on two mesyl group, whereas, **5.11** shows two distinct singlets at 3.27 and 3.35 ppm which each integrate for six protons.

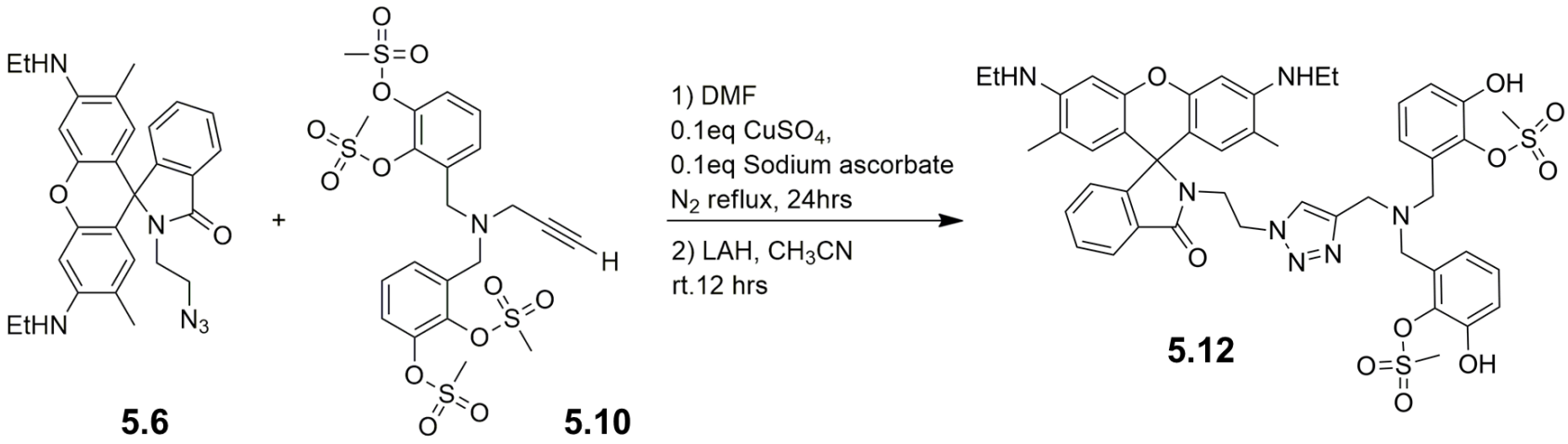

Scheme 5.2 *General synthesis of compound* ***5.12***

5.5 Experimental Methods

5.5.1 General Experimental Conditions

The same conditions that were applied to chapter 3 apply to this study. Refer to the general experimental conditions in chapter 3.7.1 for the conditions used in the characterization of each of the compounds in this chapter.

5.5.2 Mass Spectrometry Methods

Samples were prepared in HPLC grade MeOH or CH_3CN at 1.0 $mg \cdot mL^{-1}$. Data was acquired in both positive and negative mode.

5.5.3 Synthetic Methods

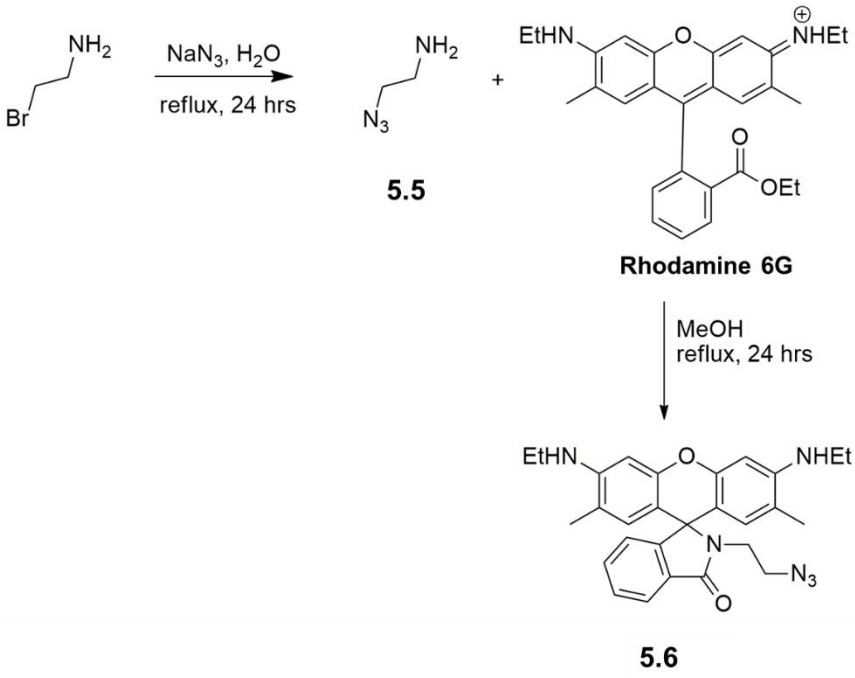

Figure 5.6 *General synthesis of compounds **5.5** and **5.6***

*Preparation of compound **5.5***

The experimental procedure for the synthesis of compound **5.5** was modified from literature.[52] Sodium azide (1.77 g, 0.026 mol) and 2-bromoethylamine hydrobromide (1.77 g, 0.009 mol) were added to a 50 mL RBF and dissolved in 5.0 mL of deionized water. The solution was then and refluxed for 24 hours after which a small aliquot of the sample was removed from the flask and analyzed via FT-IR spectroscopy to confirm the conversion of the bromide to the azide. The reaction mix was then cooled to 0 °C followed by the addition of 10 M KOH to the solution to adjust the pH to 9. The solution was then extracted with ether (3 × 20 mL) followed by washing of the combined organic layers with 20 mL of brine solution. The organic layer was then dried using sodium sulfate (Na_2SO_4) followed by filtration of the product over celite. Lastly, the solvent was removed under reduced pressure yielding compound **5.5** as a yellow oil. The yield of compound **5.5** was not calculated due to the volatility of the compound. As a result, in all future experiments compound **5.5** was not isolated prior to being reacted with rhodamine 6G. ^{1}H NMR (400 MHz, $CDCl_3$) δ, ppm: 3.35 (1H, t, *J* = 5.6 Hz), 2.86 (2H, t, *J* = 5.6 Hz), 1.52 (2H, s). ^{13}C NMR (100 MHz, $CDCl_3$) δ, ppm: 53.6, 40.3. IR; 3363 ν_{N-H} (br), 2938 ν_{C-H} (w), 2097 $\nu_{N=N=N}$ (m).

*Preparation of compound **5.6***

Rhodamine 6G (0.495 g, 0.001 mol) was dissolved in 20 mL of MeOH and added to the solution of compound **5.5**. The mixture was refluxed for 24 hours, after which ~90% of the solvent was removed under reduced pressure, yielding a dark pink precipitate. The precipitate was then filtered and washed with cold deionized water (3 × 20 mL) yielding

compound **5.6** as a dark pink powder which was dried overnight in a desiccator. Yield 0.473 g, 95.0 %. ^{1}H NMR (400 MHz, $CDCl_3$) δ, ppm: 7.96 - 7.93 (1H, m), 7.48 - 7.45 (2H, m), 7.07 - 7.04 (1H, m), 6.35 (2H, s), 6.23 (2H, s), 3.53 (2H, t, *J* = 5.1 Hz), 3.29 (2H, t, *J* = 7.0 Hz), 3.26 - 3.18 (4H, m), 2.94 (2H, t, *J* = 7.0 Hz), 1.91 (6H, s), 1.33 (6H, t, *J* = 7.1 Hz). ^{13}C NMR (100 MHz, $CDCl_3$) δ, ppm: 168.4, 153.5, 151.7, 147.6, 132.7, 130.8, 128.4, 128.2, 123.8, 123.0, 105.7, 96.5, 65.0, 48.8, 39.0, 38.4, 16.7, 14.7. IR; 3369 ν_{N-H} (w), 2969, 2928 ν_{C-H} (w), 2100 $\nu_{N=N=N}$ (m), 1682 $\nu_{C=O}$ (s). HRMS: m/z 483.249894 ($[M + H]^+$); M^+ calculated 482.2

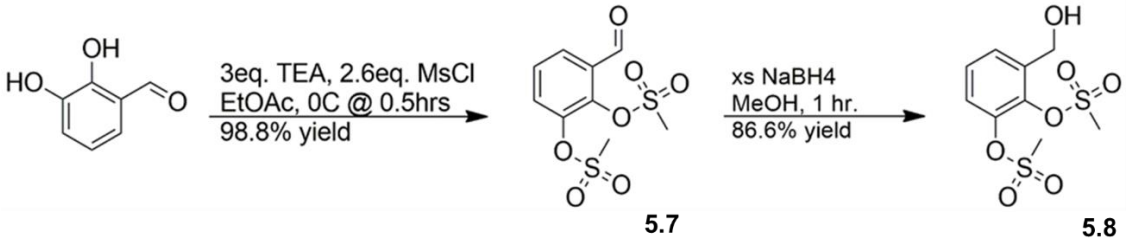

Figure 5.7 *General synthesis of compounds **5.7** and **5.8***

*Preparation of compound **5.7***

2,3-dihydroxybenzaldehyde (2.00 g, 0.014 mmol) was dissolved in ethyl acetate (50 mL) in a 100 mL RBF (100 mL) and cooled to 0 °C. Triethylamine (TEA, ~6.0 mL, 0.042 mol) was then added to the RBF followed by the dropwise addition of methanesulfonyl chloride (2.9 mL, 0.038 mol). A yellow precipitate was immediately observed. The mixture was allowed to stir at room temperature for an additional 30 minutes after which TLC analysis was used to confirm conversion of the starting material to **5.7**. The reaction was then quenched with water (~30 ml) followed by extraction with EtOAc (3 × 20 mL). The combined organic layers were then dried using Na_2SO_4 and filtered over celite. The

filtrate was then concentrated under reduced pressure to remove excess solvent which yielded **5.7** as a thick orange oil. Yield 4.20 g, 98.8% yield. ^{1}H NMR (400 MHz, $CDCl_3$) δ, ppm: 10.23 (1H, s), 7.89 (1H, dd, *J* = 1.5, 7.9 Hz), 7.73 (1H, dd, *J* = 1.6, 8.2 Hz), 7.52 (1H, t, *J* = 8.0 Hz), 3.44 (3H, s), 3.30 (3H, s). ^{13}C NMR (100 MHz, $CDCl_3$) δ, ppm: 142.3, 141.9, 131.7, 129.2, 128.9, 128.5, 39.7, 38.8. IR; 3030 ν_{C-H} (w), 2929, 2894 ν_{C-H} (w), 1699 $\nu_{C=O}$ (s).

*Preparation of compound **5.8***

Compound **5.7** (2.00 g, 0.007 mol) was dissolved in MeOH (~ 3.0 mL) and added to a 20 mL RBF equipped with a stir bar. Sodium borohydride (0.265 g, 0.007 mol) was then dissolved in MeOH (~5 mL) and added dropwise to the solution of **5.7** over 10 minutes. The mixture was then stirred for 30 minutes, during which time the solution changed from orange to a pale-yellow color. The MeOH was then removed under reduced pressure and the crude product was extracted with EtOAc and deionized water. The aqueous layer was extracted three times with EtOAc (20 mL), after which the combined organic layers were washed with brine and dried using Na_2SO_4. The solution was then filtered over celite, followed by concentration of the filtrate under reduced pressure to yield compound **5.8** as a thick, pale-yellow oil. Yield 1.74 g, 86.6% yield. ^{1}H NMR (400 MHz, $CDCl_3$) δ, ppm: 7.49 (1H, dd, *J* = 2.1, 7.4 Hz), 7.39 (2H, dd, *J* = 2.0, 8.2 Hz), 7.34 (2H, t, *J* = 7.8 Hz), 4.73 (2H, s), 3.38 (3H, s), 3.21 (3H, s), 2.74 (1H, s). ^{13}C NMR (100 MHz, $CDCl_3$) δ, ppm: 141.7, 139.1, 137.5, 128.9, 128.4, 122.7, 59.9, 39.4, 38.4. IR; 3533 ν_{O-H} (s), 3021 ν_{C-H} (w), 2936 ν_{C-H} (w).

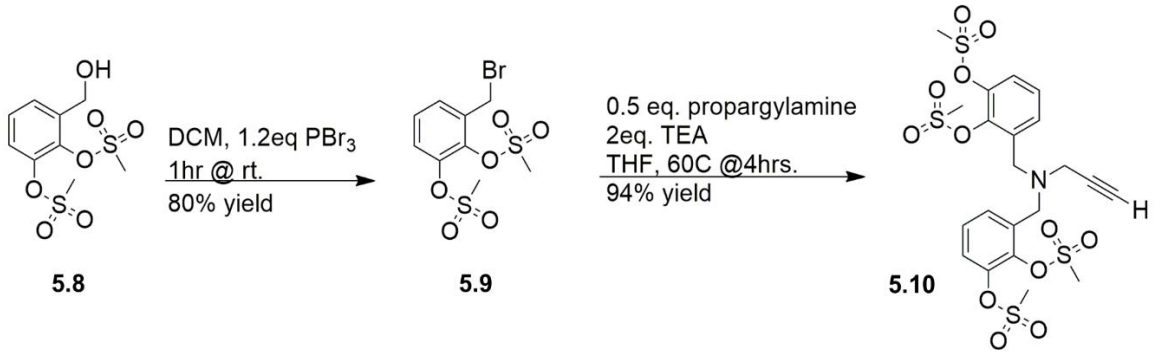

Figure 5.8 *General Synthesis of compounds **5.9** and **5.10***

*Preparation of compounds **5.9***

Compound **5.8** (1.66 g, 0.006 mol) was added to a 50 mL RBF followed by the addition of DCM (~10 mL). The contents of the flask were cooled to 0 °C followed by the dropwise addition phosphorous tribromide (0.639 mL, 0.007 mol) to the flask. The solution was allowed to stir at room temperature for one hour, after which the contents of the flask were poured into a separatory funnel. The solution was then extracted with DCM (3 × 15 mL) and water (15 mL). The combined organic layers were then washed with brine (20 mL) and dried using Na_2SO_4. The solution was filtered over celite and the filtrate was concentrated under reduced pressure to yield compound **5.9** as a beige solid (1.60 g, 80% yield). ^{1}H NMR (400 MHz, $CDCl_3$) δ, ppm: 7.49 (1H, dd, *J* = 1.7, 3.7 Hz), 7.46 (1H, dd, *J* = 1.6, 4.5 Hz), 7.35 (1H, dd, *J* = 7.7, 8.4 Hz), 4.60 (2H, s), 3.46 (3H, s), 3.24 (3H, s). ^{13}C NMR (100 MHz, $CDCl_3$) δ, ppm: 142.0, 139.4, 134.5, 130.2, 128.4, 123.5, 39.9, 38.4, 26.3. IR; 3084, 3032 ν_{C-H} (w), 2934 ν_{C-H} (w), 1586 $\nu_{C=C}$ (w).

*Preparation of compound **5.10***

Compound **5.9** (0.50 g, 0.001 mol), THF (~10 mL), TEA (0.390 mL, 0.003 mol), and propargylamine (0.096 mL, 0.001 mol) were added to a 50 mL RBF. The solution was then stirred at reflux for 4 hours. Another equivalent of compound **5.9** (0.50 g, 0.001 mol), as well as TEA (0.390 mL, 0.003 mol) was added to RBF and the mixture was allowed to reflux for an additional 12 hours. Once the reaction was complete, the THF was evaporated under reduced pressure and the contents of the RBF were transferred to a separatory funnel and extracted with DCM (3 ×15 mL) and water (20 mL). The combined organic layers were then washed with brine (20 mL) and dried with Na_2SO_4 followed by filtering of the solution over celite. The filtrate was then concentrated under reduced pressure to yield compound **5.10** as a golden yellow solid. Yield 0.57 g, 94%. ^{1}H NMR (400 MHz, $CDCl_3$) δ, ppm: 7.57 (1H, dd, *J* = 1.6, 7.8 Hz), 7.50 (1H, dd, *J* = 1.6, 7.7 Hz), 7.42 (1H, dd, *J* = 1.7, 5.2 Hz), 7.40 (1H, dd, *J* = 1.8, 5.3 Hz), 7.33 (2H, dt, *J* = 2.4, 11.9 Hz), 4.01 (2H, s), 3.90 (2H, s), 3.46 (2H, d, *J* = 2.4 Hz), 3.44 (3H, s), 3.35 (3H, s), 3.24 (3H, s), 3.22 (3H, s), 2.27 (1H, t, *J* = 2.4 Hz). ^{13}C NMR (101 MHz, $CDCl_3$) δ, ppm: 141.9, 140.2, 135.1, 129.7, 127.9, 122.2, 51.9, 42.3, 39.7, 38.3. IR; 3283 $\nu_{sp\ C\text{-}H}$ (w), 3033 $\nu_{sp^2\ C\text{-}H}$ (w), 2921, 2850 $\nu_{sp^3\ C\text{-}H}$ (w), 1584 $\nu_{C=C}$ (w). HRMS: m/z 634.015562 ($[M + Na]^+$); M^+ calculated 611.0.

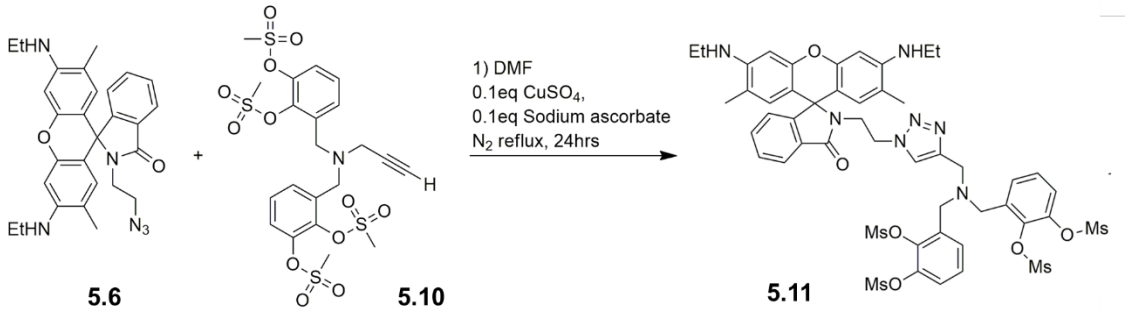

Figure 5.9 *Preparation of compound **5.11***

*Preparation of compound **5.11***

Compound **5.6** (0.11 g, 0.228 mmol) and ompound **5.10** (0. 127 g, 0.208 mmol) were added to a 50 mL 2-neck RBF followed by the addtion of DMF (~5 mL) and a stir bar. The RBF was then flushed with N_2 gas and the solution was stirred and heated to 70 C to ensure that all reagents completely dissolved. Copper(II) sulphate pentahydrate (5.18 mg, 0.0208 mmol) and L-ascorbic acid (41.11 mg, 0.208 mmol) were then dissolved in deionized water (~1 mL) and added to the RBF dropwise via a syringe. The solution was allowed to reflux for 24 hours, afterwhich the contents of the flask were transferred to a separatory funnel and extracted with DCM (3 × 15 mL) and water (~10 mL). The combined organic layers were then washed with deionized water (3 ×10 mL) to ensure the removal of DMF from the organic layer. The organic layer was dried with Na_2SO_4 followed by filtration of the solution over celite. The pink filtrate was then concentrated under reduced pressure and redisolved in a mixture of 90:10 $CHCl_3$ to be separated via column chromatogrophy. Compound **5.11** was isolated as a light pink, glassy solid and dried overnight in a dessicator. Yield (0.143 g, 63%). ^{1}H NMR (400 MHz, CD_3CN): δ, ppm 7.77 - 7.73 (1H, m), 7.66 (2H, dd, J = 2.3, 7.1 Hz), 7.48 (2H, ddt, J = 2.1, 12.4, 10.9

Hz), 7.42 (1H, s), 7.37 - 7.30 (4H, m), 6.99 - 6.95 (1H, m), 6.32 (2H, s), 6.16 (2H, d, J = 0.8 Hz), 4.11 (2H, t, J = 4.9 Hz), 4.05 (2H, t, J = 6.6 Hz), 3.76 (4H, s), 3.62 (2H, s), 3.47 (2H, q, J = 4.5 Hz), 3.35 (6H, s), 3.27 (6H, s), 3.22 - 3.14 (4H, m), 1.83 (6H, s), 1.25 (6H, t, J = 7.2 Hz). ESI mass spectrometry: m/z 1094.3 ($[M + H]^+$); M^+ calculated 1093.3

CHAPTER VI Conclusion

The research presented in this dissertation is a part of a broad study that investigates the design and synthesis of LMFPs for transition metal ions. Chapter two highlighted the self-assembly process between compound **2.4** and Fe^{3+} ions in purely organic systems, specifically CH_3CN. Despite the addition of a water-soluble sugar motif to the hydrophobic pyrene chromophore, compound **2.4** was not able to detect Fe^{3+} ions in aqueous environments. The inability to measure Fe^{3+} ions in aqueous solution is due to the hydrolysis of iron species in water as well as inhibition of the self-assembly process by water molecules.

Though we were unable to use **2.4** to measure Fe^{3+} ions in aqueous systems, we did gain valuable information regarding the role of solvent systems in metal ion coordination, as well as how the formation of coordination compounds affects the fluorescence quantum yields and lifetimes of LMFPs. We were able to prove, through literature searches and experimental data, that pyrenyl derivatives exhibit decreased fluorescence lifetimes, molar extinction coefficients, and fluorescence quantum yields than unmodified pyrene. The formation of coordination compounds between pyrene derivatives and metal ions however increases the number of radiative decay processes within the species which in turn further decreases the fluorescence lifetime but increases the fluorescence quantum yield of the system. With our knowledge of coordination environments and the role of solvent systems, we chose to switch our focus to the rhodamine chromophore as these molecules are well known for their characteristic brightness in a broad range of solvent systems.

Chapter 3 of this dissertation reinforced some of the findings of chapter 2 but went a step further. With the use of compound **3.10**, we showed that oxygen containing solvents in general i.e., MeOH, DMSO, THF and H_2O, inhibit binding between LMFPs and metal ions if the coordination compound formed is not very stable. By utilizing the chelate effect, we were able to demonstrate the improved stability of coordination compounds formed between metal ions and **3.11a**, **3.12**, and **3.13** in organic and aqueous solvents. We also proved the importance of analyzing metal salts with different counterions as the counterion can adversely affect complex stability; this was observed between compound **3.11a** and $FeCl_3$ where $K_{11} < 1$.The bridging nature of the Cl^-anion is likely responsible for the formation of ill-defined species in solution.

One unique and unexpected aspect of the LMFPs in chapter 3 is highlighted in the fluorescence studies. Though Cu^{2+} and Fe^{3+} ions are paramagnetic, the coordination of these metal ions to compound **3.11a** resulted in a fluorescence enhancement rather than a quenching mechanism. This allowed us to be able to study the lifetimes of the coordination compounds formed between **3.11a** and Cu^{2+} and Fe^{3+} ions. Similar to chapter 2, the formation of the coordination compounds led to an decrease in the fluorescence lifetime which is indicative of an increase in the number or radiative decay processes. In chapter 3, we were also able to demonstrate the improved selectivity of compounds **3.11a** and **3.12** for Cu^{2+} ions as we moved from organic to aqueous systems. This improved selectivity is attributed the formation of iron hydrolysis products in aqueous solutions above pH = 4. The propensity of these probes to bind to Cu^{2+} ions in aqueous solution led us to synthesize a water soluble LMFP, compound **4.6.**

Compound **4.6** proved to be selective for Cu^{2+} ions in organic and aqueous solvents. Even though **4.6** is 100% water soluble, quantitative metal analysis in purely aqueous solutions proved to be more challenging than we expected. The use of water as a solvent requires longer times for samples to equilibrate than is required for organic solvents. Furthermore, protonation of the rhodamine chromophore and subsequent ring opening is readily observed in aqueous systems. The use of buffered solutions to inhibit ring opening also presented new challenges as many buffers tend to coordinate to Cu^{2+} ions. As a result, we found that mixtures of organic and aqueous solvents were necessary to determine binding constants between **4.6** and Cu^{2+} ions. Lastly, because we maintained the same coordination environment and signaling motif that was utilized in chapter 3, compound **4.6** was able to be used as a fluorescence sensor for Cu^{2+} ions in aqueous systems. This is significant because not only because Cu^{2+} ions typically act as fluorescence quenchers, but water is also known to quench the fluorescence of fluorophores.

Finally, chapter 5 of this work focused on the synthesis of a siderophore inspired LMFP. Having proved that our probes are selective for Fe^{3+} and Cu^{2+} ions in a range of solvents, we believe the addition of catechol motifs to the rhodamine 6G backbone will allow for the detection of Fe^{3+} ions in aqueous solution. These catechol groups would act as solubilizing agents, similar to the catechol groups on Enterobactin. The synthesis of compound **5.13** has proven to be more challenging that initially expected, however once the probe is isolated, we will conduct in depth analyses to determine the selectivity of the probe as well as its ability to bind Fe^{3+} ions in aqueous solutions.

APPENDIX A

A.1 Additional Tables and Figures

Table A.1 *Classification of species as Hard, Soft, or borderline Lewis acids and bases*

Type of Acid/Base	**Characteristics**	**Examples**
Hard acids	• Small ionic radii (<90 pm). • High positive charge. • Empty orbitals in their valence shells. • Low electronegativity (0.7-1.6) and low electron affinity. • Likely to be strongly solvated. • High energy LUMO.	H^+, Li^+, Na^+, K^+, Be^{2+}, Mg^{2+}, Ca^{2+}, Sr^{2+}, Sn^{2+} Al^{3+}, Ga^{3+}, In^{3+}, Cr^{3+}, Co^{3+}, Fe^{3+}, Ir^{3+}, La^{3+}, Si^{4+}, Ti^{4+}, Zr^{4+}, Th^{4+},U^{4+}, VO^{2+} , UO_2^{2+} $BeMe_2$, BF_3, BCl_3, $B(OR)_3$, $AlMe_3$
Soft acids	• Large radii (>90 pm). • Low or partial positive charge. • Completely filled orbitals in their valence shells. • Intermediate electronegativities (1.9-2.5) • Low energy LUMOs	Cu^+, Ag^+, Au^+, Hg^+ , Cs^+, Tl^+ , Hg^{2+} , Pd^{2+}, Cd^{2+} , Pt^{2+} Metal atoms in zero oxidation states BH_3
Borderline acids		Fe^{2+} , Co^{2+} , Ni^{2+} , Cu^{2+} , Zn^{2+} , Pb^{2+} , $B(CH_3)_3$, SO_2, NO^+
Hard bases	• Small radii (around 120pm) & highly solvated. • Electronegative atomic centers (3.0-4.0). • Weakly polarizable. • Difficult to be oxidized. • High energy HOMO.	H_2O, OH^-, F^-, Cl^-, CH_3CO_2-, PO_4^{3-}, SO_4^{2-}, CO_3^{2-}, NO_3^-, ClO_4^-, ROH, RO^-, R_2O, NH_3, RNH_2, N_2H_4

Table A.2 *Advantages and disadvantages of several transition metal ions on human health, as well as the allowable daily intake concentrations in adults as defined by the World Health Organization (WHO)*[50]

Metal Ion	Essential Biological role	Deficiency	Excess	Upper limit allowable intake in adults ($mg \cdot day^{-1}$)
Cu^{2+}	Oxygen and electron transport, and aerobic respiration	Anemia-like symptoms, neutropenia, bone abnormalities, hypopigmentation, impaired growth, increased incidence of infections, osteoporosis, and hyperthyroidism	Generation of reactive oxygen species, and Wilsons's disease	1-1.5
Hg^{2+}	N/A	N/A	Paresthesia, loss of physical coordination, heart attack, death	0.0001
Pb^{2+}	N/A	N/A	Adversely affects almost every organ system in the body	0.005
Fe^{2+}, Fe^{3+}	Oxygen and electron transport	Iron-deficiency anemia	Produces highly reactive free radicals that can damage cellular components and lead to	45

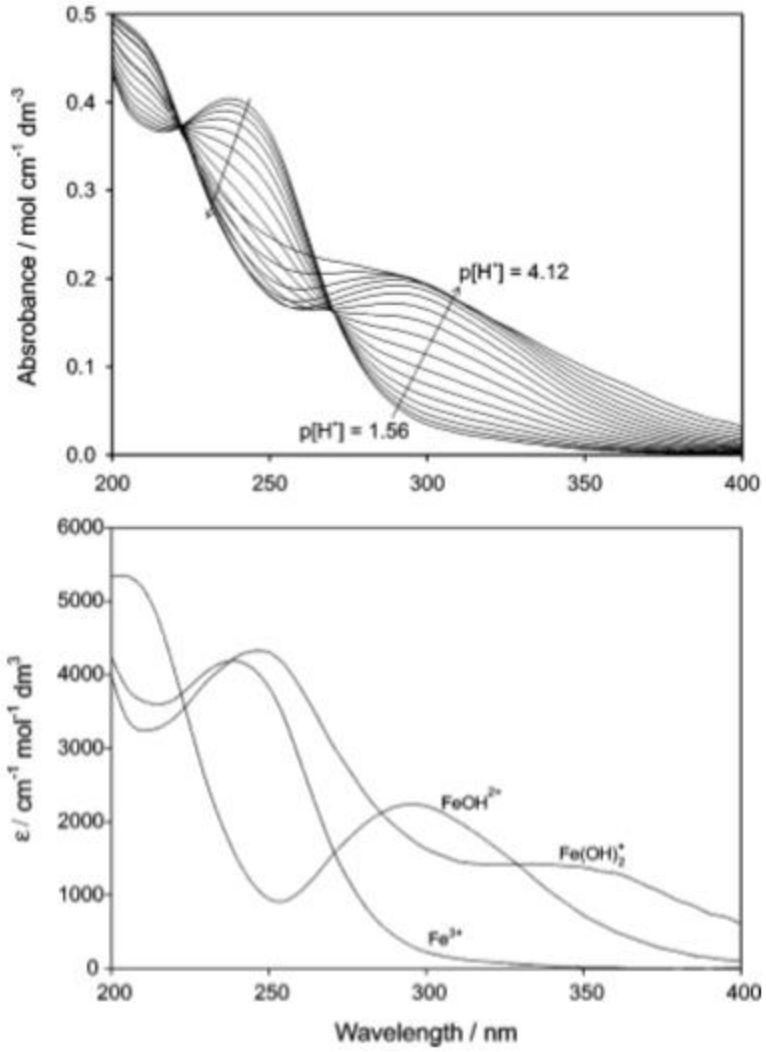

Figure A.1 *Fe^{3+} absorption spectra as a function of p[H^+] at 1.0 M $NaClO_4$. [Fe^{3+}]= 1.91 ×10^{-5} M, and 50mm optical path length. "Reprinted with permission from (Brown, P. L.; Ekberg, C., First Transition Series Metals. In Hydrolysis of Metal Ions Vol. 2.). Copyright (2016) John Wiley and Sons."*

A.2 NMR Spectra

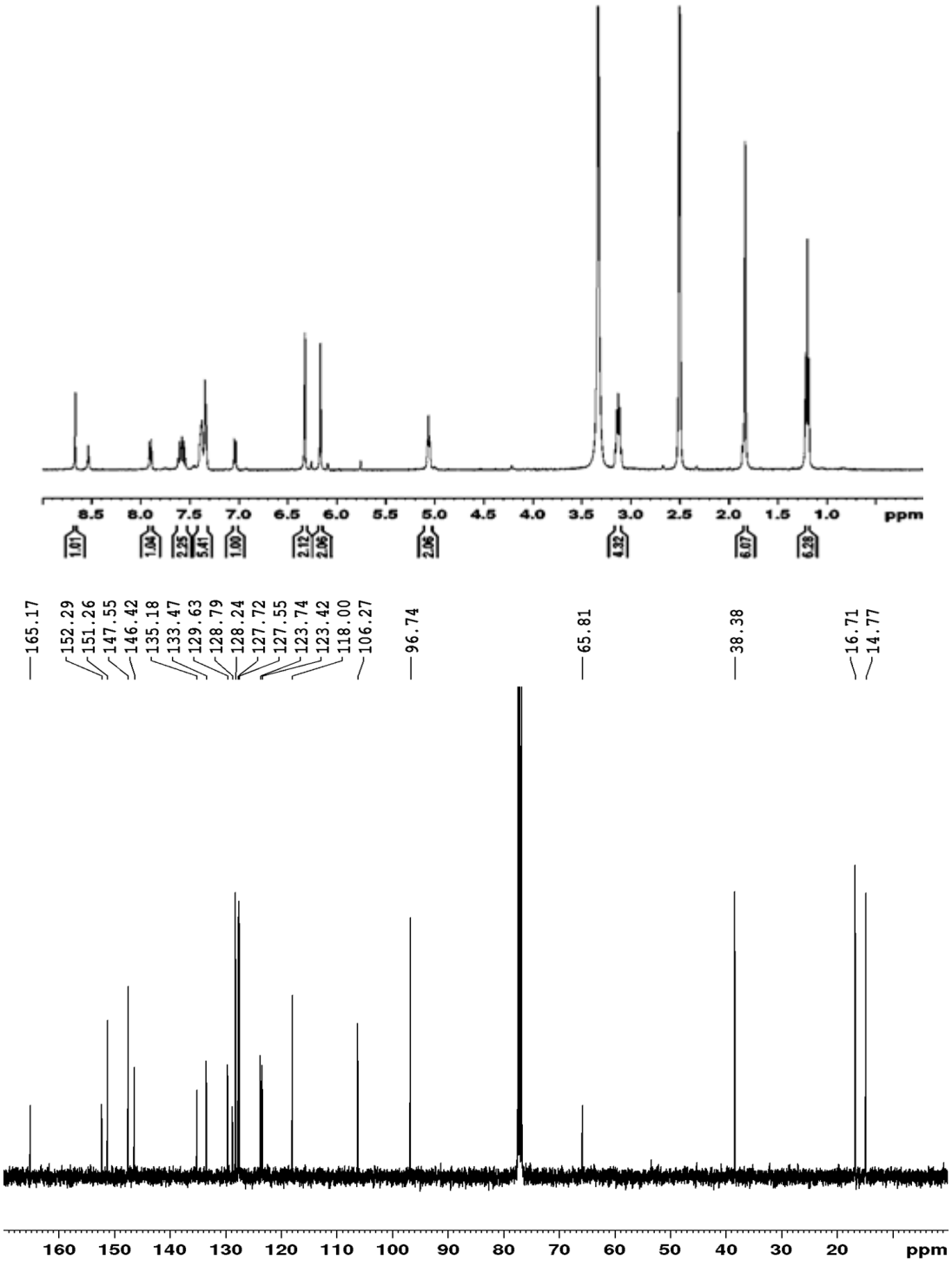

Figure A.2 *Proton and carbon NMR of compound **3.10** in $(CD_3)_2SO$ and $CDCl_3$, respectively*

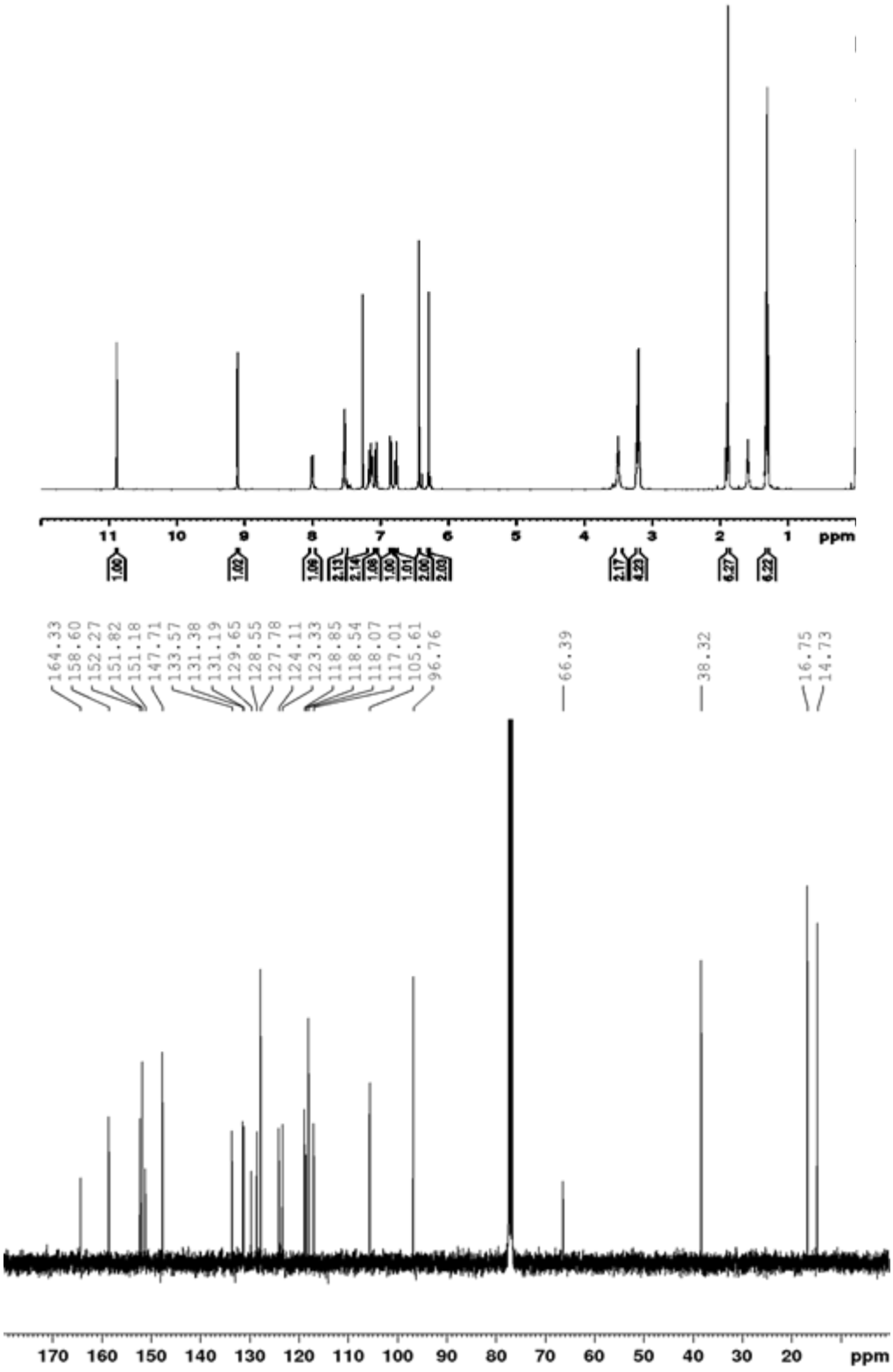

Figure A.2 *Proton and carbon NMR of compound* ***3.11a*** *in* $CDCl_3$

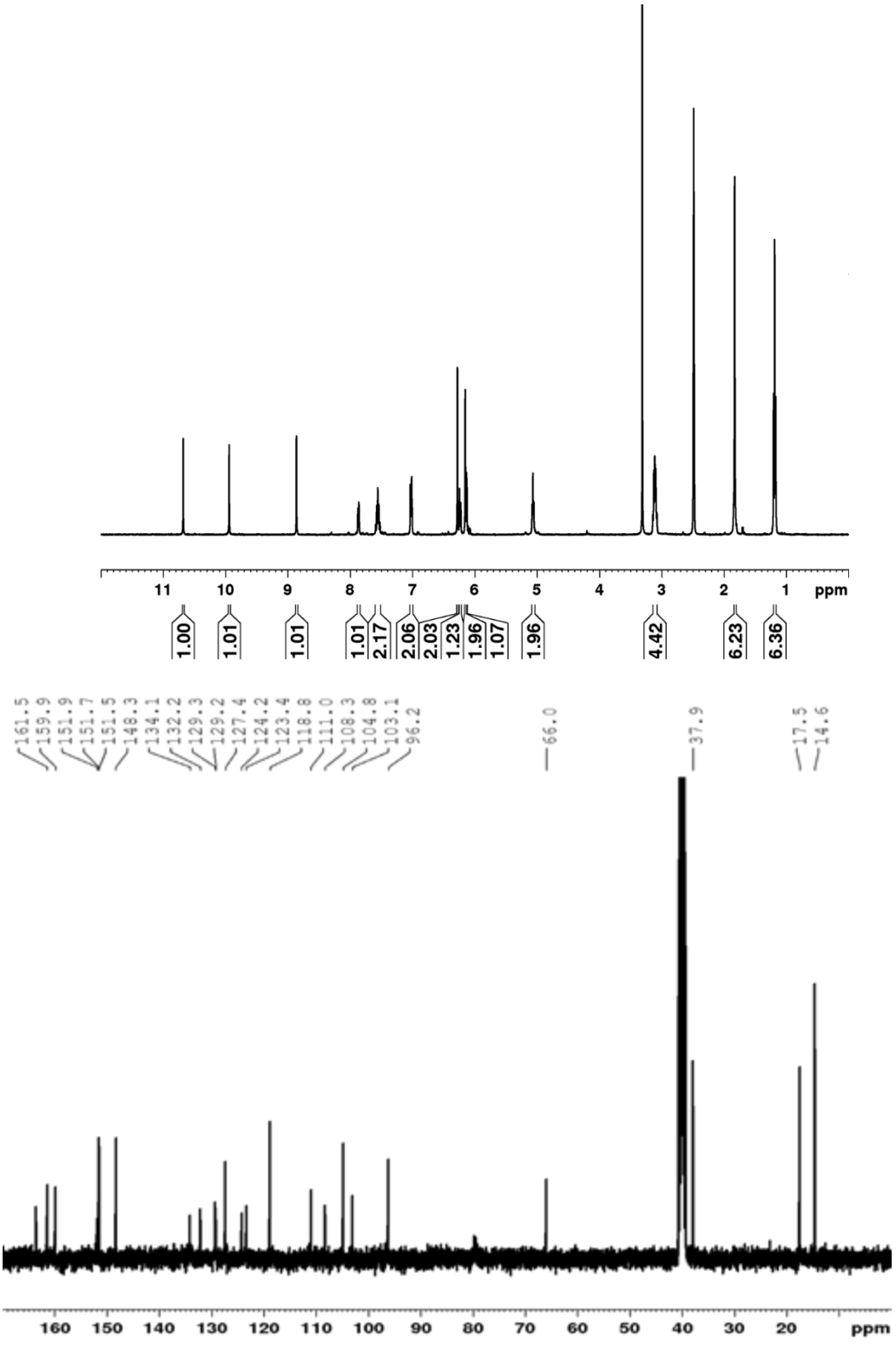

Figure A.3 *Proton and carbon NMR of compound **3.12** in DMSO*

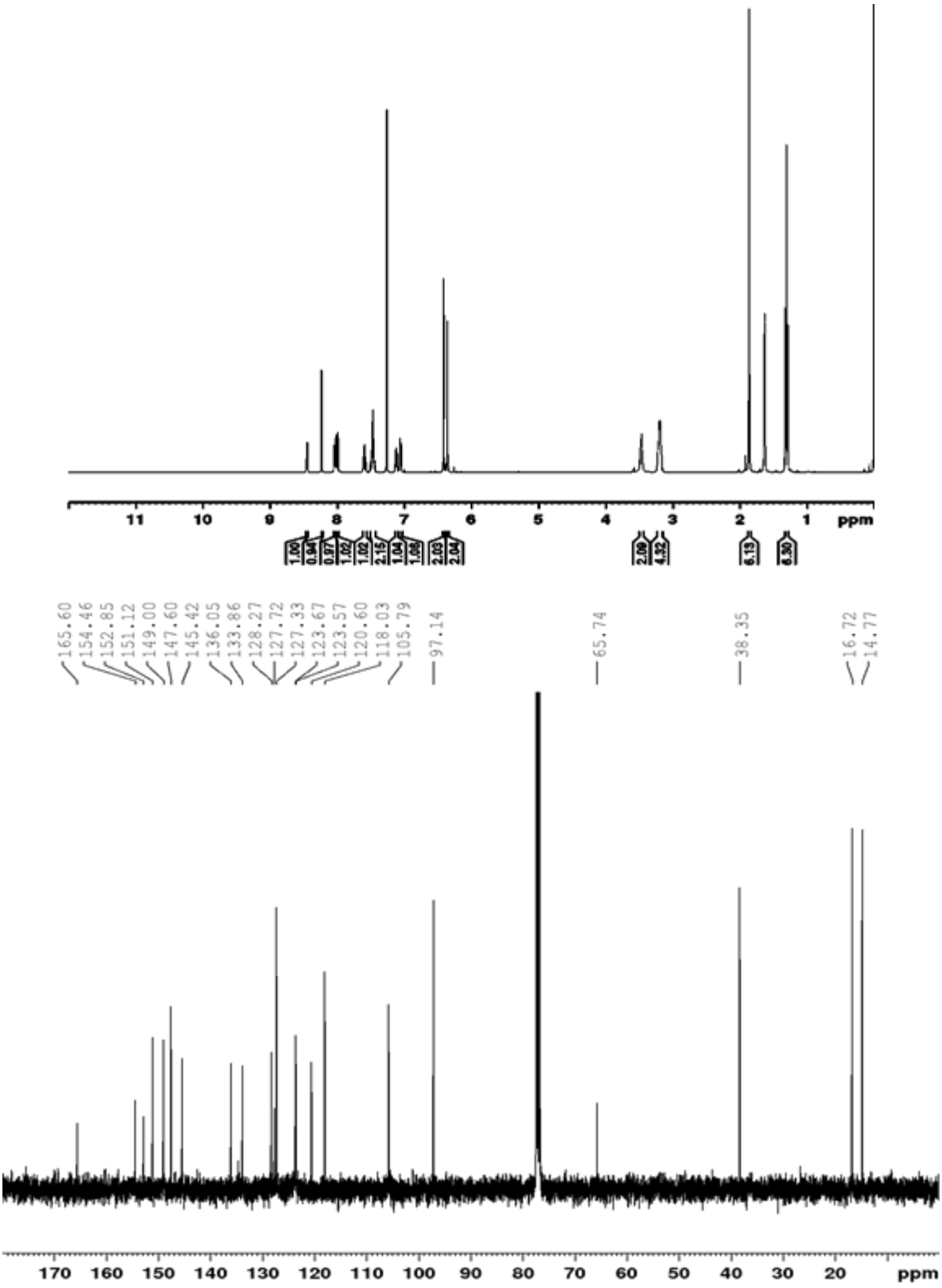

Figure A.4 *Proton and carbon NMR of compound **3.13** in $CDCl_3$*

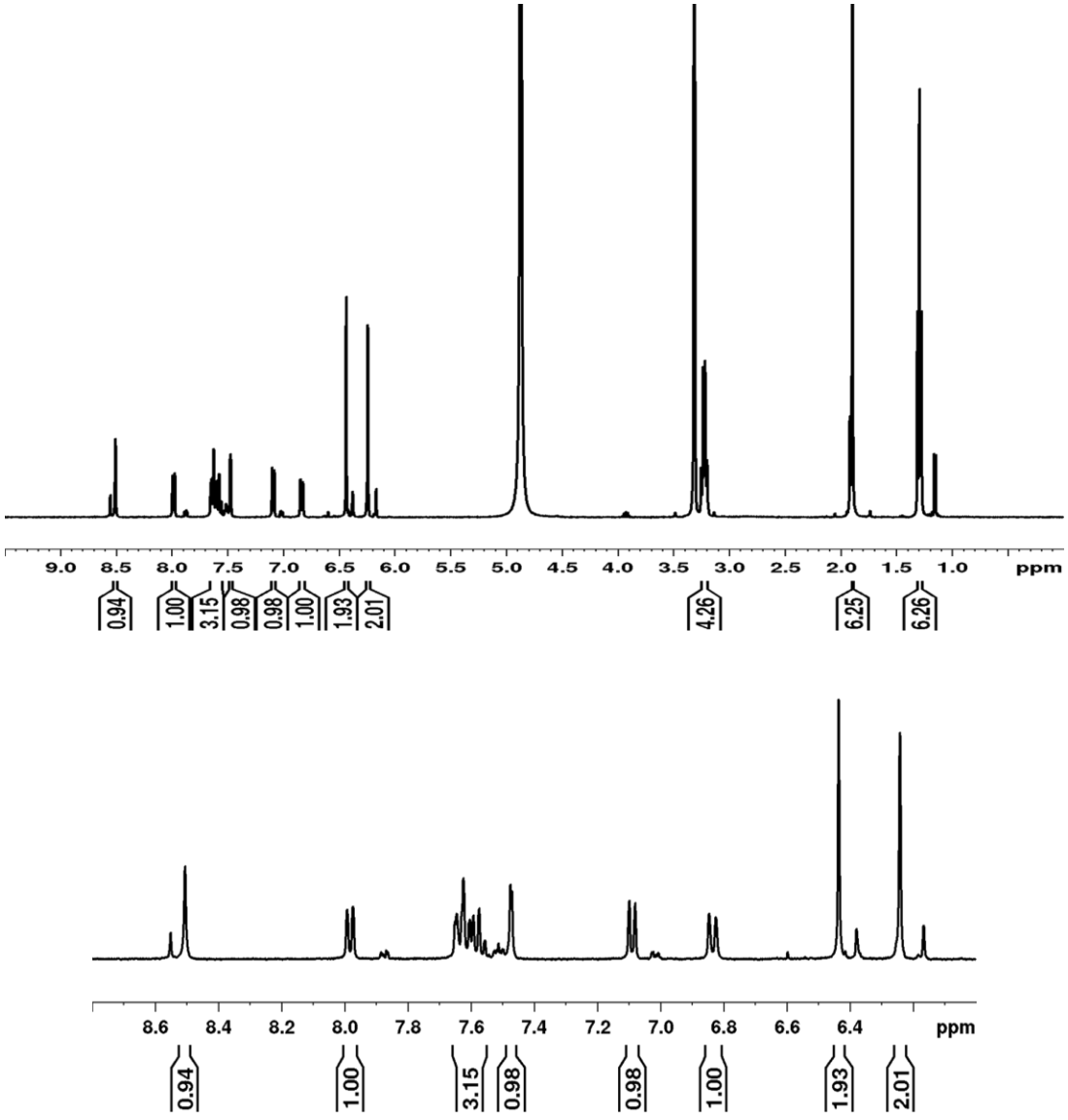

Figure A.5 *Proton NMR of compound **4.6** in MeOD.*

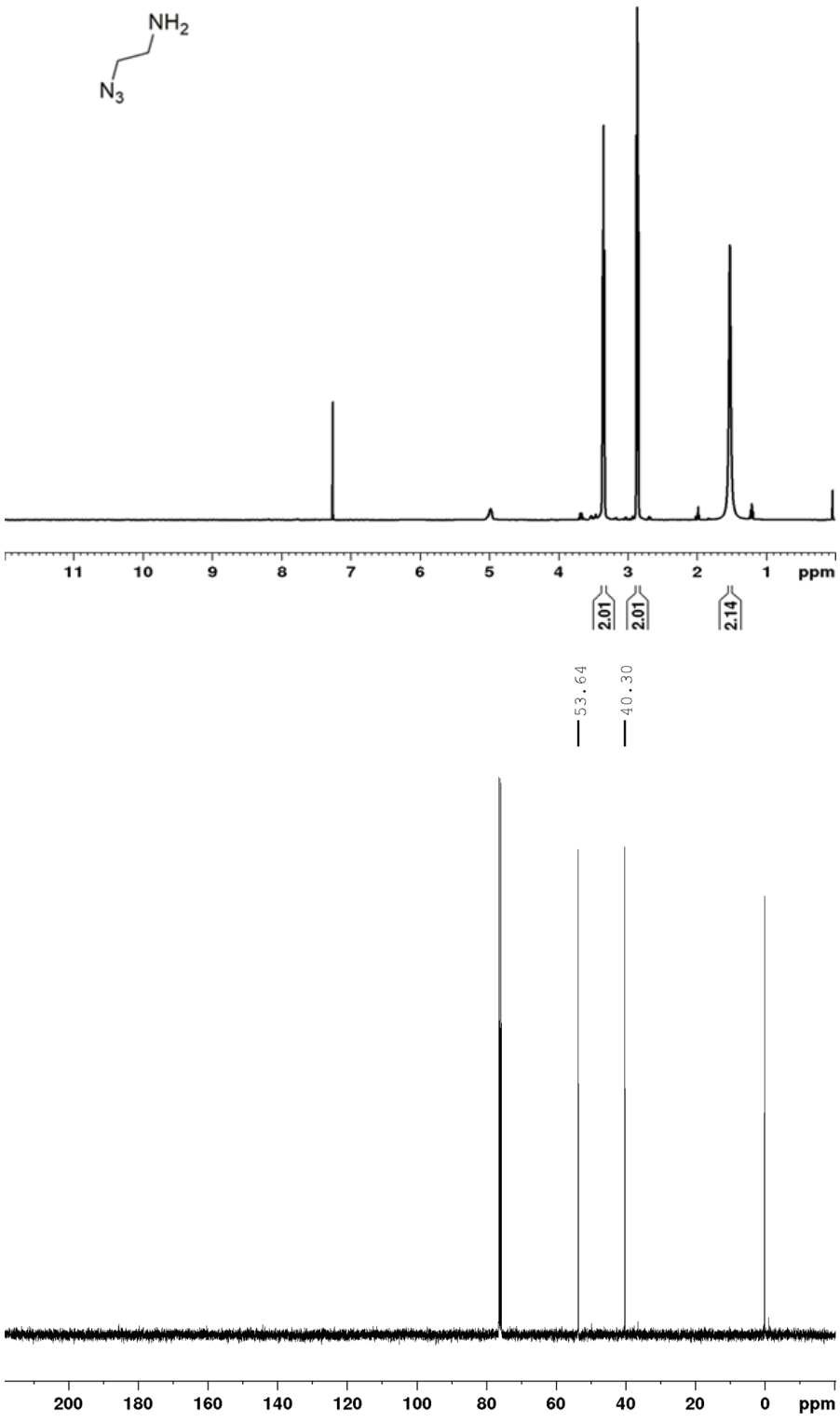

Figure A.6 *Proton and carbon NMR of compound* ***5.5*** *in* $CDCl_3$

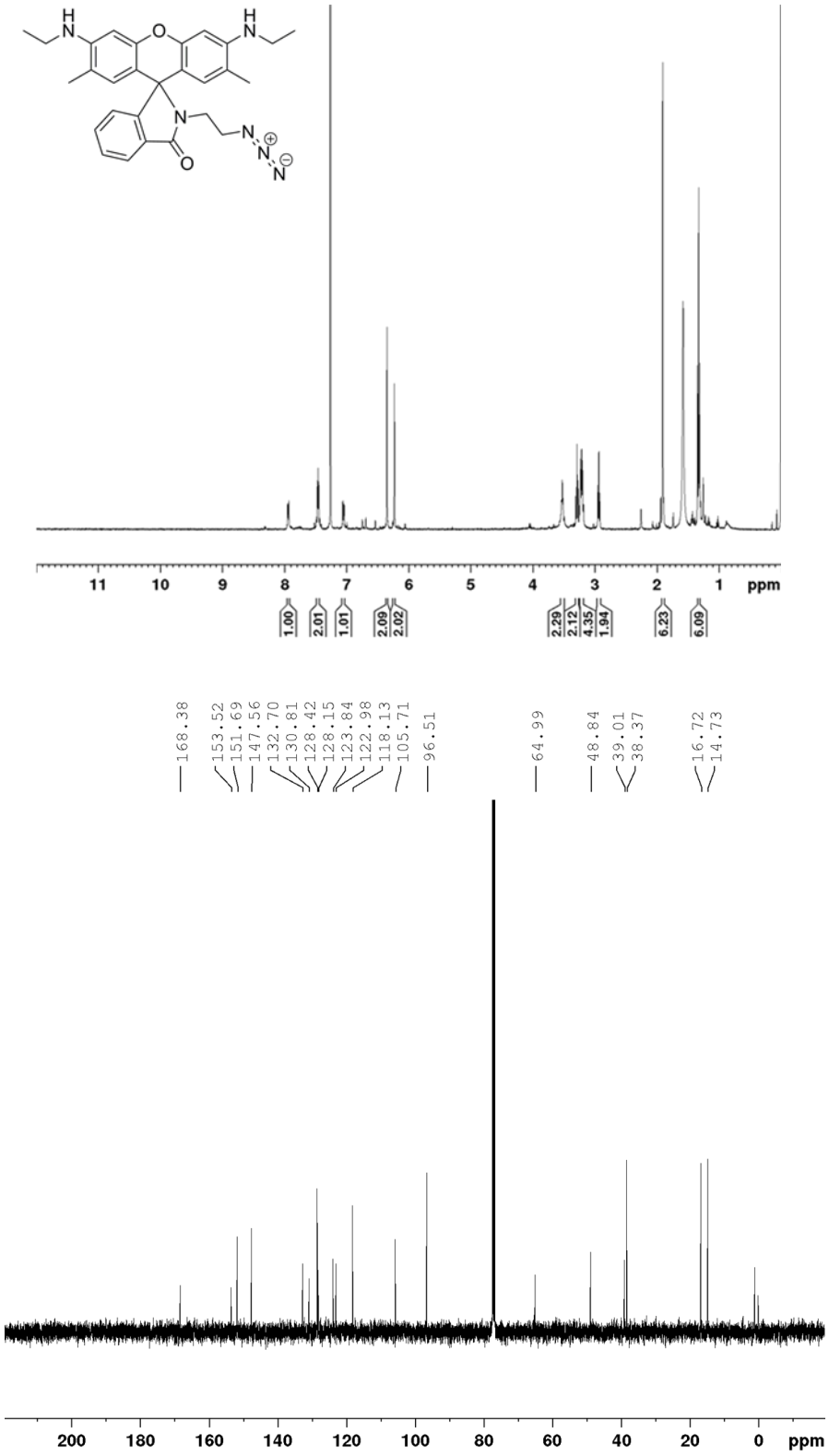

Figure A.7 *Proton and Carbon NMR of compound* ***5.6***

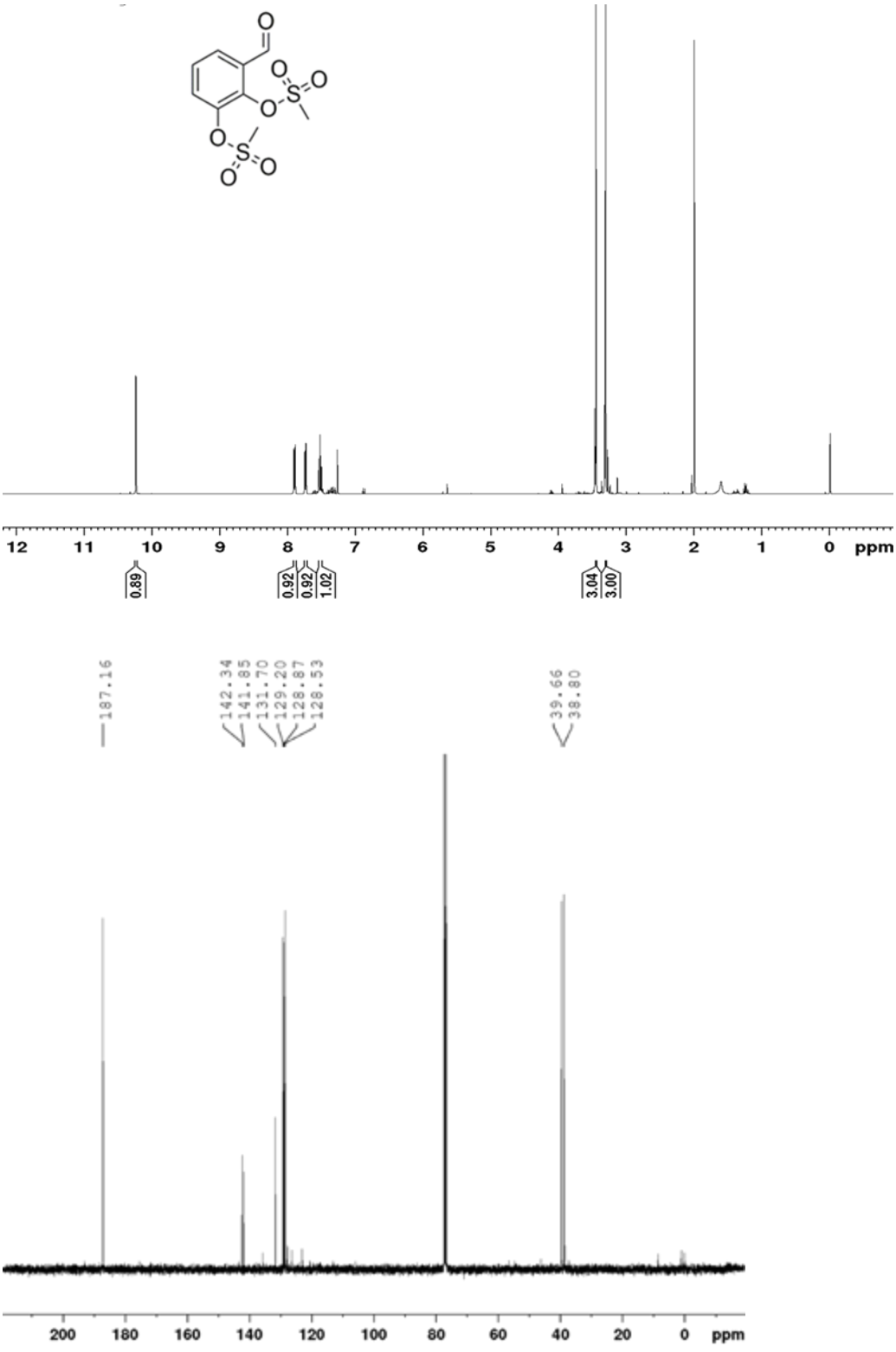

Figure A.8 *Proton and Carbon NMR of compound* ***5.7***

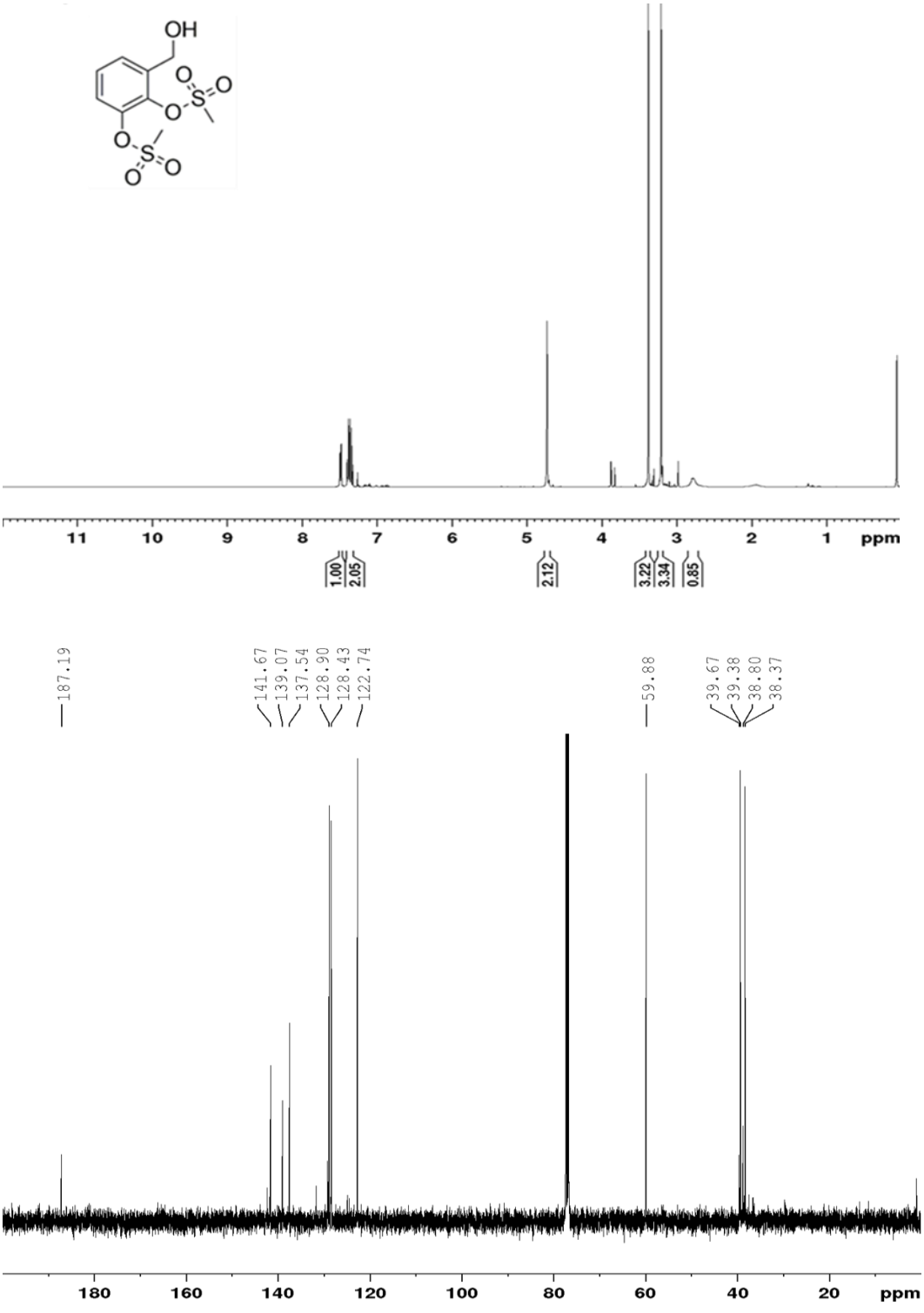

Figure A.9 *Proton and carbon NMR of compound **5.8***

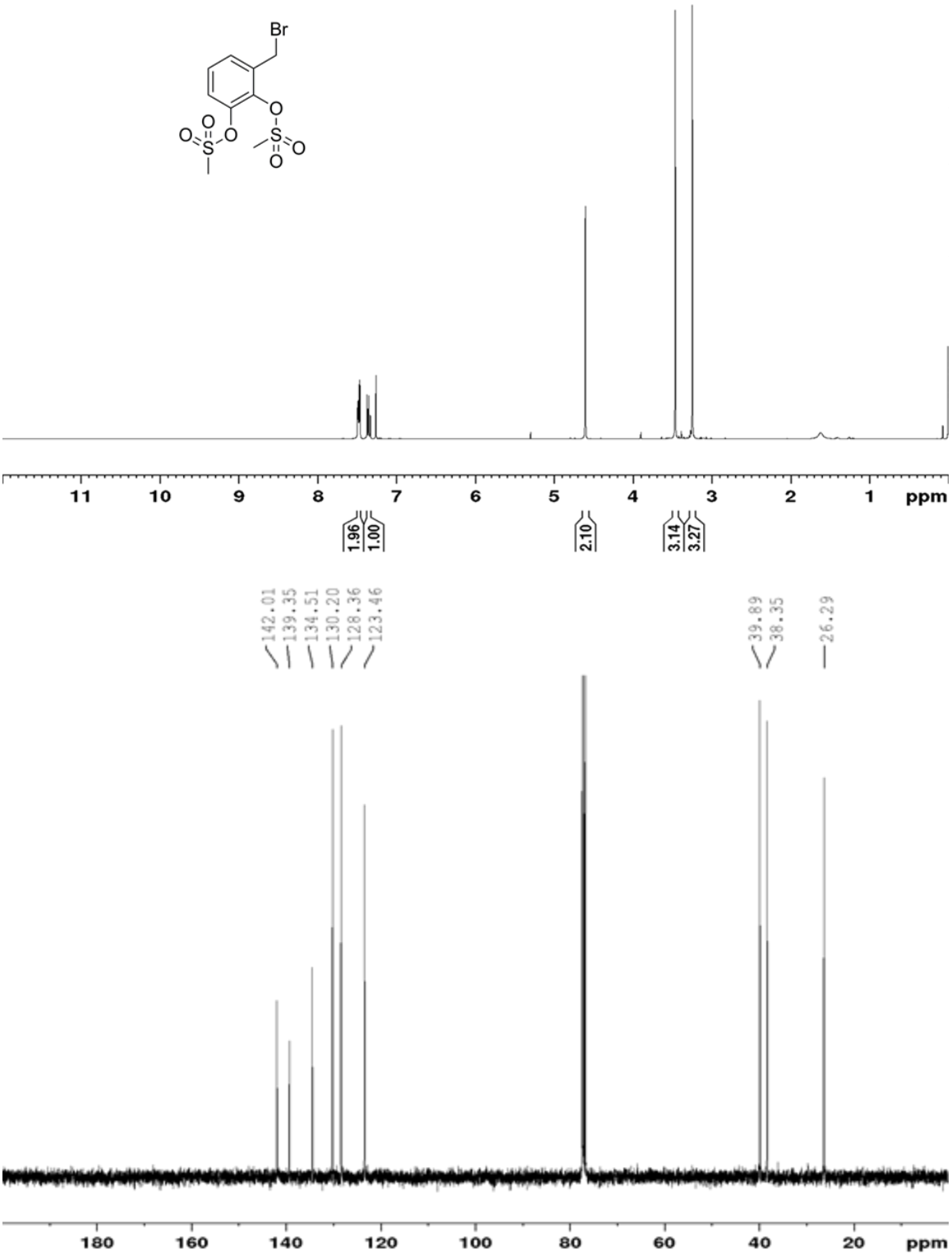

Figure A.10 *Proton and carbon NMR of compound* ***5.9***

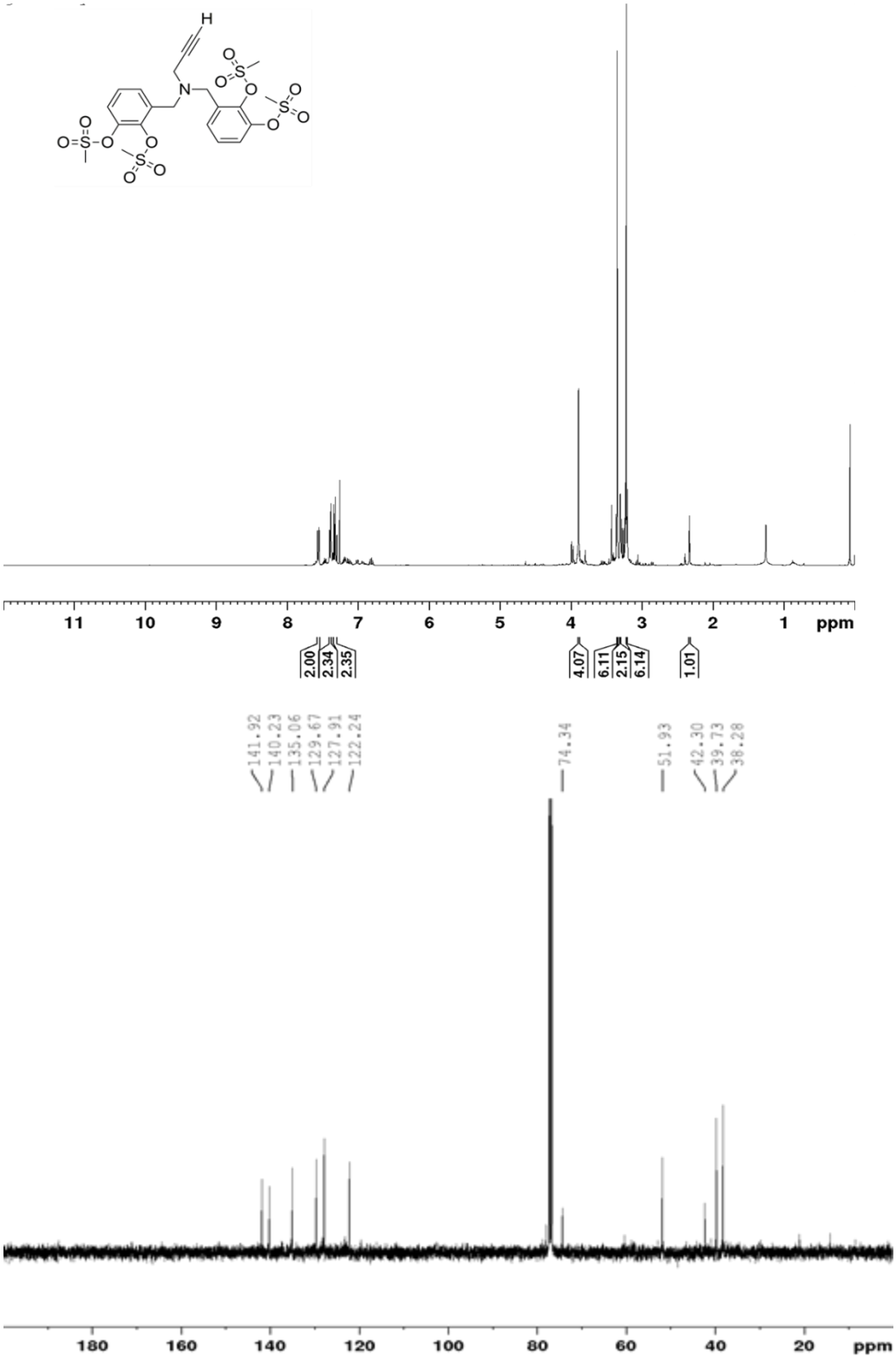

Figure A.11 *Proton and carbon NMR of compound* ***5.10*** *in* $CDCl_3$

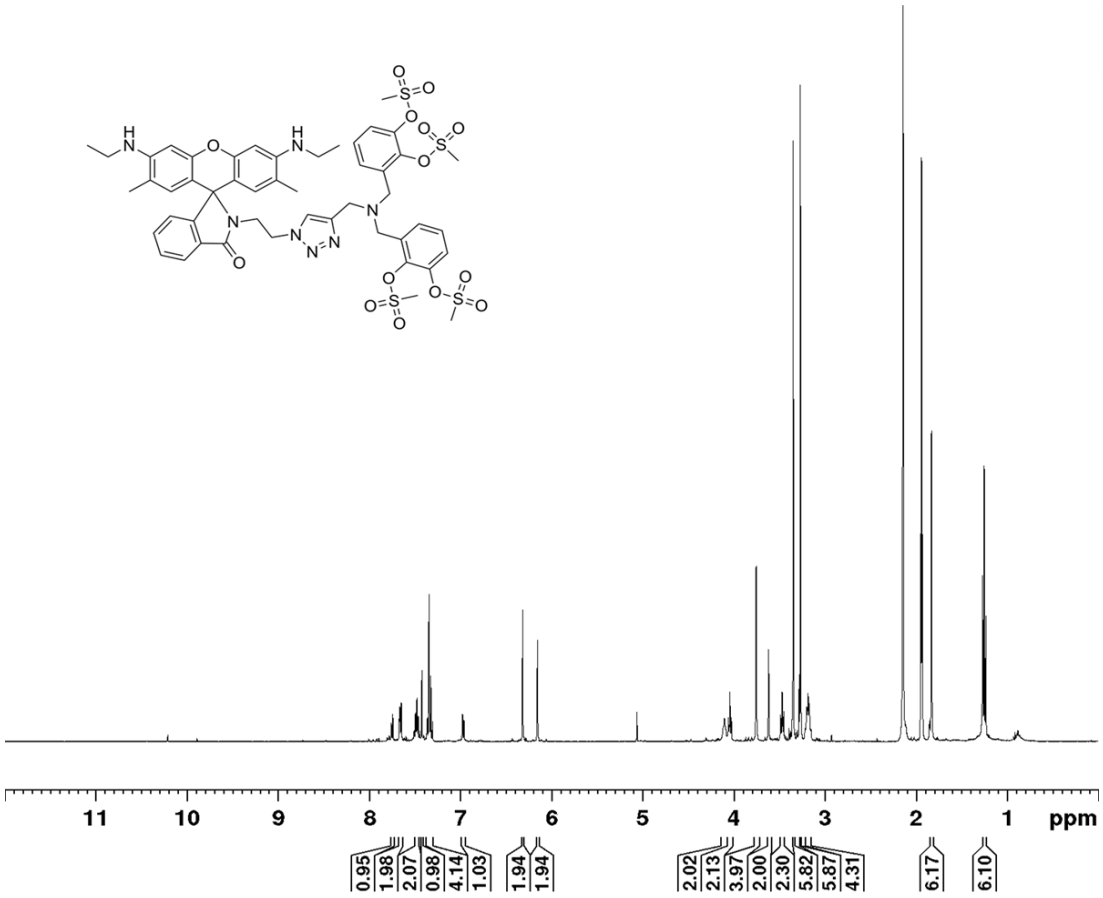

Figure A.12 *Proton NMR of compound* ***5.11*** *in* CD_3CN

A.3 Mass Spectra

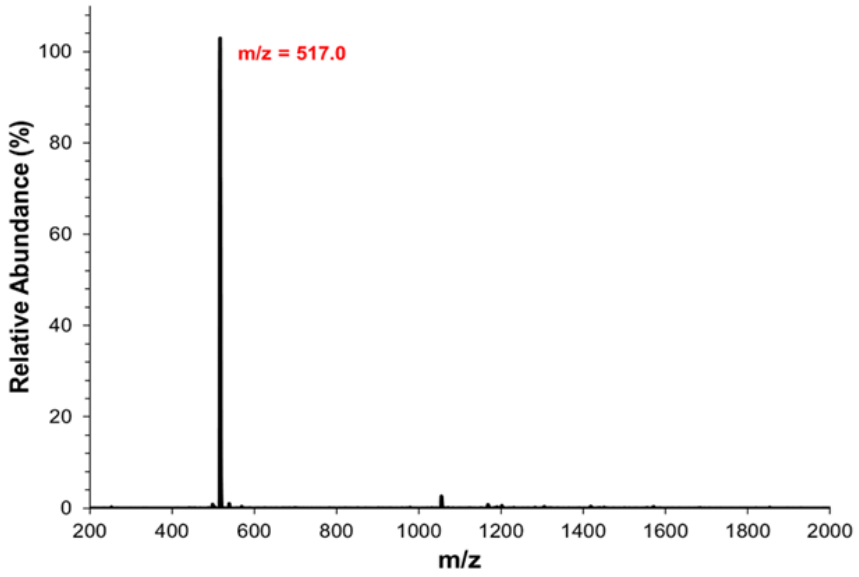

Figure A.13 *ESI-MS of compound* ***3.10*** *in* CH_3CN

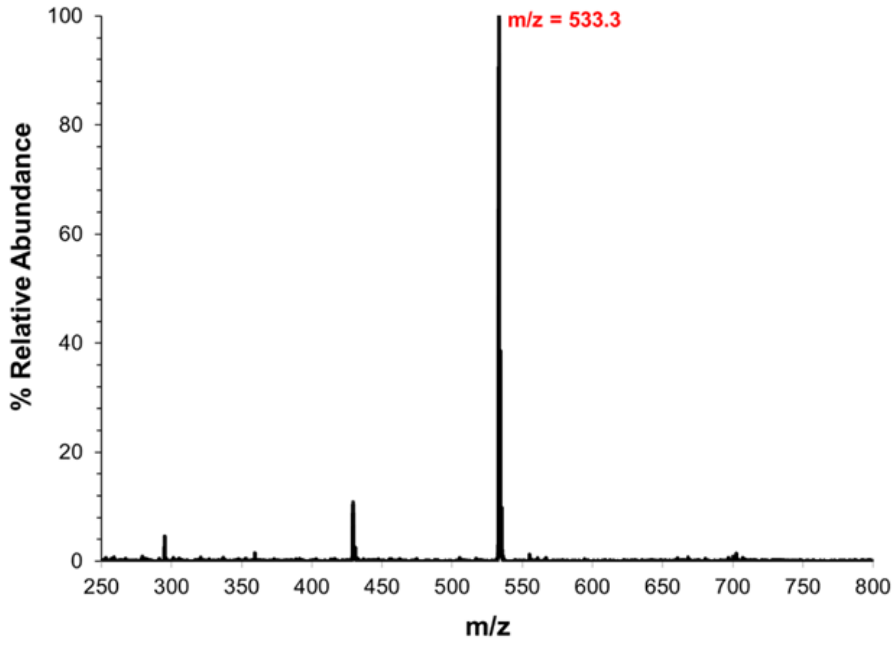

Figure A.14 *ESI-MS of compound* ***3.11a*** *in* CH_3CN

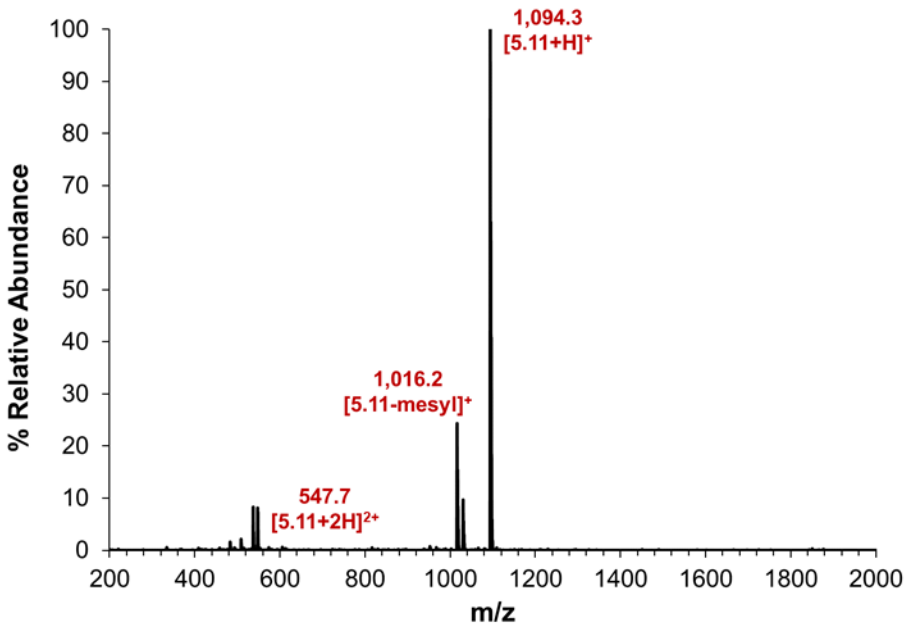

Figure A.15 *ESI-MS of compound* ***5.11*** *in* CD_3CN

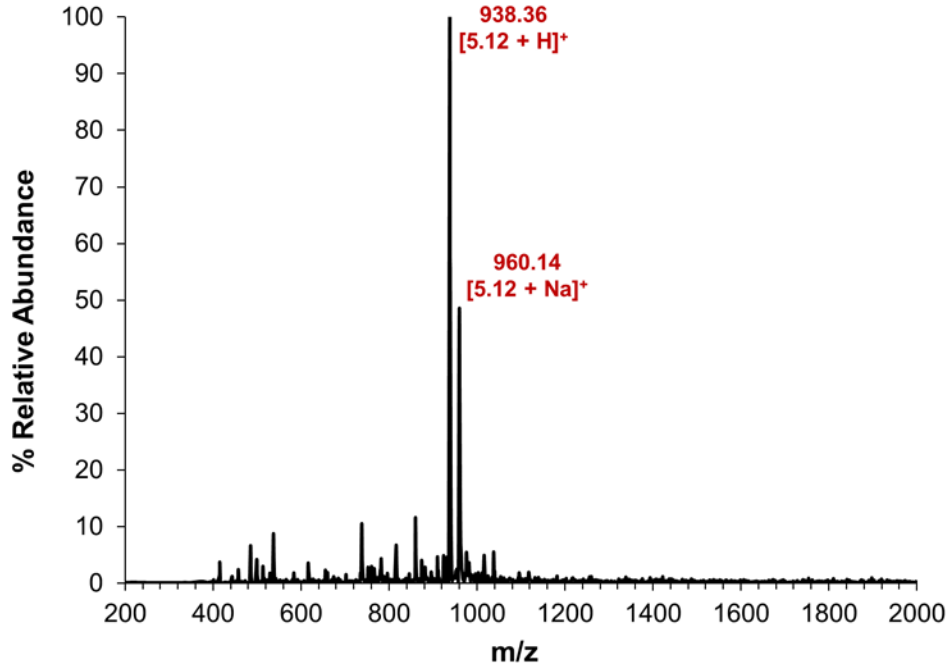

Figure A.16 *ESI-MS of compound* ***5.12*** *in MeOH*

A.4 IR Spectra

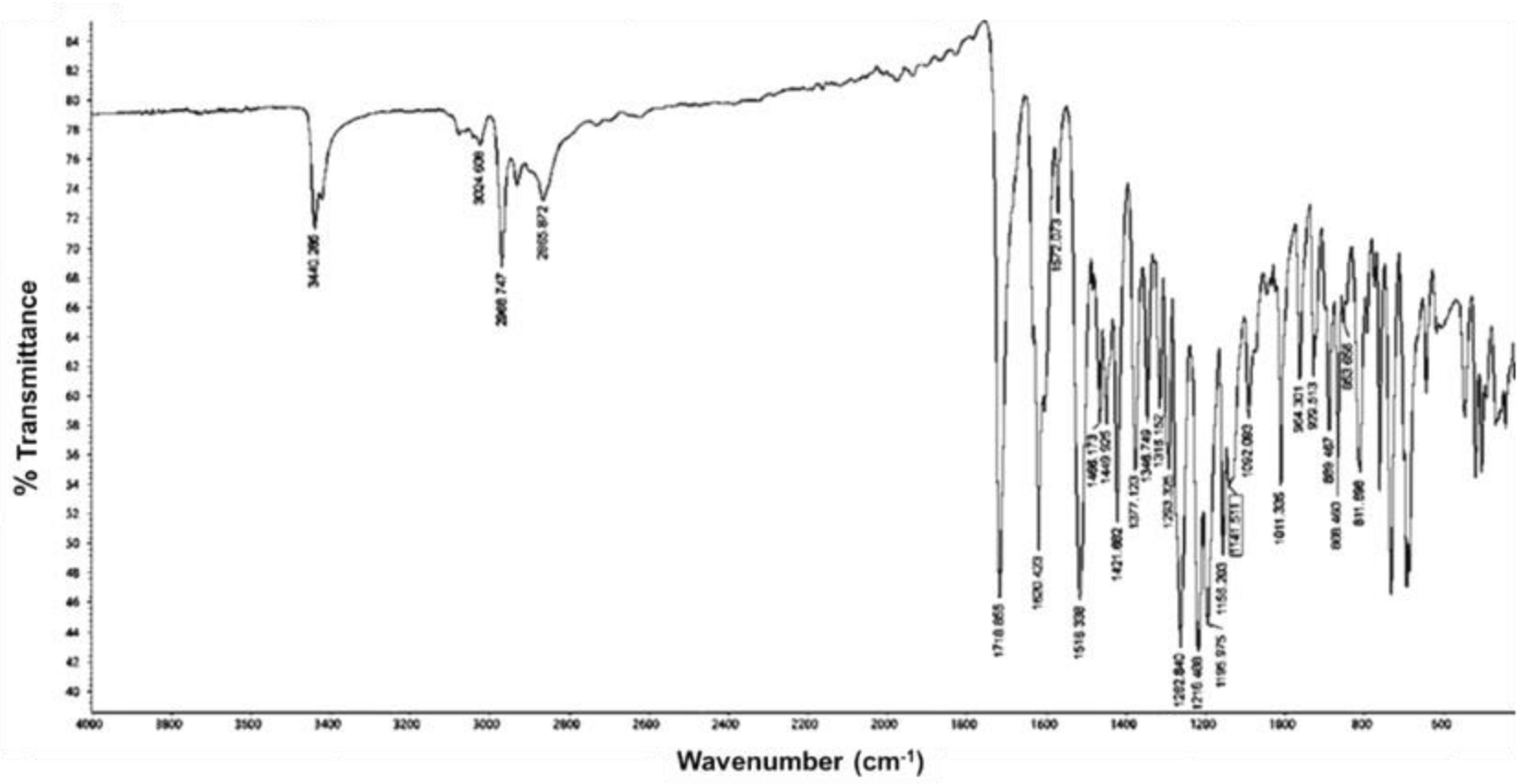

Figure A.17 *FT-IR spectrum of compound **3.10***

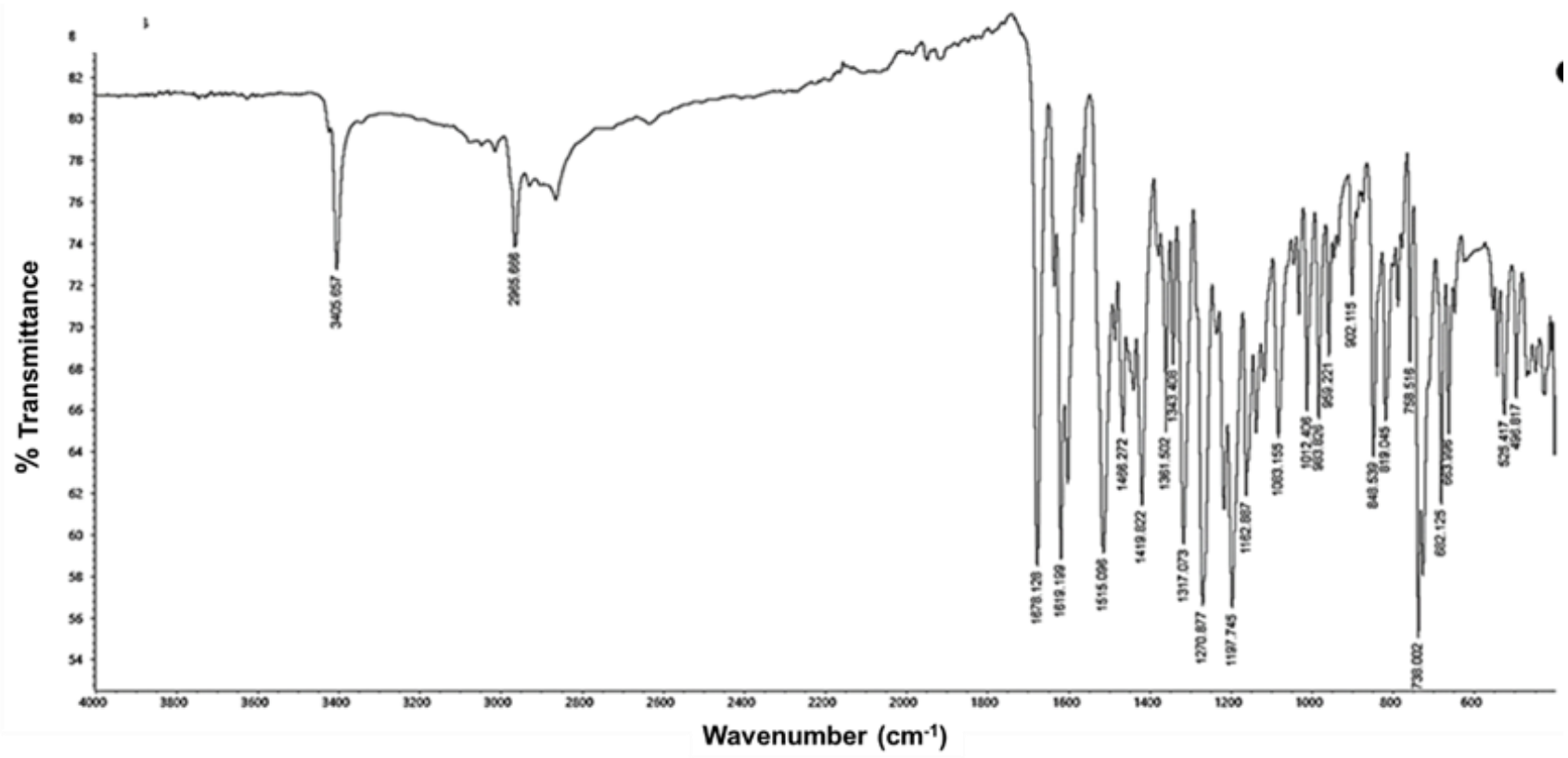

Figure A.18 *FT-IR spectrum of compound* ***3.11a***

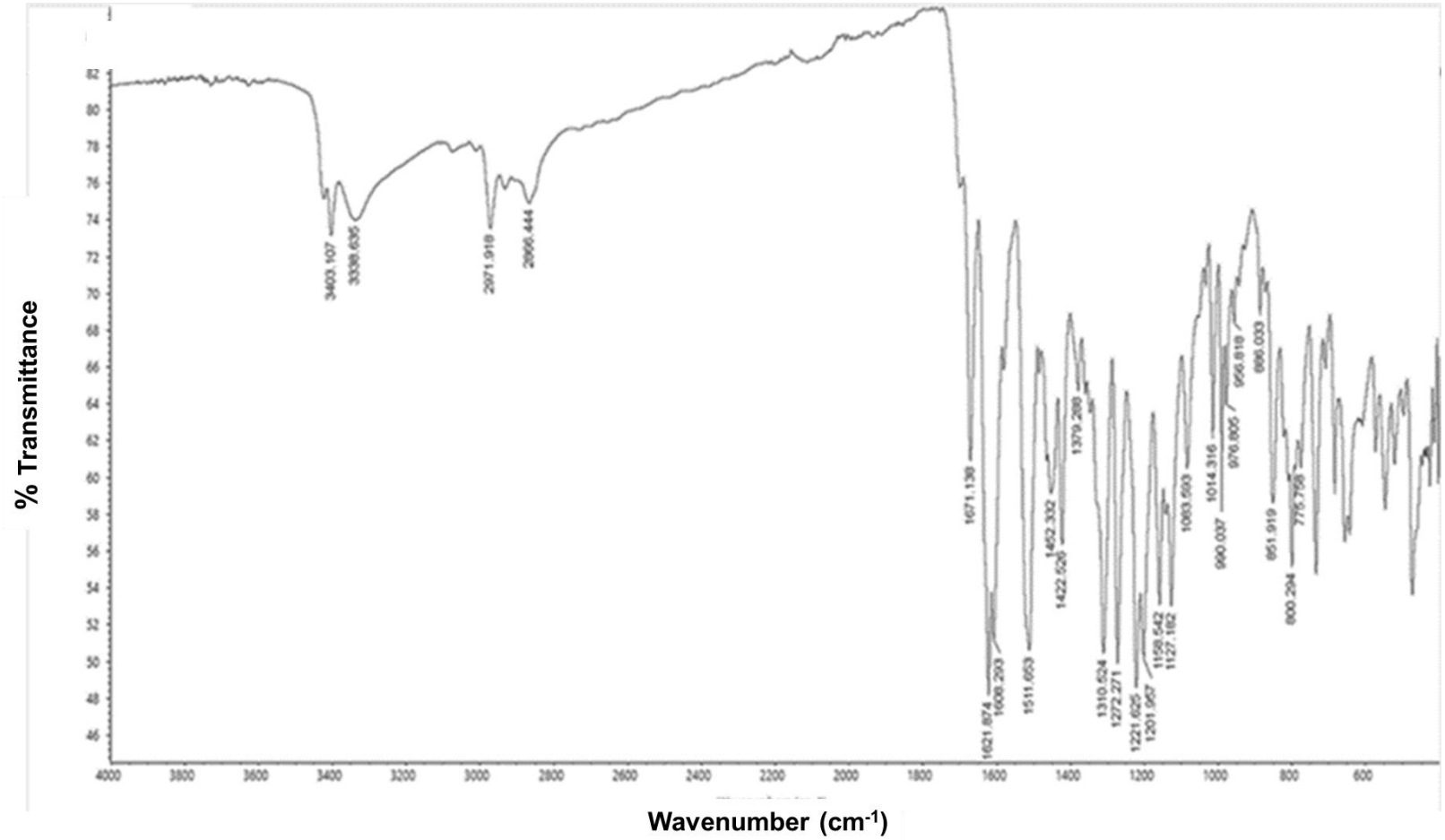

Figure A.19 *FT-IR spectrum of compound* ***3.12***

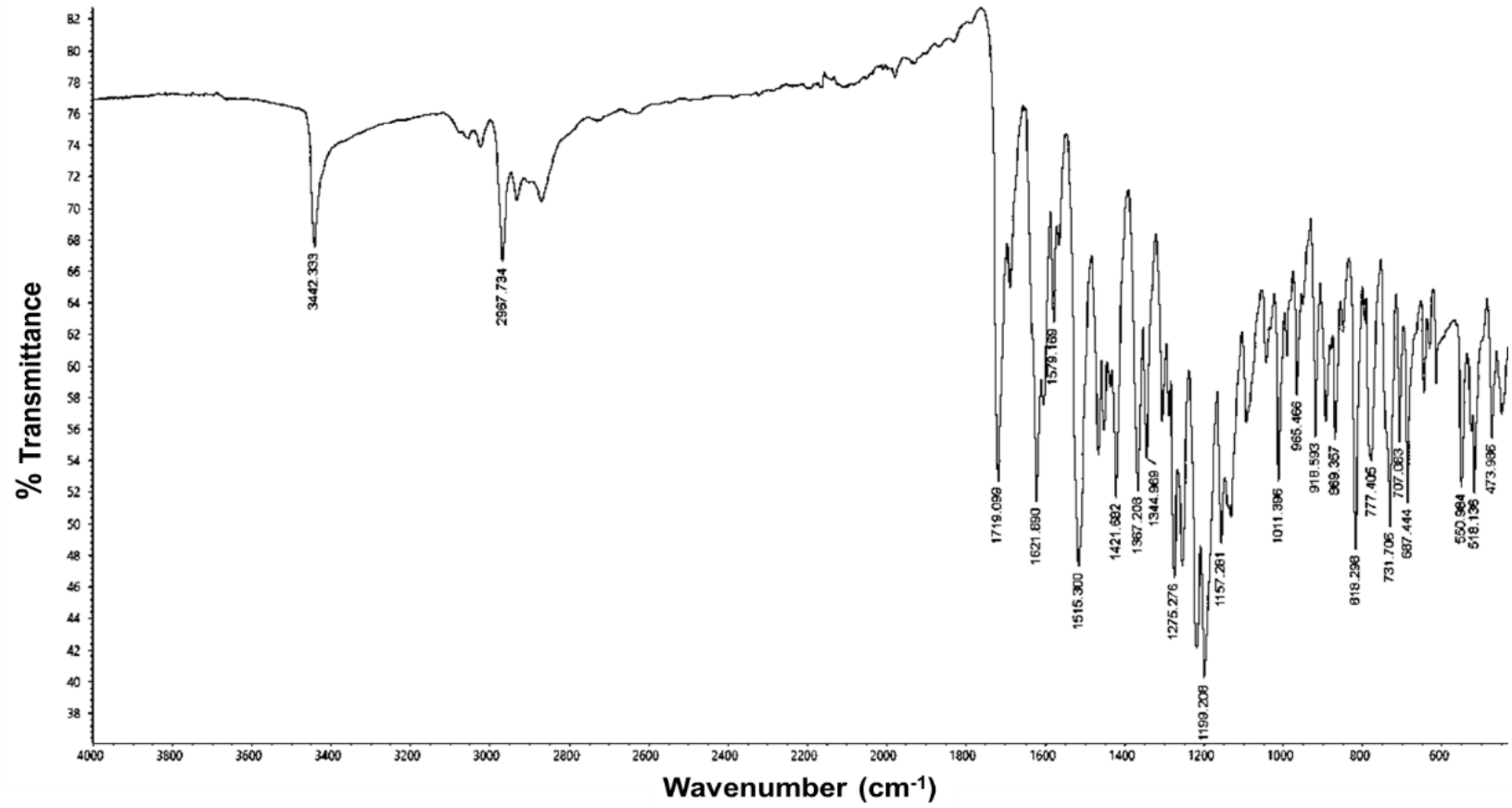

Figure A.20 *FT-IR spectrum of compound* ***3.13***

A.5 Optical Spectroscopy

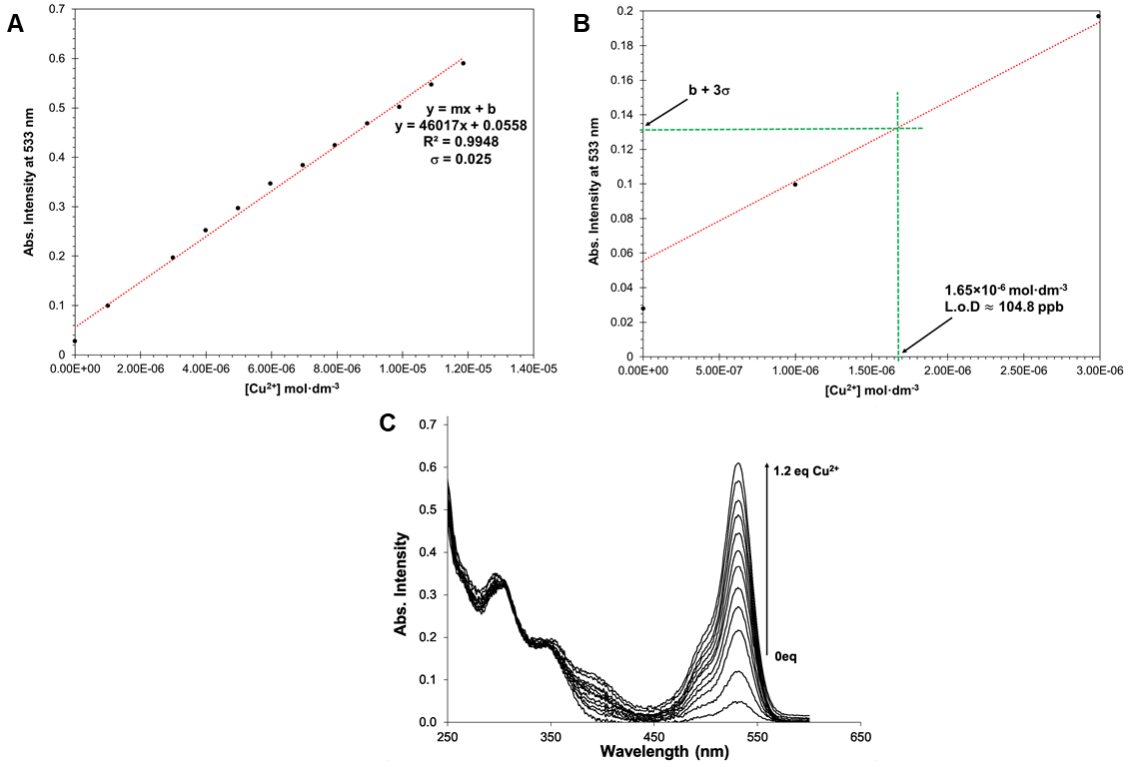

Figure A.21 *(A) Calibration curve used to calculate the LoD for $Cu(NO_3)_2$ with compound **3.11a** in a solution of DMSO-MES (1:1, v/v, pH=6.5) (B) Expansion of diagram A. (C) Absorbance data used for LoD calculation with compound **3.11a***

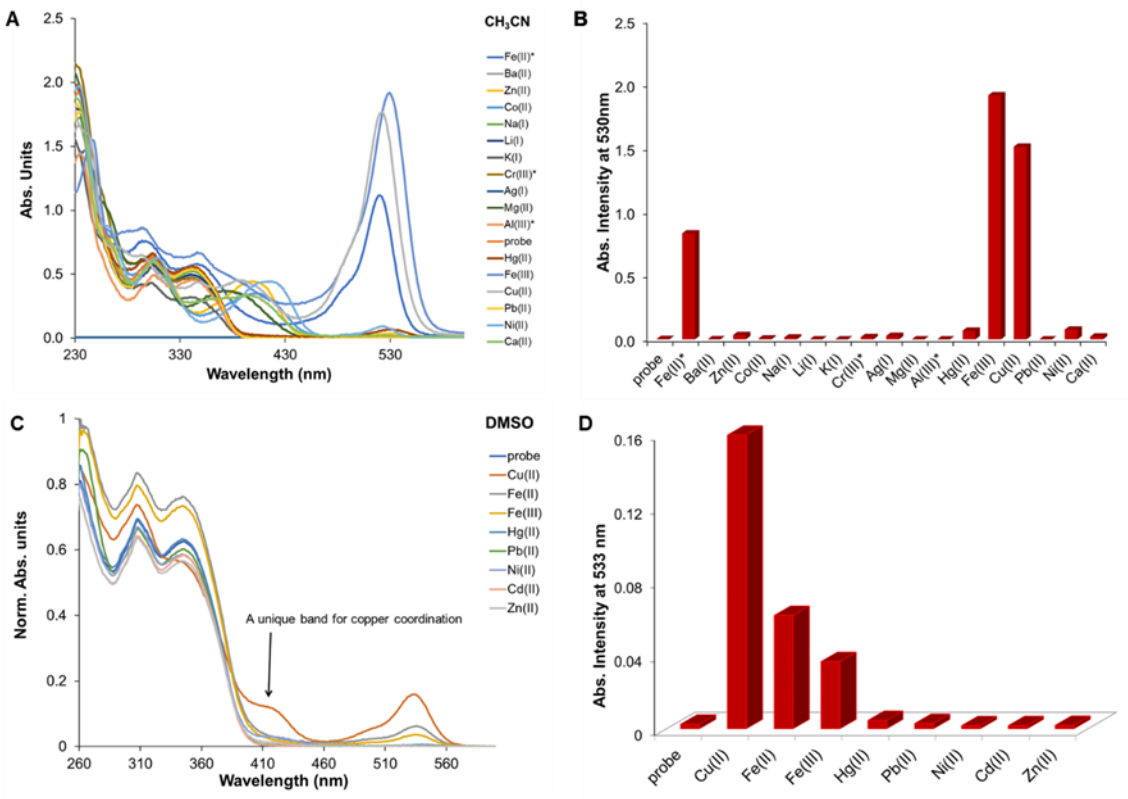

Figure A.22 *Metal screen of 25 μM of compound* ***3.12*** *with 50 μM of various metal ions in (A-B) CH_3CN, (C-D) DMSO*

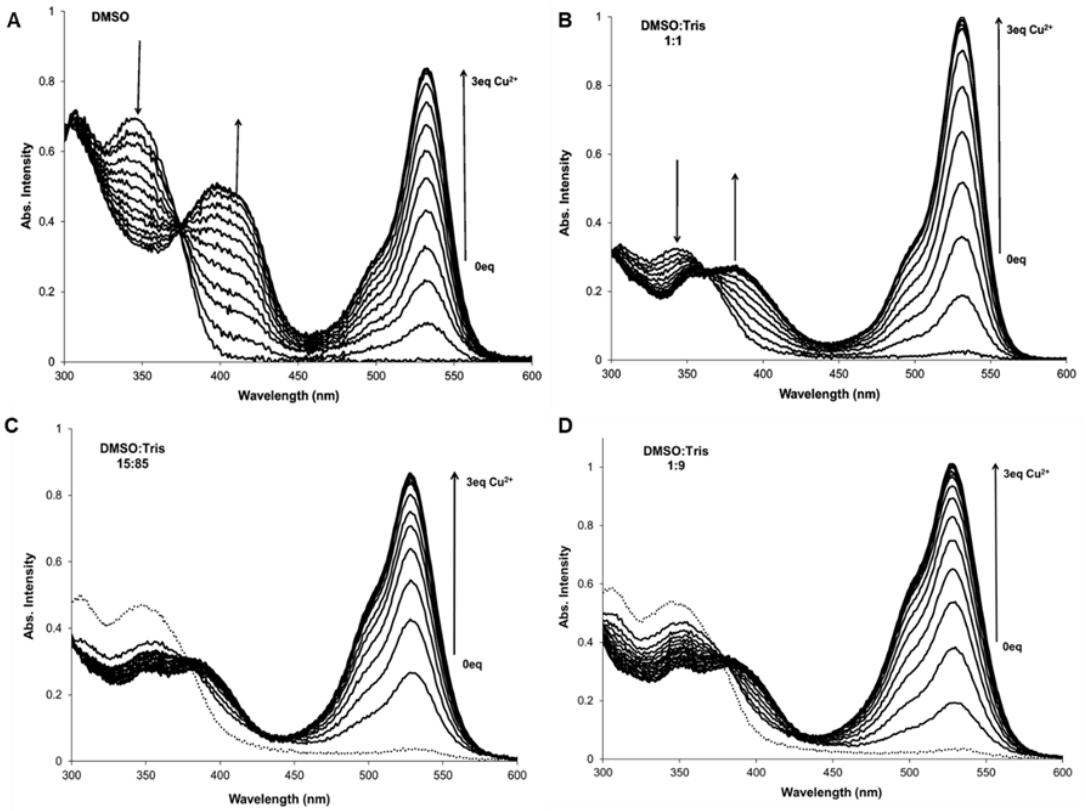

Figure A.23 *Absorbance titration data for the addition of 75 µM $CuCl_2$ into 25 µM solutions of compound* ***3.12*** *in various solvent systems. (A)DMSO, (B) DMSO-Tris (1:1, v/v), (C) DMSO-Tris (15:85, v/v), (D) DMSO-Tris (1:9, v/v).The concentration of Tris buffer was 30mM for each aqueous solution with pH ≈ 7.5*

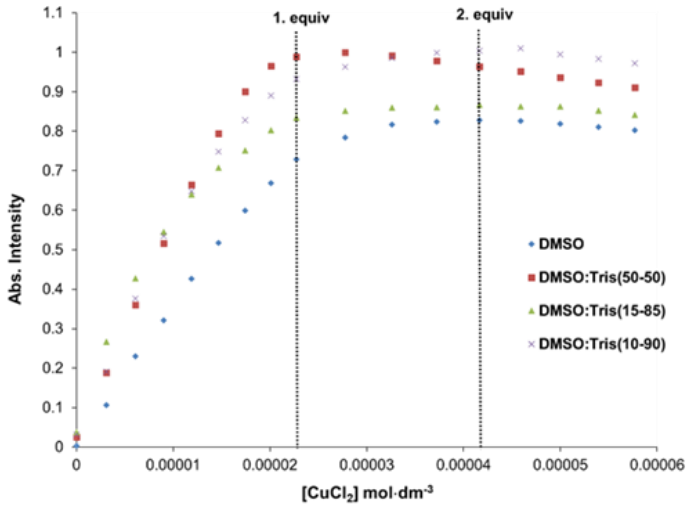

Figure A.24 *Binding isotherms plotted from the absorbance titrations of 25 µM solutions of compound* ***3.12*** *and $CuCl_2$ in a range of solvent systems*

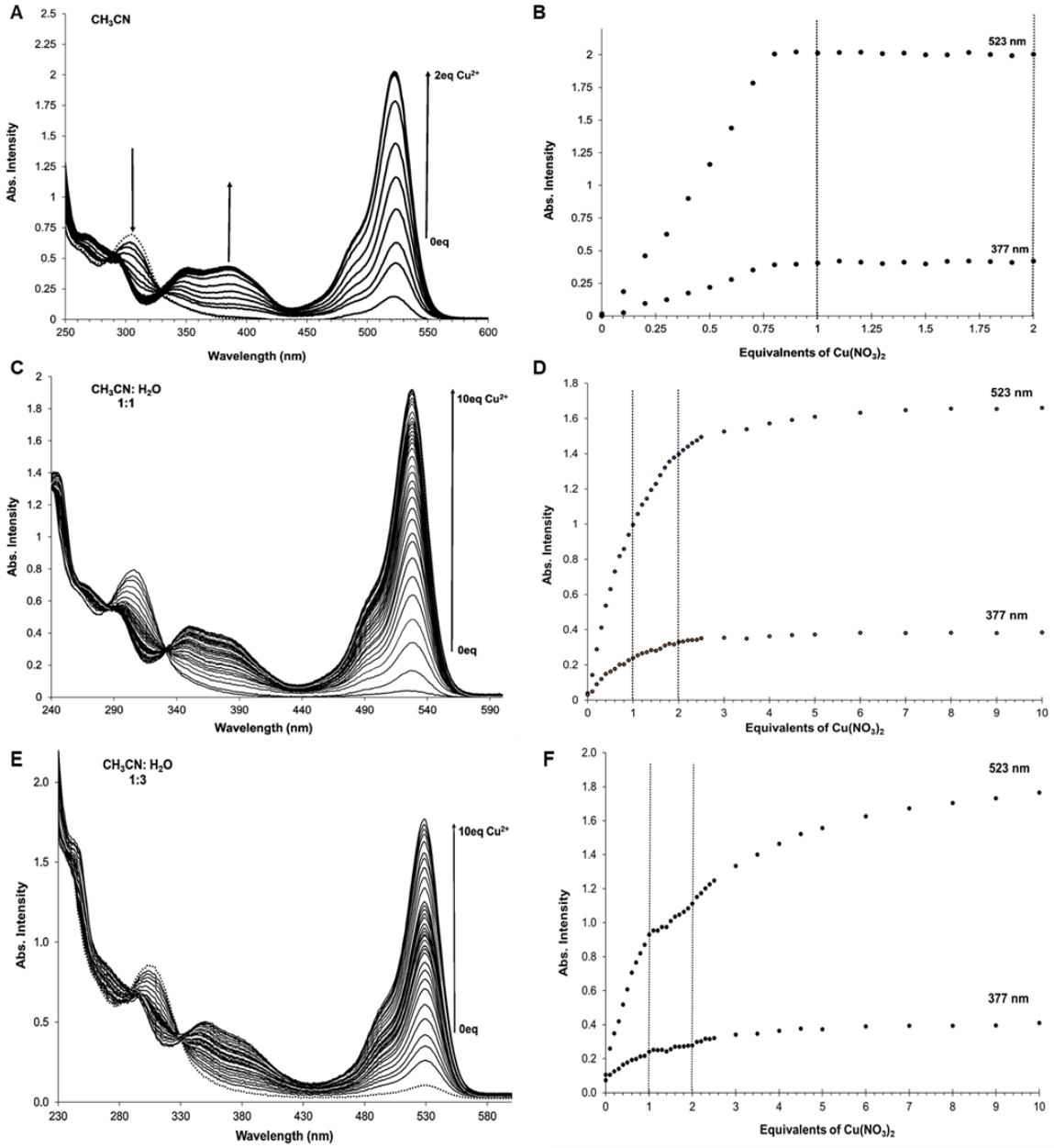

Figure A.25 *Titrations of $Cu(NO_3)_2$ into 25 µM solutions of compound* ***3.13*** *in various solvent systems with corresponding binding isotherms. (A-B) CH_3CN, (C-D) CH_3CN-water (1:1, v/v), (E-F) CH_3CN-water (1:3, v/v).*

Table A.3 *Binding constants for compound* ***3.13*** *with* $Cu(NO_3)_2$ *salt in different solvent systems*

[3.13]	Solvent	K_a [Cu^{2+}:3.13]
1.25×10^{-5} M	CH_3CN	$K_{11} = 3.0 \times 10^6$ $K_{12} = 2.7 \times 10^6$ $K_{21} = 2.6 \times 10^5$
1.25×10^{-5} M	CH_3CN: H_2O 1:1	$K_{11} = 5.2 \times 10^4$ $K_{12} = 2.0 \times 10^4$

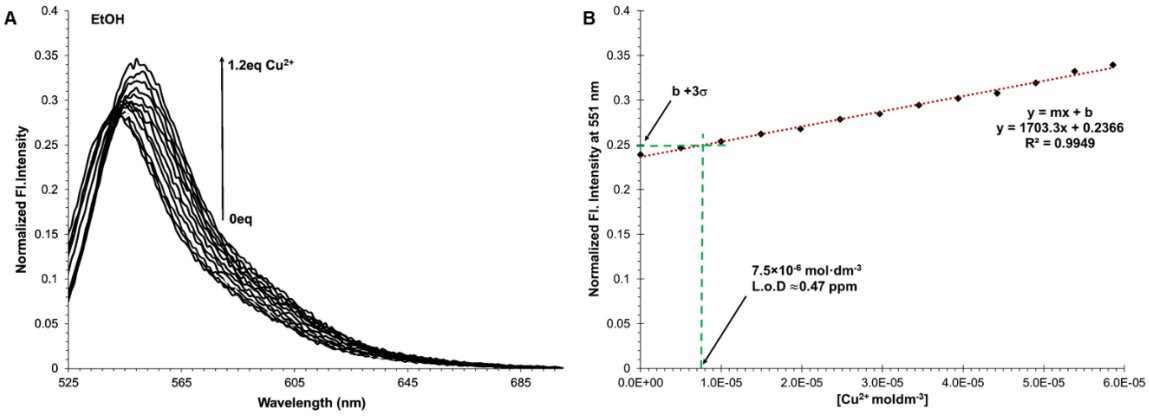

Figure A.26 *(A) Fluorescence data used for LoD calculation with compound* ***4.6*** *in EtOH. (B) Calibration curve used to calculate the LoD for Cu(NO3)2 with compound* ***4.6*** *in EtOH.*

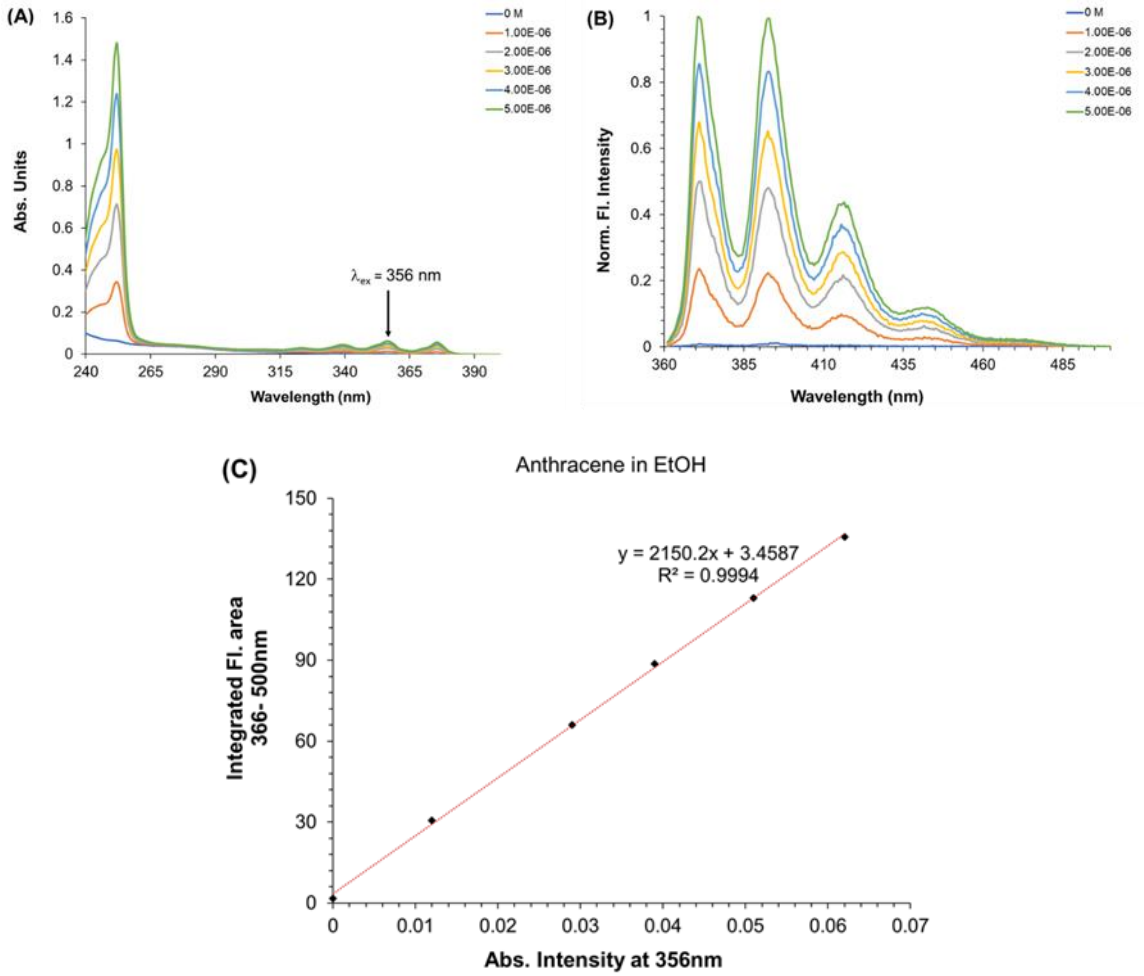

Figure A.27 *Spectral data used for anthracene quantum yield (Φ) calculations. (A) Absorbance spectrum of anthracene in EtOH. (B) Fluorescence spectrum of anthracene in EtOH (λ_{ex} = 356 nm). (C) Linear plot used in anthracene QY calculation.*

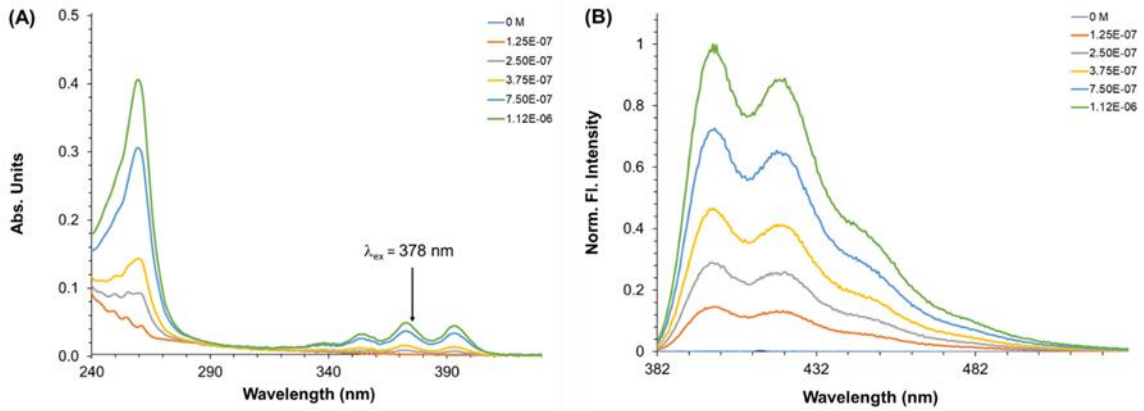

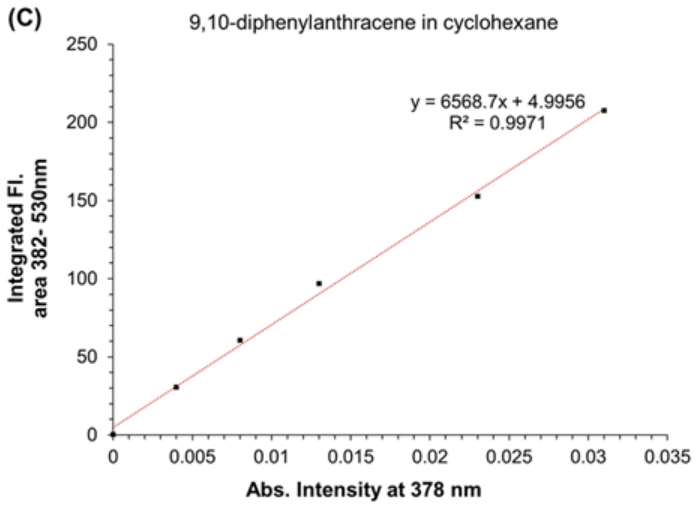

Figure A.28 *Spectral data used for 9,10-diphenylanthracene quantum yield (Φ) calculations. (A) Absorbance spectrum of 9,10-diphenylanthracene in cyclohexane. (B) Fluorescence spectrum of 9,10-diphenylanthracene in cyclohexane (λ_{ex} = 378 nm). (C) Linear plot used in 9,10-diphenylanthracene quantum yield calculation.*

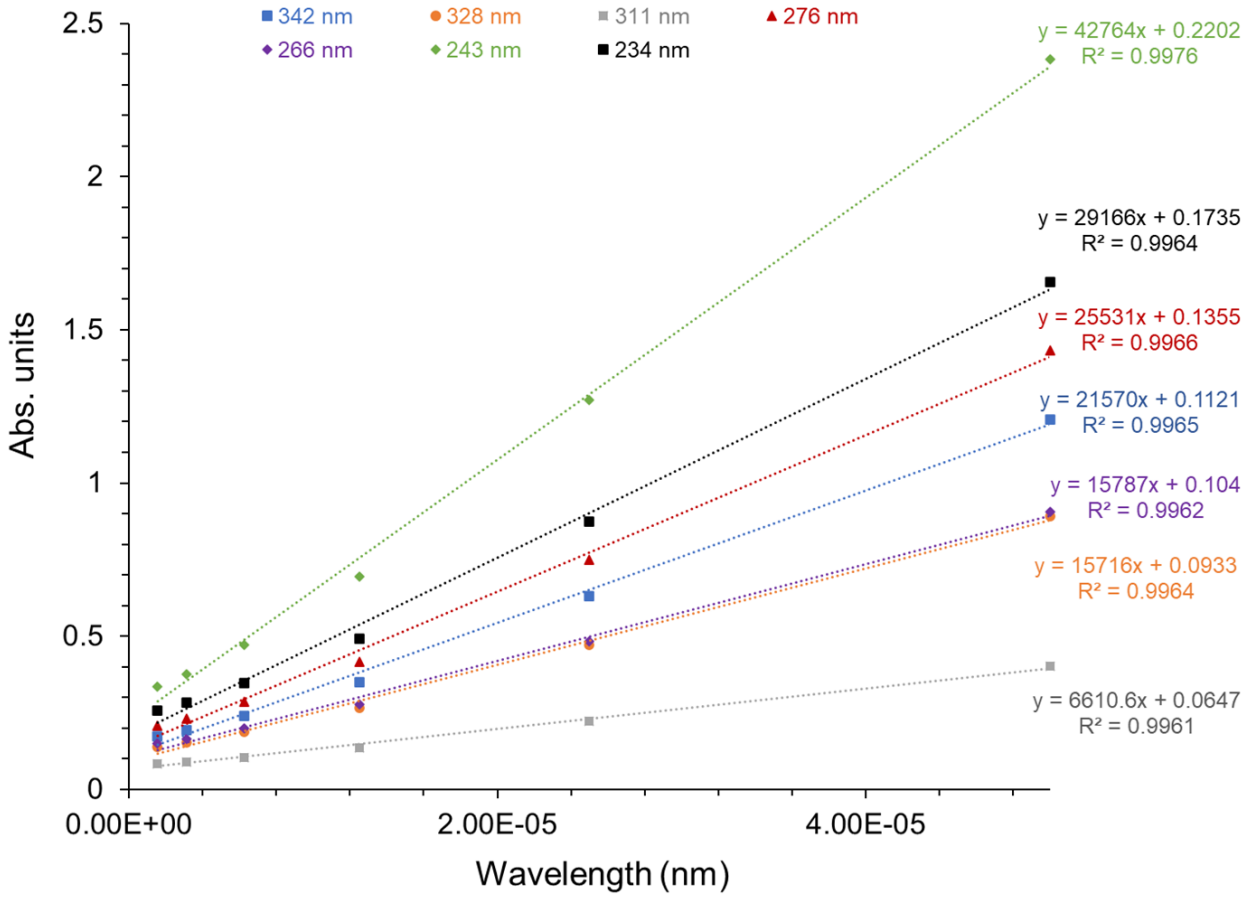

342 nm	328 nm	311 nm	276 nm	266 nm	243 nm	234 nm
21,570	15,716	6,610	25,531	15,787	42,764	29,166

Figure A.29 *Molar extinction coefficient* ($M^{-1}\cdot cm^{-1}$) *data for compound* ***2.4*** *in* CH_3CN

REFERENCES

1. Eggins, B. R., *Chemical Sensors and Biosensors*. Johns Wiley & Sons: Chichester, UK, 2007.
2. Ashrafi, A. M.; Koudelkova, Z.; Sedlackova, E.; Richtera, L.; Adam, V., Electrochemical Sensors and Biosensors for Determination of Mercury Ions. *J. Electrochem. Soc.* **2018,** *165*, B824-B834.
3. National Research Council, Expanding the Vision of Sensor Materials; National Academies Press:. Washington, DC, USA, 1995; pp 73-88.
4. McNaught, A. D.; Wilkinson, A., IUPAC Compendium of Chemical Terminology. 2 ed.; Blackwell Scientific Publications: Oxford, UK, 2014.
5. Macielag, M. J., Chemical Properties of Antimicrobials and Their Uniqueness. In *Antibiotic Discovery and Development*, Dougherty, T. J.; Pucci, M. J. (eds). Springer: Boston, 2012; pp 793-820.
6. Carter, K. P.; Young, A. M.; Palmer, A. E., Fluorescent Sensors for Measuring Metal Ions in Living Systems. *Chem. Rev.* **2014,** *114* (Bioinorganic Enzymology), 4564-4601.
7. Emsley, J., *The Elements*. Clarendon Press: 1998.
8. General Aspects of Trace Analytical Methods—IV. Recommendations for Nomenclature, Standard Procedures and Reporting of Experimental Data for Surface Analysis Techniques. *Pure & Appl. Chem*, **1979,** *51* (11), 2243-2250.
9. Bertini, I.; Gray, H. B.; Stiefel, E. I.; Valentine, J. S., *Biological Inorganic Chemsitry*. 1st ed.; Eds.;University Science Books: Sausalito, California, 2007.

10. Darr, J. A.; Poliakoff, M., New directions in inorganic and metal-organic coordination chemistry in supercritical fluids. *Chem. Rev* **1999,** *99,* 495-542.

11. Carter, S.; Fisher, A. S.; Hinds, M. W.; Lancaster, S.; Marshall, J., Atomic spectrometry update. Review of advances in the analysis of metals, chemicals and materials. *J. Anal. Atom. Spectrom.* **2013,** *28,* 1814-1869.

12. Shazzo, Y. K.; Karpov, Y. A., Laser sampling in inductively coupled plasma mass spectrometry in the inorganic analysis of solid samples. Elemental fractioning as the main source of errors. *J. Anal. Chem.* **2016,** *71*, 1069-1080.

13. Chen, S.-H.; Li, Y.-X.; Li, P.-H.; Xioa, X.-Y.; Jiang, M.; Li, S.-S.; Zhou, W.-Y.; Yang, M.; Huang, X.-J.; Liu, W.-Q., Electrochemical spectral methods for trace detection of heavy metals; A review. *TrAC Trends Anal. Chem.* **2018,** *106,* 139-150.

14. Fen, Y. W.; Yunus, W. M. M., Surface plasmon resonance spectroscopy as an alternative for sensing heavy metal ions. A review. *Sens. Rev.* **2013,** *33,* 305-314.

15. Sneddon, J., Atomic absorption spectrometry. In *Handbook of Instrumental Techniques for Analytical Chemistry,* Settle, F. A., Ed. Prentice Hall: Upper Saddle River, New Jersey, 1997; pp 373-393.

16. Varnes, A. W., Inductively coupled plasma mass spectrometry. In *Handbook of Instrumental Techniques,* Settle, F. A., Ed. Prentice Hall: Upper Saddle River, New Jersey, 1997; pp 419-439.

17. Kounaves, S. P., Voltammetric Techniques. In *Handbook of Instrumental Techniques for Analytical Chemistry,* Settle, F. A., Ed. Prentice Hall: Upper Saddle River, New Jersey, 1997; pp 709-725.

18. Havrilla, G. J., X-ray fluorescence spectrometry. In *Handbook of Instrumental Techniques for Analytical Chemistry*, Settle, F. A., Ed. Prentice Hall: Upper Saddle River, New Jersey, 1997; pp 459-479.

19. Valeur, B.; Leray, I., Design principles of fluorescent molecular sensors for cation recognition. *Coord. Chem. Rev.* **2000,** *205*, 3-40.

20. Kang, J.; Huo, F.; Zhang, Y.; Chao, J.; Glass, T. E.; Yin, C., A novel near-infrared ratiometric fluorescent probe for cyanide and its bioimaging applications. *Spectrochimica Acta Part A* **2019,** *209*, 95-99.

21. Czerwieniec, R.; Yu, J.; Yersin, H., Blue light emission of Cu(I) complexes and singlet harvesting. *Inorg. Chem.* **2011,** *50*, 8293-8301.

22. Zu, F.; Yan, F.; Bai, Z.; Xu, J.; Wang, Y.; Huang, Y.; Zhou, X., The quenching of the fluorescence of carbon dots. A review on the mechanisms and applications. *Microchim. Acta* **2017,** *184*, 1899-1914.

23. Lu, H.; Zeng, Y.; Zhao, X.; Wang, L.; Ma, S.; Han, X.; Xu, B.; Tian, W.; Gao, H., Highly efficient far/near-infrared solid fluorophores: Aggregation-induced emission, intramolecular charge transfer, twisted molecular conformation, and bioimaging applications. *Angew. Chem. Int. Ed.* **2016,** *55*, 155-159.

24. Padalkar, V. S.; Seki, S., Excited-state intramolecular proton transfer (ESIPT)-inspired solid state emitters. *Chem. Soc. Rev* **2016,** *45*, 169-202.

25. Rasheed, T.; Bilal, M.; Nabeel, F.; Iqbal, H. M.; Li, C.; Zhou, Y., Fluorescent sensor based models for the detection of environmentally-related toxic heavy metals. *Sci. Total Environ.* **2018,** *615*, 476-485.

26. Lipton, M., Chapter 1. Electronic Structure and Chemical Bonding. In *Organic Chemistry I*, Lipton, Ed. Libre Texts ed.: Purdue University, 2017.

27. Garcia, J. M.; Garcia, F. C.; Serna, F.; De la Pena, J. L., Fluorogenic and chromogenic polymer chemosensors. *Polym. Rev* **2011,** *51* (4), 341-390.

28. Kumar, R.; Bhalla, V.; Kumar, M., Cu^{2+} and CN^{-} - selective fluorogenic sensors based on pyrene appended and thiacalix[4]arenes. *Tetrahedron* **2008,** *64* (35), 8095-8101.

29. Suzuki, T.; Fujikura, K.; Higashiyama, T.; Takata, K., DNA Staining for Fluorescence and Laser Confocal Microscopy. *Journal of Histochemistry & Cytochemistry* **1997,** *45* (1), 49-53.

30. Min, W.; Lu, S.; Chong, S.; Roy, R.; Holtom, G. R.; Xie, X. S., Imaging chromophores with undetectable fluorescence by stimulated emission microscopy. *Nature* **2009,** *461*, 1105-1109.

31. Fluorophores. In *Principles of Fluorescence Spectroscopy*, Lakowicz, J. R., Ed. Springer US: Boston, MA, 2006; pp 63-95.

32. Lakowicz, J. R., *Principles of Fluorescence Spectroscopy*. 3rd ed.; Springer: New York, 2006.

33. Hardman, R., A toxicology review of quantum dots: Toxicity depends on physiochemical and environmental factors. *Environ. Health Perspect.* **2006,** *114* (2), 165-172.

34. Clark, J. Coordinate (Dative Covalent) Bonding. (accessed 2/8/2017).

35. Metal Chelation Chemistry. In *Chemosensors:Principles, Strategies, and Appplications*, Anslyn, E. V., Ed. John Wiley & Sons: Hoboken, New Jersey, 2011.

36. Anslyn, E. V.; Dougherty, D. A., *Modern Physical Organic Chemistry*. University Science Books: 2006.

37. Lakowicz, J. R., Introduction to Fluorescence. In *Principles of Fluorescence Spectroscopy*, 3rd ed.; Springer US: 2006; p 1.

38. Introduction to Fluorescence. (2003, June 20) Retrieved from https://micro.magnet.fsu.edu/primer/techniques/fluorescence/fluorointrohome.html

39. Lakowicz, J. R., Introduction to Fluorescence. In *Principles of Fluorescence Spectroscopy*, 3rd ed.; Springer US: 2006; p 15.

40. Lakowicz, J. R., *Principles of Fluorescence Spectroscopy. 3rd Edition*. Springer: New York, 2006.

41. Goswami, S.; Manna, A.; Paul, S.; Das, A. K.; Nandi, P. K.; Maity, A. K.; Saha, P., A turn on ESIPT probe for rapid and ratiometric fluorogenic detection of homocysteine and cysteine in water with live cell-imaging. *Tetrahedron Lett.* **2014,** *55* (2), 490-494.

42. Manandhar, E. Molecular probes for the detection of Zn^{2+}, and Fe^{3+} ions. University of Southern Mississippi, 2014.

43. Banfalvi, G., Heavy Metals, Trace Elements and their Cellular effects. In *Effects of Heavy Metals*, Springer: 2011; pp 3-28.

44. Tchounwou, P. B.; Yedjou, C. G.; Patlolla, A. K.; Sutton, D. J., Heavy Metals Toxicity and the Environement. *Exp Suppl.* **2012,** *101*, 133-164.

45. Singh, R.; Gautam, N.; Mishra, A.; Gupta, R., Heavy Metals and Living Systems: An Overview. *Indian Journal of Pharmacology* **2011,** *43* (3), 246-253.

46. Halim, M.; Conte, P.; Piccolo, A., Potential Availability of Heavy Metals to Phytoextraction From Contaminated Soils Induced By Exogenous Humic Substances. *Chemosphere* **2003,** *52* (1), 265-275.

47. Wuana, R. A.; Okiemen, F. E., Heavy Metals in Contaminated Soils: A Review of Sources, Chemistry, Risks and Best Available Strategies For Remediation. *International Scholarly Research Notices* **2011,** *2011*, 20.

48. Selvan, G. T.; Varadaraju, C.; Selvan, R. T.; Enoch, I. V. M. V.; Selvakumar, P. M., On/Off Fluorescent Chemosensor for Selective Detection of Divalent Iron and Copper Ions: Molecular Logic Operation and Protein Binding. *ACS OMEGA* **2018,** *3*.

49. Clayton, D. G.; Clayton, F. E., *Patty's industrial hygiene and toxicology: volume 2: part C, Toxicology*. 3 ed.; John Wiley & Sons: New York, NY, 1981.

50. WHO/FAO/IAEA *Trace elements in human nutrition and health*; World Health Organization: Geneva, 1996; pp 123-139.

51. Epsztejn, S.; Glickstein, H.; Picard, V.; Slotki, I. N.; Breuer, W.; Beaumont, C.; Cabantchik, Z., H-Ferritin subunit overexpression in erythroid cells reduces the oxidative stress response and induces multidrug resistance properties. *Blood* **1999,** *94* (10), 3593-3603.

52. Kaplan, C. D.; Kaplan, J., Iron acquisition and transcriptional regulation. *Chem. Rev.* **2009,** *109* (10), 4536-52.

53. Morrissey, J.; Guerinot, M. L., Iron uptake and transport in plants: The good, the bad, and the ionome. *Chem. Rev. (Washington, DC, U. S.)* **2009,** *109* (10), 4553-4567.

54. Sandy, M.; Butler, A., Microbial iron acquisition: Marine and terrestrial siderophores. *Chem. Rev. (Washington, DC, U. S.)* **2009,** *109* (10), 4580-4595.

55. Xing, W.; Liu, G., Iron biogeochemistry and its environmental impacts in freshwater lakes. *Fresenius Environ. Bull.* **2011,** *20* (6), 1339-1345.

56. Sahoo, S. K.; Sharma, D.; Bera, R. K.; Crisponi, G.; Callan, J. F., Iron(III) selective molecular and supramolecular fluorescent probes. *Chem. Soc. Rev.* **2012,** *41* (21), 7195-7227.

57. Krauss, S., Mitochondria: Structure and Role in Respiration. In *Nature Encyclopedia of Life Science*, Nature Publishing Group: 2001.

58. Beard, J., Iron deficiency alters brain development and functioning. *J. Nutr.* **2003,** *133* (5S-1), 1468S-1472S.

59. Erikson, K. M.; Jones, B. C.; Hess, E. J.; Zhang, Q.; Beard, J. L., Iron deficiency decreases dopamine D1 and D2 receptors in rat brain. *Pharmacol. Biochem. Behav.* **2001,** *69* (3/4), 409-418.

60. Hulthen, L., Iron deficiency and cognition. *Scandinavian Journal of Nutrition* **2003,** *47* (3), 152 - 156.

61. Ward, R. J.; Zucca, F. A.; Duyn, J. H.; Crichton, R. R.; Zecca, L., The role of iron in brain ageing and neurodegenerative disorders. *Lancet Neurol.* **2014,** *13* (10), 1045-1060.

62. Crichton, R., *Inorganic Biochemistry of Iron Metabolism: From Molecular Mechanisms to Clinical Consequences, Second Edition*. John Wiley & Sons: 2001; p No pp. given.

63. Hogarth, P., Neurodegeneration with brain iron accumulation: diagnosis and management. *J. Mov. Disord.* **2015,** *8* (1), 1-13.

64. Rivera-Mancia, S.; Perez-Neri, I.; Rios, C.; Tristan-Lopez, L.; Rivera-Espinosa, L.; Montes, S., The transition metals copper and iron in neurodegenerative diseases. *Chem.-Biol. Interact.* **2010,** *186* (2), 184-199.

65. Thompson, K. J.; Shoham, S.; Connor, J. R., Iron and neurodegenerative disorders. *Brain Res. Bull.* **2001,** *55* (2), 155-164.

66. Kozlowski, H.; Janicka-Klos, A.; Brasun, J.; Gaggelli, E.; Valensin, D.; Valensin, G., Copper, iron, and zinc ions homeostasis and their role in neurodegenerative disorders (metal uptake, transport, distribution and regulation). *Coord. Chem. Rev.* **2009,** *253* (21-22), 2665-2685.

67. Crichton, R., *Inorganic Biochemistry of Iron Metabolism*. 2nd ed ed.; John Wiley & Sons LTD: New York, 2001.

68. Richardson, D. R.; Lane, D. J. R.; Becker, E. M.; Huang, M. L.-H.; Whitnall, M.; Rahmanto, Y. S.; Sheftel, A. D.; Ponka, P., Mitochondrial iron trafficking and the integration of iron metabolism between the mitochondrion and cytosol. *PNAS* **2010,** *107* (24), 10775-10782.

69. IUPAC, Compendium of Chemical Terminology. In *The Gold Book* [Online] 2nd ed.; McNaught, A. D.; Wilkinson, A., Eds. Blackwell Scientific Publications, Oxford (1997): Online version (2019-) created by S. J. Chalk, 2014.

70. Davies, G.; Hanrissat, B., Structures and mechanisms of glycosyl hydrolysases. *Structure* **1995,** *3* (9), 853-859.

71. Lodish, H.; Berk, A.; Zipursky, S. L.; Matsudaira, P.; Baltimore, D.; Darnell, J. E., Cellular Energetics: Glycosis, Aerobic Oxidation, and Photosynthesis. In *Molecular Cell Biology*, 4th ed.; Tenney, S., Ed. W.H. Freeman and Company: New York, 2000.

72. Brown, P. L.; Ekberg, C., Introduction. In *Hydrolysis of Metal Ions*, Brown, P. L.; Ekberg, C., Eds. Wiley-VCH Verlag GmbH & Co.: Germany, 2016; Vol. 2.

73. Martell, A. E.; Hancock, R. D., *Metal Complexes in Aqueous Solutions*. Plenum Press: New York, 1996; p 8-9.

74. Lemire, R. J.; Berner, U.; Musikas, C.; Palmer, D. A.; Taylor, P.; Tochiyama, O., *Chemical Thermodynamics of Iron Part 1*. OECD: 2013; Vol. 13a.

75. Powell, K. J.; Brown, P. L.; Byrne, R. H.; Gajda, T.; Hefter, G.; Sjoberg, S.; Wanner, H., Chemical Speciation of Environmentally Significant Metals with Inorganic Ligands. *Pure Appl. Chem* **2007,** *79* (5), 895-950.

76. De Robertis, A.; De Stefano, C.; Foti, C.; Signorino, G., Thermodynamic parameters for the formation of dimeric hydrolytic species of copper(II) in aqueous $NaClO_4$ solution at different ionic strengths. *Talanta* **1997,** *44* (10), 1839-1846.

77. Fenwick, F., The equilibrium between cupric ion, cuprous ion, and metallic copper. *J. Am. Chem. Soc.* **1926,** *48* (4), 860-870.

78. Das, T. K.; Wati, M. R.; Fatima-Shad, K., Oxidative stress gated by fenton and haber Weiss reactions and its association with Alzheimer's diseaseOxidative

Stress Gated by Fenton and Haber Weiss Reactions and Its Association With Alzheimer's Diseas. *Arch Neurosci.* **2014,** *3*.

79. Brown, P. L.; Ekberg, C., First Transition Series Metal. In *Hydrolysis of Metal Ions*, Wiley-VCH Verlag GmbH & Co.: Germany, 2016; Vol. 2.

80. Plyasunova, N. V.; Wang, M.; Zhang, Y.; Muhammad, M., Critical evaluation of thermodynamics of complex formation of metal ions in aqueous solutions II. Hydrolysis of hydroxo-complexes of Cu^{2+} at 298.15K. *Hydrometallurgy* **1997,** *45*, 37-51.

81. Stefansson, A., Iron(III) Hydrolysis and Solubility at 25 °C. *Environ. Sci. Technol.* **2007,** *41* (17), 6117-6123.

82. Cotton, F. A.; Wilkinson, G.; Murillo, C. A.; Bochmann, M., The Elements of the First Transition Series: Iron. In *Advanced Inorganic Chemistry*, 6 ed.; John Wiley & Sons, Inc.: New York, 1999; pp 775-814.

83. Lu, J.-B.; Jian, J.; Huang, W.; Li, J.; Zhou, M., Experimental and theoretical identification of the Fe(VII) oxidation state in FeO_4^-. *Phys. Chem. Chem. Phys.* **2016,** (45).

84. Sunda, W.; Huntsman, S., Effect of pH, light, and temperature on Fe-EDTA chelation and Fe hydrolysis in seawater. *Marine Chemistry* **2003,** *84*, 35-47.

85. Byrne, R. H.; Luo, Y.-R.; Young, R. W., Iron hydrolysis and solubility revisited: observations and comments on iron hydrolysis characterizations. *Marine Chemistry* **2000,** *70* (1-3), 23-35.

86. Dzombak, D. A.; Morel, F. M. M., *Surface Complexation Modeling: Hydrous Ferric Oxide*. John Wiley & Sons: New York, 1990.

87. Byrne, R. H.; Yao, W.; Luo, Y.-R.; Wang, B., The dependence of Fe^{III} hydrolysis on ionic strength in NaCl solutions. *Marine Chemistry* **2005,** *97* (1-2), 34-48.

88. Ziemniak, S. E.; Jones, M. E.; Combs, K. E. S., Magnetite solubility and phase stability in alkaline media at elevated temperatures. *J Solution Chem*. **1995,** *24* (9), 837-877.

89. v. Bünau, G., J. B. Birks: Photophysics of Aromatic Molecules. Wiley-Interscience, London 1970. 704 Seiten. Preis: 210s. *Berichte der Bunsengesellschaft für physikalische Chemie* **1970,** *74* (12), 1294-1295.

90. Cho, H. K.; Lee, D. H.; Hong, J.-I., A fluorescent pyrophosphate sensor via excimer formation in water. *Chem. Commun.* **2005,** (13), 1690-1692.

91. Manandhar, E.; Wallace, K. J., Host–guest chemistry of pyrene-based molecular receptors. *Inorganica Chimica Acta* **2012,** *381*, 15-43.

92. Manandhar, E.; Broome, H. J.; Myrick, J.; Lagrone, W.; Cragg, P. J.; Wallace, K. J., A pyrene-based fluorescent sensor for Zn^{2+} ions: a molecular 'butterfly'. *Chem. Commun.* **2011,** (31).

93. Gao, Y. Y.; Ma, T. T.; Ou, Z. Z.; Cai, W. J.; Yang, G. Q.; Li, Y.; Xu, M. H.; Li, Q. Q., Highly sensitive and selective turn-on fluorescent chemosensors for Hg2+ based on thioacetal modified pyrene. *Talanta* **2018,** *178*, 663-669.

94. Manandhar, E.; Cragg, P. J.; Wallace, K. J., Detection of Zn(II) ions by fluorescent pyrene-derived molecular probes. *Supramolecular Chemistry* **2014,** *26* (3), 141-150.

95. Shyamal, M.; Maity, S.; Maity, A.; Maity, R.; Roy, S.; Misra, A., Aggregation induced emission based "turn-off" fluorescent chemosensor for selective and swift sensing of mercury (II) ions in water. *Sens. Actuators B-Chemical* **2018,** *263*, 347-359.

96. Birks, J. B., Excimers. *Rep. Prog. Phys.* **1975,** *38* (8), 903-974.

97. Karuppannan, S.; Chambron, J.-C., Supramolecular Chemical Sensors Based on Pyrene Monomer–Excimer Dual Luminescence. *Chemistry – An Asian Journal* **2011,** *6* (4), 964-984.

98. Wu, C.; Wang, C.; Yan, L.; Yang, C. J., Pyrene excimer nucleic acid probes for biomolecule signaling. *J. Biomed Nanotechnol* **2009,** *5* (5), 495-504.

99. Wakchaure, V. C.; Das, T.; Babu, S. S., Boron-Conjugated Pyrenes as Fluorescence-Based Molecular Probes and Security Markers. *ChemPlusChem* **2019,** *84* (9), 1253-1256.

100. Detriche, S.; Devillers, S.; Seffer, J. F.; Nagy, J. B.; Mekhalif, Z.; Delhalle, J., The use of water-soluble pyrene derivatives to probe the surface of carbon nanotubes. *Carbon* **2011,** *49* (9), 2935-2943.

101. Singh, G.; Singh, P. K., Stimulus-Responsive Supramolecular Host–Guest Assembly of a Cationic Pyrene Derivative with Sulfated β-Cyclodextrin. *Langmuir* **2019,** *35* (45), 14628-14638.

102. Shellaiah, M.; Rajan, Y. C.; Balu, P.; Murugan, A., A pyrene based Schiff base probe for selective fluorescence turn-on detection of Hg2+ ions with live cell application. *New J. Chem.* **2015,** *39* (4), 2523-2531.

103. Brynn Hibbert, D.; Thordarson, P., The death of the Job plot, transparency, open science and online tools, uncertainty estimation methods and other developments in supramolecular chemistry data analysis. *Chem. Commun.* **2016,** *52* (87), 12792-12805.

104. Mukherjee, S.; Talukder, S., A Reversible Pyrene-based Turn-on Luminescent Chemosensor for Selective Detection of Fe3+ in Aqueous Environment with Logic Gate Application. *Journal of Fluorescence* **2016,** *26* (3), 1021-1028.

105. Manandhar, E. Molecular Probes for the Detection of Zn2+ and Fe3+ Ions. University of Southern Mississippi, 2014.

106. Taylor, V. F.; March, R. E.; Longerich, H. P.; Stadey, C. J., A mass spectrometric study of glucose, sucrose, and fructose using an inductively coupled plasma and electrospray ionization. *Int. J. Mass Spectrom.* **2005,** *243* (1), 71-84.

107. Berlman, I. B., 5 - SOME USES OF FLUORESCENCE COMPOUNDS. In *Handbook of Fluorescence Spectra of Aromatic Molecules (Second Edition)*, Berlman, I. B., Ed. Academic Press: 1971; pp 96-106.

108. Farhangi, S.; Duhamel, J., Pyrenyl Derivative with a Four-Atom Linker That Can Probe the Local Polarity of Pyrene-Labeled Macromolecules. *J. Phys.Chem. B* **2016,** *120* (4), 834-842.

109. Siu, H.; Duhamel, J., Molar Absorption Coefficient of Pyrene Aggregates in Water. *J. Phys.l Chem. B* **2008,** *112* (48), 15301-15312.

110. Chen, S.; Yu, Y.-L.; Wang, J.-H., Inner filter effect-based fluorescent sensing systems: A review. *Analytica Chimica Acta* **2018,** *999*, 13-26.

111. Martínez, R.; Espinosa, A.; Tárraga, A.; Molina, P., New Hg2+ and Cu2+ Selective Chromo- and Fluoroionophore Based on a Bichromophoric Azine. *Org. Lett.* **2005,** *7* (26), 5869-5872.

112. Becker, W.; Bergmann, A., Lifetime Imaging Techniques for Optical Microscopy. *Research Gate* **2003**.

113. Lakowicz, J. R.; Szmacinski, H.; Nowaczyk, K.; Berndt, K. W.; Johnson, M., Fluorescence lifetime imaging. *Anal. Biochem*. **1992,** *202* (2), 316-30.

114. Lakowicz, J. R.; Malicka, J.; Gryczynski, I., Silver particles enhance emission of fluorescent DNA oligomers. *Biotechniques* **2003,** *34* (1), 62-6, 68.

115. Beija, M.; Afonso, C. A. M.; Martinho, J. M. G., Synthesis and applications of Rhodamine derivatives as fluorescent probes. *Chem. Soc. Rev.* **2009,** *38* (8), 2410-2433.

116. Best, M.; Porth, I.; Hauke, S.; Braun, F.; Herten, D.-P.; Wombacher, R., Protein-specific localization of a rhodamine-based calcium-sensor in living cells. *Org. Biomol. Chem*. **2016,** *14* (24), 5606-5611.

117. Grimm, J. B.; English, B. P.; Chen, J.; Slaughter, J. P.; Zhang, Z.; Revyakin, A.; Patel, R.; Macklin, J. J.; Normanno, D.; Singer, R. H.; Lionnet, T.; Lavis, L. D., A general method to improve fluorophores for live-cell and single-molecule microscopy. *Nature Methods* **2015,** *12* (3), 244-250.

118. Ceresole, M. Production of new red coloring matter. US377349, 1888.

119. Brannon, J.; Magde, D., Absolute quantum yield determination by thermal blooming : fluorescein. *J. Phys. Chem*. **1978,** *82* (6), 705-709.

120. Fischer, M.; Georges, J., Fluorescence quantum yield of rhodamine 6G in ethanol as a function of concentration using thermal lens spectrometry. *Chem Phys Lett* **1996,** *260*, 115-118.

121. Arbeloa, F. L.; Ojeda, P. R.; Arbeloa, I. L., The fluorescence quenching mechanisms of rhodamine 6G in concentrated ethanolic solution. *J. Photochem. Photobiol. A: Chemistry* **1988,** *45*, 313-323.

122. Karstens, T.; Kobe, K., Rhodamine B and Rhodamine 101 as reference substances for fluorescence qantum yield measurements. *J. Phys. Chem.* **1980** *84*, 1871-1872.

123. Kubin, R. F.; Fletcher, A. N., Fluorescence quantum yields of some rhodamine dyes. *J. Lumin.* **1982,** *27* (4), 455-462.

124. Ramette, R. W.; Sandell, E. B., Rhodamine B equilibriums. *J. Am. Chem. Soc.* **1956,** *78*, 4872-4878.

125. Yang, Y.; Zhao, Q.; Feng, W.; Li, F., Luminescent Chemodosimeters for Bioimaging. *Chem. Rev.* **2012,** *113*, 192-270.

126. Dujols, V.; Ford, F.; Czarnik, A. W., A Long-Wavelength Fluorescent Chemodosimeter Selective for Cu(II) Ion in Water. *J. Am. Chem. Soc.* **1997,** *119* (31), 7386-7387.

127. Eftink, M. R., Fluorescence Quenching: Theory and Application. In *Topics in Fluorescence Spectroscopy*, Lakowicz, J. R., Ed. Kluwer Academic Publishers: New York, 2002; Vol. 2.

128. Bakkialakshmi, S.; Selvarani, P.; Chenthamarai, S., Fluorescence quenching of rhodamine B base by two amines. *Spectrochimica Acta Part A: Molecular and Biomolecular Spectroscopy* **2013,** *105*, 557-562.

129. Best, Q. A.; Xu, R.; McCarroll, M. E.; Wang, L.; Dyer, D. J., Design and investigation of a series of rhodamine-based fluorescent probes for optical measurements of pH. *Org. Lett.* **2010,** *12* (14), 3219-3221.

130. Liang, Y.; Wang, R.; Liu, G.; Pu, S., Bifunctional Cu2+/Fe3+ Probe with Independent Signal Outputs Based on a Photochromic Diarylethene with a Dansylhydrazine Unit. *ACS Omega* **2019,** *4* (4), 6597-6606.

131. Sun, Y.-Q.; Liu, J.; Lv, X.; Liu, Y.; Zhao, Y.; Guo, W., Rhodamine-Inspired Far-Red to Near-Infrared Dyes and Their Application as Fluorescence Probes. *Angew. Chem. Int. Edit.* **2012,** *51* (31), 7634-7636.

132. Geng, T.-M.; Wu, D.-Y.; Huang, W., Dual turn-on fluorescent chemosensor for Cu^{2+} and Hg^{2+} in aqueous medium based on a water-soluble polyacrylamide containing rhodamine. *J. Polym. Res.* **2015,** *22* (40).

133. Wang, X.; Tao, J.; Chen, X.; Yang, H., An ultrasensitive and selective "off-on" rhodamine-based colorimetric and fluorescent chemodosimeter for the detection of Cu^{2+}. *Sens. Actuators B: Chemical* **2017,** (244), 709-716.

134. Xua, L.; Weia, S.; Diaob, Q.; Maa, P.; Liua, X.; Ying Suna; Songa, D.; Wang, X., Sensitive and selective rhodamine-derived probes for fluorometric sensing of pH and colorimetric sensing of Cu^{2+}. *Sens. Actuators B: Chemical* **2017,** *246*, 395-401.

135. Weerasinghe, A. J.; Abebe, F. A.; Sinn, E., Rhodamine based turn-ON dual sensor for Fe^{3+} and Cu^{2+}. *Tetrahedron Letters* **2011,** (52), 5648-5651.

136. Ferreira, C. M. H.; Pinto, I. S. S.; Soares, E. V.; Soares, H. M. V. M., (Un)suitability of the use of pH buffers in biological, biochemical and

environmental studies and their interaction with metal ions- a review. *RSC Adv.* **2015,** (39), 30989-31003.

137. Goswami, S.; Das, S.; Aich, K.; Sarkar, D.; Mondal, T. K.; Quah, C. K.; Fun, H.-K., CHEF induced highly selective and sensitive turn-on fluorogenic and colorimetric sensor for Fe^{3+}. *Dalton Trans.* **2013**.

138. Chereddy, N. R.; Thennarasu, S.; Mandal, A. B., A highly selective and efficient single molecular FRET based sensor for ratiometric detection of Fe^{3+} ions. *Analyst* **2013,** (5).

139. Ferreira, B. R. V.; Correa, D. N.; Eberlin, M. N.; Vendramini, P. H., Fragmentation reactions of rhodamine B and 6G as revealed by high orbitrap tandem mass spectrometry. *J. Braz. Chem. Soc.* **2017,** *28* (1).

140. Mazumdar, S.; Banerjee, S., Electrospray Ionization Mass Spectrometry: A Technique to Access the Information beyond the Molecular Weight of the Analyte. *International Journal of Analytical Chemistry* **2012**.

141. Chatterjee, A.; Banerjee, M.; Khandare, D. G.; Gawas, R. U.; Mascarenhas, S. C.; Ganguly, A.; Gupta, R.; Joshi, H., Aggregation-Induced Emission-Based Chemodosimeter Approach for Selective Sensing and Imaging of Hg(II) and Methylmercury Species. *Anal. Chem.* **2017,** *89* (23), 12698-12704.

142. karimi, M.; Badiei, A.; Ziarani, G. M., A Novel Naphthalene-Immobilized Nanoporous SBA-15 as a Highly Selective Optical Sensor for Detection of Fe3+ in Water. *Journal of Fluorescence* **2015,** *25* (5), 1297-1302.

143. Sasaki, S.; Drummen, G. P. C.; Konishi, G.-i., Recent advances in twisted intramolecular charge transfer (TICT) fluorescence and related phenomena in materials chemistry. *J. Mater. Chem. C* **2016,** *4* (14), 2731-2743.

144. Sahana, A.; Banerjee, A.; Lohar, S.; Sarkar, B.; Mukhopadhyay, S. K.; Das, D., Rhodamine-Based Fluorescent Probe for Al3+ through Time-Dependent PET–CHEF–FRET Processes and Its Cell Staining Application. *Inorg. Chem.* **2013,** *52* (7), 3627-3633.

145. Sun, Y.; Hays, N. M.; Periasamy, A.; Davidson, M. W.; Day, R. N., Monitoring Protein Interactions in Living Cells with Fluorescence Lifetime Imaging Microscopy. *Methods Enzymol.* **2012,** *504*, 371-391.

146. Selanger, K. A.; Falnes, J.; Sikkeland, T., Fluorescence lifetime studies of Rhodamine 6G in methanol. *J. Phys.Chem.* **1977,** *81* (20), 1960-1963.

147. Liu, G.; Lu, H., Laser-induced Fluorescence of Rhodamine B in Ethylene Glycol Solution. *Procedia Engineering* **2015,** *102*, 95-105.

148. Hammler, D.; Marx, A.; Zumbusch, A., Fluorescence-Lifetime-Sensitive Probes for Monitoring ATP Cleavage. *Chem. Eur. J.* **2018,** *24* (57), 15329-15335.

149. Xiang, Y.; Zifan, L.; Chen, X.; Tong, A., Highly sensitive and selective optical chemosensor for determination of Cu^{2+} in aqueous solution. *Talanta* **2008,** *74*, 1148-1153.

150. Zhao, M.; Yang, X.-F.; He, S.; Wang, L., A rhodamine-based chromogenic and fluorescent chemosensor for copper ion in aqueous media. *Sens. Actuators B: Chemical* **2009,** *135* (2), 625-631.

151. Shyamal, M.; Mazumdar, P.; Maity, S.; Samanta, S.; Sahoo, G. P.; Misra, A., Highly Selective Turn-On Fluorogenic Chemosensor for Robust Quantification of Zn(II) Based on Aggregation Induced Emission Enhancement Feature. *ACS Sensors* **2016,** *1* (6), 739-747.

152. *Copper in Drinking Water*. The National Academies Press: Washington, D.C, 2000.

153. Raju, M.; Nair, R. R.; Raval, I. H.; Haldar, S.; Chatterjee, P. B., A water soluble Cu2+-specific colorimetric probe can also detect Zn2+ in live shrimp and aqueous environmental samples by fluorescence channel. *Sens. Actuators B: Chemical* **2018,** *260*, 364-370.

154. Swamy, K. M. K.; Ko, S.-K.; Kwon, S. K.; Lee, H. N.; Mao, C.; Kim, J.-M.; Lee, K.-H.; Kim, J.; Shin, I.; Yoon, J., Boronic acid-linked fluorescent and colorimetric probes for copper ions. *Chem Comm*. **2008,** (45), 5915-5917.

155. Yu, C.; Zhang, J.; Wang, R.; Chen, L., Highly sensitive and selective colorimetric and off-on fluorescent probe for Cu2+ based on rhodamine derivative. *Org. Biomol. Chem*. **2010,** *8* (23), 5277-5279.

156. Serra-Gómez, R.; Tardajos, G.; González-Benito, J.; González-Gaitano, G., Rhodamine solid complexes as fluorescence probes to monitor the dispersion of cyclodextrins in polymeric nanocomposites. *Dyes and Pigments* **2012,** *94* (3), 427-436.

157. Liu, J.; Cheng, J.; Ma, X.; Zhou, X.; Xiang, H., Photophysical properties and pH sensing applications of luminescent salicylaldehyde derivatives. *Research on Chemical Intermediates* **2016,** *42* (5), 5027-5048.

158. Guerinot, M. L., Microbial Iron Transport. *Annu. Rev. Micro.* **1994,** *48* (1), 743-772.

159. Krewulak, K. D.; Vogel, H. J., Structural biology of bacterial iron uptake. *Biochimica et Biophysica Acta (BBA) - Biomembranes* **2008,** *1778* (9), 1781-1804.

160. Raines, D. J.; Sanderson, T. J.; Wilde, E. J.; Duhme-Klair, A. K., Siderophores. In *Reference Module in Chemistry, Molecular Sciences and Chemical Engineering*, Elsevier: 2015.

161. Miethke, M.; Marahiel, M. A., Siderophore-Based Iron Acquisition and Pathogen Control. *Microbiol. Mol. Biol Rev.* **2007,** *71* (3), 413.

162. Loomis, L. D.; Raymond, K. N., Solution equilibria of enterobactin and metal-enterobactin complexes. *Inorg. Chem.* **1991,** *30* (5), 906-911.

163. Rütschlin, S.; Böttcher, T., Chapter Three - Engineering siderophores. In *Methods in Enzymology*, Shukla, A. K., Ed. Academic Press: 2020; Vol. 633, pp 29-47.

164. Phillips, D. J.; Davies, G.-L.; Gibson, M. I., Siderophore-inspired nanoparticle-based biosensor for the selective detection of Fe3+. *J. Mater.Chem B* **2015,** *3* (2), 270-275.

165. Ouchetto, H.; Dias, M.; Mornet, R.; Lesuisse, E.; Camadro, J. M., A new route to trihydroxamate-containing artificial siderophores and synthesis of a new fluorescent probe. *Bioorganic & Medicinal Chemistry* **2005,** *13* (5), 1799-1803.

166. Noël, S.; Guillon, L.; Schalk, I. J.; Mislin, G. L. A., Synthesis of Fluorescent Probes Based on the Pyochelin Siderophore Scaffold. *Org. Lett.* **2011,** *13* (5), 844-847.